Universiteit
Leiden
The Netherlands

A molecular journey : tales of sublimating ices from hot cores to comets

Bogelund, E.G.

Citation
Bogelund, E. G. (2019, March 14). *A molecular journey : tales of sublimating ices from hot cores to comets*. Retrieved from https://hdl.handle.net/1887/69725

Version:	Not Applicable (or Unknown)
License:	Licence agreement concerning inclusion of doctoral thesis in the Institutional Repository of the University of Leiden
Downloaded from:	https://hdl.handle.net/1887/69725

Note: To cite this publication please use the final published version (if applicable).

Cover Page

Universiteit Leiden

The handle http://hdl.handle.net/1887/69725 holds various files of this Leiden University dissertation.

Author: Bogelund, E.G.
Title: A molecular journey : tales of sublimating ices from hot cores to comets
Issue Date: 2019-03-14

A Molecular Journey

Tales of sublimating ices from hot cores to comets

ISBN: 978-94-028-1374-6

A Molecular Journey

Tales of sublimating ices from hot cores to comets

Proefschrift

ter verkrijging van
de graad van Doctor aan de Universiteit Leiden,
op gezag van Rector Magnificus prof. mr. C.J.J.M. Stolker,
volgens besluit van het College voor Promoties
te verdedigen op donderdag 14 maart 2019
klokke 10:00 uur

door

Eva Graulund Bøgelund
geboren te Kopenhagen, Denemarken
in 1987

Promotores:	Prof. dr. E.F. van Dishoeck Prof. dr. M.R. Hogerheijde
Promotiecommissie:	Prof. dr. H.J.A. Röttgering Prof. dr. A.G.G.M. Tielens Prof. dr. P. Schilke (University of Cologne) Prof. dr. I. de Pater (University of California, Berkeley) Dr. S. Charnley (Goddard Space Flight Center, NASA)

Cover design and layout by Wijnand Blok-Salinas Poblete

Image credit: Adobe Stock (backgrounds)
ESO/S. Guisard, www.eso.org/∼sguisard (ALMA antennas)

An electronic version of this thesis can be found at openaccess.leidenuniv.nl

"Vor Tid er Eventyrets Tid."
— H.C. Andersen, *Dryaden (1868)*

Table of contents

1 Introduction **1**
- 1.1 The formation of stars and planetary systems . . . 2
- 1.2 Chemistry in star-forming regions . . . 9
- 1.3 Star formation in the era of ALMA . . . 13
- 1.4 This thesis . . . 14
  - 1.4.1 Analysis tools used in the thesis . . . 16
  - 1.4.2 Overview of chapters and general conclusions . . . 17
- 1.5 A look to the future . . . 21

2 Low levels of methanol deuteration in the high-mass star-forming region NGC 6334I **25**
- 2.1 Introduction . . . 27
- 2.2 Observations and analysis method . . . 30
  - 2.2.1 Observations . . . 30
  - 2.2.2 Analysis method . . . 30
- 2.3 Results . . . 34
  - 2.3.1 $^{13}CH_3OH$ . . . 34
  - 2.3.2 $CH_3^{18}OH$ . . . 35
  - 2.3.3 CH_2DOH . . . 37
  - 2.3.4 CH_3OD . . . 39
- 2.4 Methanol deuteration fractions . . . 39
  - 2.4.1 NGC 6334I . . . 39
  - 2.4.2 Comparison with other sources . . . 45
  - 2.4.3 Comparison with models . . . 47
- 2.5 Summary and conclusion . . . 49

Appendix . . . 52

3 Methylamine and other simple N-bearing species in the hot cores NGC 6334I MM1 – 3 **77**
- 3.1 Introduction . . . 79
  - 3.1.1 Previous detections and potential formation routes for methylamine and related species . . . 79
  - 3.1.2 NGC 6334 . . . 81
- 3.2 Observations and method . . . 81
  - 3.2.1 Observations . . . 81

3.2.2 Method . . . 82
3.3 Results . . . 84
3.3.1 Methylamine CH_3NH_2 . . . 87
3.3.2 Summary of results on methanimine, methyl cyanide and formamide . . . 90
3.4 Discussion . . . 90
3.4.1 Methylamine towards NGC 6334I . . . 90
3.4.2 Methylamine towards other objects . . . 94
3.4.3 Comparison with comet 67P . . . 95
3.4.4 Other N-bearing species . . . 96
3.5 Summary . . . 96
Appendix . . . 98

4 Molecular complexity on disk-scales uncovered by ALMA: The chemical composition of the high-mass protostar AFGL 4176 113
4.1 Introduction . . . 115
4.1.1 AFGL 4176 . . . 116
4.2 Observations and methods . . . 117
4.2.1 Observations . . . 117
4.2.2 Methods for line identification and modelling . . . 119
4.3 Results . . . 120
4.3.1 Upper limit on the column density of glycolaldehyde . . . 122
4.3.2 Isotopologues with only blended lines . . . 123
4.3.3 Spatial distribution of selected species . . . 123
4.4 Discussion . . . 124
4.4.1 Comparison with the high-mass star-forming regions in Sgr B2(N) and Orion KL . . . 127
4.4.2 Comparison with the low-mass protobinary IRAS 16293–2422 . . . 130
4.4.3 Comparison with chemical models . . . 131
4.5 Summary . . . 133
Appendix . . . 134

5 Exploring the volatile composition of comets C/2012 F6 (Lemmon) and C/2012 S1 (ISON) with ALMA 143
5.1 Introduction . . . 145
5.2 Observations . . . 146
5.3 Spatial distribution of molecules . . . 148
5.3.1 Comet Lemmon . . . 148
5.3.2 Comet ISON . . . 149
5.4 Model . . . 149
5.4.1 Molecular production rates and parent scale lengths . . . 156
5.4.2 Formation scenarios for detected molecules . . . 158
5.4.3 Integrated intensity maps . . . 160
5.4.4 HCN(4–3)/(3–2) line ratio . . . 160
5.5 Conclusion . . . 163

Bibliography **165**

Nederlandse Samenvatting **175**

Dansk resumé **183**

English Summary **191**

List of Publications **199**

Curriculum Vitae **201**

Acknowledgements **203**

Introduction

Throughout the Milky Way, stars are continuously being born, evolving and dying in a life cycle dictated by simple laws of physics. During this cycle, the material from which the stars form is processed in a number of different reactions under varying environmental conditions. The reservoir which holds this material is called the interstellar medium (ISM) and is found throughout the Galaxy. The ISM is generally a heterogeneous structure, however; small, cool and dense regions exist within it and it is in these regions that new stars are formed. As the stars evolve, their material is processed in the stellar interiors through a succession of nuclear fusion reactions which enrich the material with heavy elements. The enriched material is eventually returned to the ISM, either in a continuous manner via stellar winds or in an instantaneous manner via supernova explosions. This injection of stellar mass back into the ISM is accompanied by the release of large amounts of energy, generating turbulent motions and triggering new star formation in dense regions. With this last step, the loop of the ISM cycle is closed (see Fig. 1.1).

The subject of this thesis is the chemistry associated with the regions of the Galaxy in which new stars are being formed. Specifically, the thesis focuses on characterising the complex molecules found in these regions and compares the reservoirs of species found in sites of low- and high-mass star formation, respectively. The molecular compositions associated with the star-forming clouds are also compared with the chemical inventory of Solar System comets in an attempt to better understand the initial conditions of the Solar Nebula.

The subsequent sections will outline the primary physical and chemical processes associated with the formation of stars and planetary systems. Next, the main scientific questions investigated in the thesis will be summarised. The general conclusions drawn on the basis of the presented work will then be stated before the introduction is concluded by an outlook.

1.1 The formation of stars and planetary systems

Stars form from clouds of interstellar gas and dust that become so dense that they no longer are able to withstand the force of gravity, making them unstable, and bringing them to collapse. During this collapse, the material of the cloud is heated due to release of gravitational potential energy until the temperature and density in the centre of the forming star finally reaches such heights that nuclear fusion processes can take place. At this point the forming star has reached a state of hydro- and thermodynamical equilibrium and settles onto the main sequence; it has reached the end of its formation and has emerged from its natal cloud (see, e.g, Stahler & Palla, 2005).

The simple formation process outlined above is in reality a much more complicated affair, intrinsically linked to a number of physical mechanisms including gravity, magnetic field interactions, turbulence and gas- and radiation pressure. Despite each of these phenomena being fairly well understood by themselves, when combined, they still comprise a multitude of unanswered questions. These include speculations of whether stars form primarily from spontaneous gravitational insta-

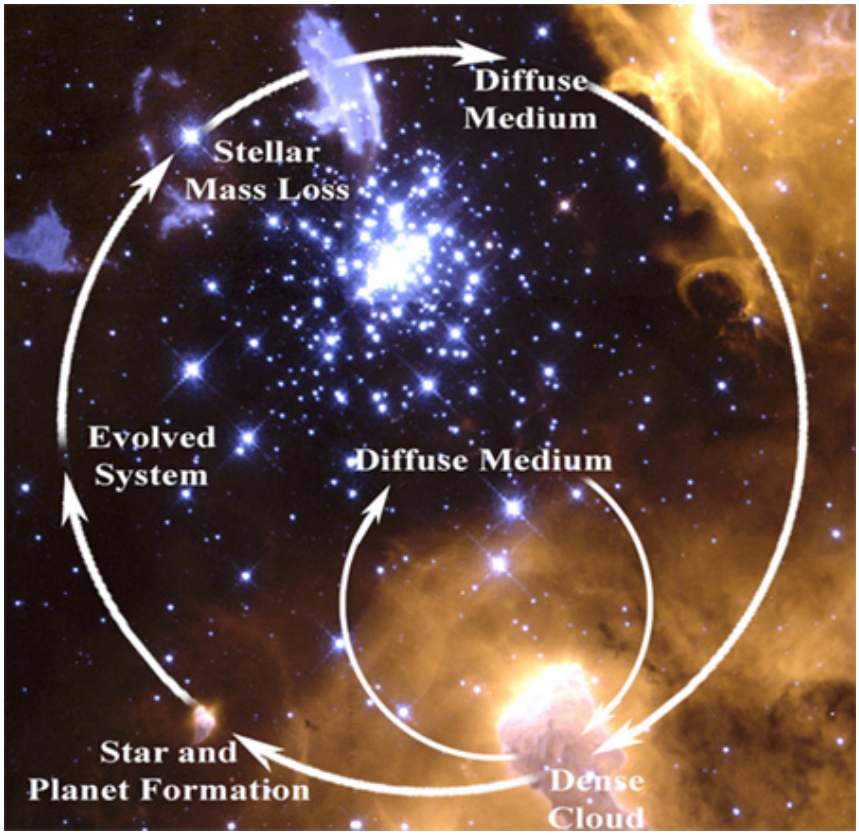

Figure 1.1: The life cycle of interstellar material. Main stages are as follows: (1) the formation of stars and planetary systems as dense and cold clouds collapse. (2) The processing of light elements into heavy elements by nuclear fusion as stars evolve. (3) The recycling of enriched materials into interstellar space by stellar mass loss as stars evolve and die. (4) New stars forming from the enriched material and the process beginning anew. Composite image adapted form the website of NASA/Goddard Space Flight Center/GCA. Background: NGC 3603 imaged by HTS. Credit: NASA/ESA/STScI-JPL/IPAC-UW-UI-UC.

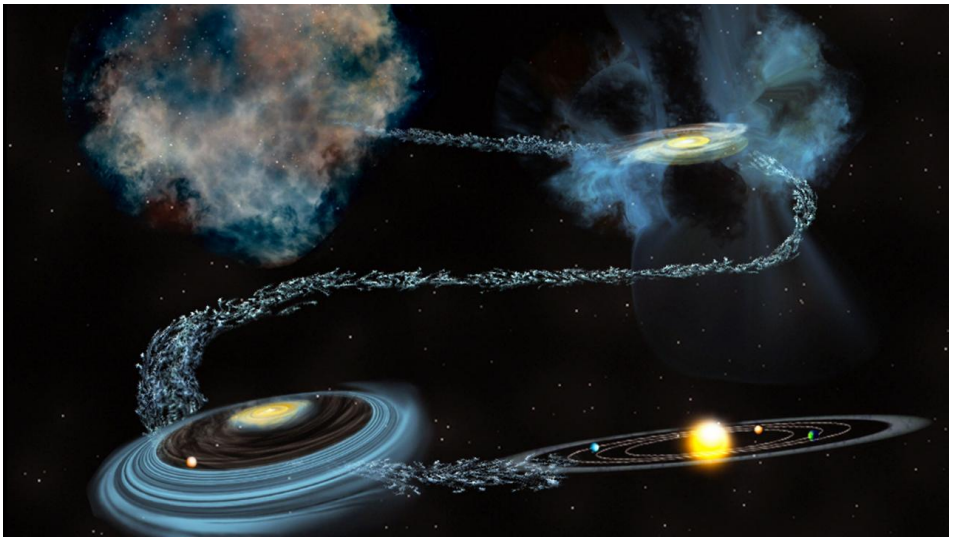

Figure 1.2: Artist impression of the evolutionary progression from the molecular cloud through the stages of a star-disk system embedded in a surrounding envelope, a star-disk system without an envelope and finally a mature star and planetary system. Image credit: B. Saxton/NSF/AUI/NRAO.

bilities or if their formation is externally triggered; if the formation of high-mass stars differs from that of low-mass stars; and whether accretion is continuous or episodic and how fast and efficient the formation process is. In summary, it remains a challenge to understand the wide variety of interlinked physical and chemical processes involved in star formation.

Despite the open questions above, the current understanding of star formation is sufficient to provide a comprehensive theory. The following sections will give an overview of the main evolutionary stages. It should be noted, however, that the understanding of these stages is based primarily on studies of low-mass stars forming in relative isolation. At the end of the section a few notes will be given on the formation of high-mass stars ($> 8M_{\odot}$) which is not as well understood as that of their low-mass counterparts.

The next sections focus mainly on the physical changes which occur as the system develops while the chemical evolution accompanying these changes will be discussed in sect. 1.2. Figure 1.2 presents an overview of these formation stages: the molecular cloud from which the stars condense, a protostar and disk which are embedded in the remnant material of their parent cloud, the so-called envelope, and finally, a mature star and planetary system.

From molecular cloud to dense core

The clouds of gas that hold the raw material from which stars form, are found throughout the ISM and are known as *giant molecular clouds*. These structures are among the largest cohesive entities found in the Galaxy, with radii of ∼5 to

200 pc (see, e.g, Table 1 of Murray, 2011) and masses ranging from $\sim 10^2$ $M_\odot$ for small clouds at high galactic latitudes and in the outer disk of the Milky Way, up to $\sim 10^7$ $M_\odot$ for giant clouds in the Galactic Center (see review by Dobbs et al., 2014). Typical densities are $\sim$100 cm^{-3}, though the clouds are highly inhomogeneous and density distributions have large contrasts. These inhomogeneities are observed throughout the clouds as complex patterns of long and narrow filaments, with typical widths of the order 0.1 pc ($\sim 20\times10^3$ au), compact ridges and irregular clumps (see review by André et al., 2014). It is within these clumpy, filamentary structures that the new stars are forming.

The clouds are predominantly comprised of atomic (H) and molecular hydrogen (H_2), although atomic helium (He), traces of carbon (C), oxygen (O) and nitrogen (N), as well as small molecules such as CO and CN, are also present, albeit at much lower abundances (e.g., Herbst & van Dishoeck, 2009). Physical conditions vary throughout the cloud and processes which shape the cloud structure include effects of gravity, turbulence, magnetic fields, galactic sheer motions and various forms of feedback such as supernovae and H_{II} regions associated with massive, newborn stars (Heyer & Dame, 2015). Generally, the outer and more diffuse parts of the clouds, which are more transparent to radiation from neighbouring stars, tend to be warm (temperatures of $\sim$100 K or higher), and are subjected to ultraviolet radiation, causing the H_2 molecules to dissociate (Mathis et al., 1983). In contrast, the H_2 molecules located in the inner parts of the cloud complex are shielded from UV radiation, both by the gas on the edges of the cloud, mainly H_2 itself, but also by the assortment of small solid particles that form the interstellar dust grains. These grains, which consist primarily of a mixture of carbonaceous material and silicates (and perhaps with traces of metals), have sizes ranging from nanometres to millimetres and efficiently absorb and scatter light with wavelengths smaller than their diameters (~ 0.1 μm). Because of the obscuring effects of dust at short wavelengths, and the subsequent re-emission at longer wavelengths, these regions are best studied at infra-red through radio wavelengths using both emission from spectral lines and continuum emission from the dust (see review by Dunham et al., 2014).

Regions where the dust effectively blocks the light from background stars are traditionally known as *dark clouds* since they appear dark at optical wavelengths. As long as the dark cloud is not disrupted by external forces the system is relatively stable and will remain in hydrostatic equilibrium. The critical mass above which the gas pressure is insufficient to support the cloud, bringing it to collapse, is called the Jeans Mass (Jeans, 1902). The original work by Jeans (1902) assumes that the collapsing cloud is spherically symmetric, isothermal and includes only thermal and gravitational effects. A more realistic description of how and why the cloud collapses would have to include physical effects such as rotation, turbulence and magnetic field interactions. However, including these effects does not interfere with the general conclusion that stars form in dense, low temperature regions. Such regions are referred to as *dense cores* and are found as substructures throughout the molecular clouds, particularly along filament ridges or at locations were filaments intersect or merge. In particular, studies of molecular clouds in the Gould Belt have shown that approximately 70% of the dense cores from which stars will eventually

condense are associated with filaments (André et al., 2014). This implies that the high column densities accumulated in the filaments may provide the initial conditions necessary for new stars to form. Typical densities in the dense cores are 10^4–10^6 cm^{-3} and temperatures can be as low as 10 K. At such low temperatures, most gas-phase species freeze out onto the dust grains leaving only substantial amounts of H_2, H and He in the gas-phase (Herbst & van Dishoeck, 2009).

A protostar and disk is formed

After the initial collapse of the dense core, a protostar is formed at its centre. As the system evolves, material from the cloud continues to fall towards the centre of the core, through the envelope, and the protostar enters its main accretion phase. Due to the conservation of angular momentum, a flattened disk is formed around the protostar. This disk is referred to as a circumstellar or protoplanetary disk. After the initial disk has formed, infalling material is accreted onto the disk before being transported further inwards and finally falls onto the protostar itself. Simultaneously, the disk continues to grow in mass and radius (Dunham et al., 2014, and references therein). Protostars in this stage are also associated with powerful, highly-collimated ejections in the form of jets and winds which sweep up surrounding material and form bipolar outflows extending along the axis of the system's angular momentum. These outflows help carry away mass and excess angular momentum from the forming system.

As the young protostar evolves, it starts to heat its surroundings, creating a region of warm (>100 K) gas, the so-called *hot core*. The increased temperature in this region, causes thermal desorption of icy grain mantles, enriching the gas with complex molecules and providing a snapshot of the chemical evolution which has taken place on the dust grains since the initial freeze-out of species in the dark cloud. The hot core stage is therefore essential when studying the chemical evolution of star-forming regions since it reflects the chemical processes which have occurred during earlier stages of formation which are challenging to probe directly.

The composition of the forming system initially reflects that of the ISM, with gas amounting to 99% of the total mass, while solids represent only 1%. However, as the system evolves and the disk is gradually dispersed, the gas-to-dust ratio decreases.

The formation of a planetary system

Ultimately, through the combined effects of incorporation of envelope material into the disk and central protostar and the dissipative role of outflows and jets, the cocoon of material surrounding the young system is disrupted and the star-disk system becomes optically visible.

In this final stage of the formation process the disk which surrounds the young star disappears. During the dispersion, the gas in the disk is processed mainly through viscous accretion and photoevaporation due to UV and X-ray radiation, both from the central star and from external stars. This results in a disk which is composed of ionised and atomic gas at the disk surface and upper layers while the composition of the molecular gas in the interior of the disk is generally left

intact. Also the disk solids undergo dramatic changes. These occur as the grains, which initially are small ($\sim$0.1 μm) and follow the motion of the gas, grow due to collisions and agglomeration. As the grains grow, they decouple from the gas and settle towards the disk midplane where the increased dust density accelerates the grain growth even further. In this way, the dust grains, which in the parent cloud are mostly micron-sized, grow in the disk to centimetre-sized pebbles and meter-sized rocks on their path to become first planetesimals and eventually full planets (see review of dust evolution in protoplanetry disks by Testi et al., 2014). Eventually, the remaining gas is removed from the disk completely. This happens rather rapidly via inside-out erosion as the accretion rate of gas drops below the photoevaporation rate of the newly formed star (see review by Williams & Cieza, 2011).

After the gas has been removed from the disk, the only remaining constituents are solid bodies which may eventually evolve into planets. Statistical studies of exoplanets, that is planets orbiting stars other than the Sun, suggest that most stars in the Milky Way host at least one planet (Tuomi et al., 2014). This indicates that the formation of planets is a natural by-product of star formation. Indeed, observations over the past few decades have revealed a wealth of exoplanetary systems, some even hosted by stars similar to the Sun (see review by Winn & Fabrycky, 2015). Although none of these are directly equivalent, in terms of its broad characteristics, the Solar System is not expected to be extremely rare (Martin & Livio, 2015). The fact that Solar System-like systems do not appear to be very infrequent implies that physical parameters, related to the architecture of planetary systems, are likely not the limiting factor for life.

Not all solids in the disk are incorporated into planets: some reside in smaller bodies such as asteroids and comets. Contrary to asteroids, comets are thought to have spent the majority of their lifetime in the outermost regions of the system, well away from the heat of the star, and the chaotic assembly of planets. These bodies are therefore considered the most pristine tracers of the protoplanetary disk. In a similar way, the frozen, fossil record preserved in Solar System comets, offers a unique view into the composition and chemical evolution undergone by the disk which eventually formed Earth.

To date, a number of cometary nuclei have been imaged and more than 20 molecular species have been detected in the comae of comets through various remote and in situ missions (see reviews by A'Hearn, 2011; Mumma & Charnley, 2011). The most recent, and most spectacular, of these is ESA's *Rosetta* mission which followed the comet 67P/Churyumov-Gerasimenko (hereafter 67P) for more than two years (August 2014 to September 2016) and succeeded in landing a module, *Philae*, on its surface. Throughout the mission, the *Rosetta* orbiter monitored the comet's evolution closely and provided the most detailed mapping of a cometary nucleus to date (Fig. 1.3). Data from the orbiter also confirmed the presence of many complex species such as CH_3OH, C_2H_5OH, CH_3CHO, $(CH_2OH)_2$ and CH_3NH_2, which are also observed towards star-forming regions (Le Roy et al., 2015; Altwegg et al., 2017), proving that the chemical complexity which is known to evolve during the star-forming precess is preserved in comets.

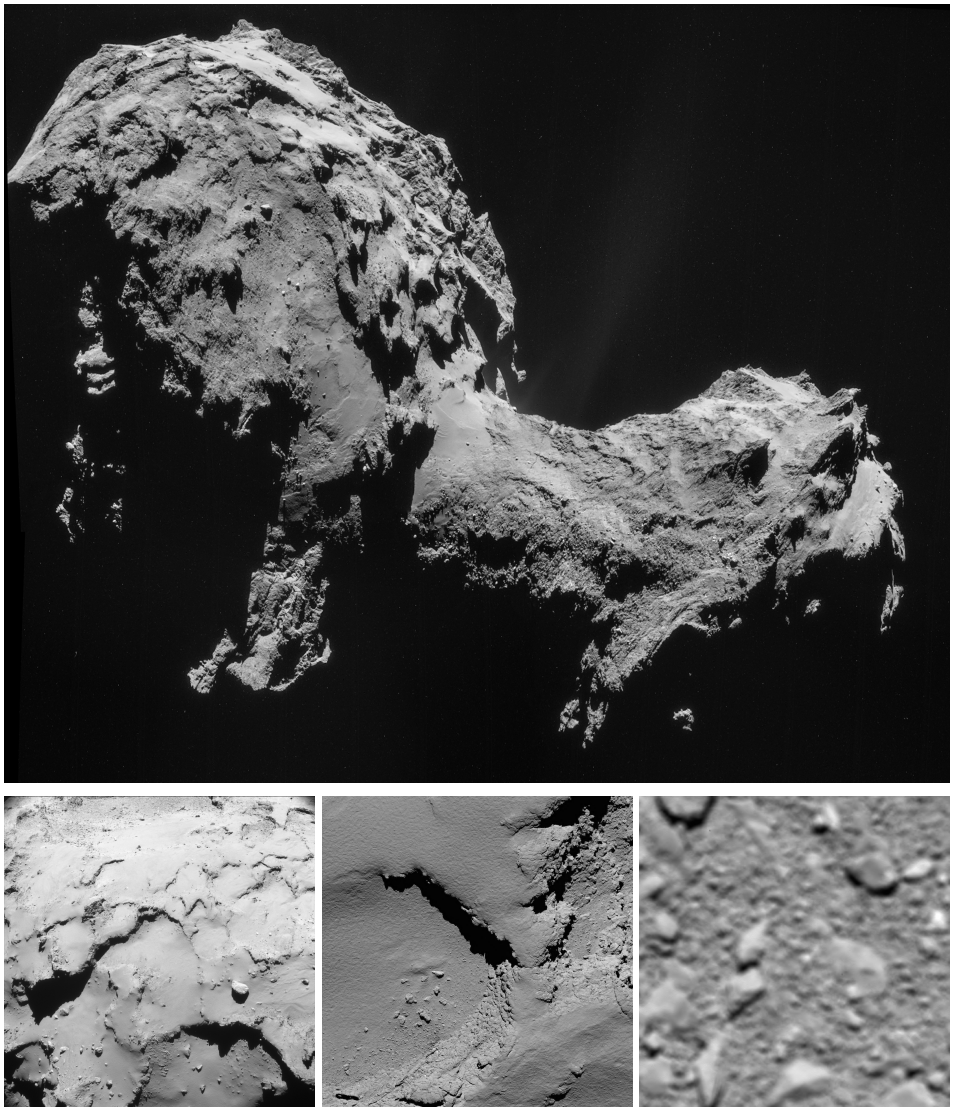

Figure 1.3: *Top*: Comet 67P/Churyumov-Gerasimenko as seen by Rosetta on 9 September 2014, at a distance of 28.6 km from the comet. *Bottom*: Sequence of images of comet 67P as seen by Rosetta on 30 September 2016, during the spacecraft's final descent. From left to right: Rosetta's last navigation camera image taken just after the collision manoeuvre sequence, when the probe was ∼15.4 km above the comets surface. Image of surface taken ∼5.8 km above the surface. Rosetta's final image of comet 67P, taken shortly before impact, at an estimated distance to the surface of ∼25 m. The images reveal the topography of the cometary surface which displays both sites of ridges and cliffs, as well as planes covered by smooth, fine-grained material and bulky rocks. Credit top: ESA/Rosetta/NAVCAM, credit bottom left: ESA/Rosetta/NAVCAM - CC BY-SA IGO 3.0, credit bottom middle, right: ESA/Rosetta/MPS for OSIRIS Team

Formation of high-mass stars

While the formation of high-mass stars, that is stars with masses exceeding 8 $M_\odot$, likely follows more or less the same sequence of formation steps as their low-mass sibling, the physical processes related to these are not as well understood. Nevertheless, it is important to understand the formation of these sources since massive stars play dominant roles in terms of their feedback and synthesis and dispersal of heavy elements. The weaker constraints on the formation of high-mass stars as compared to those of low-mass sources, are due in part to the larger distances to these sources. Sites of high-mass star formation are generally located more than 1 kpc away from the Sun, making spatially resolved studies difficult. Another reason is the much shorter time-scales on which these massive objects form, reaching the main sequence even before accretion has subsided (see review by Tan et al., 2014, and references therein). High-mass protostars are also associated with strong radiation fields, potentially capable of halting accretion. In order to overcome this radiation pressure, significantly enhanced accretion rates compared to those of low-mass sources are likely required for the massive stars to form. Another puzzle is the fact that a core large enough to form a massive star is likely to fragment before the massive star has had time to assemble. Finally, since high-mass stars are often found in clusters, forming simultaneously with other stars, studying their formation implies dissecting their parental dense cores from those of their companions. High angular resolution imaging at far-IR and (sub)millimetre wavelengths are therefore essential for resolving these deeply embedded sources (Motte et al., 2018).

1.2 Chemistry in star-forming regions

Accompanying the many physical changes to the star-forming environment, is a dramatic increase in the degree of chemical complexity. The chemical processes governing this increased complexity can be roughly divided into two types, namely those occurring in the gas-phase and those occurring on the surfaces of dust grains. Generally put, these reactions account for the formation, destruction or re-arrangement of chemical bonds between atoms or molecules. That is, they link atoms into molecules, break down molecules into smaller constituents or transfer parts of one reactant to another.

Due to the low density of gas in the ISM, even in molecular clouds, atoms and molecules do not often meet and therefore the opportunity for species to react is limited. For example, a neutral molecule in a dense core with a H_2 density of 10^4 cm^{-3}, will collide with a H_2 molecule only once every month, while the time scale for collisions with neutral molecules other than H_2 is a few hundred years (Sakai & Yamamoto, 2013). In addition, the low temperatures characterising the dense cores ($T_{\rm gas} \approx T_{\rm dust} \approx 10$ K) mean that only exothermic reactions (i.e., reactions which release energy), and reactions which have no activation barrier between reactants and products, can occur. These constraints mean that reactions have to be efficient, if a rich gas-phase chemistry is to be achieved. This chemistry therefore mainly proceeds via barrierless ion-neutral reactions (i.e., a neutral molecule

reacting with a positive ionised atom or molecule), followed by ion-electron interactions to generate neutral molecules (see review by Herbst & van Dishoeck, 2009, and references therein). On the other hand, cold dust grains provide a surface onto which atoms and molecules can accrete, creating a high density environment and enhancing the probability for these to meet and react. Also, the dust grain acts as a third-body, absorbing excess energy released in chemical reactions, thereby stabilising the reaction product. In gas-phase reactions, this excess energy is often stored as internal energy in the newly formed molecule and may result in the subsequent dissociation of the species. The dust grain therefore acts both as a reservoir of molecules and as a solid-state catalyst (although the surface itself does not participate in reactions).

On the grain, reactions occur primarily between radicals, that is atoms or molecules with unpaired electrons, resulting in high reactivity. These reactions mainly involve hydrogen atoms, which are abundantly present on the grain surface at low temperatures, and which, for example, form water (H_2O) by reactions with atomic oxygen (see van Dishoeck et al., 2013, and references therein). Overall, the efficiency of grain-surface chemistry is determined by the accretion rate of species onto the grain, which in turn is determined by a species' sticking efficiency and binding energy, the diffusion of species on the grain surface and the availability of additional energy, delivered by, for example, cosmic rays and photons.

While each of these processes, that is gas-phase and grain surface reactions, respectively, dominate the formation of a subset of molecular species as well as different physical regions and stages of the star-forming process, there is also a strong level of interplay between the mechanisms. Molecules which are originally formed in the gas-phase may subsequently freeze out onto the dust grains and here participate in new reactions. Likewise, species formed on the surface of grains may be released into the gas-phase and undergo further processing there. A key example is H_2 which is formed on the grain surface but forms the base for the formation of other species in the gas-phase (see review by Caselli & Ceccarelli, 2012, and references therein).

The following sections will summarise the chemical evolution of molecules in various astronomical environments. The first section will focus on the chemistry occurring in the ISM, specifically the buildup of simple molecules in molecular clouds, while the second section will describe the chemical processes associated with the hot core and protoplanetary disk.

Chemistry of the interstellar medium and molecular clouds

The gas which constitutes 99% of the total mass of the ISM is primarily composed of H and He, 90% and 8% by number, respectively, with heavier elements making up the remainder. The heavy elements are predominately O, C and N, which have abundances of 4.9, 2.7 and 0.7×10^{-4} that of H, respectively. Refractory species such as magnesium (Mg), silicon (Si) and iron (Fe) are present at lower abundances of $\sim 3 \times 10^{-5}$ (van Dishoeck, 2014, and references therein). The remaining 1% of the ISM total mass is made up of dust grains.

The gas of the ISM can be divided into different components depending on local

temperatures and densities. The main phases of these components are an ionised phase (gas temperatures, $T_{\rm gas}$, $\sim 10^4$ – 10^6 K, density of H-nuclei, n, $\sim 10^{-3}$ cm^{-3}) an atomic phase ($T_{\rm gas}$ $\sim$ 1000 K, n $\sim$ 0.1 – 10 cm^{-3}) and a molecular phase ($T_{\rm gas}$ $\sim$ 100 K or colder, n $\geq 10^2$ cm^{-3}; e.g. Table 1 of Ferrière, 2001). It is the latter of these phases which is of interest for the formation of molecular complexity. Going from diffuse to dense interstellar clouds, densities gradually increase, resulting in a higher degree of shielding from the InterStellar Radiation Field (ISRF, Mathis et al., 1983) and subsequently a drop in temperature. Even on the outer, more diffuse, edges of the molecular clouds, self-shielding against the ISRF, primarily by H and H_2, will prevent molecules produced in the gas-phase from being photodissociated. A notable example of this is carbon monoxide (CO), the most abundant interstellar molecule after H_2 (van Dishoeck & Black, 1988).

The next step in the formation process is the freeze-out of gas-phase species onto the surface of dust grains. This freeze-out is a natural consequence of the quiescent nature of the molecular cloud, as the low temperatures characterising these regions prevent species which have landed on the surface of grains from thermally sublimating.

Atomic species such as H, C, O and N will first accrete onto the grain and thereafter diffuse on its surface. In particular, the abundant and light hydrogen atoms will diffuse quickly and engage often in so-called hydrogenation reactions. These reactions result in the build-up of large amounts of water, followed by smaller amounts of methane (CH_4) and ammonia (NH_3) (e.g., reviews by Tielens & Hagen, 1982; van Dishoeck et al., 2013; Linnartz et al., 2015). Diffusion reactions will also form carbon dioxide (CO_2) after CO molecules, which are formed in the gas-phase, start to freeze out on the dust grains at sufficiently low temperatures. Together, these simple molecules coat the grains in a layer of molecular ice whose dominate component is water.

Due to its volatile nature, the bulk of the gas-phase CO will freeze out only at the coldest temperatures of the dense core stage (the sublimation temperature for pure CO is $\sim$20 K compared with $\sim$45 K for CO_2 and $\sim$90 K for H_2O, Boogert et al., 2015). Once these are reached, a catastrophic freeze-out of CO will follow, creating a distinct CO layer on top of the water-dominated layer. Further hydrogenation reactions of CO then result in the formation of formaldehyde (H_2CO) and methanol (CH_3OH). This basic, layered structure of the ice mantle on grains has been observed with various infra-red space observatories (see Boogert et al., 2015, for a review).

Further chemical complexity in the ice mantels can occur as a result of successive addition of C- and H-atoms to CO, forming for example both acetaldehyde (CH_3CHO) and ethanol (C_2H_5OH; Tielens & Charnley, 1997). In additon, laboratory experiments, which simulate the CO freeze-out stage, have shown that even molecules as large as glycolaldehyde ($CH_2(OH)CHO$) and ethylene glycol ($(CH_2OH)_2$) may also be formed in the ice (Fedoseev et al., 2015).

Due to the low temperatures which characterise the centres of dense molecular clouds, the majority of molecules are expected to be frozen-out in these regions. However, some molecules have been detected in the gas-phase towards cold dense cores (e.g., Bacmann et al., 2012; Cernicharo et al., 2012). These observations can

be partly explained by gas-phase reactions but also by a fraction of the species, which reside in the icy grain mantle, being returned to the gas-phase via non-thermal desorption mechanisms such as photodesorption and reactive or chemical desorption (Öberg et al., 2007; Minissale et al., 2016; Oba et al., 2018; Chuang et al., 2018). These desorption processes are driven mainly by cosmic rays and include energetic processing of the grain mantle by cosmic-ray bombardment as well as dissociation by cosmic ray-induced UV photons (see review by Caselli & Ceccarelli, 2012).

Chemistry in hot cores and protoplanetary disks

As the forming star starts to heat up its surroundings, the molecules which were formed in the ice on the surface of grains in the dense clouds become increasingly mobile and react to form new, more complex species on the grain surface. In particular, biologically relevant molecules such as glycine, the smallest amino acid, may be formed at this stage of the star-forming process (e.g., Garrod et al., 2008; Garrod, 2013).

When sufficiently high temperatures are reached ($T_{\rm gas} \sim 100$ K), the ice mantles which have build up during the dense core stage, will sublimate completely and enrich the inner envelope with a considerable amount of gas-phase complex molecules. As mentioned in sect. 1.1, this stage in the star-forming process is referred to as a hot core. The spectroscopic fingerprint of the species which are released into the gas-phase during the hot core stage can be observed through their rotational transitions, which are accessible in the millimetre wavelength regime. These transitions are more easily excited compared with vibrational or electronic transitions and therefore even species with low abundances may be detected. In particular, the Atacama Large Millimeter/submillimeter Array (ALMA) has in recent years provided a wealth of information on the chemical composition of star-forming regions (e.g., Jørgensen et al., 2016; Belloche et al., 2016; Pagani et al., 2017).

At the same time, molecules released from the grains also set the stage for warm gas-phase chemistry, resulting in the formation of additional molecular species (see review by Sakai & Yamamoto, 2013). These processes may proceed either via pure gas-phase reactions or via gaseous species interacting with species still residing on the grain surfaces. Molecular species can also be destroyed as a consequence of the increasingly powerful radiation field associated with the forming star. Also, outflowing material, transported away from the forming system in the form of jets, will create shocks when encountering the quiescent gas of the envelope and surrounding molecular cloud. These shocks sputter the icy grain mantles and in some cases even vaporise refractory grains completely (Caselli & Ceccarelli, 2012). Both of these processes result in a partial reset of chemistry.

Contrary to the material in the hot core, the gas and dust residing in the protoplanetary disk stays largely shielded from radiation and temperatures remain low. As material flows from the envelope towards the centrally forming star, the chemistry which evolved in the icy grain mantles during the dense core stages, is fed into the disk, where it can continue to evolve in a similar fashion. The

chemical and physical structure of the disk may be traced through observations of simple molecules such as DCO^+ and DCN and it has become apparent that in particular the disk midplane is cold enough to maintain grain surface chemistry (e.g., Drozdovskaya et al., 2016; Salinas et al., 2017; Carney et al., 2018). As a consequence, the pristine composition which formed in the ice in the dense core stage may be preserved on the dust grains residing here. On the other hand, the inner regions of the disk, closest to the forming star, as well as the upper layers of the disk, are warmer and significantly more irradiated compared to the midplane. These regions are therefore dominated by molecules produced by gas-phase chemistry and species released from grains (see review by Bergin et al., 2007). Observations of these molecules therefore provide a glimpse of the chemical inventory of the dust grains in the disk midplane which are otherwise very difficult to probe (Öberg et al., 2015; Walsh et al., 2016).

Finally, as dust in the disk midplane coagulates, a fraction of the icy grains are likely preserved and consequently end up in planetesimals, the seeds of comets, asteroids and planets. Subsequent processing of the planetesimals as the planetary system evolves may alter this pristine material significantly. However, because comets predominantly reside in the outer parts of the disk, well away from the heat of the forming star, these objects are believed to preserve a nearly pristine record of the disk (A'Hearn et al., 2012). Characterising the composition of comets is therefore key when studying the final phase of chemical evolution during star formation. In addition to storing a record of this evolution, comets in the Solar System likely also acted as 'polluters' of the young Earth, potentially providing the planet with the essential prebiotic building block from which life evolved (Mumma & Charnley, 2011).

1.3 Star formation in the era of ALMA

When studying sites of star formation, the main observational challenges relate to achieving high spatial and spectral resolutions as well as high sensitivity. High spatial resolution observations are essential in order to probe individual objects so that confusion of material associated with different regions or averaging over environments which are different, either in terms of chemical composition or in terms of physical characteristics, may be avoided. Similarly, high spectral resolutions are needed in order to dissect the very line rich spectra associated with star-forming regions. Finally, because the column densities associated with sites of star formation are high, the transitional lines of the most abundant species are often optically thick. These species are therefore best probed through their less abundant, rarer isotopologues. Because the transitions of these isotopologues are often weak, high sensitivity observations are necessary for their detection.

Whereas single dish observations often suffer from at least one of these limitations, to greater or lesser extent, ALMA has been a true game changer. Constructed on the Chajnantor plateau in the Atacama Desert located in the northern part of Chile, ALMA is currently the world's largest radio telescope. The facility is composed of 66 high-precision antennas, operating as an interferometer with

baselines of up to 16 km, making it possible to resolve spatial scales down to a few milliarcsecond. To date, antennas are equipped with 8 receivers (Band 3 – Band 10) covering the frequency range from 84 to 950 GHz (0.3 mm up to 3.6 mm), with the Band 1 receivers, operating in the range 35 to 50 GHz (6 – 8.5 mm), currently under construction. Both the sensitivity and resolving power offered by ALMA are unprecedented. Therefore, it is not surprising that since the start of operation in 2011, observations carried out with ALMA have revealed structures in star-forming clouds (e.g., Plunkett et al., 2015; Brogan et al., 2016; Tobin et al., 2016; Pagani et al., 2017) and protoplanetary disks (e.g., van der Marel et al., 2013; Andrews et al., 2016; Cieza et al., 2016; Pérez et al., 2016) which were never seen before. Examples of these structures are shown in Fig. 1.4. Specifically, the high angular resolution offered by ALMA has allowed star-forming regions and protoplanetary disks to be studied on solar system scales. In contrast, the much larger beam sizes associated with single dish studies, frequently result in insufficient spatial resolution and consequently may cover multiple sites of star-formation in a single beam making the characterisation of a region much less accurate. Furthermore, ALMA observations do not suffer from effects of beam dilution which may result in large uncertainties on derived molecular column densities if not accounted for correctly in single dish studies. In addition, the high spectral resolution and high sensitivity of ALMA observations has also resulted in numerous detections of new molecular species in various environments (e.g., Jørgensen et al., 2016; McGuire et al., 2018, and Fig. 1.5).

With the advances of ALMA, the chemical composition of star-forming regions may be probed on smaller scales and through weaker transitional lines, for example belonging to rare isotopologues, than were accessible through single dish observations. In addition, the high spectral resolution of ALMA observations also allows spectral features which are blended at lower resolution, to be resolved into contributions from individual species. By modelling the emission of these species and comparing the modelled spectra with the observations of ALMA, the molecular inventory of star-forming regions may be characterised in great detail.

1.4 This thesis

The overarching question addressed in this thesis is how interstellar chemistry evolves as a function of time and changing physical architectures during the formation of stars. This question is motivated by the insights in the complex nature of star-forming regions which have been gained over the last few years, thanks to the high sensitivity offered by ALMA, and an aspiration to better understand how the Solar System came to be, which processes led to its chemical composition and ultimately, what enabled life to evolve on Earth. To answer these questions, the ideal target to study would be a system which will eventually evolve into a star similar to the Sun, and potentially the planetary system that orbits it, but that is currently under formation. Despite such systems being very numerous in the Galaxy, detailed analysis of their chemical composition and physical structure is extremely challenging because these systems are faint, obscured by the clouds

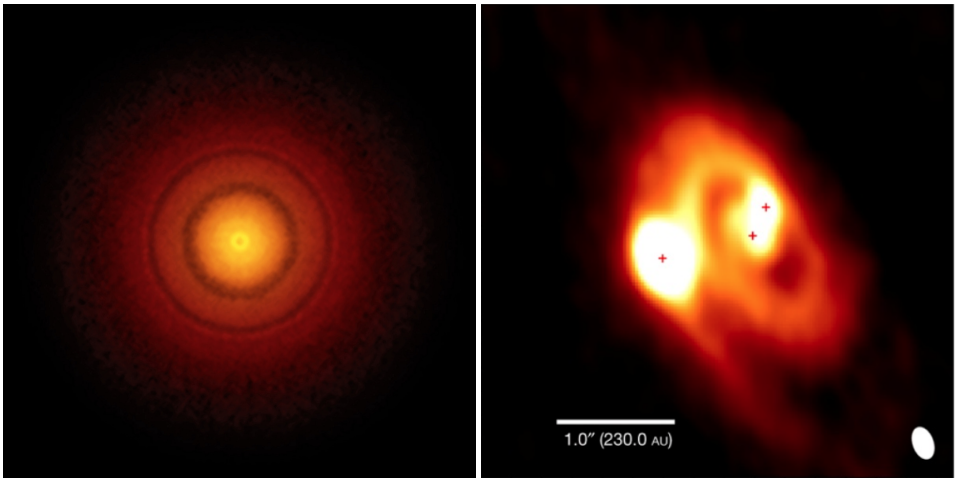

Figure 1.4: *Left*: Millimetre dust emission from the disk around the young star TW Hydrae observed by ALMA. Substructures in the disk in the form of rings and gaps in the distribution of the dust hint at dynamical processes associated with planet formation. *Right*: Millimetre dust emission from the extended disk around the triple system L1448 IRS3B revealed by ALMA. The positions of the three protostars are indicated by red crosses. Gravitational interactions between the forming stars leave clear imprints on the distribution of the surrounding material which appears to form a spiral arm emerging from the close pair (IRS3B-a and b) and extending to IRS3B-c. Credit left: Andrews et al. (2016), credit right: Tobin et al. (2016).

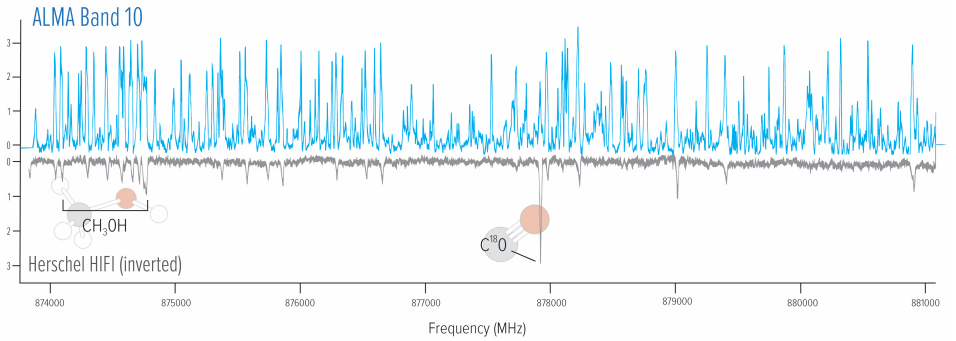

Figure 1.5: Comparison of ALMA data (top) to observations by ESA's *Herschel* Space Observatory (bottom) towards the high-mass star-forming region NGC 6334I. The line density of the ALMA spectrum is higher than that of the *Herschel* spectrum by more than a factor of ten (note that the *Herschel* data have been inverted for comparison). Lines of CH_3OH and $C^{18}O$ are labelled.
Credit: NRAO/AUI/NSF, McGuire et al. (2018).

from which they are forming and occupy a small spatial scale. In contrast, systems evolving into massive stars are much brighter and more easily resolved. In particular the high-mass star-forming regions located near the Galactic Center and in the Orion Nebula have been favoured targets for studies of chemical complexity. This is due to the high activity of star-formation in these regions, resulting in the sublimation of many ice species, making them more easily accessible for studies of molecular inventories. Also, the proximity of the Orion Nebula ($\sim$ 400 pc), making it visible to the naked eye and the closest region of massive star-formation to the Sun, has resulted in this region being a preferred target. However, in this thesis, the molecular composition of additional sites of high-mass star-formation, located away from the Galactic central region, are analysed. Studying these sites is important in order to better understand how star formation proceeds under less extreme conditions than those found in the Galactic Center and will eventually provide a link to the formation of low-mass, Solar-type, stars. In order to achieve this link, the thesis investigates the chemical composition found in high-mass star-forming regions located away from the Galactic Center and compares their composition to the composition of the few low-mass sources which have been extensively studied as well as to the composition derived for Solar System comets. Specifically, the chapters of the thesis investigate the following questions:

- How does the chemical composition of high-mass hot cores compare to the composition of their low-mass counterparts?
- How does the chemical composition of a star-forming region reflect its physical properties?
- Which molecules are available in hot cores for the formation of larger, more complex species?
- Does the inventory of Solar System comets reflect the composition of the hot cores?

The results presented in the following chapters are based on observations carried out with ALMA which, for the first time, has allowed sites of massive star-formation to be probed on solar system scales. In addition, the high sensitivity offered by ALMA ensures a more complete and more accurate characterisation of the chemical inventory of these sites compared with those derived based on single dish observations.

1.4.1 Analysis tools used in the thesis

For the analysis presented in the thesis, two main modelling tools have been used: Chapters 2 trough 4 make use of the CASSIS[1] software for generating synthetic spectra while the analysis in Chapter 5 has been carried out using the LIME (Line Modeling Engine) radiative transfer code (see Brinch & Hogerheijde, 2010, for details). This section will shortly introduce each of these tools.

[1] Centre d'Analyse Scientifique de Spectres Instrumentaux et Synthétiques: http://cassis.irap.omp.eu

CASSIS

The CASSIS software has been developed by CESR/IRAP and can be used to identify and analyse spectral lines. The software reads spectroscopic data from common databases such as JPL (Jet Propulsion Laboratory[2], Pickett et al., 1998) and CDMS (Cologne Database for Molecular Spectroscopy[3], Müller et al., 2001, 2005) and use these to generate synthetic spectra according to the inputs provided by the user. These inputs include excitation temperatures, column densities of the studied species, the source velocity of the studied object, the full width at half maximum of the lines as well as the angular size of the emitting region. By comparing an observed spectrum with the synthetic spectra generated by CASSIS, the molecular inventory of the region of interest may be characterised and excitation conditions determined. Within the CASSIS framework, model parameters may be optimised to fit an observed spectrum using a minimal χ^2 approach. CASSIS can be run assuming either local thermodynamical equilibrium (LTE) or non-LTE excitation conditions and can handle multiple temperature components as well as effects of optical depth.

LIME

LIME is a non-LTE radiative transfer code for modelling continuum and spectral line radiation, optimised for ALMA data. The code works in arbitrary, three dimensional geometries and may be used to model a variety of environments including giant molecular clouds, the disks and envelopes associated with forming stars, and in the case of this thesis, the coma surrounding a cometary nucleus. The code can solve the radiation transfer for an unlimited set of molecular species simultaneously and can handle overlapping lines. In addition to a physical model, the LIME code takes as input molecular collision rates, which may be adopted from, for example, the Leiden Atomic and Molecular Database (LAMDA; Schöier et al., 2005). This database holds collisional rates between H_2 and a number of the most abundant astronomical species. The output of LIME is a modelled sky brightness distribution that can easily be compared to observations.

1.4.2 Overview of chapters and general conclusions

In this section the main results presented in the individual chapters are summarised and the general concessions of the thesis presented.

Chapter 2 – Low levels of methanol deuteration in the high-mass star-forming region NGC 6334I

In this chapter, the methanol (CH_3OH) content of the high-mass star-forming region NGC 6334I is investigated. Since methanol is one of the most abundant organic species in star-forming regions it is often used as a reference when comparing chemical composition across sources. The characterisation of this species is

[2]http://spec.jpl.nasa.gov
[3]http://www.ph1.uni-koeln.de/cdms/

therefore essential. Utilising the high sensitivity and spatial resolution offered by ALMA, transitions of the less abundant, optically thin, methanol-isotopologues $^{13}CH_3OH$, $CH_3^{18}OH$, CH_2DOH and CH_3OD are identified in spectra extracted at nine locations across the NGC 6334I region. Based on these, the excitation temperature and molecular column density of each isotopologue is derived and the methanol deuteration fraction is compared between the different regions. The chapter concludes that both the CH_2DOH/CH_3OH and CH_3OD/CH_3OH values derived towards the hot cores in NGC 6334I are considerably lower than those derived towards low-mass star-forming regions, but only slightly lower than those derived for the high-mass star-forming regions in Orion and near the Galactic Center. Chemical modelling of the low methanol deuteration ratios indicate a grain surface temperature during the time of the systems formation of ∼30 K, at which the efficiency of the formation of deuterated species is significantly reduced. This temperature is higher than what is predicted for low-mass star-forming regions where the levels of deuterium in simple molecular species indicate a dust temperature at the time of formation below 20 K.

Chapter 3 – Methylamine and other simple N-bearing species in the hot cores NGC 6334I MM1 – 3

This chapter continues the exploration of the chemical composition of the hot cores in NGC 6334I, with a focus on the simple nitrogen-bearing species methanimine (CH_2NH), methylamine (CH_3NH_2), formamide (NH_2CHO) and the ^{13}C- and ^{15}N-methyl cyanide (CH_3CN) isotopologues. These species are of particular interest when searching for the building blocks of life since nitrogen-containing bonds are essential for the formation of various biological structures, such as nucleobases and the linking of amino acids. In particular CH_3NH_2 is thought to be a key prebiotic species, but so far has only been securely detected in the giant molecular cloud Sagittarius B2, located near the Galactic Center. Using the same set of observations as in Chapter 2, a number of transitions of each of the N-bearing species are identified in spectra extracted at three locations across NGC 6334I. For each species and location, column densities and excitation temperatures are derived in order to investigate the relevance of the individual species as precursors of biogenic molecules. The chapter reports the first detection of CH_3NH_2 towards the hot cores in NGC 6334I. Taking methanol as a reference, the abundance of CH_3NH_2 derived towards NGC 6334I is slightly lower than towards Sagittarius B2 but higher by an order of magnitude as compared with the upper limit value derived for the low-mass protostar IRAS 16293–2422B. Based on the good agreement between model predictions of CH_3NH_2 ratios and the observations towards NGC 6334I, the chapter concludes that the formation of CH_3NH_2 is more likely to proceed via radical recombination reactions on grain surfaces than via gas-phase reactions. This process may be stimulated further by high grain temperatures allowing a lager degree of radical mobility, consistent with the relatively high dust temperature derived in Chapter 2.

Chapter 4 – Molecular complexity on disk-scales uncovered by ALMA: The chemical composition of the high-mass protostar AFGL 4176

This chapter presents an extensive analysis of the molecular inventory of the high-mass protostar AFGL 4176. By studying this inventory, the link between the chemical composition and evolutionary stage of the star-forming system is investigated and the source is placed in the broader context of star-formation. The AFGL 4176 system is of particular interest because it is one of the few known examples of a high-mass protostar for which signatures of a Keplerian-like disk have been detected. The analysis presented in this chapter is based on high sensitivity, high angular and spectral resolution observations obtained with ALMA, allowing many weak transitions to be identified. Across a total bandwidth of ∼4.7 GHz, 354 lines are identified towards AFGL 4176 with a signal-to-noise of three or higher. Of these lines, 324 are assigned to 23 different molecular species and their isotopologues. For each detected species, the column density is derived and the abundance with respect to methanol is compared with abundances derived towards other high- and low-mass sources. The chapter concludes that AFGL 4176 comprises a rich chemical inventory including fourteen complex species, that is, species consisting of six or more atoms. The majority of the detected species are oxygen-bearing while fewer contain nitrogen, sulphur or a combination thereof. Taking methanol as a reference, the O-bearing species are three times more abundant than the N-bearing species. Overall, the chapter concludes that the chemical composition of AFGL 4176 is more similar to that of the low-mass protostar IRAS 16293–2422B than to that of the high-mass star-forming region Sagittarius B2(N). This similarity indicates that the production of complex species does not depend strongly on the luminosity of sources, but may be universal despite differences in physical conditions, or that the composition of species is set already in the ice during the cold cloud stage.

Chapter 5 – Exploring the volatile composition of comets C/2012 F6 (Lemmon) and C/2012 S1 (ISON) with ALMA

This chapter explores the volatile composition of the comae of comets C/2012 F6 (Lemmon) and C/2012 (ISON). These comets likely formed in the outer and cold parts of the disk which eventually evolved into the Solar System. Assuming that the comets have undergone no major processing since their formation, studying their composition can provide insight in the pristine composition of the Solar Nebula. Thereby, the comets provide a link between the chemical composition of the low-mass hot core equivalent from which the Sun formed and the planetary system which orbits the Sun today. As in the previous chapters, the analysis presented in this chapter is based on observations carried out with ALMA, making it possible to resolve the comae on spatial scales of ∼300 km. The chapter presents the first ALMA detection of carbon sulphide (CS) in the coma of comet ISON as well as several newly detected transitions of methanol and one new transition of hydrogen cyanide (HCN) towards comet Lemmon. In addition, the previously reported transitions of HCN, hydrogen isocyanide (HNC) and formaldehyde (H_2CO) are confirmed towards both comets. Based on their spatial distribution, the chapter

concludes that HCN and CH_3OH are parent species, that is, species sublimated directly from the cometary nucleus, while CS, HNC and H_2CO are either daughter species, resulting from gas-phase chemistry in the coma, or parent species transported away from the nucleus by some refractory compound before being evaporated. For each detected transition, the line intensity is modelled and molecular production rates with respect to water are derived. These are consistent with ratios reported in the literature for other comets. The chapter concludes that the challenges faced when deriving molecular production rate ratios with respect to water due to the unknown collisional cross sections between water and other species, can be circumvented when only the innermost part of cometary comae is sampled. In this region of the coma, the densities are high and excitations therefore close to local thermodynamic equilibrium (LTE) meaning that the exact value of the collisional cross sections becomes less important. To achieve this sampling, the spatial resolution offered by ALMA is crucial.

In addition to the conclusions drawn on basis of the individual chapters the following lessons can be learned from the thesis as a whole:

- For the chemical characterisation of a star-forming region to be accurate and complete, high-quality observations, both in terms of sensitivity and in terms of resolution, are essential. As illustrated in Chapter 2, the high sensitivity of ALMA allows rare isotopologues, including deuterated species, to be detected. In turn, these detections provide a means by which the abundance of the corresponding main isotopologue, which is often optically thick in star-forming regions, can be estimated. In this way, a solid basis for comparisons of molecular species, both within a single sources and across different objects, is achieved. Similarly, the spectral resolution of observations is a critical factor for the secure detection of species in star-forming regions since spectra extracted from these are often very crowded and have many blended lines. Finally, as illustrated in Chapters 4 and 5, the high spatial resolution offered by ALMA makes it possible to sample cometary comae and star-forming regions on scales small enough to avoid confusion with surrounding material or averaging over environments that are different, thereby providing a purer picture of the molecular inventory of these objects. However, since opacities (of dust as well as gas) in regions of high-mass star formation can be high on these small scales, the necessity of high sensitivity observations, allowing isotopologue lines to be detected, as stated above, is even more crucial.

- The low deuteration of methanol observed towards the high-mass star-forming regions in NGC 6334I, similar to the levels of deuteration derived for regions near the Galactic Center, suggests that on cloud scales, the material of the star-forming region is ”warm”. In contrast, the higher relative abundance of O-bearing species compared with N-bearing species detected in the disk around the forming high-mass star AFGL 4176, similar to the ratios derived for the low-mass system IRAS 16293–2422, suggests that the material in this disk (and star) is cold, and may have been inherited from the densest, coldest, part of the parent cloud. If that is the case, the material which comprises

the disks around high- and low-mass stars, respectively, may have originated in environments which were equally cold. This implies that the disks in either region may be more similar than the conditions on cloud-scale suggest. Alternatively, AFGL 4176 may have formed in a relatively isolated environment rather than a cluster, which is otherwise typical for high-mass stars. In addition, many of the complex organic molecules detected towards high-mass stars (both in the NGC 6334I clouds and the disk around AFGL 4176), are also present in Solar System comets but have so far proven elusive in disks around low-mass stars, where they likely remain frozen. Disks around high-mass stars, where such organics are more easily detected, may therefore be very useful when making the connection between the composition of comets and the composition of disks around low-mass stars.

1.5 A look to the future

The search for complex molecular species in star-forming region is a highly active field of research and will continue to be so in many years to come. Historically, sites of high-mass star formation have been favoured in these searches since high-mass sites are generally brighter and have higher abundances of molecular species compared with low-mass regions, making them observationally more easily accessible. As telescopes have gained in sensitivity, many of the species known to exist in high-mass regions are now also being detected towards low-mass star-forming sites and in particular the high sensitivity offered by ALMA has played a crucial role in expanding the database of molecular inventories towards both high- and low-mass sources.

With the database growing, both in terms of the number of investigated sources and in the range of detected species, it becomes possible to test and refine the star-formation paradigm. In this respect, the statistical basis provided by the ever-growing database is essential, in order to ensure that the conclusions drawn regarding the processes occurring during the star-forming epoch may be free form observational biases due to a limited sample of sources. Detections of new species as well as revised abundances of known molecules in a wide variety of different sources will also help constrain their chemical formation pathways which can in turn be incorporated or updated in models of chemical reaction networks.

While the high spatial resolution offered by ALMA allows star-forming regions to be dissected and investigated on scales small enough to limit confusion from surrounding material, its high sensitivity enables the detection of many rare isotopologues, including deuterated species. A lot can be gained by studying these as the primary isotope of many of the most common and abundant species found in star-forming regions are optically thick and therefore cannot be used to derive column densities and excitation temperatures. In addition, the isotopologues likely trace different regions of the star-forming sites compared to those traced by the primary isotopes and may therefore provide a window through which regions that have so far not been accessible can be viewed. It is important to keep in mind, that if the search for rare isotopologues and deuterated species is to be a success, it

is of the utmost importance that the spectroscopic data of these species are available. To this end, laboratory investigations and theoretical calculations of the spectra of the species are essential. Finally, as the detection of rare isotopologues become routine in ALMA surveys, and the spectroscopic databases continue to be expanded with new species and transitions, the prospects for future studies of star-forming regions are bright.

In addition to the advances of ALMA, the future also brings exciting new possibilities for infra-red observations with the planned launch of the James Webb Space Telescope (JWST) in 2021. JWST will observe in the visible through mid-infrared (0.6 – 27 μm) wavelength regime, making it possible to probe the icy content of star-forming regions and study the molecular species found there. Also, the angular resolution of the JWST will allow the observations to zoom in on the innermost regions around forming stars as well as the ice in the dark clouds. In this way, a direct link between the complex species observed in hot cores and the species found in ices in dark clouds can be made.

Lastly, continued monitoring of Solar System comets is important and will provide tighter constrains on the composition of the Solar Nebula as well as an indication of the degree of molecular complexity present already at the planet-forming stage. In this respect, it will be important to characterise both the composition of comets but also the evolution and time variation observed in their comae as they are heated by the Sun. This will allow for a better separation of the chemistry induced in comets at later stages, such as thermal processing of the cometary surface near the Sun, from that which has been preserved from the protoplanetary disk stage. However, the short-term (less than an hour) time variability of comets also comprise a challenge for future observations since deep integrations will provide only a time-averaged view of the coma.

2

Low levels of methanol deuteration in the high-mass star-forming region NGC 6334I

E. G. Bøgelund, B. A. McGuire, N. F. W. Ligterink, V. Taquet, C. L. Brogan, T. R. Hunter, J. C. Pearson, M. R. Hogerheijde and E. F. van Dishoeck

Astronomy & Astrophysics
Volume 615, Article A88 (2018)

Abstract

Context. The abundance of deuterated molecules in a star-forming region is sensitive to the environment in which they are formed. Deuteration fractions, in other words the ratio of a species containing D to its hydrogenated counterpart, therefore provide a powerful tool for studying the physical and chemical evolution of a star-forming system. While local low-mass star-forming regions show very high deuteration ratios, much lower fractions are observed towards Orion and the Galactic centre. Astration of deuterium has been suggested as a possible cause for low deuteration in the Galactic centre.
Aim. We derive methanol deuteration fractions at a number of locations towards the high-mass star-forming region NGC 6334I, located at a mean distance of 1.3 kpc, and discuss how these can shed light on the conditions prevailing during its formation.
Methods. We use high sensitivity, high spatial and spectral resolution observations obtained with the Atacama Large Millimeter/submillimeter Array to study transitions of the less abundant, optically thin, methanol-isotopologues: $^{13}CH_3OH$, $CH_3^{18}OH$, CH_2DOH and CH_3OD, detected towards NGC 6334I. Assuming LTE and excitation temperatures of $\sim$120 – 330 K, we derive column densities for each of the species and use these to infer CH_2DOH/CH_3OH and CH_3OD/CH_3OH fractions.
Results. We derive column densities in a range of $(0.8 - 8.3)\times10^{17}$ cm^{-2} for $^{13}CH_3OH$, $(0.13 - 3.4)\times10^{17}$ cm^{-2} for $CH_3^{18}OH$, $(0.03 - 1.63)\times10^{17}$ cm^{-2} for CH_2DOH and $(0.15 - 5.5)\times10^{17}$ cm^{-2} for CH_3OD in a $\sim1''$ beam. Interestingly, the column densities of CH_3OD are consistently higher than those of CH_2DOH throughout the region by factors of 2 – 15. We calculate the CH_2DOH to CH_3OH and CH_3OD to CH_3OH ratios for each of the sampled locations in NGC 6334I. These values range from 0.03% to 0.34% for CH_2DOH and from 0.27% to 1.07% for CH_3OD if we use the ^{13}C isotope of methanol as a standard; using the ^{18}O-methanol as a standard, decreases the ratios by factors of between two and three.
Conclusions. All regions studied in this work show CH_2DOH/CH_3OH as well as CH_2DOH/CH_3OD values that are considerably lower than those derived towards low-mass star-forming regions and slightly lower than those derived for the high-mass star-forming regions in Orion and the Galactic centre. The low ratios indicate a grain surface temperature during formation $\sim$30 K, for which the efficiency of the formation of deuterated species is significantly reduced. Therefore, astration of deuterium in the Galactic centre cannot be the explanation for its low deuteration ratio but rather the high temperatures characterising the region.

2.1 Introduction

The abundance of deuterium (D) formed in the Big Bang sets the primordial D/H in the universe. As stars form and start processing D in their interiors, the deuterium abundance should drop if no other source of D exists. The best estimate of the cosmic D/H is therefore obtained by observing environments with little star formation and chemical processing such as the diffuse interstellar medium (ISM) for which D/H is $\sim(1.5 - 2.0)\times10^{-5}$ (Linsky, 2003; Prodanović et al., 2010). On the other hand, environments with high star-formation rates would be expected to show lower D/H fractionation ratios as a consequence of astration, that is the processing of D in stellar interiors, and a generally higher temperature. This however, contradicts observations of molecules in both high and low-mass star-forming regions that not only show D/H values which are orders of magnitude higher than that of the ISM, but also display multiply deuterated species. An example of a source exhibiting such high deuterium fractionation is the well-studied low-mass protostellar binary IRAS 16293–2422 (hereafter IRAS 16293; van Dishoeck et al., 1995; Ceccarelli et al., 1998). This source is especially interesting because it was the first source towards which both doubly as well as triply-deuterated methanol was detected (Parise et al., 2002, 2004). More recently, IRAS 16293 has been studied by Jørgensen et al. (2018) who have characterised the isotope composition of a number of complex organic molecules. They derived D/H values, that is the column density ratio of isotopologues with respect to their hydrogenated counterparts including the statistical correction for the location of the substituted deuterium, for all detected species in the range 2 – 8%. Specifically, the D to H ratio of methanol (CH_3OH) is found to be ∼2%. In addition, the detection of singly and doubly-deuterated formaldehyde (H_2CO) and methanol towards seven other low-mass protostars, with deuteration fractions similar to those observed towards IRAS 16293, is reported by Parise et al. (2006). For high-mass star-forming regions the most thorough studies of deuterated species have been carried out towards the hot cores located in the Galactic centre and the Orion Complex. For Sagittarius B2 (Sgr B2), Belloche et al. (2016) report D/H values of 0.38% for acetonitrile (CH_3CN) and (0.05 – 0.12)% for the tentative detections of CH_3CH_2CN, HC_3N and CH_3OH. Approximately the same low levels of deuteration were found by Neill et al. (2013), who studied ammonia (NH_3), formaldehyde and methanol towards Orion KL and find D/H $\sim(0.2 - 0.8)$% towards the compact ridge and hot core regions. Similar levels of deuterium in methanol are found by Peng et al. (2012).

While these observations clearly illustrate that deuterated species, including CH_3OH, are enhanced in star-forming regions, the explanation of how the various ratios came to be remains incomplete. For the low-mass objects, the high deuteration ratios can, for the most part, be explained by gas-grain astrochemical models where high densities and low dust temperatures allow simple deuterated species to build up rapidly in precursor dark cores (Taquet et al., 2012). In the case of Sgr B2 however, the low deuteration fractions are attributed to the combined effects of astration and a less efficient deuteration process at the high temperatures characterising the Galactic centre. In order to quantify which of these processes influence the deuteration fractionation more, observations of other high-mass star-forming

regions, located away from the Galactic centre, are essential.

Deuterium fractionation of simple interstellar molecular species was first studied in detail by Watson (1976) who argued that the large D/H values, especially present in DCN and DCO^+, can be understood as a result of ion-molecule exchange reactions in the gas and the difference in zero-point vibrational energies of the hydrogen versus deuterium-containing molecules. The observed deuterated species are then the end product of a chain of reactions starting with the formation of H_2D^+ from H_3^+ and HD, reacting with neutral molecules to form deuterated ions and subsequently recombining with electrons. This recombination also results in enhanced atomic D/H in the gas at low temperatures, which increases even more when CO, the main destroyer of H_3^+ and H_2D^+, is frozen out on grains (Roberts et al., 2003). As pointed out by Tielens (1983), this enhanced atomic D/H in the gas can be transferred to those molecules that are primarily formed by hydrogenation on grain surfaces. Key examples are H_2CO and CH_3OH, which both result from the hydrogenation of CO. Thus, the abundances of these deuterated molecules are good tracers of the physical conditions in the gas.

The process of deuteration at low temperatures has also been studied in the laboratory. In particular, Nagaoka et al. (2005) have shown that grain-surface H-D abstraction-addition reactions in solid methanol can account for the methanol D/H values derived from observations. They also note that if the gaseous atomic D/H is higher than 0.1, deuterated methanol may be formed directly through successive hydrogenation or deuteration of CO.

The focus of this work is on methanol, especially its isotopologues $^{13}CH_3OH$, $CH_3{}^{18}OH$ and the two single deuterated species CH_2DOH and CH_3OD. As described above, methanol is formed primarily on the surface of dust grains (Watanabe & Kouchi, 2002; Geppert et al., 2005; Fuchs et al., 2009) and therefore presents a good tracer of the chemistry of interstellar ice. In addition, if formed in environments with high gaseous atomic D/H, methanol will be deuterated. Deuteration levels can therefore be considered a fossil record of the chemical composition not only of the ice, but also of the gas, characterising the region in which it was formed, with the highest ratios associated with the lowest temperatures. However, in order to deduce accurate deuteration ratios, it is critical that the transitions used to derive column densities are optically thin. If this is not the case, deuterium fractions are likely to be overestimated since the lines of the more abundant hydrogenated species are generally optically thick, resulting in underestimated values. To ensure transitions are optically thin, one generally needs to target lines that are weak, that is to say have low Einstein A_{ij} values. Observations of such weak lines have however presented a challenge since line surveys have, for the most part, been conducted using single dish telescopes which are, by and large, less sensitive when compared with interferometric observations. These observations have therefore mostly targeted the brightest lines which may in many cases be optically thick and therefore result in deuteration ratios which are higher than is actually the case. With the unique sensitivity and resolving power offered by the Atacama Large Millimeter/submillimeter Array (ALMA), this is changing. With ALMA it has become possible to probe molecular transitions that are both weaker and are emitted from objects less bright than ever before. Consequently,

the field of molecular line surveys and analysis has entered a new epoch where column density determinations no longer, or to a much lesser extent, suffer from misinterpretation due to the increased access to transitions in the optically thin regime.

In this work we focus on NGC 6334I, a region of active high-mass star-formation in the giant molecular cloud complex NGC 6334, also referred to as the Cat's Paw Nebula. The complex is located in the Scorpius constellation in the southern hemisphere. The region constitutes six main dense cores, identified as discrete continuum sources in the far-infrared, labelled with Roman numerals I - VI (McBreen et al., 1979). Later, an additional, very low temperature source, NGC 6334I(N) was identified $\sim 2'$ north of NGC 6334I (Gezari, 1982). The distance to the NGC 6334 site has commonly been cited as (1.7 ± 0.3) kpc (Russeil et al., 2012) but recent work on H_2O and CH_3OH masers associated with the star-forming complex, carried out by Reid et al. (2014) and Chibueze et al. (2014), place the region closer, at distances of 1.34 and 1.26 kpc respectively. Here we will assume a mean distance of 1.3 kpc, corresponding to a galactocentric distance, d_{GC}, of ∼7.02 kpc. With a synthesised beam of the observations of $1\farcs00 \times 0\farcs74$, this allows us to probe NGC 6334I at scales of ∼1300 au. NGC 6334I is complex both in structure and composition and very rich in molecular lines (McCutcheon et al., 2000), but has the great advantage of lines with widths of only ∼3 km s^{-1} (as compared to ∼20 km s^{-1} for Sgr B2), reducing the problem of line confusion considerably. The molecular diversity of the region is demonstrated by Zernickel et al. (2012) who use the *Herschel* Space Observatory and Submillimeter Array (SMA) to investigate ∼4300 emission and absorption lines belonging to 46 different molecules and their isotopologues.

NGC 6334I is comprised of multiple hot cores, some of which are themselves multiples. This multiplicity was shown by Brogan et al. (2016) who recently presented an in-depth, high-resolution continuum study of the morphology of the site. In addition to the four previously known millimetre sources associated with the region, labelled MM1-4 and identified by Hunter et al. (2006), Brogan et al. (2016) identify six new sources: five at millimetre wavelengths, MM5-9, and one at centimetre wavelengths, CM2, all within a radius of $\sim 10''$ corresponding to 0.06 pc at the distance of the site. Another centimetre source, CM1, is identified $18''$ (∼0.1 pc) west of the main cluster. In addition to molecular lines and the far-IR and radio continuum sources, indicative of cool, dense and dusty cores, NGC 6334I displays a variety of other star-formation tracers including ultra-compact HII regions and outflows (see e.g. Persi et al., 1996; Leurini et al., 2006; Qiu et al., 2011, and references therein).

The paper is structured in the following way: Section 2.2 introduces the observations, the data reduction process and the analysis method. In Sect. 2.3 the process of identifying and fitting individual lines and estimating molecular column densities is presented. Section 2.4 discusses the deuteration levels derived and compare these to those obtained for other objects as well as the predictions from astrochemical models. Finally, Sect. 2.5 summarises our findings.

2.2 Observations and analysis method

2.2.1 Observations

The observations have been described in detail in McGuire et al. (2017), while the analysis and reduction procedures are described in detail in Brogan et al. (2016) and Hunter et al. (2017), and as such only a brief discussion is presented here. Two sets of observations are used. The primary dataset (ALMA Project 2015.1.00150.S) was taken in Cycle 3 at $\sim 1''$ resolution ($\sim$1300 au at the distance of NGC 6334I), centred on 302 GHz, and covering $\sim$3 GHz of total bandwidth with an rms noise of $\sim$500 mK. The second dataset (ALMA Project 2015.A.00022.T) was also observed in Cycle 3 but at $\sim 0\farcs2$ (260 au) resolution, centred around four frequency windows at approximately 281, 293, 338, and 350 GHz each $\sim$3.75 GHz wide, and with an rms noise of $\sim$620 mK and $\sim$900 mK in the lower and higher frequency ranges, respectively. In each case, the most line-free continuum channels were selected and used for both self calibration and continuum subtraction.

2.2.2 Analysis method

Nine spectra are extracted from the data cube. Each spectrum represents the average of a $1\farcs00 \times 0\farcs74$ region, equivalent to the area of the synthesised beam. The coordinates of the central pixel of each of the regions are summarised in Table 2.1 and the locations shown in Fig. 2.1. The positions are chosen so they present a fairly homogeneous sampling of the continuum sources MM1, located in the northern part of NGC 6334I, MM2, located in the western part of the region, and MM3, located in the southern part of the region, as well as their surroundings.

For our line analysis, the software package CASSIS[1] is used. CASSIS is a tool for spectral line identification and analysis which reads a list of line data, including rest frequency, ν, upper state energy, $E_{\rm up}$, and Einstein A_{ij} coefficients. Once a line has been identified, the line analysis tool is used to produce a synthetic spectrum by providing CASSIS with a number of parameters: excitation temperature, $T_{\rm ex}$ [K], column density of the species, $N_{\rm s}$ [cm^{-2}], source velocity, $v_{\rm LSR}$ [km s^{-1}], line width at half maximum, FWHM [km s^{-1}], and angular size of the emitting region (which is assumed to be equal to the area of the synthesised beam), $\theta_{\rm s}$ [$''$]. For line input the Jet Propulsion Laboratory (JPL[2]) and Cologne Database for Molecular Spectroscopy (CDMS[3]) databases are used.

For the analysis of $^{13}CH_3OH$ and $CH_3^{18}OH$, the CDMS database is used. These entries include the ground and first vibrational states for $^{13}CH_3OH$ and the ground, first and second vibrational states for $CH_3^{18}OH$. For the analysis of CH_2DOH the JPL datatbase is used. The line intensities in this list are based on the method described by Pearson et al. (2012). The JPL catalogue warns that extreme caution should be taken in determining columns (or concentrations) of CH_2DOH directly from b-type and c-type transitions as significant errors can occur, while the a-type

[1] http://cassis.irap.omp.eu
[2] http://spec.jpl.nasa.gov
[3] http://www.ph1.uni-koeln.de/cdms/

Table 2.1: Summary of regions and column densities

Region	Location (J2000)		$v_{\rm LSR}$	FWHM	$T_{\rm ex}$ [a]	$N_{\rm s}$			
	R.A.	Decl.				$^{13}CH_3OH$	$CH_3^{18}OH$	CH_2DOH [b]	CH_3OD
			[km s^{-1}]	[km s^{-1}]	[K]	[$\times10^{17}$ cm^{-2}]	[$\times10^{17}$ cm^{-2}]	[$\times10^{17}$ cm^{-2}]	[$\times10^{17}$ cm^{-2}]
MM1 I	17:20:53.437	-35:46:57.902	-5.5	4.0	336	8.3	2.0 – 3.4	0.56 – 1.63	5.5
MM1 II	17:20:53.371	-35:46:57.013	-6.7	3.0	215	7.4	2.0 – 2.4	0.25 – 0.79	3.8
MM1 III	17:20:53.397	-35:46:59.209	-8.3	3.0	157	8.3	1.7	0.38 – 1.10	2.3
MM1 IV	17:20:53.381	-35:46:56.315	-6.7	3.0	195	5.2	1.5	0.13 – 0.50	1.7
MM1 V	17:20:53.552	-35:46:57.415	-5.2	2.8	174	1.3	0.41	0.08 – 0.17	0.43
MM2 I	17:20:53.165	-35:46:59.231	-9.0	3.5	164	6.6	0.8 – 1.5	0.45 – 1.38	1.8
MM2 II	17:20:53.202	-35:46:57.613	-7.0	2.8	143	1.8	0.32	0.04 – 0.09	0.4
MM3 I	17:20:53.417	-35:47:00.697	-9.0	3.0	122	0.9	0.14	0.03 – 0.06	0.15
MM3 II	17:20:53.365	-35:47:01.541	-9.8	2.5	122	0.8	0.13	0.03 – 0.06	0.16

Notes. Range of $N_{\rm s}$ corresponds to the range in column density, within the synthesised beam of $1\farcs00\times0\farcs74$, with and without blending. [(a)] Excitation temperature of the best-fit $^{13}CH_3OH$ model. [(b)] Numbers include the vibrational correction factor of 1.25 as well as the uncertainty on the line strength (see Sect. 2.2.2).

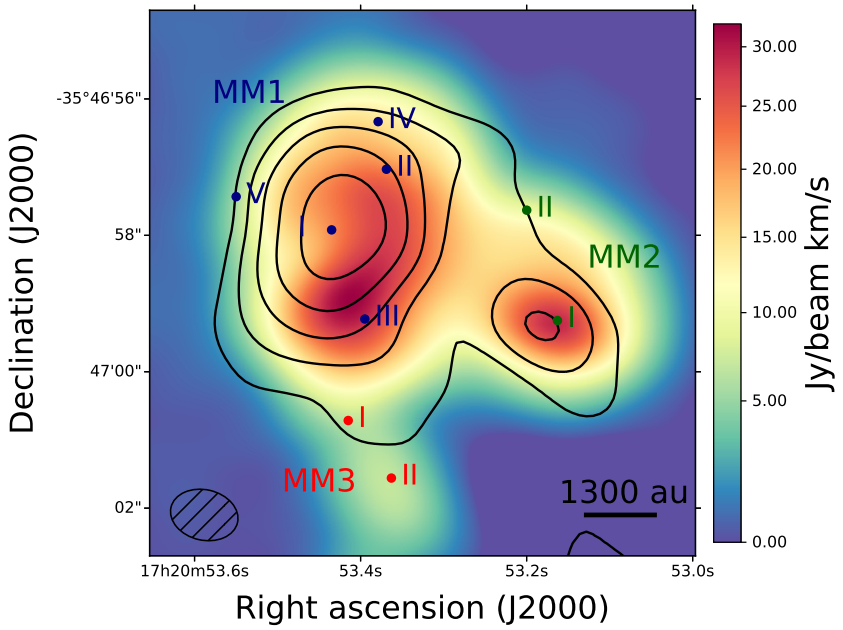

Figure 2.1: Velocity integrated intensity map of the $^{13}CH_3OH$ transition at 303.692 GHz with the 1 mm continuum image overlaid in black contours (levels are [10, 20, 40, 80, 160]σ with σ = 0.02 Jy beam^{-1}). The locations at which spectra have been extracted are marked in blue for MM1, green for MM2 and red for MM3. The synthesised beam (∼1300×962 au) is shown in the bottom left corner.

transitions are more reliable[4]. The symmetry of the transitions are defined as follows: ΔK_a = even, ΔK_c = odd for a-type, ΔK_a = odd, ΔK_c = odd for b-type and ΔK_a = odd, ΔK_c = even for c-type (Pearson et al., 2012). We optimise our CH_2DOH fit to the $12_{(2,11)}$→$12_{(1,12)}$ b-type transition at 301.514 GHz (see Sect. 2.3.3) and use an updated value for the base 10 logarithm of the integrated line intensity at 300 K for this transition of -3.84 ± 0.2 nm^2 MHz (John Pearson, priv. comm.). Also, since the CH_2DOH entry only includes the ground vibrational state, a vibrational correction factor of 1.25 has been applied to all listed values (Holger Müller, priv. comm.). To model CH_3OD we use the summary of CH_3OD frequencies reported by Walsh et al. (2000), the line strengths reported by Anderson et al. (1988) and Anderson et al. (1993) and the partition function of $CH_3^{18}OH$ (from the CDMS database) which includes the vibrational levels.

Because CH_3OH is a very abundant species in star-forming regions, the lines of the primary ^{12}C-isotope are optically thick and cannot be used to derive column densities and excitation temperatures. Fortunately, many lines of the isotopologues $^{13}CH_3OH$, $CH_3^{18}OH$, CH_2DOH and CH_3OD remain in the optically thin regime, making column density determination of these species possible. We iden-

[4]https://spec.jpl.nasa.gov/ftp/pub/catalog/doc/d033004.pdf

tify a total of fifteen transitions belonging to the methanol isotopologues in the covered frequency range: eight of these belong to $^{13}CH_3OH$, four to $CH_3^{18}OH$, one to CH_2DOH and two to CH_3OD. The transitions are summarised in Table 2.2. Since the frequency range covered is limited to ∼3 GHz (301.180 – 304.165 GHz) only a few transitions of each species are covered. This complicates the definite identification of lines, especially in the case of $CH_3^{18}OH$, CH_2DOH and CH_3OD for which many lines are either very weak or blended to an extent that it is impossible to distinguish the contribution from individual molecular species.

In order to verify the presence of these species in NGC 6334I, a second set of data, covering a larger range of frequencies, is also consulted (see Sect. 2.2). Based on transitions in these data the presence of the less abundant CH_3OH-isotopologues is confirmed. However, since these data are of higher angular resolution (∼0.″2) emission is resolved out and we are not able to constrain the column density of either of the deuterated species better than from our primary data set. The upper limits for CH_2DOH (which are similar for a- and b-type transitions covered) and CH_3OD as well as the column densities for $^{13}CH_3OH$ and $CH_3^{18}OH$ based on these data are consistent with the values derived based on our primary data set. The data are presented in Appendix A but will not be discussed further in the main manuscript.

For each methanol line candidate we carefully examine transitions belonging to other species (for which the spectroscopy is known and listed in either of the databases mentioned above) at similar frequencies to ensure lines are not incorrectly assigned. In the first step, all species which have not previously been detected in space are excluded. Secondly, species are excluded based on Einstein A_{ij} coefficient and upper state energy. For the remaining blending candidates we investigate if any additional transitions are covered in the data range and if so, whether these can provide additional constraints. If the blending candidates are isotopologues, we search for transitions belonging to the parent species and ensure that column densities are consistent. The process of line assignment and analysis of potential blended transitions will be discussed in detail in Sects. 2.3.1 – 2.3.4.

Assuming local thermodynamic equilibrium (LTE) and optically thin lines synthetic spectra are created for each methanol isotopologue. Firstly, the excitation temperatures and $^{13}CH_3OH$ column densities for each region are derived by creating a grid of models, with T_{ex} ranging between 50 and 350 K and N ranging between $5{\times}10^{16}$ and $5{\times}10^{19}$ cm^{-2}, and selecting the model with the minimal χ^2 as the best fit. The $^{13}CH_3OH$ lines are fitted first because these lines are the most numerous and span the largest range of upper state energies. Secondly, the column densities of the remaining methanol isotopologues are optimised keeping the excitation temperature fixed at the value of the best-fit ^{13}C-methanol model. The transitions of each methanol isotopologue, as well as the blending species, are modelled separately, and summed to obtain a full spectrum for each of the nine regions. These spectra are shown in Figs. B.1 – B.3.

Finally, to estimate the $^{12}CH_3^{16}OH$ column density used to calculate the deuterium fraction for each spectral region, a $^{12}C/^{13}C$ value of 62 and a $^{16}O/^{18}O$ value of 450 is adopted, both derived assuming d_{GC} ∼7.02 kpc and the relations for $^{12}C/^{13}C$ and $^{16}O/^{18}O$ reported by and Wilson (1999) respectively.

Table 2.2: Summary of detected lines

Species	Transition		Frequency	E_{up}	A_{ij}	Database
	$[QN]_{up}$ [a]	$[QN]_{low}$ [a]	[MHz]	[K]	$\times 10^{-5}$ [s^{-1}]	
$^{13}CH_3OH$	18 2 16 1	17 1 17 1	301 238.558	684.91	8.96	CDMS
	20 3 18 0	19 4 15 0	301 272.475	525.44	4.89	
	14 -1 14 0	13 2 11 0	302 166.269	243.11	0.12	
	10 0 10 0	9 1 8 0	302 590.285	137.53	6.91	
	20 3 17 0	19 4 16 0	302 882.003	525.52	4.99	
	7 1 6 0	6 2 4 0	303 319.623	84.49	4.27	
	1 1 0 0	1 0 1 0	303 692.682	16.84	32.2	
	15 -3 13 0	16 0 16 0	303 865.391	334.68	0.10	
$CH_3^{18}OH$	3 1 2 0	3 0 3 0	301 279.428	27.81	30.6	CDMS
	4 1 3 0	4 0 4 0	302 848.743	36.78	30.9	
	16 1 16 1	15 2 14 1	303 016.300	307.63	4.14	
	3 1 2 2	2 0 2 1	303 855.874	34.10	8.09	
CH_2DOH	12 2 11 0	12 1 12 0	301 514.152	183.10	8.31	JPL
CH_3OD	7 2 + 0	7 1 - 0	303 296.120	82.73	18.2	(1)
	7 4 – 0	8 3 – 0	303 904.827	130.79	2.82	

Notes. [a] Quantum numbers for $^{13}CH_3OH$, $CH_3^{18}OH$ and CH_2DOH are (J K_a K_c v) and quantum numbers for CH_3OD are (J K P v) where v=0, 1, 2 refers to the three sub-states e_0, e_1 and o_1 of the ground state respectively.

References. (1) Walsh et al. (2000), and references therein.

2.3 Results

2.3.1 $^{13}CH_3OH$

Eight transitions of $^{13}CH_3OH$ are detected towards NGC 6334I. For each of these, a synthetic spectrum is created and optimised simultaneously to obtain the best-fit values for T_{ex} and N. However, the same range of frequencies which host the ^{13}C-methanol lines are also known to be occupied by a number of methyl formate (CH_3OCHO) transitions. Especially the $^{13}CH_3OH$ transitions at 302.590, 302.882, 303.319 and 303.865 GHz are overlapping with transitions of CH_3OCHO. Fortunately, since many transitions of this species are covered in the spectral range, the column density of CH_3OCHO can be constrained to a range of (0.6 – 2.5)$\times 10^{17}$ cm^{-2} in our beam for all regions. While the contribution from CH_3OCHO to the $^{13}CH_3OH$ line fits does not change the value of the best-fit $^{13}CH_3OH$ column density, likely because the upper state energy of these transitions are high, $\sim$700 K, as compared with those of the affected $^{13}CH_3OH$ lines, it is included for completeness. Figure 2.2 shows the synthetic spectra of the best fit models to $^{13}CH_3OH$, CH_3OCHO and the combination of the two for the transition at 302.590 GHz detected towards each of the regions. Despite this transition

having the largest contribution from CH_3OCHO, it is evident that at the abundances of CH_3OCHO present in NCG 6334I, its effect on the $^{13}CH_3OH$ line is small and it is therefore reasonable to assume that the observed peak in the data at 302.590 GHz is due mainly to $^{13}CH_3OH$.

The best-fit column density and excitation temperature for $^{13}CH_3OH$ for each of the regions are listed in Table 2.1. The values range about an order of magnitude, with the lowest values associated with MM3 I and II, $(0.8 - 0.9)\times10^{17}$ cm^{-2}, while the highest, $\sim8.3\times10^{18}$ cm^{-2}, are found in MM1 I and III. For the remaining regions the values span a range of $(1.3 - 7.4)\times10^{18}$ cm^{-2}.

Zoom-ins of the spectra showing the remaining $^{13}CH_3OH$ lines can be found in Appendix C. Generally the single-T_{ex}, single-N models reproduce the data well. It should be noted however, that the transition with the lowest A_{ij} $\sim10^{-6}$ s^{-1} at 303.865 GHz is consistently under produced by the models as compared with the data by factors of between three and six. The same is true for the line at 302.166 GHz towards the regions around MM1. The reason for this could either be uncertainties in the spectroscopic values for these particular transitions, or that the lines are blended with some unknown species, the spectroscopy of which is not included in either of the JPL or CDMS databases. Alternatively, the explanation could be that some of the transitions which we assume to be optically thin are in fact slightly thick, resulting in underestimated column densities. To test this, we optimise the column density and excitation temperature to the transitions at 302.166 and 303.865 GHz. Doing so, we find that for the modelled spectra to reproduce the data at these frequencies, the column densities need to be higher by factors of between five and ten, as compared to the best-fit column density when fitting to all lines, resulting in the remaining transitions being largely saturated. To improve the fits the individual sources would need to be modelled using an excitation model taking both density and temperature gradients into account. Such a full excitation model would potentially make the saturated lines appear more gaussian.

2.3.2 $CH_3^{18}OH$

Assuming a $^{12}C/^{13}C$ value of 62 and a $^{16}O/^{18}O$ value of 450 implies that the $^{13}CH_3OH$ to $CH_3^{18}OH$ column density ratio is approximately a factor of seven. Adopting this ratio and using the best-fit column density values for $^{13}CH_3OH$, the majority of the modelled $CH_3^{18}OH$ lines appear weaker as compared with the data by about a factor of two. Indeed, when optimising the $CH_3^{18}OH$ column density, assuming T_{ex} to be the same as for $^{13}CH_3OH$, the values are only factors of between two and three lower than those of $^{13}CH_3OH$. This result suggests that the $^{13}CH_3OH$ lines, which are assumed to be optically thin, are in fact partially optically thick, and therefore the derived column densities may be slightly underestimated, as discussed above.

As in the case of $^{13}CH_3OH$, the $CH_3^{18}OH$ lines are also partly blended. Especially the line at 303.016 GHz overlaps with the transition from another molecular species: $O^{13}CS$, although the slight shift in frequency of the $O^{13}CS$ line with respect to the line of $CH_3^{18}OH$ means that the observed peak in the data cannot be

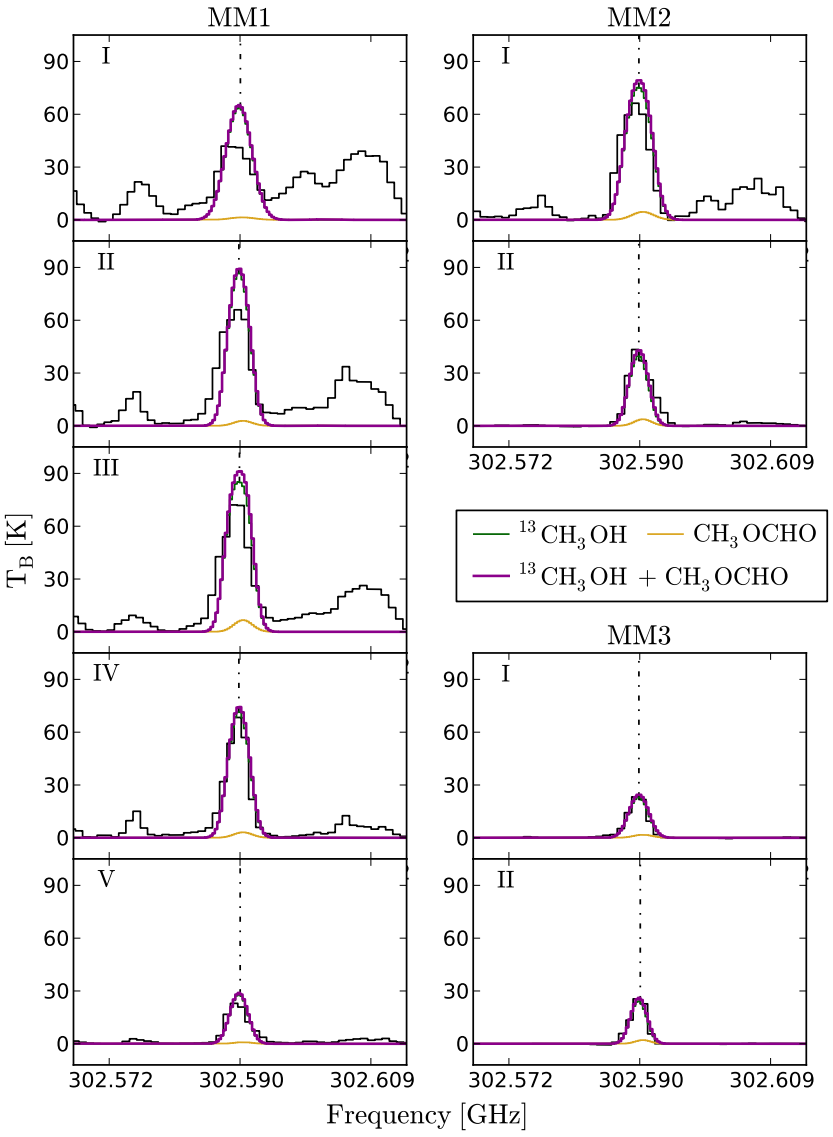

Figure 2.2: $^{13}CH_3OH$ $10_{(0,10)} \rightarrow 9_{(1,8)}$ transition at 302.590 GHz (indicated by dash-dotted lines) detected towards each region. Frequencies are shifted to the rest frame of the individual regions. Green lines represent the modelled spectra of $^{13}CH_3OH$ without blending, i.e., excluding the contribution from CH_3OCHO (including the contribution from CH_3OCHO does not change the $^{13}CH_3OH$ column density of the best-fit model). Yellow lines represent the modelled spectra of CH_3OCHO and magenta lines represent the sum of the $^{13}CH_3OH$ and CH_3OCHO spectra.

due purely to $O^{13}CS$. Unfortunately no other lines of $O^{13}CS$ are covered in our frequency range and likewise only one line of the parent species, OCS, is in the data range. It is therefore difficult to constrain the contribution of $O^{13}CS$ to the blend from the data itself. Instead the column density for OCS derived by Zernickel et al. (2012) of 1.2×10^{18} cm^{-2} (assuming a source size of 2.5″) at $T_{\rm ex}$ = 100 K and the $^{12}C/^{13}C$ value of 62 is used to estimate a column density of $O^{13}CS$ in NGC 6334I of 1.9×10^{16} cm^{-2}. The modelled spectra of this transition as well as the data are shown in Fig. 2.3. A column density of $O^{13}CS$ of 1.9×10^{16} cm^{-2} is also consistent with the data in Appendix A; however, while the $O^{13}CS$ lines covered here are not overproduced at this column density, they cannot be better constrained due to blends. To derive the column density of $CH_3^{18}OH$ two sets of fits are preformed: the first excludes the $O^{13}CS$-blended line and optimises the column density to the remaining three transitions (for which no known species listed in the databases contribute significantly to the data peaks), this value is used to set an upper limit for the column density. In the second fit, a contribution from $O^{13}CS$ is included and the $CH_3^{18}OH$ column density is optimised to all lines. The $O^{13}CS$ contribution is kept constant for all regions.

The column densities derived for $CH_3^{18}OH$ are listed in Table 2.1. For most regions, the difference between the fit purely considering $CH_3^{18}OH$ and the fit of $CH_3^{18}OH$ with a contribution from $O^{13}CS$, is less than a factor of two. For regions MM1 III-V, MM2 II and MM3 however, the $O^{13}CS$ column density derived from Zernickel et al. (2012) results in modelled spectra that overshoot the data at the specific frequency. For these regions only the value for the pure-$CH_3^{18}OH$ fit is reported. As is the case of $^{13}CH_3OH$, the derived $CH_3^{18}OH$ column densities are lowest in regions MM3 I and II, with values between $(1.3 - 1.4)\times10^{16}$ cm^{-2}. Slightly higher values, $(0.32 - 1.5)\times10^{17}$ cm^{-2} and $(0.41 - 2.4)\times10^{17}$ cm^{-2}, are derived for regions MM2 I and II and MM1 II-V respectively. The highest value is again associated with region MM1 I, $(2.0 - 3.4)\times10^{17}$ cm^{-2}. Zoom-ins of all detected $CH_3^{18}OH$ transitions can be seen in Appendix D. Again, the single density and temperature models reproduce the data well, keeping in mind that the main contributor to the peak at 303.016 GHz is $O^{13}CS$.

2.3.3 CH_2DOH

For CH_2DOH, the $12_{(2,11)}\rightarrow12_{(1,12)}$ transition at 301.514 GHz is detected. Unfortunately, this line too is blended. We constrain the column density of the blending species, CH_3NC, based on its characteristic double feature around 301.53 GHz, and derive values in the range $(1.1 - 2.0)\times10^{14}$ cm^{-2} for the regions MM1 I-IV and MM2 I. As in the case of $O^{13}CS$, these column densities are consistent with the data in Appendix A but cannot be further constrained. For the remaining regions, MM1 V, MM2 II and MM3 I-II, the data do not display any signs of CH_3NC. Figure 2.4 shows the modelled spectra of CH_2DOH, both with and without the contribution from the blending species, CH_3NC, as well as the sum of the spectra of CH_2DOH with blending and CH_3NC. For the regions where CH_3NC is detected, the difference between the values of the column density of CH_2DOH fitted with and without the contribution from CH_3NC is approximately a factor of three. No

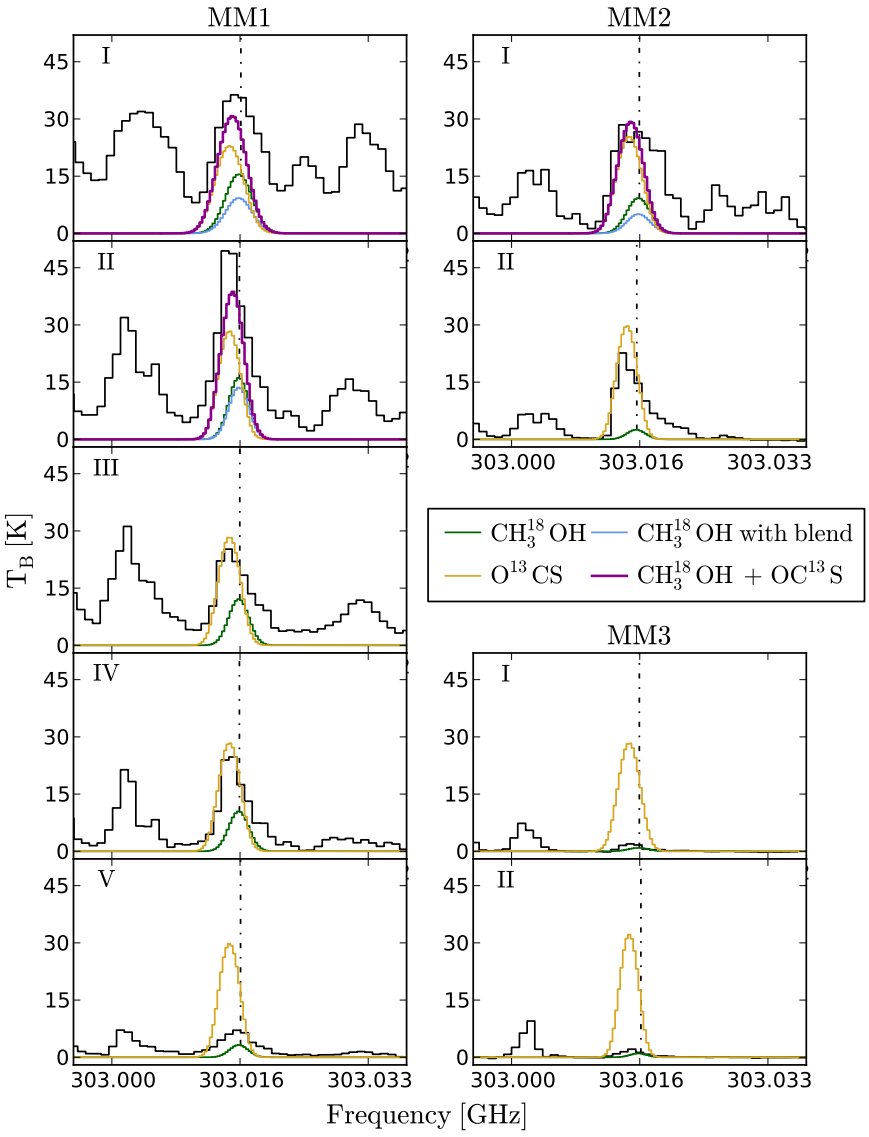

Figure 2.3: $CH_3^{18}OH$ $16_{(1,16)}\rightarrow15_{(2,14)}$ transition at 303.016 GHz (indicated by dash-dotted lines) detected towards each region. Frequencies are shifted to the rest frame of the individual regions. Blue and green lines represent the modelled spectra of $CH_3^{18}OH$ with and without blending, i.e., including and excluding the contribution from $O^{13}CS$, respectively. Yellow lines represent the modelled spectra of $O^{13}CS$, assuming a fixed column density of 1.9×10^{16} cm^{-2} for all regions, and magenta lines represent the sum of the spectra of $CH_3^{18}OH$ with blending and $O^{13}CS$.

transitions of the more common isomer CH_3CN are covered by the data, so the ratio of -CN/-NC cannot be constrained.

The column densities derived for CH_2DOH are listed in Table 2.1. We note that these include the vibrational correction and uncertainty on the line strength as discussed in Sect. 2.2.2. As regions MM1 V, MM2 II and MM3 I-II show no clear CH_3NC feature, only the value for the pure CH_2DOH fit is reported. As in the case of $^{13}CH_3OH$ and $CH_3^{18}OH$, the lowest CH_2DOH column densities are detected towards regions MM3 I and II, both with values in the range of (3.0 – 6.0)$\times10^{15}$ cm^{-2}. Region MM2 II also displays low values, (4.0 – 9.0)$\times10^{15}$ cm^{-2}, while the values detected towards MM2 I are fairly high, (0.45 – 1.38)$\times10^{17}$ cm^{-2}. The highest column density is again detected towards MM1 I, (0.56 – 1.63)$\times10^{17}$ cm^{-2}, with the remain regions extracted from the area around MM1 show column densities spanning a range of about an order of magnitude, (0.08 – 1.10)$\times10^{17}$ cm^{-2}.

2.3.4 CH_3OD

In addition to the transitions of CH_2DOH, we have searched for lines belonging to CH_3OD, for which two transitions, one at 303.296 GHz and one at 303.904 GHz (see summary by Walsh et al., 2000), are covered. To derive a column density for this isotopologue, our fits were optimised to the transition at 303.296 GHz. No other transitions in either the JPL nor the CDMS databases are listed at this frequency so the line in the data is considered to be purely due to CH_3OD. The modelled spectra and data are shown in Fig. 2.5 and Appendix E and the derived column densities are listed in Table 2.1.

As in the case of CH_2DOH, the lowest column densities of CH_3OD are detected towards the regions MM3 I and II, with values in the range of (1.5 – 1.6)$\times10^{16}$ cm^{-2}. Regions MM2 II and MM1 V have similar column densities of 4.0 and 4.3$\times10^{16}$ cm^{-2}, respectively. For the remaining regions, column densities in the range of (1.7 – 5.5)$\times10^{17}$ cm^{-2} are derived. The highest value is again associated with region MM1 I. It is very interesting to note that the column densities derived for CH_3OD are consistently higher than those derived for CH_2DOH in all regions.

2.4 Methanol deuteration fractions

In the following sections the CH_2DOH/CH_3OH and CH_2DOH/CH_3OD values derived for the nine regions in NGC 6334I, as well as those derived for a number of other sources, will be discussed. These are summarised in Fig. 2.6 and listed in Table 2.3.

2.4.1 NGC 6334I

Using the column densities derived from the $^{13}CH_3OH$, $CH_3^{18}OH$, CH_2DOH and CH_3OD transitions, we calculate the CH_2DOH to CH_3OH and CH_3OD to CH_3OH

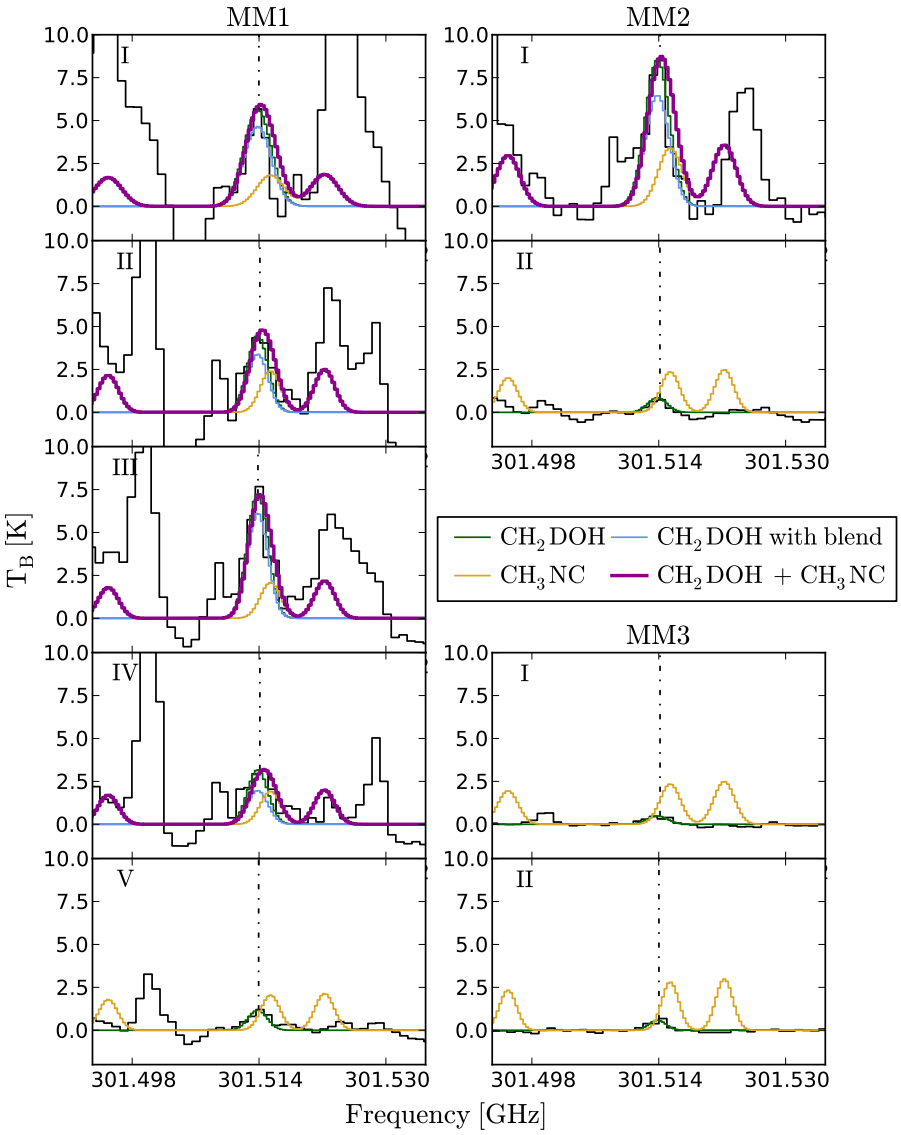

Figure 2.4: CH_2DOH $12_{(2,11)} \rightarrow 12_{(1,12)}$ transition at 301.514 GHz (indicated by dash-dotted lines) detected towards each region. Frequencies are shifted to the rest frame of the individual regions. Blue and green lines represent the modelled spectra of CH_2DOH with and without blending, i.e., including and excluding the contribution from CH_3NC, respectively. Yellow lines represent the modelled spectra of CH_3NC and magenta lines represent the sum of the spectra of CH_2DOH with blending and CH_3NC.

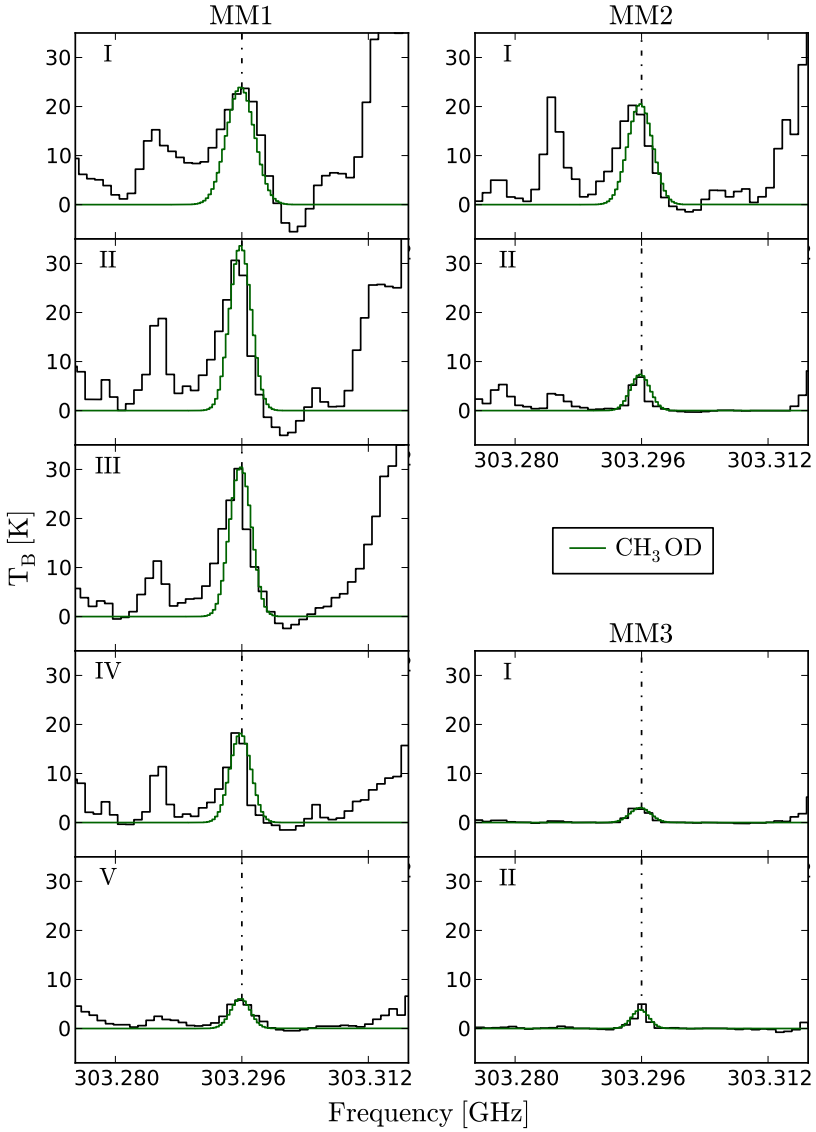

Figure 2.5: CH_3OD $7_{(2+)} \rightarrow 7_{(1-)}$ transition at 303.296 GHz (indicated by dash-dotted lines) detected towards each region. Frequencies are shifted to the rest frame of the individual regions. Green lines represent the modelled spectra of CH_3OD.

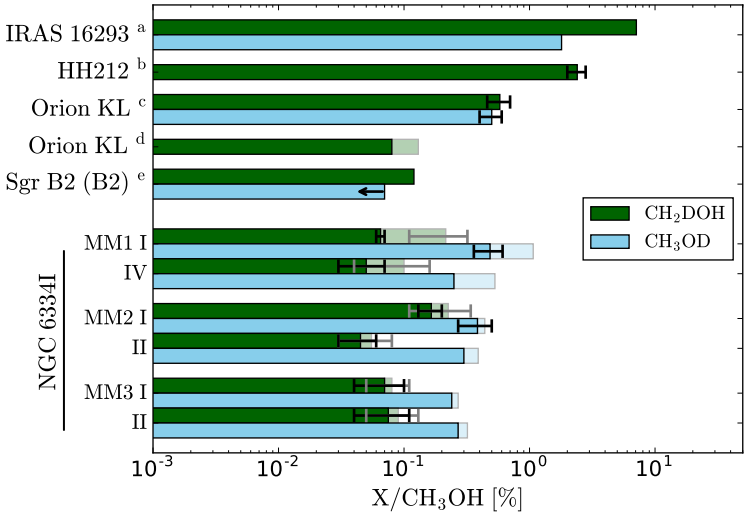

Figure 2.6: Column density ratio of CH_2DOH to CH_3OH (green) and CH_3OD to CH_3OH (blue) for NGC 6334I and other objects. For Orion KL the shaded bar indicates the range of ratios derived by Peng et al. (2012). For NGC 6334I shaded and filled bars indicate the ratios derived using the ^{13}C and ^{18}O isotopologues as base respectively. Error bars indicate the range of ratios derived with and without blending. For NGC 6334I MM1 only the region with the lowest (MM1 IV) and highest (MM1 I) ratios are plotted. **References.** $^{(a)}$ Jørgensen et al. (2018). $^{(b)}$ Bianchi et al. (2017). $^{(c)}$ Neill et al. (2013). $^{(d)}$ Peng et al. (2012). $^{(e)}$ Belloche et al. (2016).

ratios for each of the spectral regions. These are listed in Table 2.3. The CH_2DOH/CH_3OH values range between (0.03 – 0.34)% and (0.03 – 0.20)% and the CH_3OD/CH_3OH values range between (0.27 – 1.07)% and (0.22 – 0.61)%, derived from $^{12}C/^{13}C$ and $^{16}O/^{18}O$ respectively. In the case of CH_2DOH/CH_3OH, both the lowest and the highest ratios are associated with region MM2, the lowest detected towards region MM1 II and the highest towards MM2 I. For the CH_3OD to CH_3OH ratio the lowest values are detected towards MM3 I and MM1 V while the highest is detected towards MM1 I. The mean values over all regions (including the vibrational correction and uncertainty on the line strength of CH_2DOH) are 0.13% ± 0.06% and 0.53% ± 0.27% based on the ^{13}C isotopologue and 0.08% ± 0.04% and 0.32% ± 0.09% based on the ^{18}O isotopologue, for CH_2DOH/CH_3OH and CH_3OD/CH_3OH respectively. Based on these means the average CH_3OD/CH_3OH value is twice that of the average CH_2DOH/CH_3OH value. The CH_2DOH to CH_3OH and CH_3OD to CH_3OH ratios derived based on the ^{13}C and ^{18}O isotopologues agree within factors of approximately two for all regions.

If the exchange of D into the CH_3 and OH functional groups of methanol is equally efficient, the column density ratio of CH_2DOH to CH_3OD is expected to be equal to three. Interestingly, this is not the case for the regions presented here. Instead, we derive CH_2DOH to CH_3OD column density ratios of the order ∼0.3 (not including the statistical correction factor which would further decrease

Table 2.3: CH_2DOH/CH_3OH and CH_3OD/CH_3OH values derived from $^{13}CH_3OH$ or $CH_3^{18}OH$

Source	Region	CH_2DOH/CH_3OH		$(CH_2DOH/CH_3OH)_{corr}$ [a]		CH_3OD/CH_3OH		CH_2DOH/CH_3OD [b]
		$^{12}C/^{13}C$ [%]	$^{16}O/^{18}O$ [%]	$^{12}C/^{13}C$ [%]	$^{16}O/^{18}O$ [%]	$^{12}C/^{13}C$ [%]	$^{16}O/^{18}O$ [%]	
NGC 6334 I	MM1 I	0.11 – 0.32	0.06 – 0.07	0.04 – 0.11	0.02	1.07	0.36 – 0.61	0.16 – 0.19
	MM1 II	0.05 – 0.17	0.03 – 0.07	0.02 – 0.06	0.01 – 0.02	0.83	0.35 – 0.42	0.10 – 0.13
	MM1 III	0.07 – 0.21	0.06 – 0.14	0.02 – 0.07	0.02 – 0.05	0.45	0.30	0.23 – 0.29
	MM1 IV	0.04 – 0.16	0.03 – 0.07	0.01 – 0.05	0.01 – 0.03	0.53	0.25	0.12 – 0.19
	MM1 V	0.09 – 0.20	0.04 – 0.09	0.03 – 0.07	0.01 – 0.03	0.50	0.22	0.25
	MM2 I	0.11 – 0.34	0.13 – 0.20	0.04 – 0.11	0.04 – 0.07	0.44	0.27 – 0.50	0.38 – 0.50
	MM2 II	0.03 – 0.08	0.03 – 0.06	0.01 – 0.03	0.01 – 0.02	0.39	0.30	0.15
	MM3 I	0.05 – 0.11	0.04 – 0.10	0.08 – 0.04	0.01 – 0.03	0.27	0.24	0.25
	MM3 II	0.05 – 0.13	0.04 – 0.11	0.02 – 0.04	0.01 – 0.04	0.32	0.27	0.23
Sgr B2 (1)	N2	0.12	–	0.04	–	<0.07	–	>1.8
Orion KL (2,3)	Compact Ridge	0.58 ± 0.12	–	0.19	–	0.5 ± 0.1	–	1.2 ± 0.3
		(0.08 – 0.13)	–	0.03 – 0.04	–		–	0.7 ± 0.3 [c]
Orion B (4)	HH212	2.4 ± 0.4	–	0.8 ± 0.1	–	–	–	–
IRAS 16293–2422 (5)	B	–	7.1 [d]	–	2.4 [d]	–	1.8	3.9

Notes. Ranges of CH_2DOH/CH_3OH and CH_3OD/CH_3OH correspond to the range in column density of $^{13}CH_3OH$, $CH_3^{18}OH$ and CH_2DOH with and without blending. All CH_2DOH/CH_3OH values include the vibrational correction of 1.25 as well as the uncertainy in the line strength. (a) Corrected for statistical weight of the location of the substituted deuterium. For CH_2DOH this value is 3, for CH_3OD it is 1. (b) Ratios do not include statistical correction factors. (c) Mean ratio over central region. (d) Includes vibration correction factor for CH_2DOH of 1.457 at 300 K (see Section 2.2 of Jørgensen et al. (2018)).

References. (1) Belloche et al. (2016). (2) Neill et al. (2013). (3) Peng et al. (2012). (4) Bianchi et al. (2017). (5) Jørgensen et al. (2018).

the ratio by a factor of three), lower by a factor of six as compared with the lower limit derived by Belloche et al. (2016) for Sgr B2 and factors of four and two as compared with the values derived for Orion KL by Neill et al. (2013) and Peng et al. (2012) respectively. This very low CH_2DOH/CH_3OD value is just opposite to values found for pre-stellar cores and low-mass protostars, where CH_2DOH/CH_3OD values up to ten are found (Bizzocchi et al., 2014; Parise et al., 2006), although consistent with the trend of lower ratios inferred for high mass protostars (Ratajczak et al., 2011). The low CH_2DOH to CH_3OD ratio implies that the deuteration of the OH functional group is more efficient than that of the CH_3 group, or that D is more easily abstracted from the CH_3 group rather than from the OH group.

Various chemical processes in the gas and ice that can cause the CH_2DOH to CH_3OD ratio to deviate from the statistical ratio of three are described in Ratajczak et al. (2011) and in Faure et al. (2015). In the gas phase these processes include protonation and dissociative recombination reactions which destroy CH_3OD more efficiently than CH_2DOH since all recombinations of $CH_2DOH_2^+$ lead to CH_2DOH while CH_3OHD^+ can recombine to either CH_3OH or CH_3OD with an equal branching ratio (Charnley et al., 1997). However the timescale needed to significantly alter the CH_2DOH to CH_3OD ratio through these reactions is likely too long, that is more than 10^5 years, when compared with the typical lifetime of a hot core. In the solid state, experiments carried out by Nagaoka et al. (2005) have shown that H/D substitution in solid CH_3OH forms CH_2DOH but no CH_3OD. Also in the solid state, experiments by Ratajczak et al. (2009) and Faure et al. (2015) have shown that H/D exchanges can occur between water and methanol in warm ices (T $\sim$120 K), but only on the OH-functional group of methanol and not on the CH_3 group. The processes mentioned above favour the formation of CH_2DOH over that of CH_3OD and consequently lead to an increase in CH_2DOH/CH_3OD rather than decrease. The low observed ratio therefore remains unexplained.

It should be noted however, that because the spectroscopy of CH_2DOH is not well understood, the CH_2DOH/CH_3OD value derived may be higher. To better constrain the ratio, future studies are well-advised to target only a-type CH_2DOH-transitions rather than b- or c-type transitions, for which the uncertainties on the line strength are not well-constrained, in addition to preferring weak, low A_{ij} transitions, to ensure that lines are optically thin. A refinement of the accuracy of the column density of CH_2DOH, will make it possible to investigate the coupling of CH_2DOH/CH_3OD with environment and chemical evolution. Therefore it may be advantageous to focus future observations on narrow bands with high spectroscopic resolution covering a few well-chosen transitions, rather than broader bands which, albeit potentially covering more lines, might make identification and analysis difficult due to uncertainties in spectroscopic values or blending with features of other species which may not be resolved.

As discussed in Sect. 2.2.2, the excitation temperature for each region is determined based on a minimal χ^2 technique comparing a grid of models with the spectra. The excitation temperatures of the best-fit models range between $\sim$120 and 330 K, the warmest regions associated with the MM1 core and the coldest with the MM3 core. We investigate the effect of varying the excitation tempera-

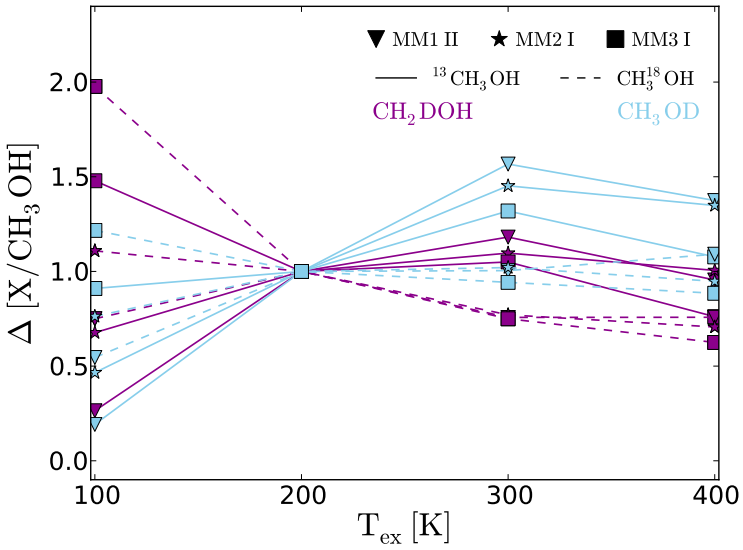

Figure 2.7: Column density ratio as function of excitation temperature. Ratios are normalised to the value derived for T_{ex} = 200 K. Magenta and blue lines represent the CH_2DOH to CH_3OH and CH_3OD to CH_3OH column density ratios respectively, while sold and dashed lines indicate the values derived assuming $^{12}C/^{13}C = 62$ and $^{16}O/^{18}O = 450$ respectively. Different regions are indicated by different markers.

ture on the derived column densities and plot the ratios of CH_2DOH to CH_3OH and CH_3OD to CH_3OH as function of T_{ex} in Fig. 2.7. From this analysis, it is evident that the spread in CH_2DOH/CH_3OH and CH_3OD/CH_3OH ascribed to different excitation temperatures (over all regions) is within a factor of two of the value derived for T_{ex}= 200 K. For the individual regions, the variations in CH_2DOH/CH_3OH and CH_3OD/CH_3OH over the full range of excitation temperatures are within factors of between two and four. Therefore, it is reasonable to assume that the lines used to optimise our fits are optically thin at excitation temperatures of 100 – 400 K and consequently that our derived CH_2DOH/CH_3OH and CH_3OD/CH_3OH values do not depend critically on an exact determination of T_{ex}. For each value of T_{ex} we also calculate the ratio of the ^{13}C- and ^{18}O-methanol column densities. These ratios differ by less than a factor of two for MM2 and MM3 and a factor of four for MM1, verifying that the transitions are excited under similar conditions. The vibrational correction factor applied to CH_2DOH has only little effect on this result.

2.4.2 Comparison with other sources

Using ALMA, Belloche et al. (2016) investigated the deuterium fractionation of complex organic molecules towards the high mass star-forming region Sgr B2 in the Galactic central region. With the high spatial resolution observations, $\sim$1.4″,

they probe scales down to 0.06 pc (∼11620 au assuming a distance ∼8.3 kpc). They report a tentative detection of CH_2DOH and derive a deuteration fraction for CH_2DOH/CH_3OH of 0.12%. Including the statistical weight of the location of the substituted deuterium this value becomes 0.04%. CH_3OD is not detected, but an upper limit of 0.07% for CH_3OD/CH_3OH is reported. This is translated into a lower limit on the CH_2DOH to CH_3OD ratio of 1.8. Their CH_3OH column density is based on LTE modelling of both the ^{13}C and ^{18}O methanol isotopologues. The authors note that the CH_2DOH/CH_3OH value they derive is lower than what is predicted by the chemical models of Taquet et al. (2014) and Aikawa et al. (2012) but may be explained by the high temperature that characterises the Galactic Center or result from an overall low abundance of deuterium in this region due to the high star formation rates.

For the high-mass star-forming regions in Orion, CH_2DOH/CH_3OH values are of the same order as for Sgr B2, ranging between (0.08 – 0.58)%, equivalent to (0.03 – 0.19)% when the statistical weights are accounted for. These values are derived by Peng et al. (2012), using observations from the IRAM Plateau de Bure Interferometer, and Neill et al. (2013), using data from *Herschel*/HIFI. In addition, Neill et al. (2013) report a CH_3OD/CH_3OH value of 0.5 ± 0.1% and a CH_2DOH/CH_3OD value of 1.2 ± 0.3. A slightly lower CH_2DOH/CH_3OD value of 0.7 ± 0.3 is reported by Peng et al. (2012). To derive CH_3OH column densities Neill et al. (2013) and Peng et al. (2012) use slightly different approaches: Neill et al. (2013) assume a $^{12}C/^{13}C$ value of 60 and derive the CH_3OH density based on transitions of $^{13}CH_3OH$, while Peng et al. (2012) detect a number of E-type methanol transitions and derive the total CH_3OH density assuming an A/E-type abundance of 1.2. Both studies of Orion KL probe scales which are smaller than those studied in Sgr B2: ∼10″ and ∼2″, corresponding to ∼4140 au and ∼830 au at the distance of Orion KL (∼414 pc), for Neill et al. (2013) and Peng et al. (2012) respectively. However, since the beam dilution factor is higher in these studies, meaning that the area over which the emission is averaged is larger, the column density derived, assuming the total emission to be the same, is lower. Also, observations with larger beam sizes, which are more sensitive to large scale structures, generally probe regions of lower temperature, meaning that some molecules may be locked up in icy grain mantles, resulting in lower gas phase abundances. This combination of effects means that the derived column densities, as well as the inferred deuteration ratios, for Orion KL may in fact be higher, if derived from observations with higher angular resolution.

An example of such high-resolution observations are presented by Bianchi et al. (2017) who use 0.15″-resolution ALMA observations to study the Sun-like class 0 protostar HH212, located in the Orion B cloud, on scales of ∼70 au. From transitions of $^{13}CH_3OH$ and CH_2DOH they derive a CH_2DOH/CH_3OH value of (2.4 ± 0.4)%, equivalent to (0.8 ± 0.1)% after accounting for statistical weights, assuming a $^{12}C/^{13}C$ value of 70. This deuteration ratio is higher than what has been derived for high-mass star-forming regions but lower by an order of magnitude as compared with observations (carried out with single dish telescopes) towards protostars in Perseus. Bianchi et al. (2017) argue that the lower deuteration ratio they find is consistent with the dust temperature of the Orion region being higher

than that of the Perseus cloud.

Similarly to HH212, the low-mass protostellar binary system IRAS 16293, located in the ρ Ophiuchi cloud complex, exhibits a CH_2DOH to CH_3OH ratio which is much higher than that of the high-mass star-forming regions. With the ALMA-PILS survey (see Jørgensen et al. 2016 for full PILS overview), sampling spatial scales of the order $0.5''$, corresponding to 60 au at the distance of the source ($\sim$120 pc), Jørgensen et al. (2018) derive a CH_2DOH to CH_3OH ratio of 7.1%, equivalent to 2.4% after corrections for statistical weights, assuming a ^{16}O to ^{18}O isotope ratio of 560 to estimate the CH_3OH abundance, and a CH_3OD to CH_3OH ratio of 1.8% resulting in a CH_2DOH/CH_3OD value of 3.9.

Because of the comparable resolution and methods used, the methanol deuteration ratios derived for IRAS 16293, HH212 and Sgr B2, may be directly compared to the ratios derived in this study. When doing so, the low levels of deuterium fractionation associated with the regions in NGC 6334I, as compared with the low-mass star-forming regions IRAS 16293 and HH212, become very apparent (Table 2.3). It is also interesting to note that while our inferred CH_2DOH/CH_3OH values for NGC 6334I are similar to what has been derived by Belloche et al. (2016) for Sgr B2, the CH_3OD/CH_3OH values are higher by up to an order of magnitude as compared with the lower limit reported for Sgr B2.

2.4.3 Comparison with models

In an effort to better understand the observed variety of deuterated species and their column density ratios, a number of astrochemical models have been put forward, among these the GRAINOBLE model. This code has been described in detail in previous studies (Taquet et al., 2012, 2013, 2014) and here we give only a brief presentation before discussing how the model compares with the levels of deuteration we find in the regions of NGC 6334I.

GRAINOBLE follows the gas-ice interstellar chemistry through a three-phase (gas, ice surface, ice bulk) rate equations approach initially developed by Hasegawa & Herbst (1993). The model takes into account a number of gas-grain processes including the accretion of species onto the grains, desorption back into the gas-phase and reactions between particles at the ice surface and in the ice mantle. The gas-phase chemical network is described in Taquet et al. (2014) and includes the spin states of H_2, H_2^+, and H_3^+, as well as the deuterated isotopologues of hydrogenated species with four or less atoms and molecules involved in the chemistry of water, methanol, ammonia, and formaldehyde. The ice chemical network follows the formation and the deuteration of the main ice species, following a series of laboratory experiments, and complex organic molecules through radical-radical recombination reactions. Specifically, the pathways for formation and deuteration of methanol include both addition reactions involving atomic D and hydrogenation of solid CO and H_2CO at cold ($T = 10 - 15$ K) temperatures as well as abstraction reactions, as shown by Hidaka et al. (2009).

We investigated the effect of the dust and gas temperatures, T, assumed to be equal, and the total density, n_H, on the methanol deuteration. For this purpose, a series of pseudo-time dependent simulations in which the chemistry evolves over

time whilst the temperature and density remain constant were run. Figure 2.8 shows the final ice abundances of CO, H_2O, and CH_3OH, the deuteration in ices of methanol and the gas phase atomic D to H ratio and the CH_2DOH to CH_3OD ratio as a function of temperature. Models are shown for three different densities, $n_H = 10^4$, 10^5 and 10^6 cm^{-3}, with respective ages of $2{\times}10^7$, $2{\times}10^6$, and $2{\times}10^5$ years.

It is evident that both the ice composition and the methanol deuteration are highly dependent on the considered temperature and total density. The barrierless reactions which form water from atomic oxygen mean that this species is the least dependent on T and n_H. Methanol and its deuterated isotopologues are, on the other hand, formed through hydrogenation and/or deuteration of CO and H_2CO, which are thought to have high activation barriers. As a consequence, methanol formation can be inhibited at high densities, decreasing the CO hydrogenation, or at high temperatures where CO no longer efficiently freezes-out onto grains. Despite the lower residence time of H and CO on the grains at temperatures above $\sim$20 K, limiting the formation of H_2CO and later CH_3OH, significant deuteration of methanol occur in the model. This is due to the long timescales considered which enhance the probability that the CO and H or D particles meet on the dust grain and recombine. Also, since it is formed through hydrogenation and/or deuteration processes, the methanol deuteration is governed by the atomic D/H in the gas phase.

Specifically, the strong decrease of the methanol deuteration with temperature, up to three orders of magnitudes with an increase of T from 10 to 40 K, is due to the decreased efficiency of deuterium chemistry in the gas phase with increasing temperature. Atomic D is mostly formed via electronic recombination of H_3^+ isotopologues, formed through exothermic reactions between H_3^+ (or with its isotopologues) and HD. Because the efficiency of the backward reactions increase with an increase in temperature, the deuteration of H_3^+ and therefore the production of atomic D is limited at high temperatures. However, the solid CH_2DOH to CH_3OH ratio does not always scale with the final atomic gas phase D/H. Figure 2.8 shows how the CH_2DOH to CH_3OH ratio decreases more efficiently with temperature at high densities but remains fairly constant for $n_H = 10^4$ cm^{-3}.

The model distinguishes the formation of CH_2DOH from that of CH_3OD. As seen in Fig. 2.8, the ratio remains close to three throughout the temperature range. This is due to the three reaction channels that form CH_2DOH compared with the single channel that forms CH_3OD. Also, it is important to note that while the observations trace the methanol deuteration in the gas phase of the hot core surrounding the forming massive protostars, the model describes the predicted deuteration of ices formed during the precursor pre-stellar phase. Therefore, the analysis is implicitly based on the assumption that the gas phase composition around the hot cores reflects the composition of the ices in the pre-stellar phase. As discussed in Sect. 2.4.1, a number of processes may alter the ice methanol deuteration. Some of these processes are already accounted for in the model, for example the formation of CH_2DOH via abstraction reactions, shown experimentally by Nagaoka et al. (2005), is included in the model but contributes little to the overall abundance of CH_2DOH. Others, like the H/D exchanges shown to occur

between water and methanol in warm ices (Ratajczak et al., 2009; Faure et al., 2015) still need to be implemented and could potentially contribute significantly to the decrease of the CH_3OD/CH_3OH abundance resulting in a higher CH_2DOH to CH_3OD ratio in contrast to the low ratios derived for the regions in NGC 6334I.

Based on the model predictions, our inferred deuterium fractionation of methanol in the NGC 6334I regions, indicate a temperature during formation around 30 K. A similar dust temperature of the precursor dense core is reported by Russeil et al. (2013) who use data from *Herschel* to derive a dust temperature map of the NGC 6334 star-forming region and show that the area is dominated by temperatures $\sim$25 – 35 K. Such a warm pre-stellar cloud could be the result of heating from a nearby earlier phase of star formation, potentially associated with NGC 6334E a region located between I and I(N) and hosting an O-type star and associated large shell-like HII region (Carral et al., 2002). The small variation in deuterium fractions found towards the individual regions of NGC 6334I may reflect local differences in $n_{\rm H}$.

2.5 Summary and conclusion

In this paper we analyse the level of deuterium fractionation in methanol towards the high-mass star-forming region NGC 6334I. We use high spectral resolution observations carried out with ALMA and extract spectra from nine individual locations across the MM1, MM2 and MM3 regions. Based on these, we identify a total of 15 transitions belonging to the isotopologues of methanol. Assuming excitation temperatures of $\sim$120 – 330 K for the individual regions, we derived column densities for each of the species $^{13}CH_3OH$, $CH_3^{18}OH$, CH_2DOH and CH_3OD and calculate CH_2DOH/CH_3OH and CH_3OD/CH_3OH. These range from 0.03% to 0.34% and 0.03% to 0.20% for the ratios of CH_2DOH to CH_3OH and from 0.27% to 1.07% and 0.22% to 0.61% for the ratios of CH_3OD to CH_3OH, using the ^{13}C and ^{18}O isotopologues to derive the column density of $^{12}CH_3^{16}OH$ respectively. The highest levels of deuterium fractionation are associated with the regions MM1 I and MM2 I, which are also the brightest regions in the continuum image, while the lowest are detected towards the regions MM2 II and MM3 I both associated with less bright continuum regions. The derived deuterium fractionation ratios only vary by factors of between two and four with excitations temperatures between 100 and 400 K.

The derived CH_2DOH/CH_3OH values are consistently low throughout NGC 6334I with a mean CH_2DOH/CH_3OH value over all regions of 0.13 ± 0.06% and 0.08 ± 0.04% based on the ^{13}C and ^{18}O isotopologues respectively. This homogeneity of the CH_2DOH to CH_3OH ratios derived for the different cores indicate that they formed from the same precursor cloud. The levels are also similar to those derived towards Sgr B2 in the Galactic centre (Belloche et al., 2016) as well as those derived for the high-mass star-forming regions in Orion by Peng et al. (2012), but lower by factors of a few when compared with the values derived by Neill et al. (2013) for the same region. Because of the similar values, the low deuterium fractionation found in the Galactic centre is likely not due to astra-

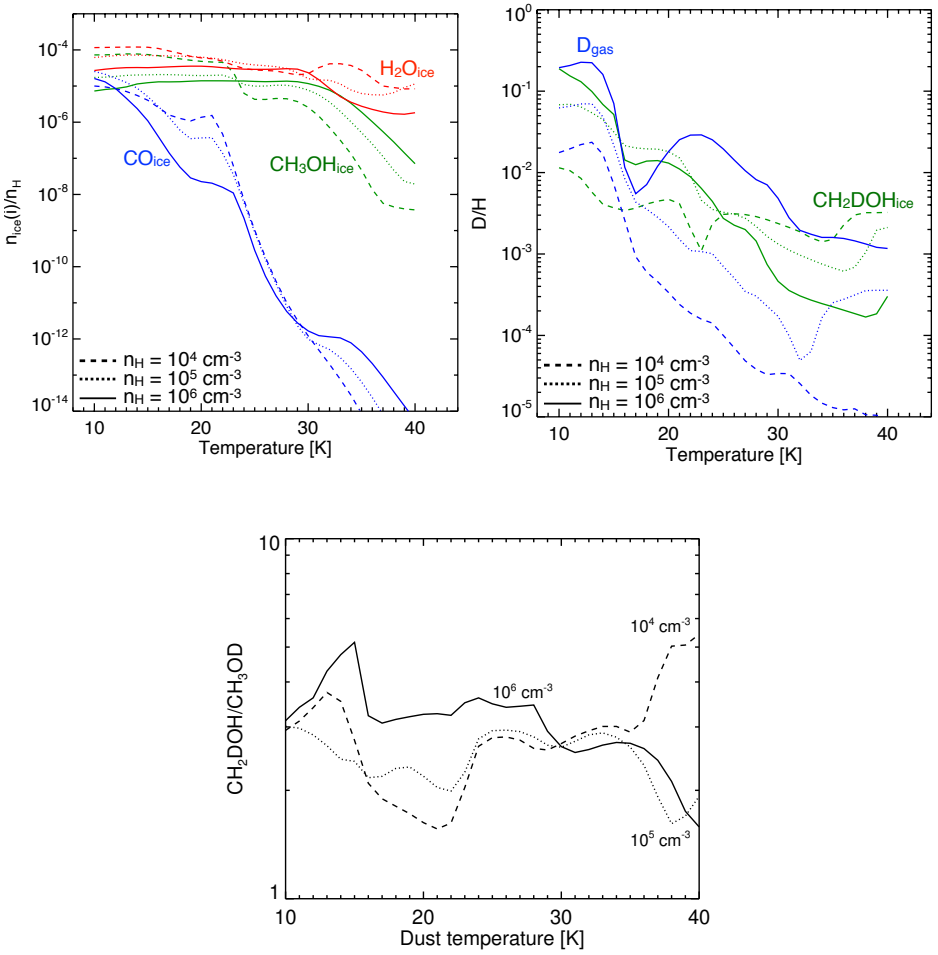

Figure 2.8: *Top panel*: Final abundances of H_2O (red lines), CO (blue lines), and CH_3OH (green lines) in ices as a function of temperature. *Middle panel*: Final CH_2DOH to CH_3OH abundance ratio in ices (green lines) and final atomic D/H in the gas phase (blue lines) as a function of temperature. *Bottom panel*: Final CH_2DOH to CH_3OD abundance ratio as function of temperature. In all panels three densities are considered: $n_{\rm H} = 10^4$ (dashed), 10^5 (dotted), and 10^6 (solid) cm^{-3}.

tion but rather the high temperatures characterising the region. The methanol deuterium fractionation levels derived for the low-mass systems HH212 and IRAS 16293 are higher by up to two orders of magnitude when compared with the values inferred for NGC 6334I, clearly illustrating the differences in physical and chemical environment prevailing in high- and low-mass star-forming regions.

Based on the chemical model of Taquet et al. (2014), the CH_2DOH to CH_3OH ratios detected towards the regions of NGC 6334I indicate a dust temperature at the time of the systems formation $\sim$30 K. This temperature is higher than what is predicted for low-mass star-forming regions where the levels of deuterium in simple molecular species indicate a dust temperature at the time of formation below 20 K.

In addition to CH_2DOH, CH_3OD is unambiguously detected towards all nine regions of NGC 6334I allowing CH_2DOH to CH_3OD ratios to be derived. These range from 0.10 – 0.50, the highest value associated with the region MM2 I and the lowest with MM1 II. Our CH_2DOH/CH_3OD values towards NGC 6334I are lower than what is expected from statistics, assuming the CH_3 and OH functional groups of methanol to be equally likely to be deuterated. While CH_2DOH to CH_3OD ratios of the order of unity have been detected towards high-mass star-forming regions previously, the low levels derived here have not been seen before and may hint at a favoured formation of CH_3OD or destruction of CH_2DOH in this region which has yet to be explained by models or experiments.

Acknowledgements. A special thanks to Dr. Holger Müller for valuable discussions of the spectroscopy of deuterated methanol. We acknowledge data reduction support from Allegro, the European ALMA Regional Center node in the Netherlands, and Dr. Luke Maud in particular for expert advice. We thank the anonymous referee for constructive comments that improved our manuscript. Support for B.A.M. was provided by NASA through Hubble Fellowship grant #HST-HF2-51396 awarded by the Space Telescope Science Institute, which is operated by the Association of Universities for Research in Astronomy, Inc., for NASA, under contract NAS5-26555. This paper makes use of the following ALMA data: ADS/JAO.ALMA#2015.1.00150.S and #2015.A.00022.T. ALMA is a partnership of ESO (representing its member states), NSF (USA) and NINS (Japan), together with NRC (Canada) and NSC and ASIAA (Taiwan) and KASI (Republic of Korea), in cooperation with the Republic of Chile. The Joint ALMA Observatory is operated by ESO, AUI/NRAO and NAOJ. This work is based on analysis carried out with the CASSIS software and JPL: http://spec.jpl.nasa.gov/ and CDMS: http://www.ph1.uni-koeln.de/cdms/ spectroscopic databases. CASSIS has been developed by IRAP-UPS/CNRS (http://cassis.irap.omp.eu).

Appendix A: ADS/JAO.ALMA#2015.A.00022.T

This appendix summarises the additional data set introduced in Sect. 2.2. The data confirm the presence of $CH_3^{18}OH$, CH_2DOH and CH_3OD in NGC 6334I but do not constrain the column densities of $O^{13}CS$ and CH_3NC better than the primary data set. This is due to blending with other species and, in the case of $O^{13}CS$, a limited number of lines covered. The column densities of $O^{13}CS$ and CH_3NC derived from the primary data set are consistent with the data in this appendix.

Table A.1: Summary of data set ALMA#2015.A.00022.T

Location (J2000)		v_{LSR}	FWHM	N_s			
R.A.	Decl.	[km s^{-1}]	[km s^{-1}]	$^{13}CH_3OH$ [$\times10^{17}$ cm^{-2}]	$CH_3^{18}OH$ [$\times10^{17}$ cm^{-2}]	CH_2DOH^a [$\times10^{17}$ cm^{-2}]	CH_3OD [$\times10^{17}$ cm^{-2}]
17:20:53.372	-35:46:58.140	-7.0	3.0	15	3	<0.63	<5.0

Notes. All models assume T_{ex} = 200 K. $^{(a)}$ Numbers include the vibrational correction factor of 1.25 .

Table A.2: CH_2DOH/CH_3OH and CH_3OD/CH_3OH upper limits from data set ALMA#2015.A.00022.T

CH_2DOH/CH_3OH		$(CH_2DOH/CH_3OH)_{corr}$ ^{a}		CH_3OD/CH_3OH		CH_2DOH/CH_3OD^b
$^{12}C/^{13}C$ [%]	$^{16}O/^{18}O$ [%]	$^{12}C/^{13}C$ [%]	$^{16}O/^{18}O$ [%]	$^{12}C/^{13}C$ [%]	$^{16}O/^{18}O$ [%]	
<0.07	<0.05	<0.02	<0.02	<0.54	<0.37	0.13

Notes. All CH_2DOH/CH_3OH values include the vibrational correction of 1.25. $^{(a)}$ Corrected for statistical weight of the location of the substituted deuterium. For CH_2DOH this value is 3, for CH_3OD it is 1. $^{(b)}$ Ratios do not include statistical correction factors.

Table A.3: Summary of covered lines with $A_{ij} > 10^{-5}$ s^{-1} and $T_{ex} < 600$ K

Species	Transition		Frequency	E_{up}	A_{ij}	Database
	$[QN]_{up}$ [a]	$[QN]_{low}$ [a]	[MHz]	[K]	$\times 10^{-5}$ [s^{-1}]	
$^{13}CH_3OH$	6 1 6 +0	5 1 5 +0	282 790.743	61.73	9.36	CDMS
	10 1 10 1	9 0 9 1	281 578.684	415.84	6.20	
	6 1 6 +1	5 1 5 +1	282 167.288	372.77	9.50	
	6 5 1 -1	5 5 0 -1	282 364.928	468.80	2.94	
	6 5 2 +1	5 5 1 +1	282 364.928	468.80	2.94	
	6 3 4 1	5 3 3 1	282 383.033	465.18	7.33	
	6 4 3 1	5 4 2 1	282 395.053	411.38	5.39	
	6 -3 3 1	5 -3 2 1	282 419.021	370.43	7.30	
	6 -2 4 1	5 -2 3 1	282 424.212	412.25	8.75	
	6 2 4 +1	5 2 3 +1	282 433.145	346.33	8.68	
	6 -4 2 1	5 -4 1 1	282 434.336	453.35	5.44	
	6 5 1 1	5 5 0 1	282 436.442	477.34	2.99	
	6 -5 2 1	5 -5 1 1	282 438.034	594.31	2.97	
	6 2 5 -1	5 2 4 -1	282 438.887	346.33	8.68	
	6 1 6 1	5 1 5 1	282 446.467	339.04	9.51	
	6 3 4 +1	5 3 3 +1	282 448.135	443.86	7.34	
	6 3 3 -1	5 3 2 -1	282 448.135	443.86	7.34	
	6 4 2 +1	5 4 1 +1	282 449.004	529.02	5.44	
	6 4 3 -1	5 4 2 -1	282 449.004	529.02	5.44	
	6 0 6 1	5 0 5 1	282 449.004	348.11	9.79	
	6 2 5 1	5 2 4 1	282 463.121	447.49	8.72	
	6 -1 5 1	5 -1 4 1	282 495.697	460.88	9.51	
	6 0 6 +1	5 0 5 +1	282 531.066	471.12	9.79	
	6 1 5 -1	5 1 4 -1	282 717.665	372.86	9.56	
	3 2 2 -0	4 1 3 -0	291 536.562	51.39	2.86	
	13 0 13 +1	12 1 12 +1	338 759.948	205.95	21.8	
	21 3 18 -0	20 4 17 -0	349 996.298	573.04	7.80	
	1 1 1 +0	0 0 0 +0	350 103.118	16.80	32.9	
	8 1 7 0	7 2 5 0	350 421.585	102.62	7.03	
$CH_3^{18}OH$	2 0 2 4	1 1 1 5	279 462.469	306.75	2.22	CDMS
	6 1 5 0	5 1 4 0	280 450.272	61.46	9.35	
	12 0 12 0	11 1 11 0	281 082.602	173.41	11.9	
	11 5 7 2	12 4 8 2	291 923.895	283.67	2.64	
	12 2 11 0	11 3 8 0	292 264.636	210.95	4.06	
	3 2 2 0	4 1 3 0	292 611.830	50.83	2.83	
	12 2 10 0	11 3 9 0	294 273.734	211.05	4.17	
	18 6 13 0	19 5 14 0	294 800.838	574.95	3.47	
	18 6 12 0	19 5 15 0	294 801.017	574.95	3.47	
	8 1 7 2	7 2 5 2	336 743.182	100.85	6.08	
	13 2 12 0	12 3 9 0	338 164.707	239.84	6.56	
	10 5 6 2	11 4 7 2	338 313.086	259.21	3.67	
	4 1 3 2	3 0 3 1	350 245.511	43.00	12.0	
	20 1 20 0	19 2 17 0	350 673.946	477.07	7.52	

Continued on next page

Continued from previous page

Species	Transition		Frequency	E_{up}	A_{ij}	Database
	$[QN]_{up}$ [a]	$[QN]_{low}$ [a]	[MHz]	[K]	$\times 10^{-5}$ [s^{-1}]	
CH_2DOH	11 2 10 0	11 1 11 0	294 323.578	157.47	11.7	JPL
	14 4 11 1	14 3 11 2	348 938.891	296.93	12.4	
	14 4 10 1	14 3 12 2	348 990.168	296.93	12.5	
	13 4 10 1	13 3 10 2	349 149.466	266.96	12.3	
	13 4 9 1	13 3 11 2	349 183.827	266.96	12.3	
	12 4 9 1	12 3 9 2	349 333.979	239.13	12.1	
	11 4 8 1	11 3 8 2	349 495.208	213.44	11.8	
	11 4 7 1	11 3 9 2	349 508.871	213.44	11.8	
	10 4 7 1	10 3 7 2	349 635.597	189.89	11.5	
	10 4 6 1	10 3 8 2	349 643.597	189.89	11.5	
	7 4 4 1	7 3 4 2	349 951.685	132.08	10.0	
	7 4 3 1	7 3 5 2	349 952.720	132.08	10.0	
	5 1 4 1	5 0 5 0	350 632.072	48.99	20.7	
	8 1 8 0	7 1 7 0	351 796.429	80.09	14.1	
CH_3OD	4 -3 – 0	5 -2 – 0	280 460.396	63.67	1.72	(1)
	9 -2 – 0	9 -1 – 0	280 630.770	115.62	13.2	
	4 1 – 0	3 0 – 0	292 141.956	30.85	7.06	
	5 1 – 0	4 0 – 0	338 196424	41.70	10.2	
	6 4 – 0	7 3 – 0	349 427.582	115.61	3.42	
	5 1 + 0	4 0 + 0	349 883.62	38.55	29.4	

Notes. For CH_2DOH only the least blended lines are listed. [(a)] QNs for $^{13}CH_3OH$, $CH_3^{18}OH$ and CH_2DOH are (J K_a K_c v) and QNs for CH_3OD are (J K P v) where v=0, 1, 2 refers to the three sub-states e_0, e_1 and o_1 of the ground state respectively.

References. (1) Walsh et al. (2000), and references therein.

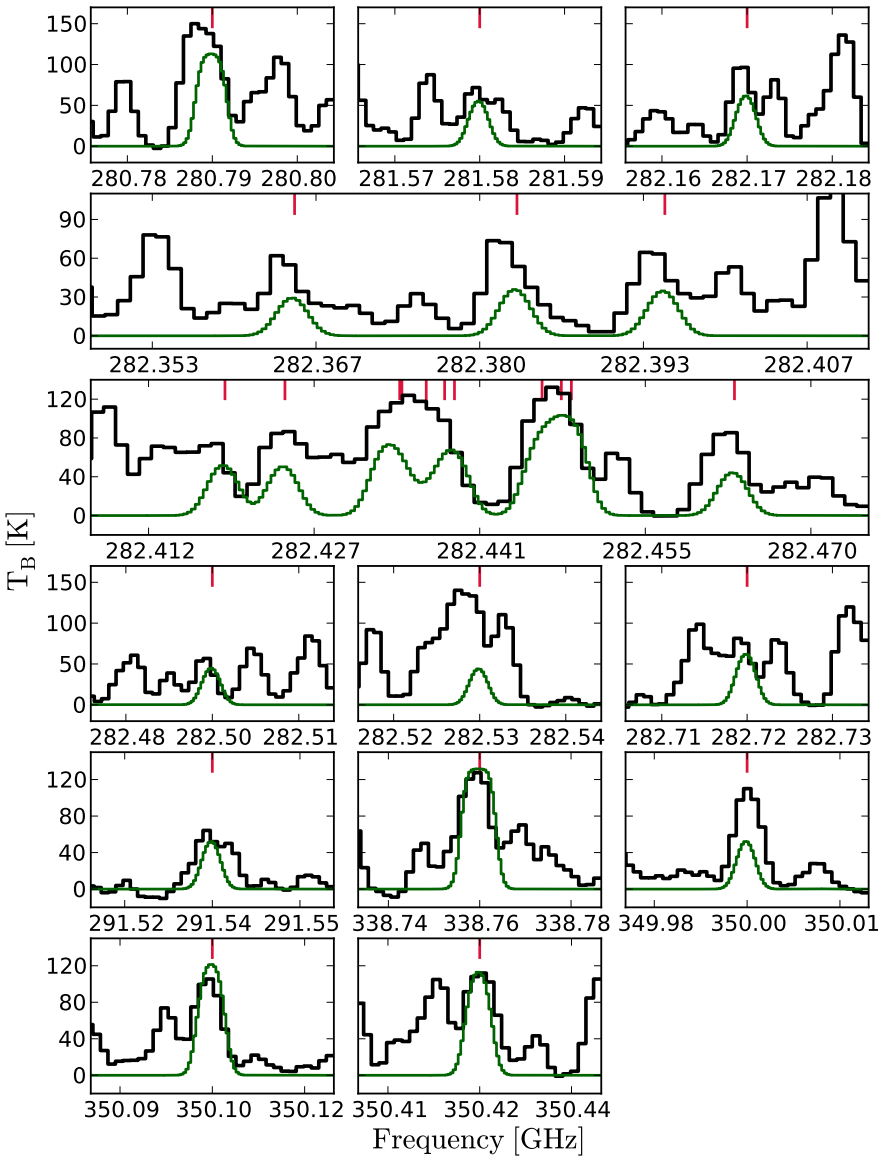

Figure A.1: $^{13}CH_3OH$ transitions with $T_{ex} < 600$ K and $A_{ij} > 10^{-5}$ s^{-1} detected towards NGC 6334I. Frequencies are shifted to the rest frame of the region. The data and model are shown in black and green respectively. Rest frequencies of individual lines are indicated in red.

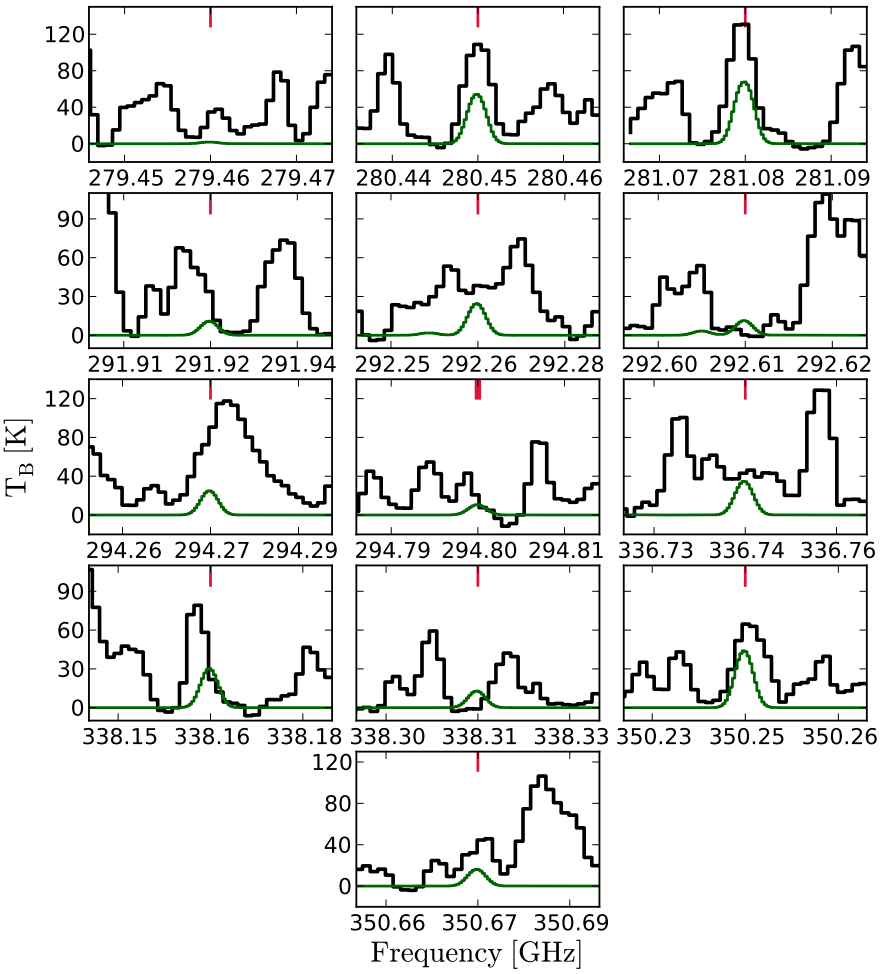

Figure A.2: $CH_3^{18}OH$ transitions with $T_{ex} < 600$ K and $A_{ij} > 10^{-5}$ s^{-1} detected towards NGC 6334I. Frequencies are shifted to the rest frame of the region. The data and model are shown in black and green respectively. Rest frequencies of individual lines are indicated in red.

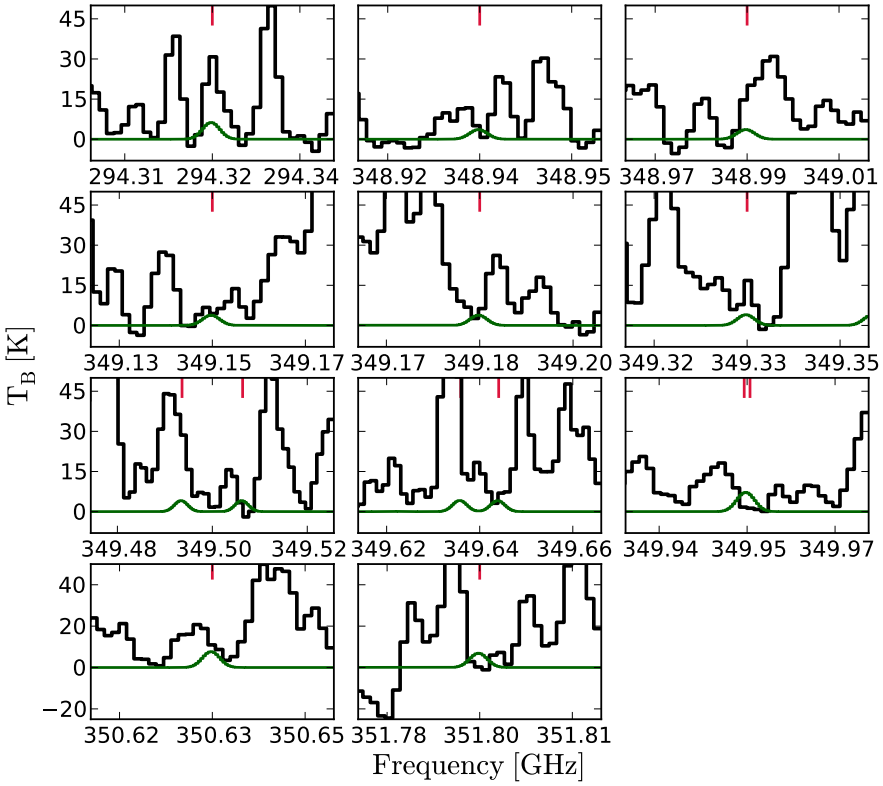

Figure A.3: Selection of CH_2DOH transitions with $T_{ex} < 400$ K and $A_{ij} > 10^{-4}$ s^{-1} detected towards NGC 6334I. Frequencies are shifted to the rest frame of the region. The data and model are shown in black and green respectively. Rest frequencies of individual lines are indicated in red.

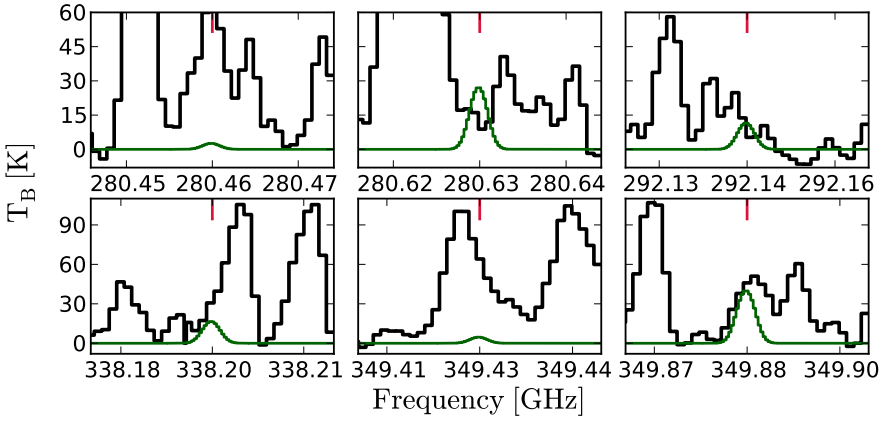

Figure A.4: CH_3OD transitions detected towards NGC 6334I. Frequencies are shifted to the rest frame of the region. The data and model are shown in black and green respectively. Rest frequencies of individual lines are indicated in red.

Appendix B: Full spectra

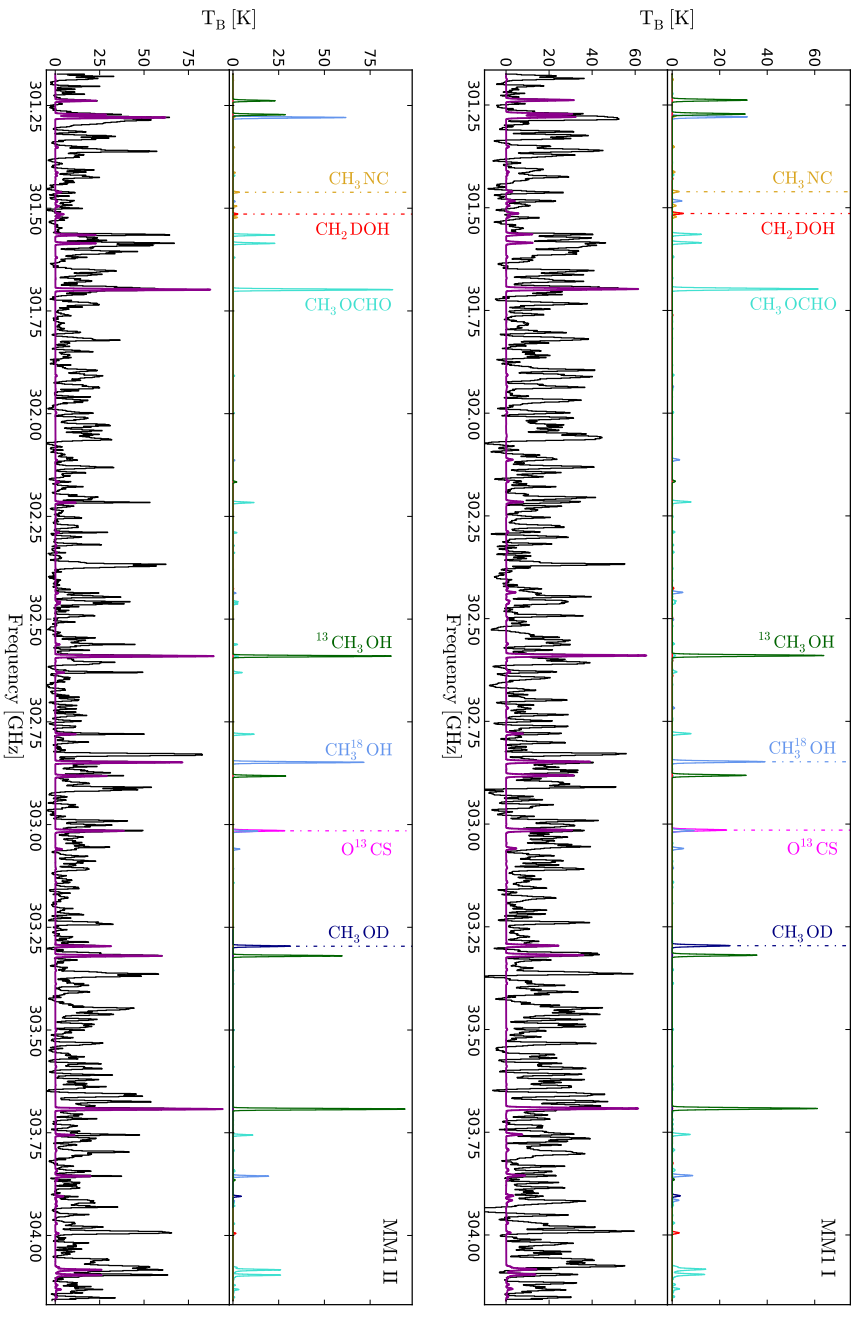

Figure B.1: MM1 I-V. *Top panels*: model components. *Bottom panels*: data (black) and full model (magenta), i.e., the linear combination of the synthetic spectrum for each species. Frequencies are shifted to the rest frame of the individual regions.

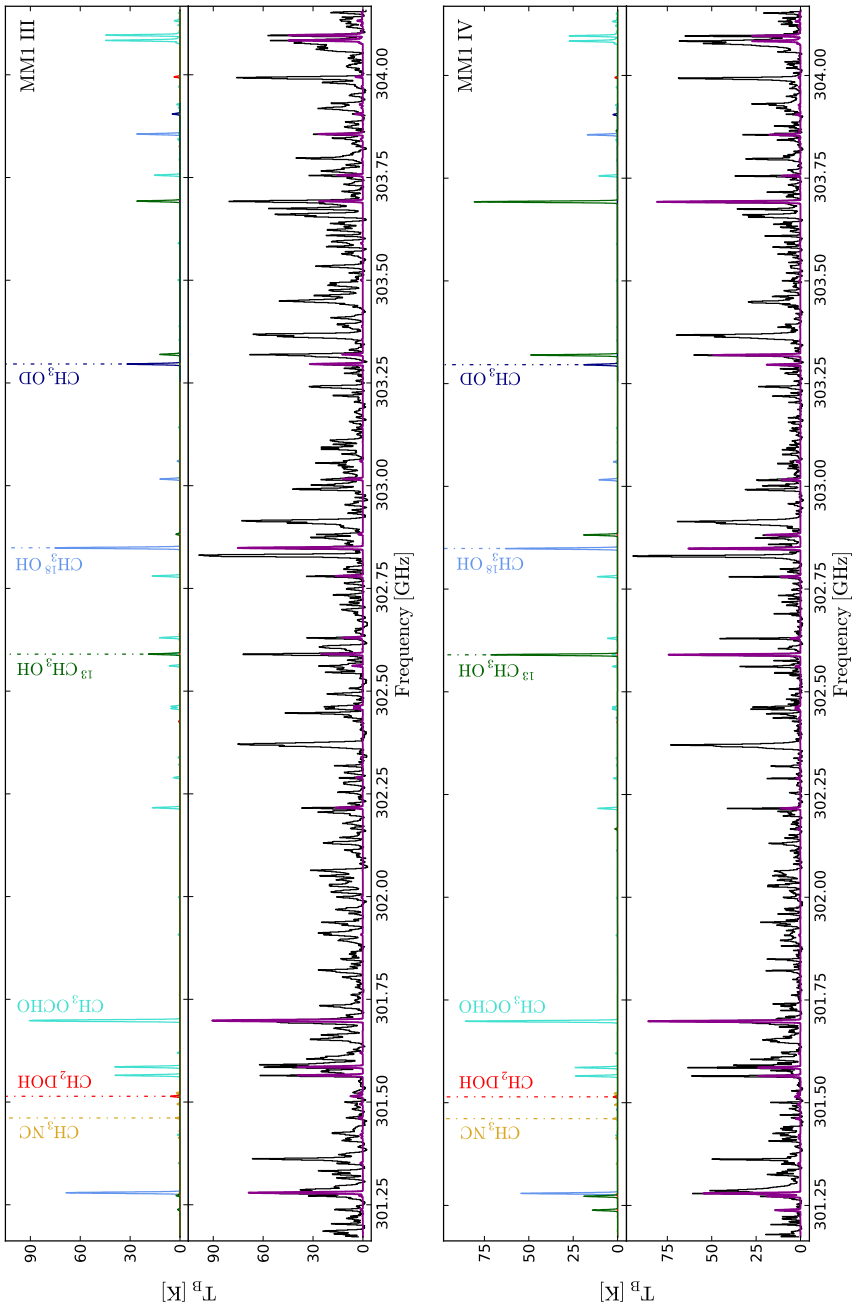

Figure B.1: Continued

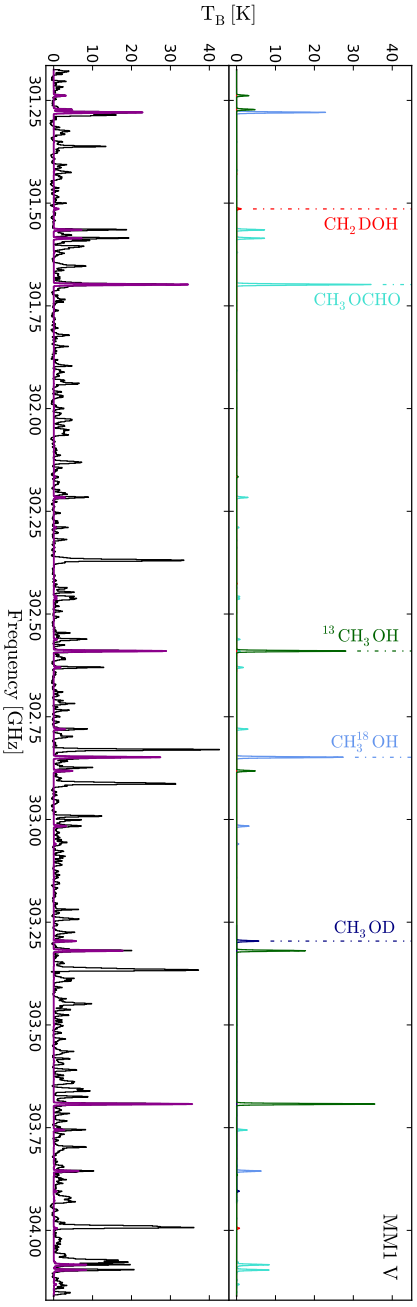

Figure B.1: Continued

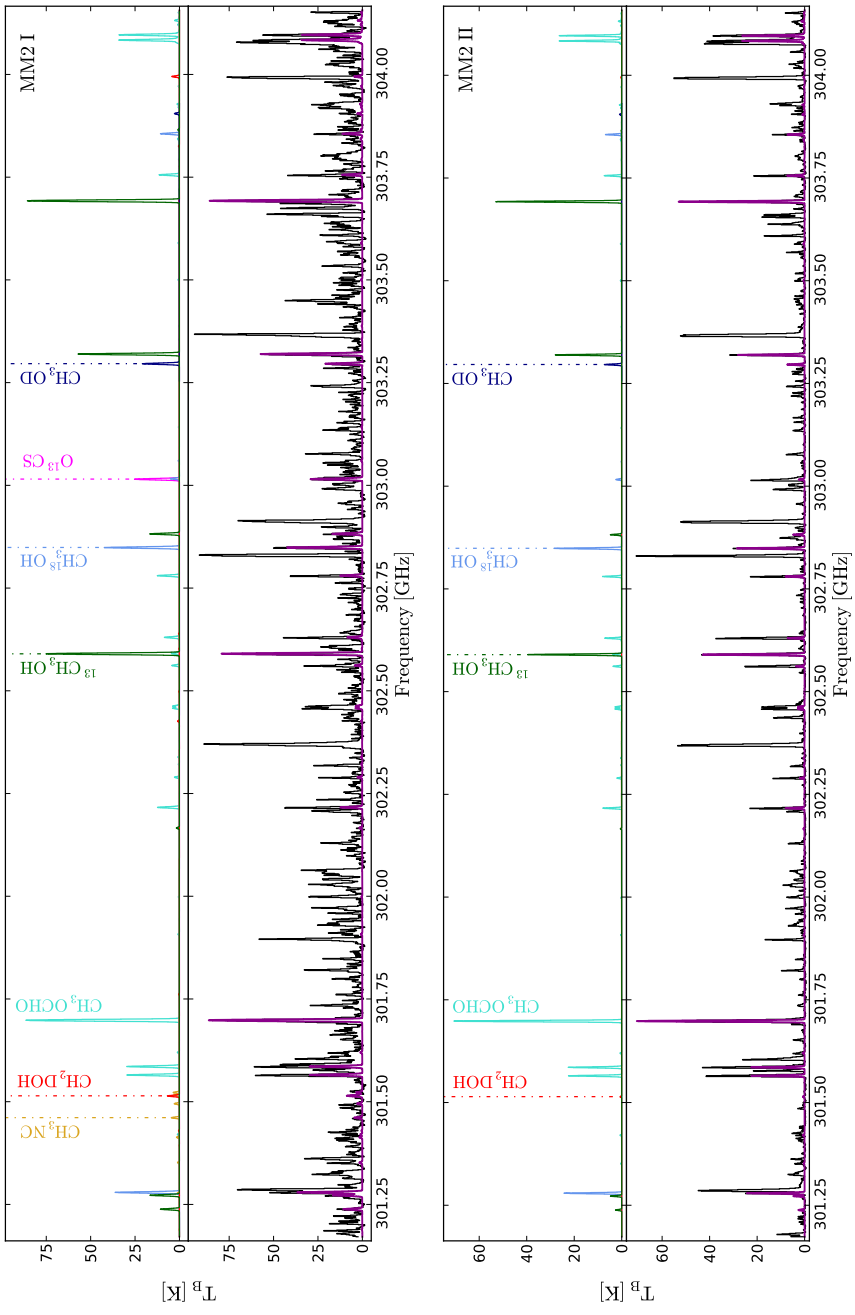

Figure B.2: MM2 I-II. *Top panels*: model components. *Bottom panels*: data (black) and full model (magenta), i.e., the linear combination of the synthetic spectrum for each species. Frequencies are shifted to the rest frame of the individual regions.

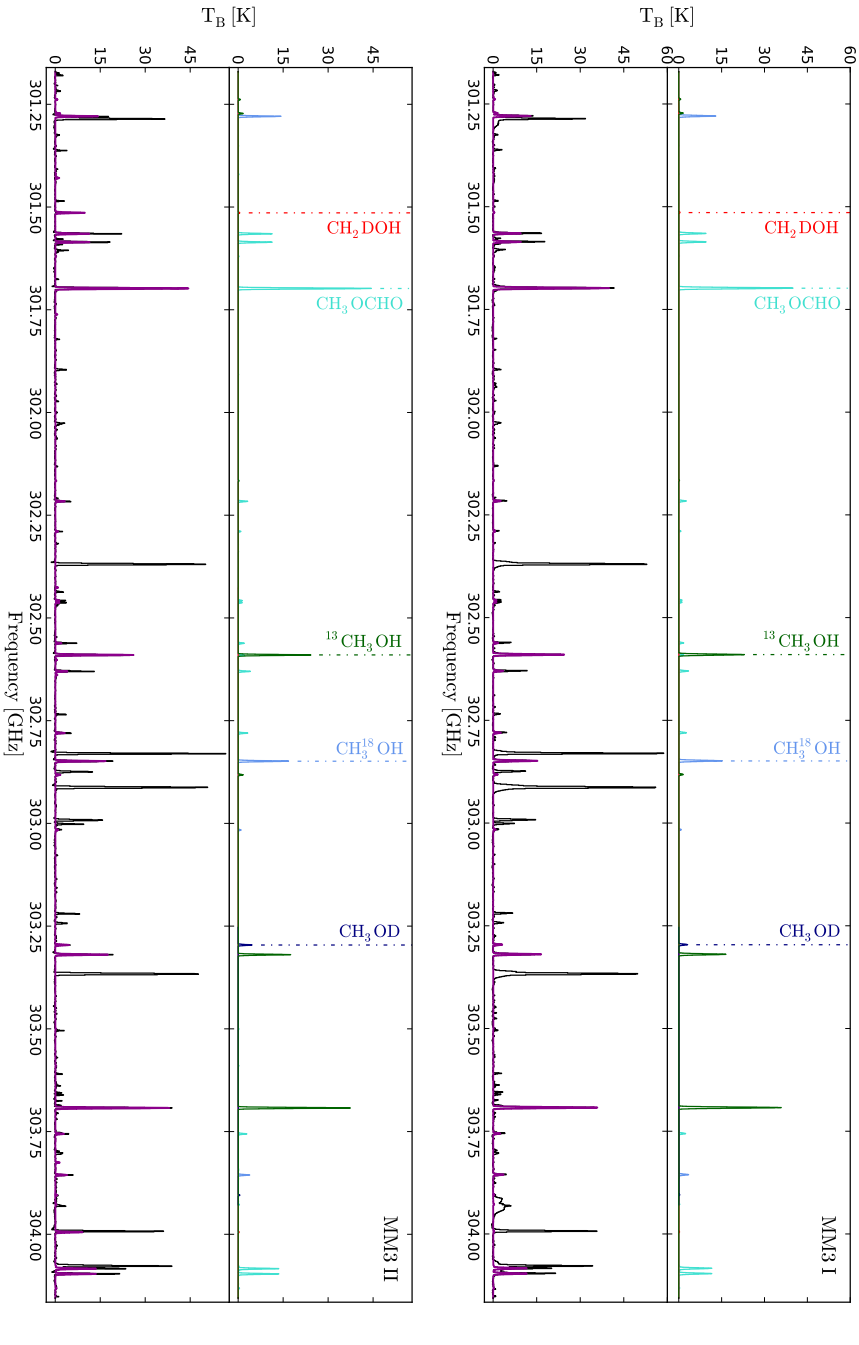

Figure B.3: MM3 I-II. *Top panels*: model components. *Bottom panels*: data (black) and full model (magenta), i.e., the linear combination of the synthetic spectrum for each species. Frequencies are shifted to the rest frame of the individual regions.

Appendix C: $^{13}CH_3OH$ transitions

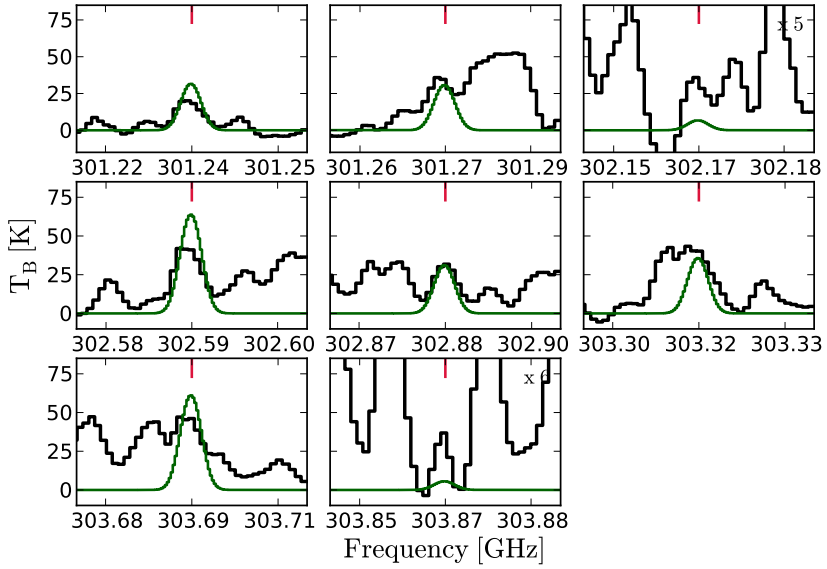

(a) MM1 I

Figure C.1: All $^{13}CH_3OH$ lines detected towards NGC 6334I MM1 I-V. Frequencies are shifted to the rest frame of the individual regions. Green lines represent the modelled spectra of $^{13}CH_3OH$ without blending, i.e., excluding the contribution from CH_3OCHO (including the contribution from CH_3OCHO does not change the $^{13}CH_3OH$ column density of the best-fit model). To enhance the readability of some panels, both data and model have been scaled up by the factor in the top right corner of the respective panel.

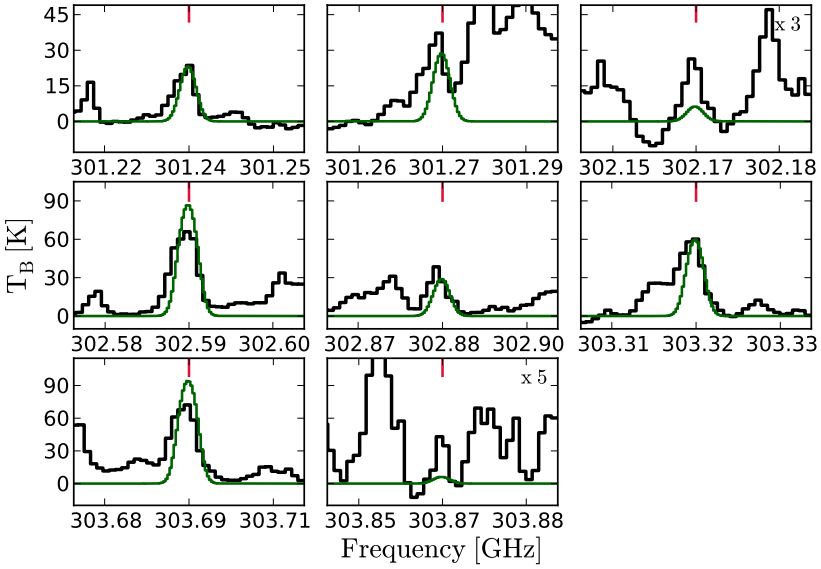

(b) MM1 II

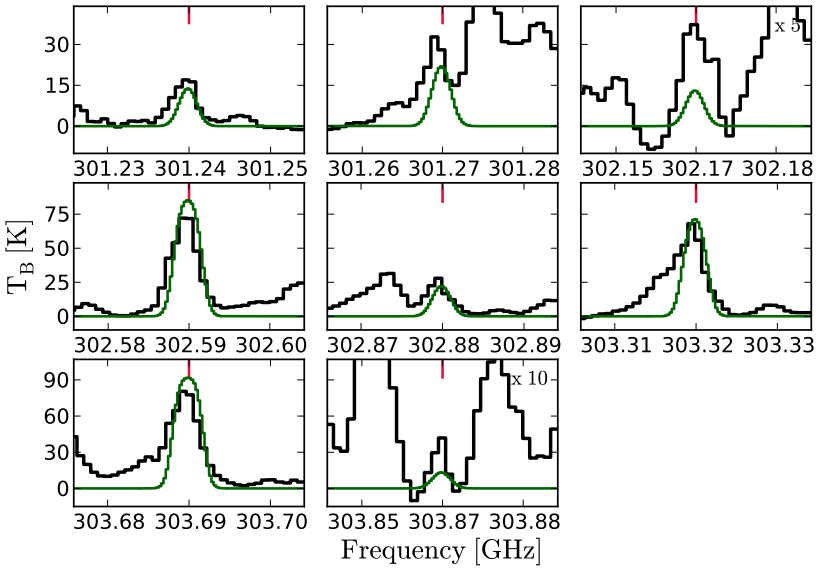

(c) MM1 III

Figure C.1: Continued

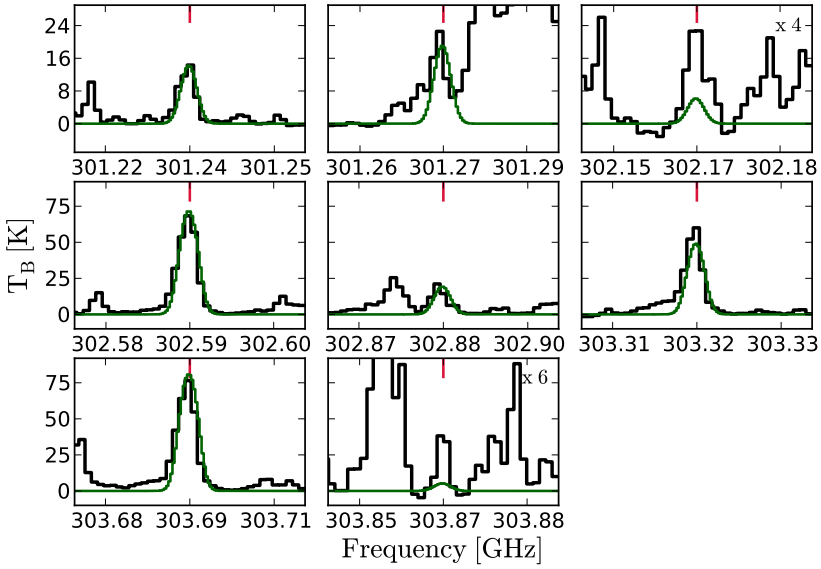

(d) MM1 IV

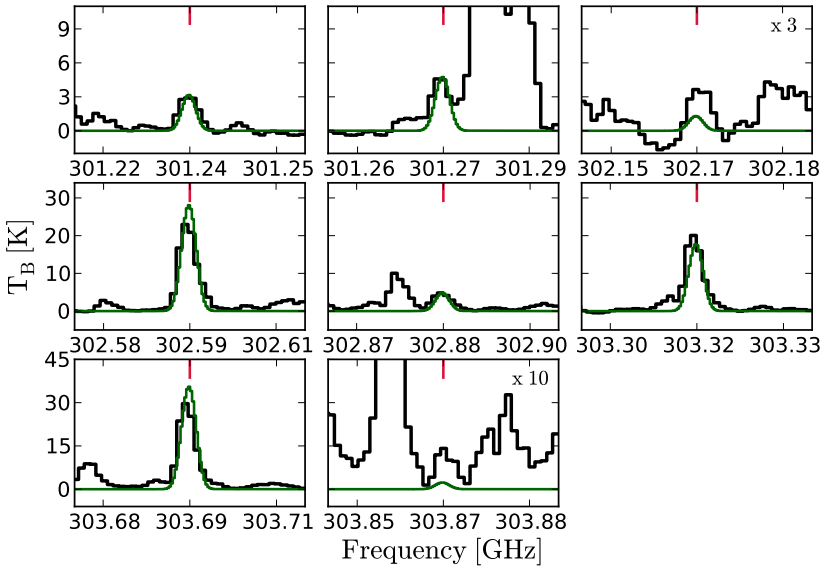

(e) MM1 V

Figure C.1: Continued

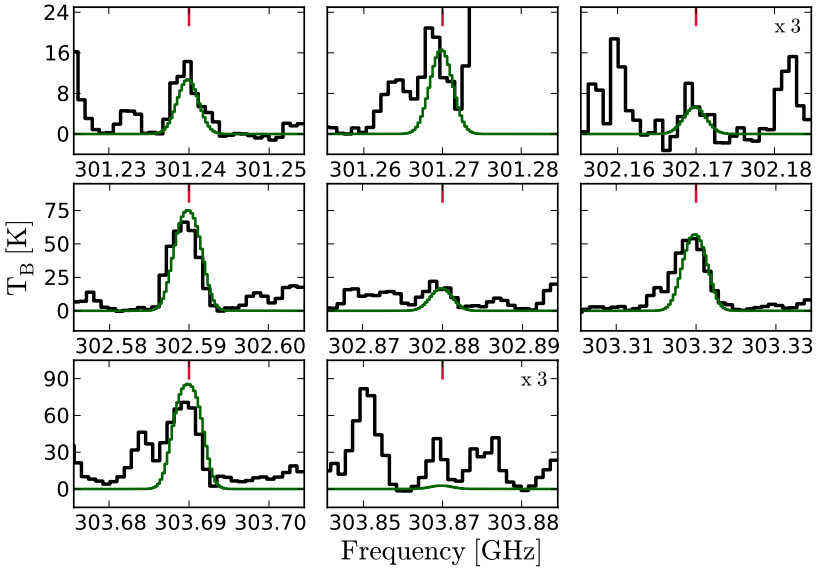

(a) MM2 I

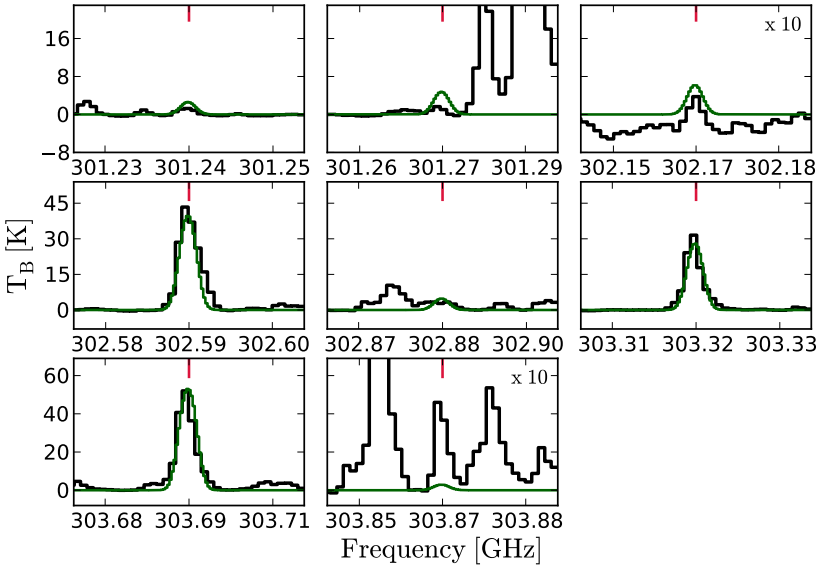

(b) MM2 II

Figure C.2: All $^{13}CH_3OH$ lines detected towards NGC 6334I MM2 I-II. Frequencies are shifted to the rest frame of the individual regions. Green lines represent the modelled spectra of $^{13}CH_3OH$ without blending, i.e., excluding the contribution from CH_3OCHO (including the contribution from CH_3OCHO does not change the $^{13}CH_3OH$ column density of the best-fit model). To enhance the readability of some panels, both data and model have been scaled up by the factor in the top right corner of the respective panel.

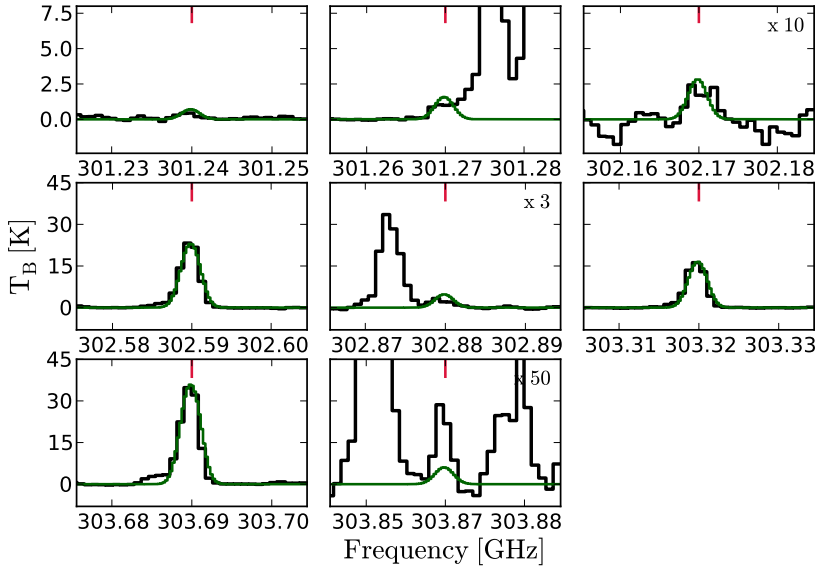

(a) MM3 I

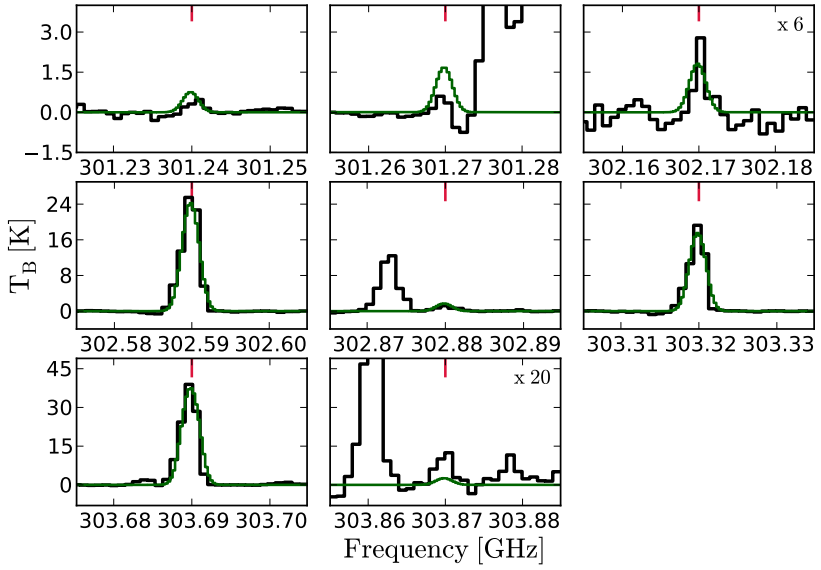

(b) MM3 II

Figure C.3: All $^{13}CH_3OH$ lines detected towards NGC 6334I MM3 I-II. Frequencies are shifted to the rest frame of the individual regions. Green lines represent the modelled spectra of $^{13}CH_3OH$ without blending, i.e., excluding the contribution from CH_3OCHO (including the contribution from CH_3OCHO does not change the $^{13}CH_3OH$ column density of the best-fit model). To enhance the readability of some panels, both data and model have been scaled up by the factor in the top right corner of the respective panel.

Appendix D: $CH_3^{18}OH$ transitions

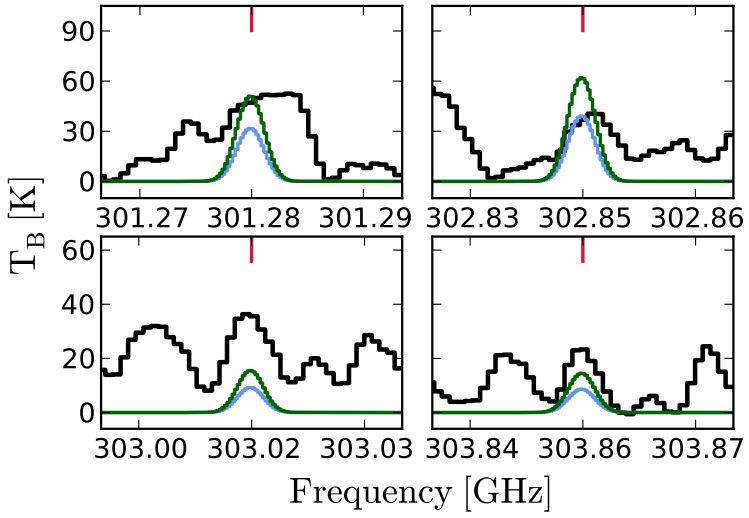

(a) MM1 I

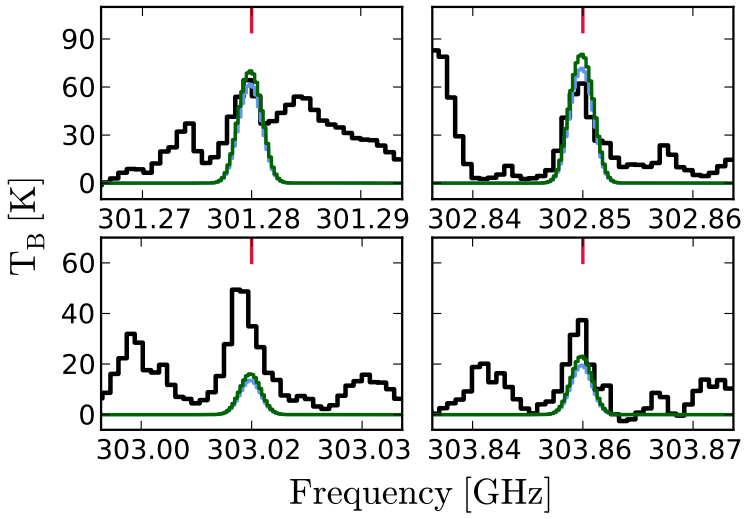

(b) MM1 II

Figure D.1: All $CH_3^{18}OH$ lines detected towards NGC 6334I MM1 I-V. Frequencies are shifted to the rest frame of the individual regions. Blue and green lines represent the modelled spectra of $CH_3^{18}OH$ in each region with and without blending, i.e., including and excluding the contribution from $O^{13}CS$, respectively. For regions MM1 III-V only the pure-$CH_3^{18}OH$ fits are shown.

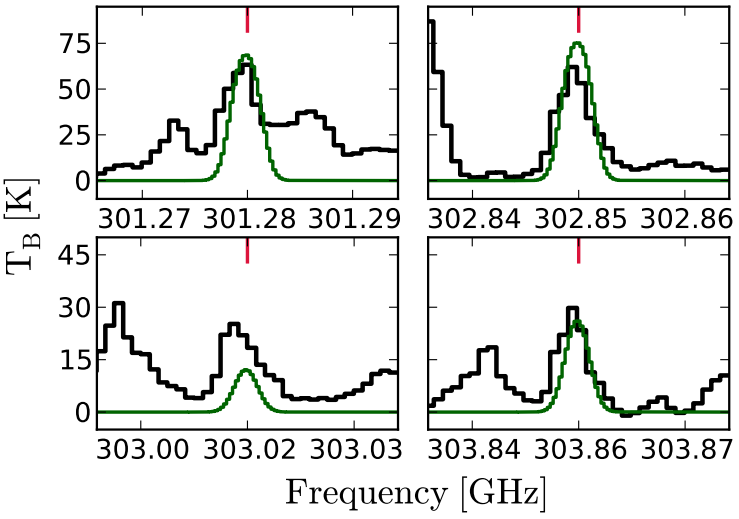

(c) MM1 III

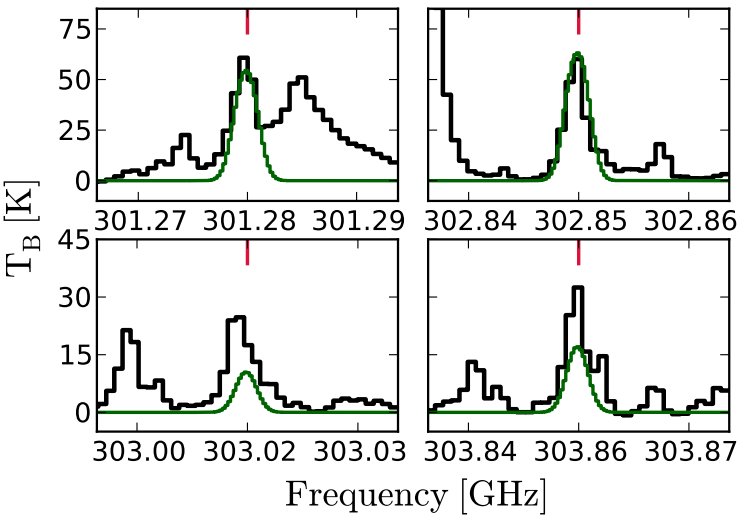

(d) MM1 IV

Figure D.1: Continued

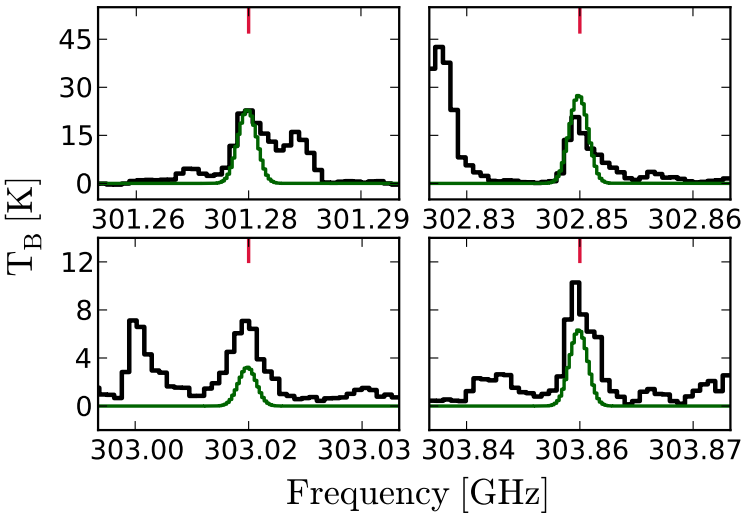

(e) MM1 V

Figure D.1: Continued

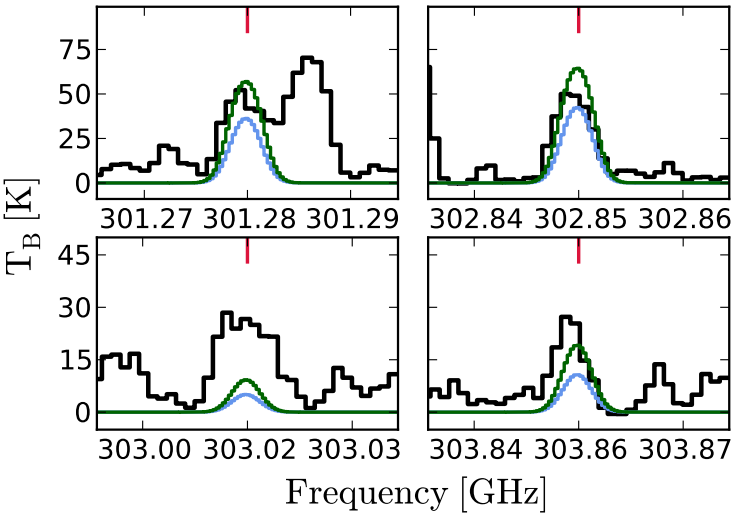

(a) MM2 I

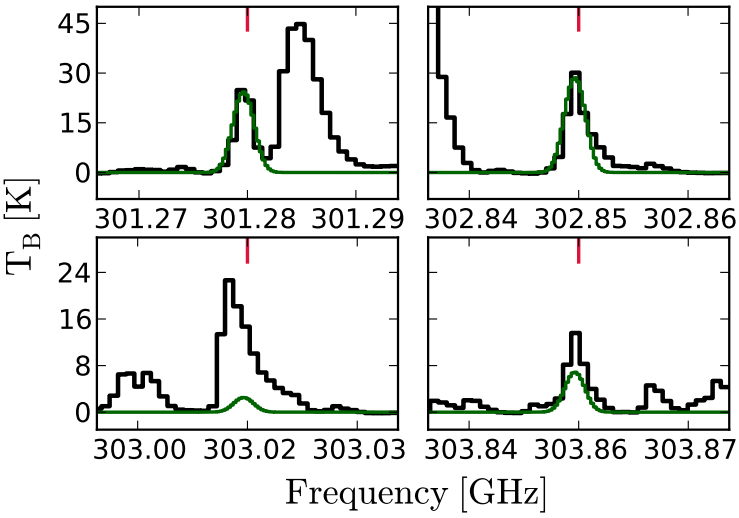

(b) MM2 II

Figure D.2: All $CH_3^{18}OH$ lines detected towards NGC 6334I MM2 I-II. Frequencies are shifted to the rest frame of the individual regions. Blue and green lines represent the modelled spectra of $CH_3^{18}OH$ in each region with and without blending, i.e., including and excluding the contribution from $O^{13}CS$, respectively. For region MM2 II only the pure-$CH_3^{18}OH$ fit is shown.

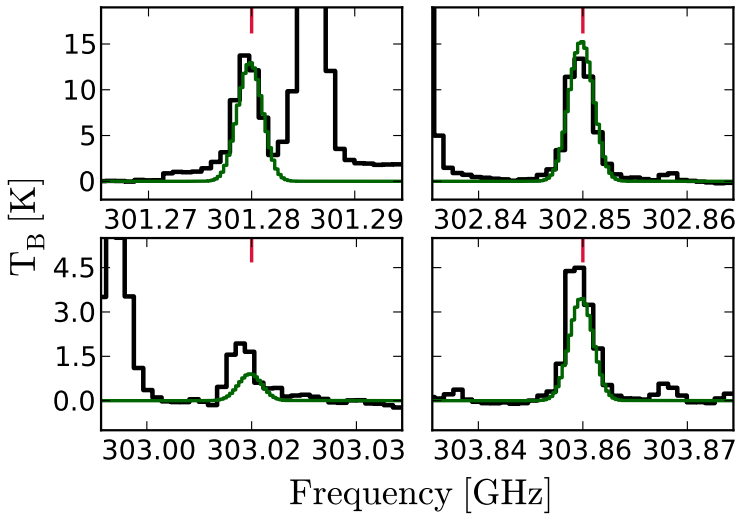

(a) MM3 I

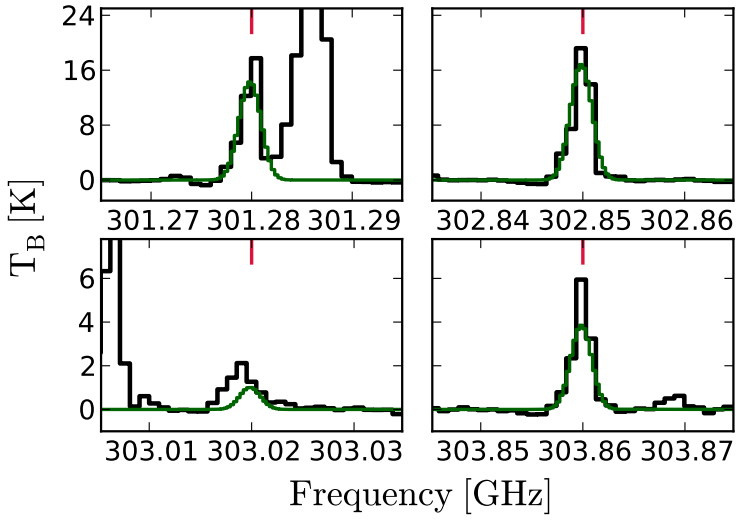

(b) MM3 II

Figure D.3: All $CH_3^{18}OH$ lines detected towards NGC 6334I MM3 I-II. Frequencies are shifted to the rest frame of the individual regions. Green lines represent the modelled spectra of $CH_3^{18}OH$ in each region without blending, i.e., excluding the contribution from $O^{13}CS$.

Appendix E: CH_3OD transitions

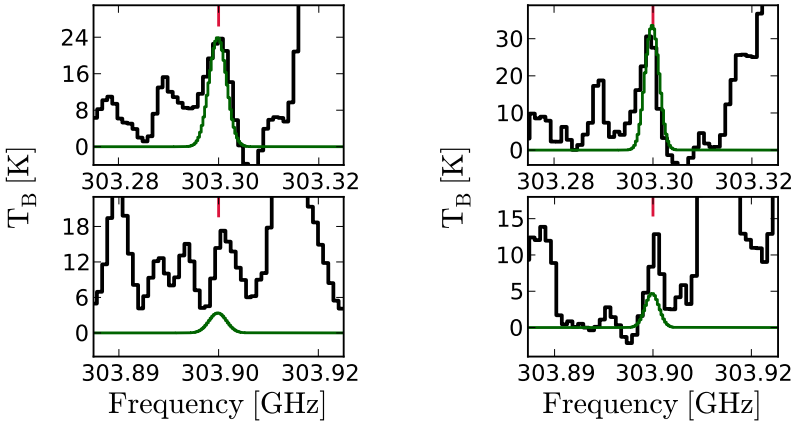

(a) MM1 I

(b) MM1 II

(c) MM1 III

(d) MM1 IV

Figure E.1: All CH_3OD lines detected towards NGC 6334I MM1 I-V. Frequencies are shifted to the rest frame of the individual regions. Green lines represent the modelled spectra of CH_3OD in each region.

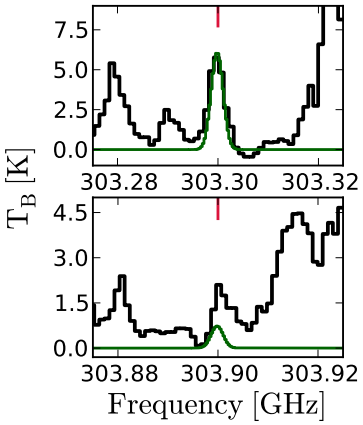

(e) MM1 V

Figure E.1: Continued

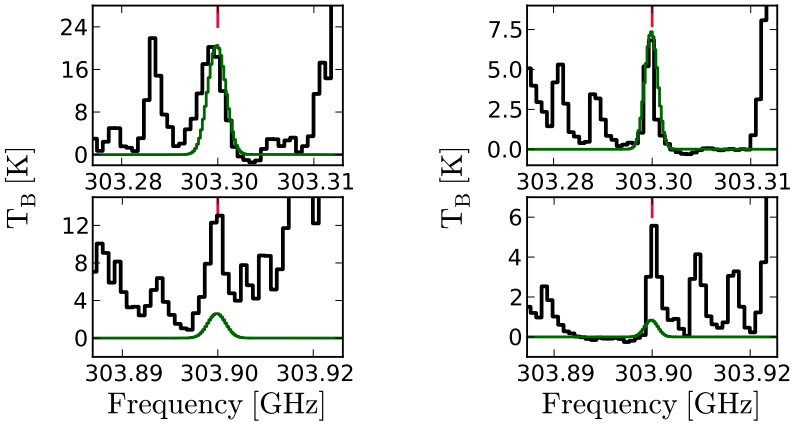

(a) MM2 I **(b)** MM2 II

Figure E.2: All CH_3OD lines detected towards NGC 6334I MM2 I-II. Frequencies are shifted to the rest frame of the individual regions. Green lines represent the modelled spectra of CH_3OD in each region.

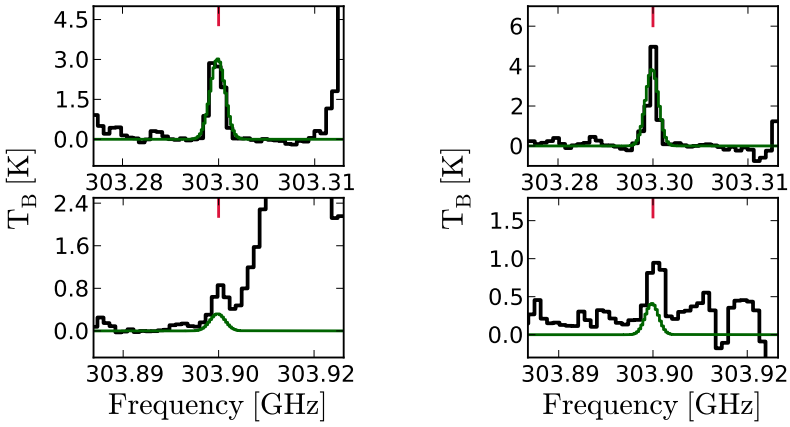

(a) MM3 I **(b)** MM3 II

Figure E.3: All CH_3OD lines detected towards NGC 6334I MM3 I-II. Frequencies are shifted to the rest frame of the individual regions. Green lines represent the modelled spectra of CH_3OD in each region.

3

Methylamine and other simple N-bearing species in the hot cores NGC 6334I MM1 – 3

E. G. Bøgelund, B A. McGuire, M. R. Hogerheijde, E. F. van Dishoeck and N. F. W. Ligterink

Submitted to Astronomy & Astrophysics

Abstract

Context. In the search for the building blocks of life, nitrogen-bearing molecules are of particular interest since nitrogen-containing bonds are essential for the linking of amino acids and ultimately the formation of larger biological structures. The elusive molecule methylamine (CH_3NH_2) is through to be a key prebiotic species but has so far only been securely detected in the giant molecular cloud Sagittarius B2.
Aim. We identify CH_3NH_2 and other simple nitrogen-bearing species involved in the synthesis of biologically relevant molecules towards three hot cores associated with the high-mass star-forming region NGC 6334I, located at a distance of 1.3 kpc. Column density ratios are derived in order to investigate the relevance of the individual species as precursors of biotic molecules.
Methods. High sensitivity, high angular and spectral resolution observations obtained with the Atacama Large Millimeter/submillimeter Array were used to study transitions of CH_3NH_2, CH_2NH, NH_2CHO and the ^{13}C- and ^{15}N-methyl cyanide (CH_3CN) isotopologues, detected towards NGC 6334I. Column densities are derived for each species assuming local thermodynamic equilibrium and excitation temperatures in the range 220 – 340 K for CH_3NH_2, 70 – 110 K for the CH_3CN isotopologues and 120 – 215 K for NH_2CHO and CH_2NH.
Results. We report the first detections of CH_3NH_2 towards NGC 6334I with column density ratios with respect to CH_3OH of 5.9×10^{-3}, 1.5×10^{-3} and 5.4×10^{-4} for the three hot cores MM1, MM2 and MM3, respectively. These values are slightly lower than the values derived for Sagittarius B2 but higher by more than order of magnitude as compared with the values derived for the low-mass protostar IRAS 16293–2422B. The column density ratios of NH_2CHO, $^{13}CH_3CN$ and $CH_3C^{15}N$ with respect to CH_3OH are $(1.5 - 1.9)\times10^{-4}$, $(1.0 - 4.6)\times10^{-3}$ and $(1.7 - 3.0)\times10^{-3}$ respectively. Lower limits of 5.2, 1.2 and 3.0 are reported for the CH_3NH_2 to CH_2NH column density ratio for MM1, MM2 and MM3 respectively. These limits are largely consistent with the values derived for Sagittarius B2 and higher than those for IRAS 16293–2422B.
Conclusions. The detections of CH_3NH_2 in the hot cores of NGC 6334I hint that CH_3NH_2 is generally common in the interstellar medium, albeit that high-sensitivity observations are essential for the detection of the species. The good agreement between model predictions of CH_3NH_2 ratios and the observations towards NGC 6334I indicate a main formation pathway via radical recombination on grain surfaces. This process may be stimulated further by high grain temperatures allowing a lager degree of radical mobility. Further observations with ALMA will help evaluate the degree to which CH_3NH_2 chemistry depends on the temperature of the grains in high- and low-mass regions respectively.

3.1 Introduction

A number of molecular species that are recognized as precursors to biologically relevant molecules have in recent years been identified in the interstellar medium (ISM). These so-called prebiotic species (see Herbst & van Dishoeck, 2009, and references therein) are involved in the formation of, for example, amino acids, the main constituents of proteins, and nucleobases, the fundamental components of DNA and RNA, and thereby constitute the basis for the building blocks of life.

Among the prebiotic molecules are the species methylamine (CH_3NH_2) and methanimine (CH_2NH), the simplest primary amine- (-NH_2) and imine- (-C=N-) containing species, respectively. Experiments in which interstellar ice analogues are subjected to thermal processing or irradiation by UV photons have shown that both CH_3NH_2 and CH_2NH are involved in reactions that form amino acids, and have specifically been proven to engage in the synthesis of glycine (NH_2CH_2COOH), the smallest member of the amino acid family (Holtom et al., 2005; Lee et al., 2009; Bossa et al., 2009; Danger et al., 2011). The formation of glycine within or upon the icy mantles of interstellar dust-grains is consistent with theoretical models by Garrod (2013) who trace and couple the gas-phase, grain-surface and bulk ice chemistry during the formation of hot cores. In addition, the connection between CH_3NH_2 and glycine has been established though the proposed formation of both these species from a common set of precursors present in carbonaceous chondrite meteorites (Aponte et al., 2017) including carbon monoxide (CO), ammonia (NH_3), hydrogen cyanide (HCN), and carbon dioxide (CO_2).

Another example of a simple progenitor of biotic molecules is formamide (NH_2CHO), the simplest amide (-NH-(C=O)-), which has the same chemical structure as the peptide bonds that link amino acids and thereby form the backbone of larger protein structures. NH_2CHO has also been shown to be involved in the formation of nucleobases and nucleobase analogues in processes which use minerals and metal oxides, including samples of primitive meteoroids, as catalysts (Saladino et al., 2006; Kumar et al., 2014; Saladino et al., 2016).

Lastly, due to its cyanide (-CN) group, the molecule methyl cyanide (acetonitrile, CH_3CN) is also of interest in relation to the synthesis of prebiotic molecules. This is due to the importance of C-N bonds for the formation of peptide structures. Reactions involving cyanides, especially HCN and its derivatives, are therefore regarded as the foundation of the formation of complex structures such as proteins, lipids and nuclei acids (Matthews & Minard, 2006; Patel et al., 2015). In addition, Goldman et al. (2010) propose that shock-induced C-N bonds due to cometary impacts on the early Earth provide a potential synthesis route for amino acids which is independent of the pre-existing atmospheric conditions and materials on the planet.

In summary, continued observations and searches for CH_3NH_2, CH_2NH, NH_2CHO, CH_3CN and other prebiotic species in the ISM, as well as in Solar System bodies, are of high interest in order to establish the relevance of the respective species in connection to the emergence of life on Earth, and potentially on other (exo)planets and moons.

3.1.1 Previous detections and potential formation routes for methylamine and related species

NH_2CHO and CH_3CN are routinely detected towards high- and low-mass hot cores (Cazaux et al., 2003; Bisschop et al., 2007; Kahane et al., 2013), and have in addition been identified towards a number of comets (see review by Mumma & Charnley,

2011), in particular the bright comet Hale-Bopp (e.g. Bockelée-Morvan et al., 1997; Remijan et al., 2008) and comet 67P/Churyumov-Gerasimenko (hereafter 67P), the target of ESA's *Rosetta* mission (Goesmann et al., 2015; Altwegg et al., 2017). In addition, CH_3CN was the first complex organic molecule (COM) to also be detected in a protoplanetary disk (Öberg et al., 2015) and thereby became one of the few prebiotic species whose presence could be traced throughout all formation phases from the earliest stages of star-formation to the last remnants in comets.

Despite the lack of firm detections of CH_2NH in comets (Irvine et al., 1998; Crovisier et al., 2004), this species has also been detected towards a variety of interstellar sources including giant molecular clouds (Dickens et al., 1997) and high- and low-mass protostellar systems (Suzuki et al., 2016; Ligterink et al., 2018a). In contrast to these detections, the structurally similar species CH_3NH_2 has proven to be an especially elusive molecule and for a long time was only securely detected towards the high-mass source Sagittarius B2 (hereafter Sgr B2) located in the Galactic Center (e.g. Kaifu et al., 1974; Belloche et al., 2013). Recently, the molecule was also detected towards the hot core G10.47+0.03 by Ohishi et al. (2017) who also report a tentative detection towards NGC 6334I though the low signal-to-noise and variations in $v_{\rm LSR}$ between transitions of the species makes the detection unclear. A tentative detection was also reported towards Orion KL by Pagani et al. (2017). In addition, a series of non-detections have been reported towards a number of high-mass young stellar objects (YSOs, Ligterink et al., 2015) and a very stringent upper limit has been set on the abundance of the species in the low-mass Sun-like protostar IRAS 16293–2422B (Ligterink et al., 2018a). Recently, the species has also been detected in the coma of comet 67P (Altwegg et al., 2017). These detections (and upper limits) indicate a range of CH_3NH_2 abundances with respect to CH_3OH, with that of IRAS 16293–2422B being at least one to two orders of magnitude lower than the values derived for Sgr B2. The discrepancies between the detections in Sgr B2 and the non-detections elsewhere has led to the suggestion that formation pathways for CH_3NH_2 are not very efficient and that they may depend strongly on the conditions which characterise the individual regions. Based on the detections of CH_3NH_2 in Sgr B2 it has therefore been speculated that the presence of relatively high dust grain temperatures or strong radiation fields enhance CH_3NH_2 formation.

The formation of CH_3NH_2 is discussed in a number of studies. On interstellar dust grains, two main formation pathways have been proposed: The first is a hydrogenation sequence starting from hydrogen cyanide: HCN + 2H → CH_2NH + 2H → CH_3NH_2 (Theule et al., 2011). Although the efficiency of formation via this pathway is ill constrained, the same hydrogenation mechanism has been used in glycine formation models to form the intermediate CH_2NH_2 radical (Woon, 2002). The second formation route involves radical recombination reactions between a methyl (-CH_3) and an amino group: CH_3 + NH_2 → CH_3NH_2. This pathway has been included in the astrochemical models presented by Garrod et al. (2008) as the main formation route for CH_3NH_2. Experimentally, electron and photon irradiated interstellar ice analogues, consisting of CH_4 and NH_3, have been shown to result in formation of CH_3NH_2 (Kim & Kaiser, 2011; Förstel et al., 2017). Though in dark clouds, both CH_3 and NH_2 can also result from H-addition to atomic C and N and therefore photodissociation is not critical for the formation of the radicals. In the gas-phase, the radical-neutral reaction CH_3 + NH_3 → CH_3NH_2 + H has been proposed to be the main CH_3NH_2 formation route. This is based on the observational study of Sgr B2 conducted by Halfen et al. (2013) who also argue that the formation of CH_3NH_2 through successive hydrogenation of CH_2NH is unlikely due to the large difference in rotational temperature, 44 ± 13 K in the case of CH_2NH and 159 ± 30 K in the case of CH_3NH_2, derived through rotational temperature diagrams.

This difference makes it unlikely that the molecules occupy the same regions thereby making CH_2NH an unlikely synthetic precursor of CH_3NH_2. A dominant gas-phase formation route for CH_2NH is also reported by Suzuki et al. (2016) though they note that hydrogenation of solid-phase CH_2NH can also form CH_3NH_2. Additional detections of CH_3NH_2 and related species, preferably towards a large number of different sources, will therefore provide valuable information and help distinguish between formation routes and conditions required for the formation of this species.

3.1.2 NGC 6334

In this work, CH_3NH_2 along with other simple prebiotic nitrogen-bearing species, in particular CH_2NH, CH_3CN and NH_2CHO, are studied towards three dense cores within the giant molecular cloud complex NGC 6334. The NGC 6334 region, located in the constellation Scorpius in the southern hemisphere, is a very active high-mass star-forming region composed of six subregions denoted I–V and I(N) (see review by Persi & Tapia, 2008, and references therein). Water and methanol (CH_3OH) maser studies have placed the region at a mean distance of 1.3 kpc from the Sun (Chibueze et al., 2014; Reid et al., 2014), equivalent to a galactocentric distance (d_{GC}) of ∼7.02 kpc. The focus of this work is on the deeply embedded source NGC 6334I which is located in the north-eastern part of the cloud. The morphology of this source has been studied in detail by Brogan et al. (2016) who identify a number of distinct peaks in the submillimetre continuum and assign these to individual high-mass star-forming systems. The region has a very rich molecular inventory as demonstrated by Zernickel et al. (2012) who identify a total of 46 molecular species towards NGC6334I including CH_2NH, CH_3CN and NH_2CHO but not CH_3NH_2.

This paper presents the first detection of CH_3NH_2 towards NGC 6334I. The work is based on high sensitivity, high spectral and angular resolution data obtained with the Atacama Large Millimeter/submillimeter Array (ALMA). Previous searches for CH_3NH_2 have, for the most part, been carried out with single dish telescopes, which are generally less sensitive when compared with interferometric observations, and have therefore focused mainly on the bright hot cores associated with the Galactic central region. With the unique sensitivity and resolving power of ALMA this is changing and the weak lines associated with CH_3NH_2 can now be probed in regions away from the Galactic Center, such as NGC 6334I, as well as in low-mass systems (Ligterink et al., 2018a).

The paper is structured in the following way: in Sect. 3.2 the observations and analysis methodology are introduced. Section 3.3 presents the observed transitions of each of the studied species and the model parameters used to reproduce the data. In Sect. 3.4 the derived column density ratios are discussed and compared between the regions in NGC 6334I as well as to the values derived for other high- and low-mass objects. Finally, our findings are summarised in Sect. 3.5.

3.2 Observations and method

3.2.1 Observations

Observations of NGC 6334I were carried out with ALMA in Cycle 3 on January 17, 2016 using the ALMA Band 7 receivers (covering the frequency range 275–373 GHz). Three spectral windows centred around 301.2, 302.0 and 303.7 GHz covering a total bandwidth of ∼3 GHz were obtained. The observations have spectral and angular resolutions of 1 km s^{-1} and ∼1″ (equivalent to ∼1300 au at the distance of NGC 6334I) respectively.

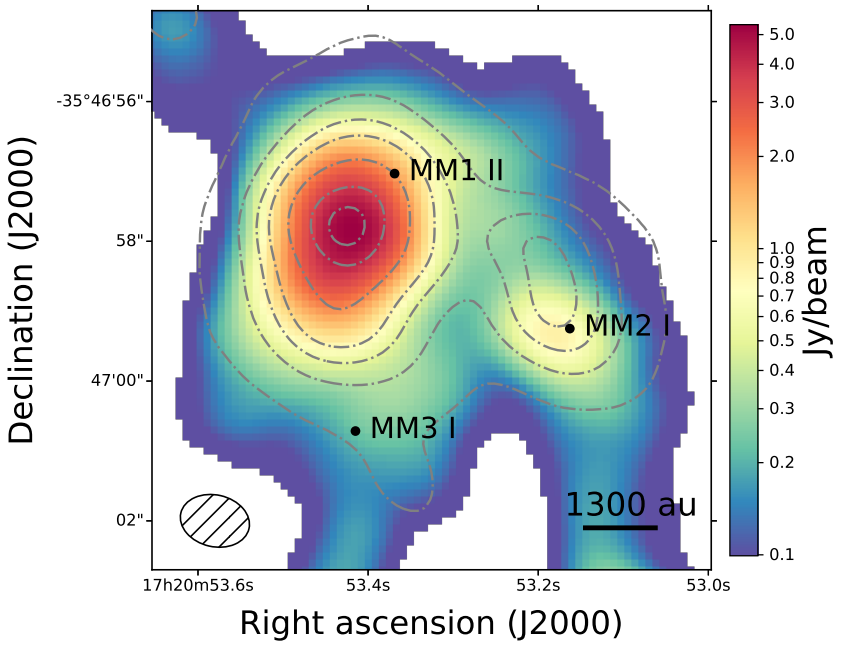

Figure 3.1: 1 mm continuum image of the NGC 6334I region with the velocity integrated intensity map of the $^{13}CH_3CN$ transition at 303.610 GHz overlaid in grey contours (levels are [3, 20, 40, 60, 100, 150, 180]σ with σ=0.07 Jy beam^{-1} km s^{-1}). Pixels with values less than 1% of the peak intensity have been masked out. The locations at which spectra have been extracted are marked for each region. The synthesised beam (∼1300×962 au) is shown in the bottom left corner.

The data were interactively self-calibrated and continuum subtracted using the most line-free channels. A detailed description of this reduction procedure may be found in Brogan et al. (2016) and Hunter et al. (2017) while a summary of all observing parameters are listed in Table 1 of McGuire et al. (2017). After calibration the data were corrected for primary beam attenuation.

3.2.2 Method

For the analysis of CH_3NH_2 and related species three spectra, extracted at different locations across the NGC6334I region, are used. For consistency we use the same locations and naming as in Bøgelund et al. (2018) and focus on the regions MM1 II, MM2 I and MM3 I. These regions are associated with each of the continuum sources MM1, MM2 and MM3 making it possible to compare the abundances of the various species across the three hot cores. Due to the greater lines widths characterising the central part of the MM1 region and the bright continuum emission, which in some cases result in negative features after continuum subtraction has been applied, we select a region away from the main continuum peak where weak emission line features are more easily identified. The extracted spectra are the average of a 1.″00×0.″74 region, equivalent to the area of the synthesised beam. The coordinates of the central pixel of each of the regions are (J2000 $17^h20^m53.371^s$, $-35°46'57.''013$), (J2000 $17^h20^m53.165^s$, $-35°46'59.''231$) and

(J2000 $17^{h}20^{m}53.417^{s}$, $-35°47'00''.697$) for MM1 II, MM2 I and MM3 I, respectively. For each of the extracted spectra, the rms noise is calculated after careful identification of line-free channels. These are ∼0.9 K (68 mJy beam^{-1}) for MM1, ∼0.6 K (45 mJy beam^{-1}) for MM2 and ∼0.04 K (3 mJy beam^{-1}) for MM3. The difference in the estimated rms noise values reflects the large variations in brightness and line density over the three regions. An overview of the NGC 6334 I region and the locations at which spectra have been extracted is shown in Fig. 3.1.

In order to identify transitions of CH_3NH_2, CH_2NH, CH_3CN and NH_2CHO, as well as to constrain the column density and excitation temperature of the species at each of the studied positions, synthetic spectra are produced using the CASSIS[1] line analysis software. The spectroscopic data for CH_2NH and the methyl cyanide and formamide isotopologues are adopted from the JPL[2] and CDMS[3] molecular databases. For CH_3NH_2, the spectroscopic data are taken from Motiyenko et al. (2014). Assuming local thermodynamic equilibrium (LTE) and optically thin lines, synthetic spectra are constructed for each species. This is done by providing CASSIS with a list of parameters including excitation temperature, $T_{\rm ex}$ [K], column density of the species, $N_{\rm s}$ [cm^{-2}], source velocity, $v_{\rm LSR}$ [km s^{-1}], line width at FWHM [km s^{-1}], and angular size of the emitting region, $\theta_{\rm s}$ [$''$], assumed to be equal to the size of the synthesised beam.

Excitation temperatures and column densities are determined for the detected species by creating grids of model spectra varying $T_{\rm ex}$ and $N_{\rm s}$ and identifying the model spectrum with the minimal χ^2 as the best fit. The CASSIS software computes the χ^2 value for each of the model spectra taking into account the rms noise of the observed spectrum and the calibration uncertainty (assumed to be 10%). χ^2 is defied as:

$$\chi^2 = \sum_{i=1}^{N} \left(\frac{(I_{{\rm obs},i} - I_{{\rm model},i})}{\sigma_i} \right)^2 ,$$

where $I_{{\rm obs},i}$ and $I_{{\rm model},i}$ is the intensity of the observed and modelled spectrum in channel i, respectively, $\sigma_i = \sqrt{rms^2 + (0.1 \times I_{{\rm obs},i})^2}$ and N is the number of fitted points, that is, the number of channels covered by each of the transitions to which the model is optimised (we consider the channels within a range of $\pm\ 2\ \times\ FWHM$).

Table A.1 lists the model grids for each of the fitted species. Since only a single CH_2NH transition and just two NH_2CHO transitions are detected, the excitation temperatures of these species cannot be constrained from the data. The reported CH_2NH and NH_2CHO column densities are therefore derived assuming $T_{\rm ex}$ to be fixed at the value derived for CH_3OH in each region by Bøgelund et al. (2018). These are 215 K for region MM1 II, 165 K for region MM2 I and 120 K for region MM3 I. The uncertainty on $N_{\rm s}$ and $T_{\rm ex}$ is listed as the standard deviation of model spectra with χ^2 within 1σ of the best-fit model. For $N_{\rm s}$, the highest uncertainty is approximately 30% while the uncertainty on $T_{\rm ex}$ is up to 65%. Through the propagation of errors, the uncertainty on listed column density ratios is conservatively estimated to be ∼40% ($\sqrt{2} \times 30\%$). Because the velocity structure of NGC 6334I is not well-known, the source velocity and FWHM line widths characterising each region are fixed throughout the fitting procedure so as not to introduce additional free parameters. As is clear from Fig. 3.2 and Figs. D.1–D.3, the fixed $v_{\rm LSR}$ and line widths are consistent with the data for all species. However,

[1] Centre d'Analyse Scientifique de Spectres Instrumentaux et Synthétiques; http://cassis.irap.omp.eu

[2] Jet Propulsion Laboratory (Pickett et al., 1998); http://spec.jpl.nasa.gov

[3] Cologne Database for Molecular Spectroscopy (Müller et al., 2001, 2005); http://www.ph1.uni-koeln.de/cdms/

examples of molecules detected towards the same region but characterised by different physical parameters have been reported (see e.g. Halfen et al., 2013).

For each identified CH_3NH_2, CH_2NH, CH_3CN or NH_2CHO transition, a thorough search for potential blending species is conducted. This search is carried out carefully in the following steps: 1) All catalogued species, that is to say all species which are listed in the JPL or CDMS databases and which have transitions at frequencies that overlap with those of CH_3NH_2, CH_2NH, CH_3CN or NH_2CHO, are identified. 2) For each potential blending species a synthetic spectrum is produced and optimised so that the column density of that species is maximised. This is done while ensuring that none of the other transitions belonging to the same species, and which are covered by the data, are overproduced with respect to the data. 3) If the potential blending species are isotopologues, step 2 is repeated for the parent species in order to ensure that column densities are consistent between isotopologues of the same species. 4) Once the spectra of the individual potential blending species have been optimised, they are summed to obtain a full spectrum for each of the three regions. Two fits are then preformed; the first fit takes only the studied species into account and is used to set an upper limit on the column density for each of these; the second fit includes the contributions from all potential blending species.

By including the maximised contribution from the potential blending species to the modelled spectrum, the contributions from CH_3NH_2, CH_2NH, CH_3CN and NH_2CHO to the same modelled spectrum are minimized and consequently the most stringent limits on the column densities of these species are achieved. It should be noted however, that maximising the column densities of some potential blending species, in particular deuterated isotopologues, leads to values which are unrealistically high when compared with parent species and therefore should be seen purely as a method to conservatively constrain the amounts of CH_3NH_2, CH_2NH, CH_3CN and NH_2CHO. The full list of potential blending species as well as model parameters are listed in Table E.1.

Finally, a $^{12}C/^{13}C$ ratio of 62, a $^{16}O/^{18}O$ ratio of 450 and a $^{14}N/^{15}N$ ratio of 422 is adopted throughout the paper, all derived assuming $d_{GC} = 7.02$ kpc and the relations for $^{12}C/^{13}C$, $^{16}O/^{18}O$ and $^{14}N/^{15}N$ reported by Milam et al. (2005) and Wilson (1999).

3.3 Results

In the following sections the detections of CH_3NH_2 will be discussed in detail alongside a summary of the main results regarding the detections of CH_2NH, CH_3CN and NH_2CHO (see Appendix D for full discussion of these species). Transition frequencies and line data for all species are listed in Table 3.1, while integrated line intensities of a select number of lines in the observational data are listed in Table B.1. In the case of CH_3NH_2, detected lines have E_{up} values ranging from 96 to 480 K. For each of the studied regions and species the column density and excitation temperature of the best-fit synthetic spectrum are derived. In Sect. 3.4 these values and their ratios with respect to CH_3OH and CH_3NH_2 will be compared between the individual regions of NGC 6334I but also discussed in relation to those derived for other objects. The parameters of the best-fit models are listed in Table 3.2 and all transitions and modelled spectra of CH_3NH_2 and other species are plotted in Fig. 3.2 and Figs. D.1–D.3 respectively.

Table 3.1: Summary of lines

Transition		Catalogue Frequency	E_{up}	A_{ij}	Catalogue
$[QN]_{up}$ [a]	$[QN]_{low}$ [a]	[MHz]	[K]	$\times 10^{-5}$ [s^{-1}]	
		CH_2NH			
$15_{2,13}$ 14	$14_{3,12}$ 13	302 565.4318	408.72	6.61	JPL
$15_{2,13}$ 16	$14_{3,12}$ 15	302 565.4883	408.72	6.64	
$15_{2,13}$ 15	$14_{3,12}$ 14	302 566.3219	408.72	6.61	
		CH_3NH_2 [b]			
16 2 A2 15	15 3 A1 14	301 247.6939	305.21	1.37	(1)
16 2 A2 17	15 3 A1 16	301 247.7074	305.21	1.55	
16 2 A2 16	15 3 A1 16	301 247.9700	305.21	1.46	
13 2 B2 13	13 1 B1 13	301 424.0139	210.13	2.69	
13 2 B2 14	13 1 B1 14	301 425.6883	210.13	2.90	
13 2 B2 13	13 1 B1 12	301 425.8175	210.13	2.50	
9 0 B2 8	8 1 B1 7	301 653.3284	95.93	2.68	
9 0 B2 10	8 1 B1 9	301 653.4789	95.93	3.36	
9 0 B2 9	8 1 B1 8	301 654.7988	95.93	3.00	
16 7 B1 16	17 6 B2 17	302 801.6275	480.13	0.83	
16 7 B2 16	17 6 B1 17	302 801.6306	480.15	0.83	
16 7 B1 17	17 6 B2 18	302 801.7834	480.13	0.88	
16 7 B2 17	17 6 B1 18	302 801.7866	480.13	0.88	
16 7 B1 15	17 6 B2 16	302 801.7912	480.13	0.78	
16 7 B2 15	17 6 B1 16	302 801.7943	480.13	0.78	
9 0 E2+1 8	8 1 E2+1 7	303 733.9183	96.20	2.63	
9 0 E2+1 10	8 1 E2+1 9	303 734.0611	96.20	3.29	
9 0 E2+1 9	8 1 E2+1 8	303 735.3214	96.20	2.94	
		$^{13}CH_3CN$			
17_5	16_5	303 518.8535	310.00	222	CDMS
17_4	16_4	303 570.0991	245.64	230	
17_3	16_3	303 609.9710	195.57	236	
17_2	16_2	303 638.4820	159.80	240	
17_1	16_1	303 655.5770	138.33	243	
17_0	16_0	303 661.2780	131.18	243	
		$CH_3C^{15}N$			
17_4	16_4	303 187.8887	245.49	229	
17_3	16_3	303 227.9360	195.41	235	
17_2	16_2	303 256.5540	159.64	240	
17_1	16_1	303 273.7300	138.17	242	
17_0	16_0	303 279.4560	131.01	243	
		NH_2CHO			
$15_{1,15}$	$14_{1,14}$	303 450.2040	120.01	205	CDMS
$14_{1,13}$	$13_{1,12}$	303 660.5390	113.01	204	
		$NH_2^{13}CHO$			
$15_{1,15}$	$14_{1,14}$	302 553.9861	119.61	203	CDMS
$14_{1,13}$	$13_{1,12}$	303 111.8280	112.78	203	

Notes. [a] Quantum numbers for CH_2NH are $J_{Ka,Kc}$ F. Quantum numbers for CH_3NH_2 are J K_a Γ F, following the notation of Motiyenko et al. (2014). Quantum numbers for $^{13}CH_3CN$ and $CH_3C^{15}N$ are J_K. Quantum numbers for NH_2CHO and $NH_2^{13}CHO$ are $J_{Ka,Kc}$. [b] Only lines with $A_{ij} > 10^{-6} s^{-1}$ are listed.

References. (1) Motiyenko et al. (2014)

Table 3.2: Best-fit model parameters

	MM1 II		MM2 I		MM3 I	
$v_{\rm LSR}$ [km s^{-1}]	[-6.7]		[-9.0]		[-9.0]	
FWHM [km s^{-1}]	[3]		[3.5]		[3]	
$\theta_{\rm s}$ [$''$]	[1]		[1]		[1]	
	$T_{\rm ex}$ [K]	$N_{\rm s}$ [cm^{-2}]	$T_{\rm ex}$ [K]	$N_{\rm s}$ [cm^{-2}]	$T_{\rm ex}$ [K]	$N_{\rm s}$ [cm^{-2}]
CH_2NH	[215]	$\leq 5.2\times10^{16}$	[165]	$\leq 5.0\times10^{16}$	[120]	$\leq 10^{15}$
CH_3NH_2	340 ± 60	(2.7 ± 0.4) $\times10^{17}$	230 ± 30	(6.2 ± 0.9) $\times10^{16}$	220 ± 30	(3.0 ± 0.6) $\times10^{15}$
$^{13}CH_3CN$	70 ± 10	(3.4 ± 1.0) $\times10^{15}$	80 ± 25	(1.4 ± 0.5) $\times10^{15}$	90 ± 15	(9.0 ± 0.8) $\times10^{13}$
$CH_3C^{15}N$	110 ± 50	(3.3 ± 0.5) $\times10^{14}$	[80]	(1.8 ± 0.4)$\times10^{14}$	70 ± 45	(2.3 ± 0.7) $\times10^{13}$
NH_2CHO	[215]	(7.0 ± 1.7) $\times10^{15}$	[165]	(7.6 ± 0.8) $\times10^{15}$	[120]	$\leq 5.0\times10^{13}$
$NH_2^{13}CHO$[a]	[215]	$\leq 2.0\times10^{15}$	[165]	$\leq 5.0\times10^{14}$	–	–

Notes. Values in square brackets are fixed. Excitation temperatures for CH_3NH_2 and CH_3CN are the values of the best-fit respective models while $T_{\rm ex}$ for CH_2NH and NH_2CHO is fixed at the best-fit model value derived for CH_3OH (Bøgelund et al., 2018). In the MM2 region, the excitation temperature for $CH_3C^{15}N$ is not well constrained and is therefore adopted from $^{13}CH_3CN$. Listed uncertainties are the standard deviation of models with χ^2 within 1σ of the best-fit model.

3.3.1 Methylamine CH_3NH_2

For CH_3NH_2, five transitional features (all covering multiple hyperfine components) are identified towards NGC6334I. These are plotted in Fig. 3.2. The CH_3NH_2 transitions are not isolated lines but blended with transitions of other species. Nevertheless, and despite the contributions from the potential blending molecules, it is evident that the data cannot be reproduced without including CH_3NH_2 in the model, especially for the MM1 II and MM3 I regions.

MM1 II: For MM1 II the CH_3NH_2 transitions are well reproduced by a model with a column density of 2.7×10^{17} cm^{-2} and an excitation temperature of 340 K. The uncertainty on each of these values is less than 20%. For lower excitation temperatures, down to 100 K, the column density is consistent with that derived for 340 K within a factor of approximately two. The same is true for $T_{\rm ex}$ up to 500 K though for very low temperatures, down to 50 K, the column density can no longer be well-constrained. Also, since the variation between the column density of the fit which only takes into account CH_3NH_2 and the fit which includes all potential blending species is less then 30%, we consider it very probable that the features in the spectrum of this region are due to CH_3NH_2. The fact that the features cannot be reproduced without including CH_3NH_2 in the model makes the detection even more convincing. Around the transition located at 301.248 GHz, a slight negative offset in the baseline is seen. This is likely caused by continuum over-subtraction resulting in a negatively displaced baseline which makes the model transition at this location appear brighter than the observed one.

MM2 I: The best-fit model for region MM2 I has a column density equal to 6.2×10^{16} cm^{-2} and an excitation temperature of 230 K. This model is optimised to fit all of the covered CH_3NH_2 transitions, although only two of these, located at 301.426 GHz and 301.653 GHz, are considered fully detected. The remaining transitions, located at 301.248 GHz, 302.802 GHz and 303.734 GHz, are considered tentative detections. This is because these transitions are blended with emission from other species (lines at 301.248 and 302.802GHz) or because no clear line is visible in the observed spectrum at the expected location (line at 303.734 GHz). The tentative detections are included in the χ^2 minimisation, as they help constrain the best-fit model. For MM2, the uncertainty on $N_{\rm s}$ and $T_{\rm ex}$ is $\sim$15%. Varying the excitation temperature down to 50 and up to 500 K does not cause the value of the column density to change by more than a factor of two with respect to the best-fit value derived at 230 K. In contrast to the CH_3NH_2 features of MM1 II however, which are all well reproduced by the single-density, single-temperature model, the lines of MM2 I are not. Particularly the line ratio of the transitions at 301.426 GHz and 301.653 GHz is off and cannot be reproduced by the model. Despite the fact that the upper state energy of the transitions is fairly different, $\sim$210 K for the 301.426 GHz transitions and $\sim$96 K for the 301.653 GHz transitions, introducing a two-component model to account for a warm and cool emission region respectively, does not improve the fit. While the transition at 301.653 GHz may be well reproduced by a model with an excitation temperature of $\sim$50 K, addition of any higher excitation temperature-components to the model results in modelled line intensities that vastly overshoot the transition at 301.653 GHz with respect to the data while the intensity of the lines at 301.426 GHz remains much weaker than the observed line. The behaviour of this last transition is especially puzzling since none of the species included in either the JPL or CDMS catalogues are able to reproduce the observed data feature. One possible explanation is of course that the feature in the spectrum of MM2 I is due to transitions of some unknown species (or unknown transition of a known species) which is not included in the spectroscopic databases. However, if that is the case, this unknown species is particular

to the MM2 I region and does not significantly affect regions MM1 II and MM3 I where the respective CH_3NH_2 models correspond well with the observations.

The dissimilarity between the CH_3NH_2 model spectrum and the observations could also indicate that the critical density for individual transitions in the MM2 I region may not be reached, removing the region from LTE. Thus, a scenario in which the density of region MM2 is so low that the critical density of one transition is reached, while that of another transition is not, could explain why the model predictions are not able to reproduce the CH_3NH_2 transitions at 301.425 and 301.655 GHz simultaneously in this region while the same lines are well-matched with the data for regions MM1 and MM3. To test this hypothesis, the collisional coefficients need to be known and the critical densities inferred for each of the transitions in question. However, since these numbers are not known for CH_3NH_2 we are unable to make the comparison but can instead conclude that it is likely that the MM2 region has a lower overall density as compared with the regions MM1 and MM3. A lower density of the MM2 region with respect to the MM1 region is consistent with the findings of Brogan et al. (2016), who estimate the dust mass associated with each of the hot cores based on their spectral energy distribution. As in the case of MM1 II, the CH_3NH_2 features cannot be reproduced satisfactory by any other species and therefore we conclude that CH_3NH_2 is likely to be present in the region despite the inadequacy of the model to fully reproduce the data.

MM3 I: For MM3 I the best-fit column density and excitation temperature values are 3.0×10^{15} cm^{-2} and 220 K respectively. The uncertainty on these values is $\sim$35% for $T_{\rm ex}$ and 20% for $N_{\rm s}$. For fixed excitation temperatures down to 50 K and up to 500 K, the CH_3NH_2 column density remains within a factor of two of the best-fit value at 220 K. The value of the column density of the best-fit model does not change when the contributions from other species are included in the fit. As in the case of the MM1 region, the good agreement between the CH_3NH_2 model and data, especially around the transitions at 301.426 GHz and 301.653 GHz, makes the presence of CH_3NH_2 in this region very convincing. Due to blending with other species at the location of the CH_3NH_2 transitions at 301.248 GHz and 302.802 GHz, we consider these as tentative detections only. In the case of the transition located at 303.734 GHz, a weak line feature is present in the observed spectrum although not at the exact same location as predicted in the model spectrum. This transition is therefore also considered a tentative detection. As in the case of MM2 I, the tentative detections are included when the model spectra are optimised.

In summary, CH_3NH_2 is securely detected towards both the MM1 and MM3 regions while the detection towards MM2 is slightly less clear. The uncertainty on the CH_3NH_2 column densities is between 15 and 20%. Despite the local variations, the overall uniformity of CH_3NH_2 makes it likely that its origin is the same throughout the NGC 6334I region. In addition to the data presented here, we included in Appendix C a confirmation of the presence of CH_3NH_2 in NGC 6334I based on ALMA Band 10 observations from McGuire et al. (2018). However, due to the difference in angular resolution and extraction location, these data probe different excitation conditions and different populations of gas and therefore cannot be compared directly with the Band 7 observations discussed above. The Band 10 spectrum and modelled CH_3NH_2 transitions shown in Fig. C.1 and listed in Table C.1 are therefore included as proof of the presence of CH_3NH_2 in NGC 6334I but will not be discussed further here. A detailed analysis of the Band 10 data is presented by McGuire et al. (2018).

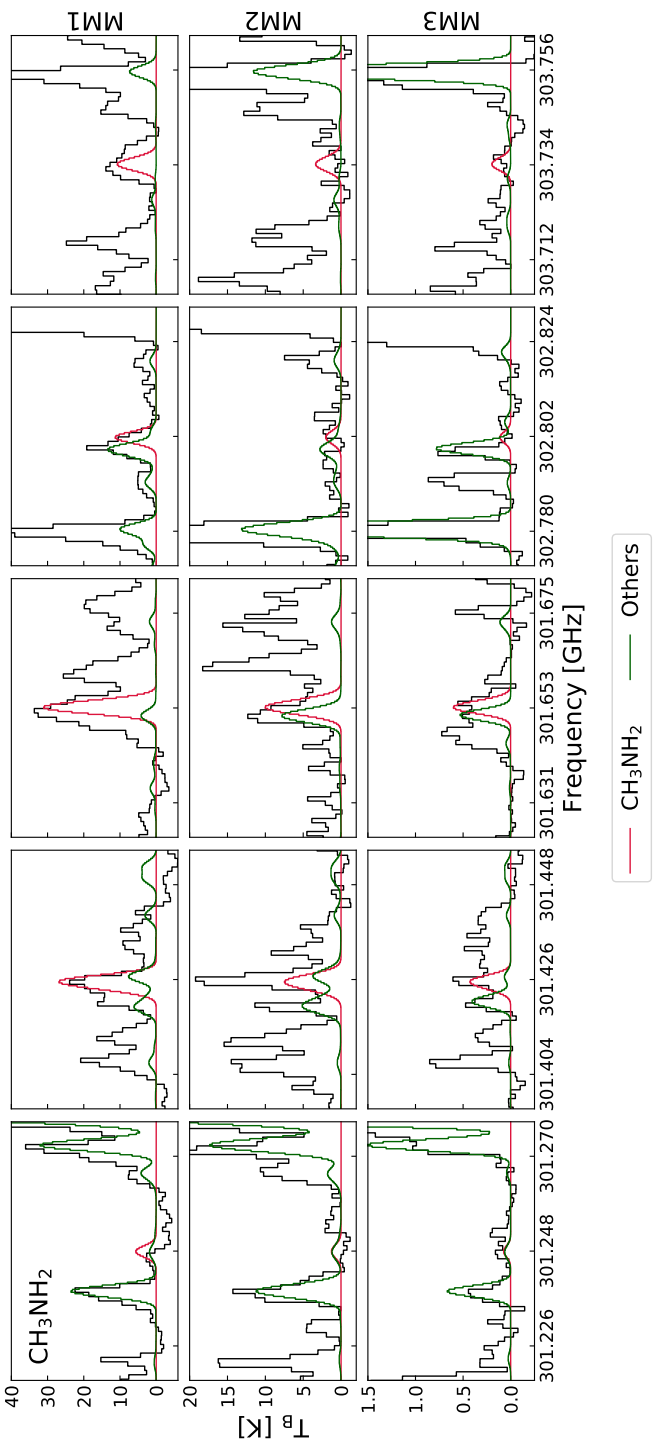

Figure 3.2: CH_3NH_2 transitions detected towards NGC6334I. Red and green lines represent the synthetic spectrum of CH_3NH_2 and the sum of spectra of other contributing species respectively. The abscissa is the rest frequency with respect to the radial velocity towards each of the hot cores (listed in Table 3.2). The data are shown in black. *Top panels*: MM1 II. *Middle panels*: MM2 I. *Bottom panels*: MM3 I.

3.3.2 Summary of results on methanimine, methyl cyanide and formamide

A single (hyperfine-split) transition of CH_2NH is covered by the data and consequently no excitation temperature can be derived for this species. In addition, the transition is blended with CH_3OCHO and the column density of CH_2NH is therefore reported as an upper limit for each of the studied regions. In contrast, a total of eleven transitions belonging to the ^{13}C- and ^{15}N-methyl cyanide isotopologues are detected towards NGC 6334I. Six of these belong to $^{13}CH_3CN$ and five to $CH_3C^{15}N$. Though some transitions are blended, both isotopologues are clearly detected towards all of the studied regions. The uncertainty on the derived column densities of $^{13}CH_3CN$ and $CH_3C^{15}N$ is up to 30% while the uncertainty on the derived excitation temperatures is up to 65%. In the case of MM2, the excitation temperature for $CH_3C^{15}N$ could not be constrained and therefore the column density of this species is derived assuming $T_{\rm ex}$ to be the same as for $^{13}CH_3CN$. As in the case of CH_2NH, no excitation temperature can be derived for NH_2CHO since only two of the 18 transitions of this species covered by the data are bright enough to be detected and these represent a very limited range of upper state energies, with a difference between the two of less than 10 K. In the case of the regions MM1 II and MM2 I, the features in the data at the location of the NH_2CHO transitions cannot be reproduced by any other species included in either the JPL or the CDMS catalogues. In contrast, the features detected towards the MM3 I region, may be reproduced by other species and the detection of NH_2CHO towards this region is therefore considered tentative. The uncertainty on the column density of NH_2CHO towards MM1 II and MM2 I is less than 25%. The full discussion of the detections of CH_2NH, CH_3CN and NH_2CHO can be found in Appendix D.

3.4 Discussion

In this section, the column densities and excitation temperatures discussed above will be compared with the predictions of the chemical models of Garrod (2013) as well as to the values derived towards a number of other sources including the high-mass star-forming regions Sgr B2 and Orion KL, the low-mass protostar IRAS 16293–2422B and the comet 67P. In order to do this, column density ratios for each of the studied species with respect to CH_3OH are derived, these are given in Table 3.3. CH_3OH is chosen as a reference because it is one of the most abundant COMs in the ISM and therefore has been studied comprehensively, also in NGC 6334I (Bøgelund et al., 2018). Secondly, in order to investigate the relation between the studied species, column density ratios of CH_3NH_2 with respect to CH_2NH, NH_2CHO and CH_3CN are derived, these are given in Table 3.4. Figures 3.3 and 3.4 summarise all ratios. In the following sections the results on CH_3NH_2 and on the other species will be discussed separately.

3.4.1 Methylamine towards NGC 6334I

The detection of CH_3NH_2 in the hot cores of NGC 6334I presented here, combined with recent (tentative) detections by Pagani et al. (2017) towards Orion KL and Ohishi et al. (2017) towards a few high-mass objects, indicate that this molecule is more common and abundant than previously thought (see for example the upper limits on the species presented by Ligterink et al., 2015). In this case, the "lacking" CH_3NH_2-detections are more likely explained by observational biases, for example the large partition function of

Table 3.3: Column density ratios with CH_3OH as reference

	CH_3NH_2/CH_3OH		NH_2CHO/CH_3OH		CH_3CN/CH_3OH				References
					$^{13}CH_3CN$		$CH_3C^{15}N$		
CH_3OH reference	^{13}C	^{18}O	^{13}C	^{18}O	^{13}C	^{18}O	^{13}C	^{18}O	
MM1 II	5.9×10^{-3}	2.5×10^{-3}	1.5×10^{-4}	6.5×10^{-5}	4.6×10^{-3}	2.0×10^{-3}	3.0×10^{-3}	1.3×10^{-3}	this work
MM2 I	1.5×10^{-3}	9.2×10^{-4}	1.9×10^{-4}	1.1×10^{-4}	2.1×10^{-3}	1.3×10^{-3}	1.9×10^{-3}	1.1×10^{-3}	this work
MM3 I	5.4×10^{-4}	4.8×10^{-4}	$\leq9.0\times10^{-6}$	$\leq7.9\times10^{-6}$	1.0×10^{-3}	8.9×10^{-4}	1.7×10^{-3}	1.5×10^{-3}	this work
Model F	7.3×10^{-3}		0.04		4.5×10^{-4}				1
Model M	4.0×10^{-3}		0.02		2.3×10^{-4}				1
Model S	1.8×10^{-3}		0.76		3.4×10^{-4}				1
Sgr B2(M)	8.0×10^{-3}		2.5×10^{-3}		0.03				2
Sgr B2(N)	0.03		0.07		0.11				2
Sgr B2(N)	0.10		0.04		2.8×10^{-3}				3
Sgr B2(N2–5)[a]	–		8.3×10^{-3} – 0.09[b]		0.06 – 0.13				4
Orion KL Compact Ridge	–		1.7×10^{-3}		0.01				5
IRAS 16293–2422B	$\leq5.3\times10^{-5}$		10^{-3}		4×10^{-3}				6, 7, 8, 9

Notes. The uncertainty on the column density ratios derived towards NGC 6334 I is estimated to be 40% (see sect. 3.2). [(a)] Range of values derived for the cores N2, N3, N4 and N5. [(b)] Excluding the upper limit on NH_2CHO for N4.

References. (1) Garrod (2013); (2) Belloche et al. (2013); (3) Neill et al. (2014); (4) Bonfand et al. (2017); (5) Crockett et al. (2014); (6) Coutens et al. (2016); (7) Ligterink et al. (2018a); (8) Jørgensen et al. (2018); (9) Calcutt et al. (2018).

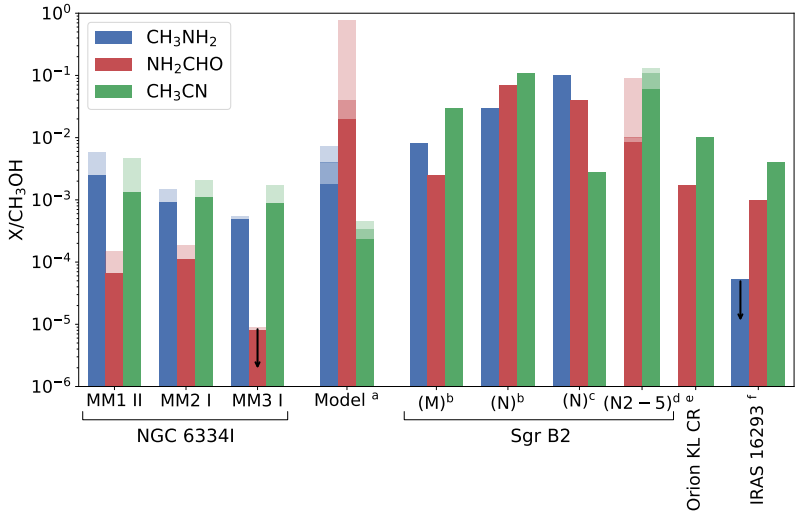

Figure 3.3: Column density ratios of CH_3NH_2 (blue), NH_2CHO (red) and CH_3CN (green) with respect to CH_3OH for NGC 6334I, model predictions and other objects. For the regions in NGC 6334I, the shaded bars indicate the range of ratios derived using the ^{13}C- and ^{18}O-methanol isotopologues as base respectively. For the models, the shaded bars indicate the range of rations derived for the fast, medium and slow models respectively. For Sgr B2(N2–5), the shaded bars indicate the range of ratios derived for each of the components N2, N3, N4 and N5 (excluding the upper limit on NH_2CHO for N4). **References.** $^{(a)}$ Garrod (2013); $^{(b)}$ Belloche et al. (2013); $^{(c)}$ Neill et al. (2014); $^{(d)}$ Bonfand et al. (2017); $^{(e)}$ Crockett et al. (2014); $^{(f)}$ Ligterink et al. (2018a).

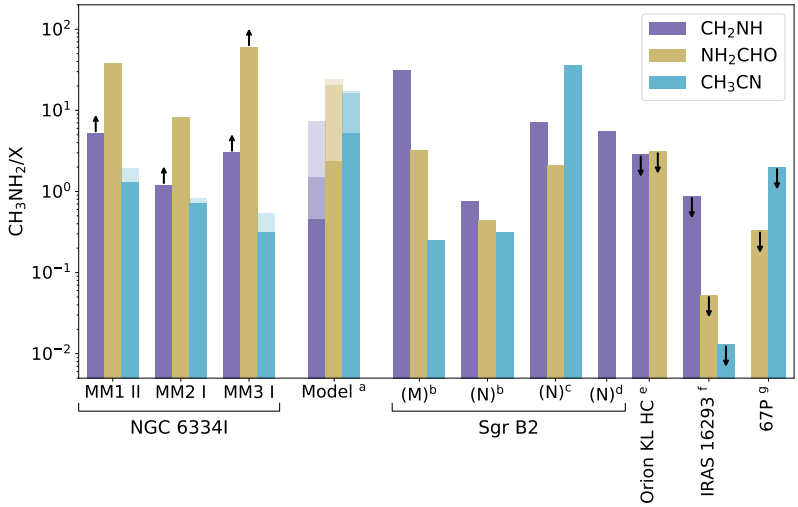

Figure 3.4: Column density ratios of CH_3NH_2 with respect to CH_2NH (purple), NH_2CHO (gold) and CH_3CN (turquoise) for NGC 6334I, model predictions and other objects. For the regions in NGC 6334I, shaded bars indicate the range of ratios derived based on the $^{13}CH_3CN$ and $CH_3C^{15}N$ isotopologues. For the models, the shaded bars indicate the range of rations derived for the fast, medium and slow models respectively. **References.** $^{(a)}$ Garrod (2013); $^{(b)}$ Belloche et al. (2013); $^{(c)}$ Neill et al. (2014); $^{(d)}$ Halfen et al. (2013); $^{(e)}$ Pagani et al. (2017), Laurent Pagani, priv. comm.; $^{(f)}$ Ligterink et al. (2018a); $^{(g)}$ Goesmann et al. (2015).

Table 3.4: CH_3NH_2 column density ratios

CH_3CN reference	CH_3NH_2/CH_2NH	CH_3NH_2/NH_2CHO	CH_3NH_2/CH_3CN ^{13}C	^{15}N	References
MM1 II	≥5.2	38	1.28	1.94	this work
MM2 I	≥1.2	8.16	0.71	0.70	this work
MM3 I	≥3.0	≥60	0.54	0.31	this work
Model F	7.27	20.5	16.3		1
Model M	1.5	24	17.1		1
Model S	0.45	2.34	5.23		1
Sgr B2(M)	31[a]	3.21	0.25		2
Sgr B2(N)	0.75	0.44	0.31		2
Sgr B2(N)	7.14	2.08	35.7		3
Sgr B2(N)	5.49	–	–		4
Orion KL Hot Core	≤2.86	≤3.13	–		5
IRAS 16293–2422B	≤0.88	≤0.053	≤0.013		6, 7
Comet 67P[b]	–	≤0.33	≤2		8

Notes. The uncertainty on the column density ratios derived towards NGC 6334 I is estimated to be 40% (see sect. 3.2). [(a)] Extended CH_2NH emission. [(b)] Listed as upper limits based on the discussion in Sect. 2.4 of Altwegg et al. (2017).

References. (1) Garrod (2013); (2) Belloche et al. (2013); (3) Neill et al. (2014); (4) Halfen et al. (2013); (5) Pagani et al. (2017), Laurent Pagani, priv. comm.; (6) Calcutt et al. (2018); (7) Ligterink et al. (2018a); (8) Goesmann et al. (2015).

CH_3NH_2 resulting in relatively weaker transitions of this species as compared with, for example, NH_2CHO, rather than actual chemical variations between objects.

Within the regions of NGC 6334I, the CH_3NH_2 abundance is fairly uniform and column density ratios with respect to CH_3OH and CH_3CN show variations within factors of four and two between regions MM1 and MM2 and up to an order of magnitude between regions MM1 and MM3. The variation over the column density ratios derived using the ^{13}C- and ^{18}O-methanol iosotopologues as a reference vary with a factor of three, while the ratios derived based on the ^{13}C- and ^{15}N-methyl cyanide isotopologues vary with a factor of two. In the case of the CH_3NH_2 to NH_2CHO ratio, the variation is a factor of seven if all three regions are considered and less than a factor of five between regions MM1 II and MM2 I. This is due to the relatively low column density of NH_2CHO in MM3 I as compared with regions MM1 II and MM2 I. Similarly, the variation of the CH_3NH_2 to CH_2NH column density ratio over the three regions is within a factor of four, though the single CH_2NH line covered by the data means that these ratios should be seen as lower limits.

Although the variations in the column density of CH_3NH_2 over the studied regions are similar to those of CH_3OH and CH_3CN, the CH_3NH_2 excitation temperatures are higher than for any of the other species. This trend is most pronounced in the case of MM1. A relatively higher excitation temperature of CH_3NH_2 compared with other species is consistent with the findings of Halfen et al. (2013).

3.4.2 Methylamine towards other objects

Compared with the CH_3NH_2 to CH_3OH ratios derived by Belloche et al. (2013) and Neill et al. (2014) towards Sgr B2 (M) and (N), the values inferred for the regions in NGC 6334I are lower by up to two orders of magnitude, though the value derived for Sgr B2 (M) is only higher by a factor of up to three when compared with the value derived for MM1. For the CH_3NH_2 to NH_2CHO, CH_3CN and CH_2NH ratios the picture is less clear; while the CH_3NH_2/NH_2CHO values derived towards Sgr B2 are all about an order of magnitude lower than those derived towards NGC 6334I, the CH_3NH_2/CH_3CN value derived by Neill et al. (2014) is higher by more than an order of magnitude while the values derived by Belloche et al. (2013) are lower by up to a factor of six. In the case of CH_3NH_2/CH_2NH, all but one of the values towards Sgr B2 are higher than the lower limits derived towards NGC 6334I. Because of these large variations it is difficult to make strong statements on the overall CH_3NH_2 distribution within the Sgr B2 region since chemical variations in the reference species are just as likely the source of the varying ratios. Also, due to the large distance to Sgr B2 ($\sim$8 kpc) and the fact that Belloche et al. (2013) and Neill et al. (2014) use single dish data, from the IRAM 30 m telescope and *Herschel* Space Observatory respectively, the observations may be biased towards large scale structures and particularly the effects of beam dilution should be considered since these studies probe spacial scales on the order of $\sim$0.5 – 1 pc ($\sim 2\times10^5$ au) as compared with $\sim$1300 au in the case of the regions in NGC 6334I.

In contrast to the studies of Sgr B2, the ALMA observations towards the Orion KL Hot Core region reported by Pagani et al. (2017) make for a more direct comparison with the observations towards NGC 6334I, since the Orion KL region is probed at spacial scales of $\sim$660 au. Though not firmly detected, the upper limits on the CH_3NH_2 to CH_2NH or NH_2CHO ratios hint that CH_3NH_2 is less abundant in the Orion KL hot core as compared with NGC 6334I or, alternatively, that NH_2CHO and CH_2NH are more abundant. Unfortunately the extended CH_3OH emission towards Orion KL could not be evaluated due to missing zero-spacing data. Without CH_3OH as a reference it is difficult to distinguish between the low-CH_3NH_2 and high-NH_2CHO or CH_2NH scenarios. In addition, the Orion KL data show that CH_3NH_2 is not associated with either NH_2CHO nor CH_2NH. This is based on the $v_{\rm LSR}$ which is 4.3 km s^{-1} for CH_3NH_2 but 5.5 km s^{-1} for NH_2CHO and CH_2NH. In NGC 6334I such a mismatch between velocity of different species is not observed toward either of the studied regions. Finally, as in the case of NGC 6334I, the excitation temperature is higher for CH_3NH_2 than for NH_2CHO and CH_2NH with values of 280, 200 and 150 K respectively.

The lowest CH_3NH_2 ratios are observed towards the low-mass protostar IRAS 16293–2422B, an analogue to the young Sun, where a deep upper limit on the column density of CH_3NH_2 was inferred by Ligterink et al. (2018a), based on the ALMA PILS survey (see Jørgensen et al., 2016, for full PILS overview) probing spacial scales of $\sim$60 au. This upper limit results in ratios with respect to CH_3OH, NH_2CHO and CH_3CN which are all lower by one to two orders of magnitude when compared with the lowest ratios derived towards NGC 6334I. The smallest variation between NGC 6334I and IRAS 16293–2422B is seen in the CH_3NH_2 to CH_2NH ratio where the value derived for IRAS 16293–2422B is within the uncertainty of value derived for the MM2 I region but lower by up to a factor of six compared with the regions MM1 II and MM3 I. These differences in ratios hint that the formation of CH_3NH_2 in the high-mass hot cores of NGC 6334I differ from the formation of CH_3NH_2 in the low-mass IRAS 16293–2422B protostar. An explanation for this difference could be the dust grain temperature. Based on the low levels of CH_3OH deuteration in NGC 6334I, Bøgelund et al. (2018) determine

a relatively warm dust grain temperature of ∼30 K during the time of CH_3OH formation. In contrast, the dust grains in the cloud from which the IRAS 16293–2422 protobinary system formed are thought to have been much cooler, with temperatures below 20 K (Jørgensen et al., 2016). At high grain temperatures the solid-state formation of CH_3NH_2 via CH_3 + NH_2 could be enhanced, due to increased mobility of the radicals or the loss of H-atoms, which at lower temperatures would hydrogenate these radicals to form the neutral species CH_4 and NH_3.

Additional indications for a grain surface formation route are found in the chemical models presented by Garrod (2013). These models evaluate the chemical evolution of high-mass hot cores as these evolve through infall and warm-up phases. The physical model adopted by Garrod (2013) consists of a collapse phase followed by a gradual warm-up of the gas and dust. For the warm-up phase, three timescales are adopted: a 'fast' scale reaching 200 K in 5×10^4 yr, a 'medium' scale reaching 200 K in 2×10^5 yr and a 'slow' scale reaching 200 K in 1×10^6 yr. Listed in Tables 3.3 and 3.4 are the predicted peak gas-phase abundance ratios for each of these models. In the models, CH_3NH_2 is formed predominantly via CH_3 and NH_2 radical recombination reactions on the grain surface. Since the predicted CH_3NH_2 ratios are quite similar to the ratios derived for the regions in NGC 6334I, and for most species agree within a factor of five, a solid state formation pathway for CH_3NH_2 seems likely. However, since the models are not optimised to the physical conditions of the hot cores of NGC 6334 I but rather general conditions found in hot cores, the comparison between observed and modelled column density ratios should only be considered as indicative of trends.

3.4.3 Comparison with comet 67P

In an effort to understand how the life we know on Earth today has come to be, the chemical composition of the Solar Nebular must be examined. The most pristine record of this composition is believed to be locked up in comets. Goesmann et al. (2015) report the first in situ analysis of organic molecules on the surface of comet 67P. Based on the measurements of the COSAC instrument aboard *Rosetta*'s *Philae* lander, Goesmann et al. (2015) derive CH_3NH_2 to NH_2CHO and CH_3CN ratios which are lower by one to two orders of magnitude for CH_3NH_2/NH_2CHO and higher by up to a factor of six for CH_3NH_2/CH_3CN, as compared with the values derived for NGC 6334I. To improve counting statistics, Goesmann et al. (2015) binned the COSAC data in bins around integer mass numbers, thereby effectively reducing the mass resolution, before identifying and deriving abundances of the detected species. However, after reanalysing the unbinned COSAC data, and using higher resolution measurements from the ROSINA mass spectrometer, aboard the *Rosetta* orbiter, as a proxy for the near-surface cometary material, Altwegg et al. (2017) conclude that a revision of the list of molecules and derived abundances reported by Goesmann et al. (2015) is needed. Specifically, the contributions from CH_3NH_2, NH_2CHO and CH_3CN to the signal in the COSAC data are likely to be significantly smaller than originally reported by Goesmann et al. (2015). Therefore, the CH_3NH_2 ratios for comet 67P are listed in this work as upper limits (following the discussion in Sect. 2.4 of Altwegg et al. (2017)). The ratios derived for the comet are consistent with the values derived for the low-mass protostar IRAS 16293–2422B.

3.4.4 Other N-bearing species

For the NH_2CHO and CH_3CN to CH_3OH ratios, the variations derived for each of the NGC 6334I regions are small and within factors of between two and four (excluding the upper limit on NH_2CHO for region MM3 I which is about an order of magnitude lower than the values for MM1 II and MM2 I). Compared with the hot core model predictions of Garrod (2013), NH_2CHO/CH_3OH is over-predicted by orders of magnitude, while CH_3CN/CH_3OH, as is the case for CH_3NH_2/CH_3OH, shows fairly good agreement with the numbers derived for NGC 6334I.

For Sgr B2, the NH_2CHO and CH_3CN ratios with respect to CH_3OH show the same trends as CH_3NH_2/CH_3OH, and are generally one to two orders of magnitude higher than the values derived for NGC 6334I, though, as in the case of the CH_3NH_2 ratios, observations may suffer from beam dilution effects or underestimated CH_3OH values since only the main CH_3OH-isotope, which may be optically thick, is detected. Although CH_3NH_2 is not included in their study, the ratios derived for NH_2CHO and CH_3CN by Bonfand et al. (2017), using ALMA observations which probe scales of ∼0.06 pc (∼13300 au), indicate that the higher NH_2CHO and CH_3CN to CH_3OH ratios reported by Belloche et al. (2013) and Neill et al. (2014), are true and not artefacts of beam dilution or opacity effects. This implies that the chemical inventory of Sgr B2 is richer in complex nitrogen-bearing species than that of NGC 6334I, in agreement with the high temperatures and complexity characterising the Galactic central region. That the NGC 6334I region is relatively poor in N-bearing species is also in agreement with the findings of Suzuki et al. (2018) who investigate the correlation between O- and N-bearing species in a sample of eight hot cores and find that the former species are more abundant than the latter in this region.

For the Orion KL Compact Ridge, Crockett et al. (2014) use observations from *Herschel* to derive NH_2CHO/CH_3OH and CH_3CN/CH_3OH values which are generally lower than those derived for Sgr B2 but higher by at least an order of magnitude as compared with NGC 6334I.

Lastly, the ALMA observations towards the low-mass protostar IRAS 16293–2422B, indicate similar CH_3CN/CH_3OH values as compared with the regions in NGC 6334I, while the values for NH_2CHO/CH_3OH are higher for IRAS 16293–2422B by about an order of magnitude as compared with the values for the regions in NGC 6334I. The generally similar CH_3CN and NH_2CHO to CH_3OH ratios between NGC 6334I and IRAS 16293–2422B indicate that the overall lower CH_3NH_2 ratios derived towards IRAS 16293–2422B reflect an actual difference in chemical composition between the two regions. As discussed above, this difference in CH_3NH_2 abundance may reflect a difference in grain temperature during the time when the species was formed. With the sensitivity and resolution provided by ALMA, continued studies of this and related species will broaden our understanding of the inventory of prebiotic species in both high- and low-mass sources and help evaluate the degree to which CH_3NH_2 chemistry depends on the grain temperature.

3.5 Summary

In this work, we present the first detection of CH_3NH_2 towards NGC 6334I and derive the column density of the species in the hot cores MM1, MM2 and MM3. Transitions of CH_2NH, NH_2CHO, $^{13}CH_3CN$ and $CH_3C^{15}N$ are also studied and their column densities inferred. Assuming LTE and excitation temperatures in the range 70–340 K, each species

is modelled separately and then summed to obtain a full spectrum for each of the studied regions.

Based on the good agreement between the CH_3NH_2 column density ratios predicted by the hot core models of Garrod (2013) and the values derived for the regions in NGC 6334I, the formation of CH_3NH_2 is more likely to proceed via radical recombination reactions on grain surfaces than via gas-phase reactions.

The detection of CH_3NH_2 towards NGC 6334I reported here and recent (tentative) detections towards the high-mass star-forming regions in Orion KL and G10.47+0.03 by Pagani et al. (2017) and Ohishi et al. (2017) respectively, also indicate that the species is not as uncommon in the ISM as was previously thought. This implies that future high-sensitivity, high-resolution searches for the species are likely to yield additional detections of the formerly so elusive molecule. In this case, observations carried out towards both high- and low-mass objects, will help assess the dependency of CH_3NH_2-grain formation efficiency on the dust grain temperature of individual regions.

Acknowledgements. We thank the anonymous referee for a careful evaluation and many useful comments that helped us clarify our manuscript. A special thanks to L. Pagani for insights into the complex structure and chemistry of Orion KL and providing column density estimates for NH_2CHO and CH_2NH. We also thank C. Brogan and T. Hunter for assistance in reducing and analysing the Band 10 data. This paper makes use of the following ALMA data: ADS/JAO.ALMA#2015.1.00150.S and #2017.1.00717.S. ALMA is a partnership of ESO (representing its member states), NSF (USA) and NINS (Japan), together with NRC (Canada) and NSC and ASIAA (Taiwan) and KASI (Republic of Korea), in cooperation with the Republic of Chile. The Joint ALMA Observatory is operated by ESO, AUI/NRAO and NAOJ. This work is based on analysis carried out with the CASSIS software and JPL: http://spec.jpl.nasa.gov/ and CDMS: http://www.ph1.uni-koeln.de/cdms/ spectroscopic databases. CASSIS has been developed by IRAP-UPS/CNRS (http://cassis.irap.omp.eu).

Appendix A: Model grids

Table A.1: Overview of model grids

Species	N_s range [cm^{-2}]		
	MM1 II	MM2 I	MM3 I
CH_2NH	10^{16} – 10^{17}	10^{16} – 10^{17}	5×10^{14} – 5×10^{15}
CH_3NH_2	5×10^{16} – 5×10^{17}	3×10^{16} – 3×10^{17}	10^{15} – 10^{16}
$^{13}CH_3CN$	10^{15} – 10^{16}	5×10^{14} – 5×10^{15}	5×10^{13} – 5×10^{14}
$CH_3C^{15}N$	10^{14} – 10^{15}	10^{14} – 10^{15}	5×10^{12} – 5×10^{13}
NH_2CHO	5×10^{15} – 5×10^{16}	5×10^{15} – 5×10^{16}	10^{13} – 10^{14}
$NH_2^{13}CHO$	5×10^{14} – 5×10^{15}	10^{14} – 10^{15}	–

Notes. All grids have T_{ex} spanning 10 – 500 K in steps of 10 K and N_s sampled by 20 logarithmically spaced steps.

Appendix B: Integrated line intensities

This appendix lists the integrated intensities of the best-fit model for each species and region, along with the integrated intensity, FWHM and v_{LSR} of a gaussian profile fitted to selected line features in the observed spectra. However, due to the high line density in the observed spectra, the majority of the listed transitions are blended. Therefore, care should be taken when interpretation the integrated intensities of the observed transitions since these fits in the majority of cases cover blended features which cannot be disentangled and therefore will included the contributions from other (unknown) species.

Table B.1: Integrated intensities of spectral line features

Transition		Region	I_{model}[b]	Fit to observed spectrum[a]		
				I_{gauss}	FWHM$_{gauss}$	$v_{LSR,gauss}$
$[QN]_{up}$[c]	$[QN]_{low}$[c]		[K km s^{-1}]	[K km s^{-1}]	[km s^{-1}]	[km s^{-1}]
			CH_2NH			
$15_{2,13}$ 14	$14_{3,12}$ 13	MM1*	46.2	37.8	2.7 ± 0.8	-8.2 ± 0.3
$15_{2,13}$ 16	$14_{3,12}$ 15	MM2*	36.8	24.1	2.4 ± 0.3	-10.4 ± 0.1
$15_{2,13}$ 15	$14_{3,12}$ 14	MM3	0.5	–	–	–
			CH_3NH_2[d]			
16 2 A2 15	15 3 A1 14	MM1	18.3	–	–	–
16 2 A2 17	15 3 A1 16	MM2	4.8	–	–	–
16 2 A2 16	15 3 A1 16	MM3	0.2	–	–	–
13 2 B2 13	13 1 B1 13	MM1*	106.0	123.6	4.8 ± 0.8	-7.9 ± 0.2
13 2 B2 14	13 1 B1 14	MM2*	32.5	74.0	3.6 ± 0.3	-11.0 ± 0.1
13 2 B2 13	13 1 B1 12	MM3	1.7	2.0	3.2 ± 0.6	-10.9 ± 0.2

Continued on next page

Continued from previous page

Transition		Region	$I_{\rm model}$[b]	Fit to observed spectrum[a]		
				$I_{\rm gauss}$	FWHM$_{\rm gauss}$	$v_{\rm LSR,gauss}$
[QN]$_{\rm up}$[c]	[QN]$_{\rm low}$[c]		[K km s^{-1}]	[K km s^{-1}]	[km s^{-1}]	[km s^{-1}]
9 0 B2 8	8 1 B1 7	MM1	115.3	–	–	–
9 0 B2 10	8 1 B1 9	MM2	41.5	–	–	–
9 0 B2 9	8 1 B1 8	MM3*	2.2	2.4	4.4 ± 1.1	-10.7 ± 0.4
16 7 B1 16	17 6 B2 17					
16 7 B2 16	17 6 B1 17					
16 7 B1 17	17 6 B2 18	MM1	36.6	–	–	–
16 7 B2 17	17 6 B1 18	MM2	7.6	–	–	–
16 7 B1 15	17 6 B2 16	MM3	0.4	–	–	–
16 7 B2 15	17 6 B1 16					
9 0 E2+1 8	8 1 E2+1 7	MM1	38.8	–	–	–
9 0 E2+1 10	8 1 E2+1 9	MM2	13.7	–	–	–
9 0 E2+1 9	8 1 E2+1 8	MM3	0.7	–	–	–
		$^{13}CH_3CN$				
		MM1*	27.5	36.9	3.6 ± 0.6	-6.8 ± 0.3
17_5	16_5	MM2*	10.8	32.2	2.8 ± 0.2	-8.0 ± 0.1
		MM3	0.9	1.1	2.4 ± 0.3	-9.2 ± 0.1
		MM1*	49.0	38.1	2.6 ± 0.4	-6.5 ± 0.2
17_4	16_4	MM2*	24.2	50.4	3.3 ± 0.3	-8.6 ± 0.1
		MM3	1.9	1.9	2.5 ± 0.2	-8.8 ± 0.1
		MM1	132.1	108.1	3.5 ± 0.4	-6.4 ± 0.2
17_3	16_3	MM2	80.9	86.2	3.4 ± 0.2	-8.3 ± 0.1
		MM3	6.7	7.1	2.3 ± 0.2	-8.7 ± 0.1
		MM1*	100.4	124.5	4.4 ± 0.7	-6.7 ± 0.2
17_2	16_2	MM2*	66.9	72.9	3.2 ± 0.2	-8.3 ± 0.1
		MM3*	5.1	5.2	2.4 ± 0.6	-8.6 ± 0.2
		MM1*	113.1	212.7	4.3 ± 0.3	-7.5 ± 0.1
17_1	16_1	MM2*	82.5	78.0	3.1 ± 0.3	-8.4 ± 0.1
		MM3*	6.6	7.5	2.3 ± 0.3	-8.7 ± 0.1
		MM1	128.5	–	–	–
17_0	16_0	MM2	91.8	–	–	–
		MM3	7.5	–	–	–
		$CH_3C^{15}N$				
		MM1	8.3	–	–	–
17_4	16_4	MM2	3.3	–	–	–
		MM3	0.3	–	–	–
		MM1	26.0	23.7	2.5 ± 0.5	-6.3 ± 0.2
17_1	16_1	MM2*	12.3	32.56	2.4 ± 0.2	-7.9 ± 0.1
		MM3	1.4	1.31	2.7 ± 0.6	-8.9 ± 0.2
		MM1*	18.6	20.2	3.2 ± 0.5	-6.5 ± 0.2
17_2	16_2	MM2*	9.8	23.0	3.8 ± 0.5	-7.7 ± 0.2
		MM3	1.2	0.65	1.6 ± 0.4	-8.5 ± 0.2
		MM1	24.7	–	–	–
17_1	16_1	MM2	13.0	–	–	–
		MM3	1.6	–	–	–
		MM1	26.7	–	–	–
17_1	16_1	MM2	16.5	–	–	–
		MM3	1.8	–	–	–

Continued on next page

Continued from previous page

Transition		Region	$I_{\rm model}$ [b]	Fit to observed spectrum [a]		
				$I_{\rm gauss}$	FWHM$_{\rm gauss}$	$v_{\rm LSR,gauss}$
$[QN]_{up}$ [c]	$[QN]_{low}$ [c]		[K km s^{-1}]	[K km s^{-1}]	[km s^{-1}]	[km s^{-1}]
			NH_2CHO			
$15_{1,15}$	$14_{1,14}$	MM1	135.1	–	–	–
		MM2	172.0	–	–	–
		MM3	1.6	–	–	–
$14_{1,13}$	$13_{1,12}$	MM1	130.7	–	–	–
		MM2	168.3	–	–	–
		MM3	1.6	–	–	–
			$NH_2^{13}CHO$			
$15_{1,15}$	$14_{1,14}$	MM1	41.4	–	–	–
		MM2	13.2	–	–	–
		MM3	–	–	–	–
$14_{1,13}$	$13_{1,12}$	MM1	40.1	–	–	–
		MM2	12.9	–	–	–
		MM3	–	–	–	–

Notes. [*] Fit to blended feature. [a] Gaussian fit to the observed line features. Listed values are the integrated intensity, FWHM and $v_{\rm LSR}$ of the fitted gaussian profile, including 1σ uncertainties. [b] Integrated intensity of the best-fit model for each region and spectral feature. [c] Quantum numbers for CH_2NH are $J_{Ka,Kc}$ F. Quantum numbers for CH_3NH_2 are J K_a Γ F, following the notation of Motiyenko et al. (2014). Quantum numbers for $^{13}CH_3CN$ and $CH_3C^{15}N$ are J_K. Quantum numbers for NH_2CHO and $NH_2^{13}CHO$ are $J_{Ka,Kc}$. [d] Only lines with $A_{\rm ij} > 10^{-6} s^{-1}$ are listed.

Appendix C: ALMA Band 10 spectrum of methylamine

The Band 10 spectrum was acquired as part of project ADS/JAO.ALMA#2017.1.00717.S. Because the primary beam at Band 10 is only $\sim 7''$, two pointing positions were needed to cover the entire source. Only one of those has been observed - the phase center was α(J2000) = $17^{\rm h}20^{\rm m}53.3^{\rm s}$, δ(J2000) = $-35^\circ 46' 59.0''$. The spectrum presented in Fig. C.1 was extracted from a position with coordinates (J2000 $17^{\rm h}20^{\rm m}53.3^{\rm s}$, $-35^\circ 46' 59.0''$), chosen off the bright continuum peak of MM1, to minimize the number of transitions driven into absorption. A detailed first look at the data is presented in McGuire et al. (2018). We present the spectrum here to support the identification of CH_3NH_2 in NGC 6334I, but caution that the excitation conditions and column density in these data at this position are not directly comparable to the Band 7 data discussed in this work. Table C.1 lists the catalogue frequencies and other spectroscopic data for the CH_3NH_2 transitions shown in Fig. C.1.

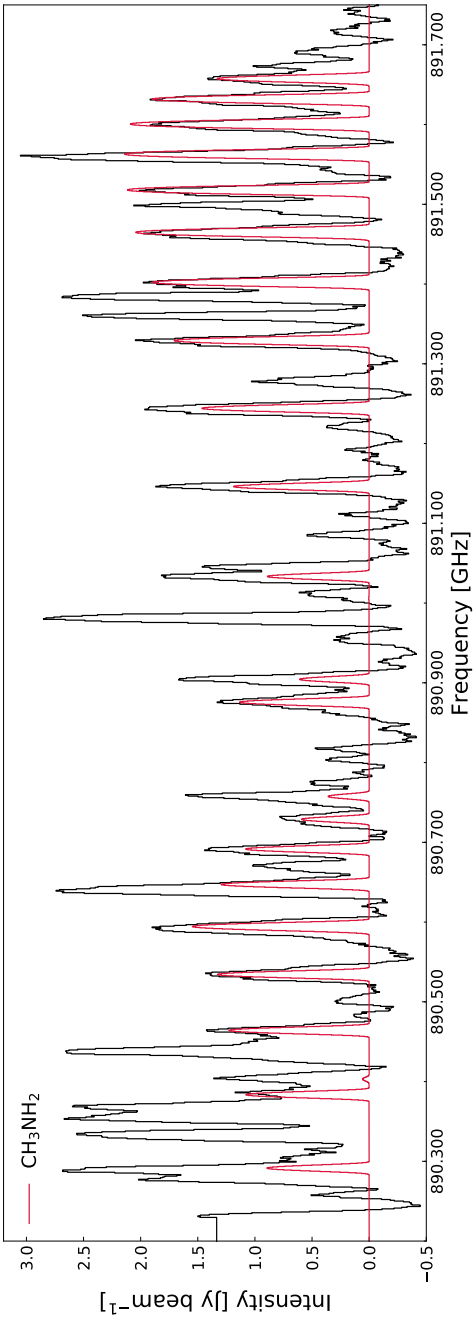

Figure C.1: CH_3NH_2 transitions detected towards NGC 6334I in the range 890.2 to 891.7 GHz (ALMA Band 10). The red line represents the synthetic spectrum of CH_3NH_2 assuming a column density of 2×10^{17} cm^{-2}, an excitation temperature of 100 K and a FWHM line width of 3.2 km s^{-1}, in a $0.''26\times0.''26$ beam (equivalent to the angular resolution of the data). The abscissa is the rest frequency with respect to the radial velocity towards the region (-7 km s^{-1}). The data are shown in black.

Table C.1: Summary of the brightest CH_3NH_2 lines between 890.2 and 891.7 GHz

Transition		Catalogue Frequency	E_{up}	A_{ij}	Catalogue
$[QN]_{up}$	$[QN]_{low}$	[MHz]	[K]	$\times 10^{-4}$ [s^{-1}]	
13 6 E1-1 13	13 5 E1-1 13	890 291.6353	333.72	8.77	(1)
13 6 E1-1 14	13 5 E1-1 14	890 291.7865	333.72	9.61	
13 6 E1-1 12	13 5 E1-1 12	890 291.7981	333.72	8.18	
12 6 E1-1 12	12 5 E1-1 12	890 383.6647	306.08	8.57	
12 6 E1-1 13	12 5 E1-1 13	890 383.8427	306.08	9.39	
12 6 E1-1 11	12 5 E1-1 11	890 383.8576	306.08	8.00	
20 6 B2 20	20 5 B1 21	890 402.2366	589.75	9.80	
20 6 B2 21	20 5 B1 21	890 402.2883	586.75	10.3	
20 6 B2 19	20 5 B1 19	890 402.2909	586.75	9.33	
20 6 B1 20	20 5 B2 21	890 404.2829	589.75	9.80	
20 6 B1 21	20 5 B2 21	890 404.3348	586.75	10.3	
20 6 B1 19	20 5 B2 19	890 404.3374	586.75	9.33	
11 6 E1-1 11	11 5 E1-1 11	890 464.2275	280.56	8.18	
11 6 E1-1 12	11 5 E1-1 12	890 464.4391	280.56	8.97	
11 6 E1-1 10	11 5 E1-1 10	890 464.4584	280.56	7.64	
10 6 E1-1 10	10 5 E1-1 10	890 534.3699	257.17	7.64	
10 6 E1-1 11	10 5 E1-1 11	890 534.6247	257.17	8.57	
10 6 E1-1 9	10 5 E1-1 9	890 534.6502	257.17	6.96	
9 6 E1-1 9	9 5 E1-1 9	890 595.0509	235.9	6.96	
9 6 E1-1 10	9 5 E1-1 10	890 595.3625	235.9	7.81	
9 6 E1-1 8	9 5 E1-1 8	890 595.3973	235.9	6.35	
8 6 E1-1 8	8 5 E1-1 8	890 647.1409	216.76	6.07	
8 6 E1-1 9	8 5 E1-1 9	890 647.5298	216.76	6.96	
8 6 E1-1 7	8 5 E1-1 7	890 647.5788	216.76	5.41	
7 6 E1-1 7	7 5 E1-1 7	890 691.4204	199.74	4.82	
7 6 E1-1 8	7 5 E1-1 8	890 691.9184	199.74	5.53	
7 6 E1-1 6	7 5 E1-1 6	890 691.9903	199.74	4.20	
6 6 E1-1 6	6 5 E1-1 6	890 728.5759	184.85	2.90	
6 6 E1-1 7	6 5 E1-1 7	890 729.5759	184.85	3.49	
6 6 E1-1 5	6 5 E1-1 5	890 729.3469	184.85	2.53	
18 6 B2 18	18 5 B1 18	890 757.4027	503.88	9.61	
18 6 B2 19	18 5 B1 19	890 757.4734	503.88	10.3	
18 6 B1 18	18 5 B2 18	890 758.1200	503.88	9.61	
18 6 B1 19	18 5 B2 19	890 758.1908	503.88	10.3	
11 3 A1 11	10 2 A2 10	890 875.8080	175.87	7.94	
11 3 A1 12	10 2 A2 11	890 875.9815	175.87	8.71	
11 3 A1 10	10 2 A2 9	890 876.0048	175.87	7.24	
17 6 B1 17	17 5 B2 17	890 904.3890	465.64	9.61	
17 6 B1 18	17 5 B2 18	890 904.4711	465.64	10.3	
17 6 B1 16	17 5 B2 16	890 904.4759	465.64	8.97	
17 6 B2 17	17 5 B1 17	890 904.7947	465.64	9.61	
17 6 B2 18	17 5 B1 18	890 904.8768	465.64	10.1	
17 6 B2 16	17 5 B1 16	890 904.8816	465.64	8.97	

Continued on next page

Continued from previous page

Transition		Catalogue Frequency	E_{up}	A_{ij}	Catalogue
$[QN]_{up}$	$[QN]_{low}$	[MHz]	[K]	$\times 10^{-4}$ [s^{-1}]	
16 6 B2 16	16 5 B1 16	891 033.4246	429.50	9.39	
16 6 B2 17	16 5 B1 17	891 033.5198	429.50	10.1	
16 6 B2 15	16 5 B1 15	891 033.5258	429.50	8.97	
16 6 B1 16	16 5 B2 16	891 033.6460	429.50	9.39	
16 6 B1 17	16 5 B2 17	891 033.7412	429.50	10.1	
16 6 B1 15	16 5 B2 15	891 033.7472	429.50	8.97	
15 6 B1 15	15 5 B2 15	891 146.2027	395.48	9.18	
15 6 B1 16	15 5 B2 16	891 146.3132	395.48	9.84	
15 6 B2 15	15 5 B1 15	891 146.3187	395.48	9.18	
15 6 B1 14	15 5 B2 14	891 146.3206	395.48	8.77	
15 6 B2 16	15 5 B1 16	891 146.4292	395.48	9.84	
15 6 B2 14	15 5 B1 14	891 146.4366	395.48	8.77	
14 6 B2 14	14 5 B1 14	891 244.3081	363.58	9.18	
14 6 B1 14	14 5 B2 14	891 244.3661	363.58	9.18	
14 6 B2 15	14 5 B1 15	891 244.4368	363.58	9.84	
14 6 B2 13	14 5 B1 13	891 244.4460	363.58	8.57	
14 6 B1 15	14 5 B2 15	891 244.4948	363.58	9.84	
14 6 B1 13	14 5 B2 13	891 244.5040	363.58	8.57	
13 6 B1 13	13 5 B2 13	891 329.2209	333.82	8.77	
13 6 B2 13	13 5 B1 13	891 329.2483	333.82	8.77	
13 6 B1 14	13 5 B2 14	891 329.3714	333.82	9.61	
13 6 B1 12	13 5 B2 12	891 329.3831	333.82	8.18	
13 6 B2 14	13 5 B1 14	891 329.3989	333.82	9.61	
13 6 B2 12	13 5 B1 12	891 329.4106	333.82	8.18	
12 6 B2 12	12 5 B1 12	891 402.3183	306.18	8.57	
12 6 B1 12	12 5 B2 12	891 402.3306	306.18	8.57	
12 6 B2 13	12 5 B1 13	891 402.4958	306.18	9.39	
12 6 B1 13	12 5 B2 13	891 402.5081	306.18	9.39	
12 6 B2 11	12 5 B1 11	891 402.5107	306.18	8.00	
12 6 B1 11	12 5 B2 11	891 402.5229	306.18	8.00	
11 6 B1 11	11 5 B2 11	891 464.8770	280.66	8.18	
11 6 B2 11	11 5 B1 11	891 464.8820	280.66	8.18	
11 6 B1 12	11 5 B2 12	891 465.0882	280.66	8.97	
11 6 B2 12	11 5 B1 12	891 465.0932	280.66	8.97	
11 6 B1 10	11 5 B2 10	891 465.1075	280.66	7.46	
11 6 B2 10	11 5 B1 10	891 465.1125	280.66	7.46	
10 6 B2 10	10 5 B1 10	891 518.0731	257.26	7.64	
10 6 B1 10	10 5 B2 10	891 518.0750	257.26	7.64	
10 6 B2 11	10 5 B1 11	891 518.3275	257.26	8.57	
10 6 B1 11	10 5 B2 11	891 518.3294	257.26	8.57	
10 6 B2 9	10 5 B1 9	891 518.3531	257.26	6.96	
10 6 B1 9	10 5 B2 9	891 518.3550	257.26	6.96	
9 6 B1 9	9 5 B2 9	891 562.9831	235.99	6.96	
9 6 B2 9	9 5 B1 9	891 562.9838	235.99	6.96	
9 6 B1 10	9 5 B2 10	891 563.2945	235.99	7.81	

Continued on next page

Continued from previous page

Transition		Catalogue Frequency	E_{up}	A_{ij}	Catalogue
$[QN]_{up}$	$[QN]_{low}$	[MHz]	[K]	$\times 10^{-4}$ [s^{-1}]	
9 6 B2 10	9 5 B1 10	891 563.2952	235.99	7.81	
9 6 B1 8	9 5 B2 8	891 563.3294	235.99	6.35	
9 6 B2 8	9 5 B1 8	891 563.3300	235.99	6.35	
8 6 B2 8	8 5 B1 8	891 600.5836	216.85	6.07	
8 6 B1 8	8 5 B2 8	891 600.5838	216.85	6.07	
8 6 B2 9	8 5 B1 9	891 600.9724	216.85	6.96	
8 6 B1 9	8 5 B2 9	891 600.9725	216.85	6.96	
8 6 B2 7	8 5 B1 7	891 601.0213	216.85	5.41	
8 6 B1 7	8 5 B2 7	891 601.0215	216.85	5.41	
7 6 B1 7	7 5 B2 7	891 631.7493	199.83	4.82	
7 6 B2 7	7 5 B1 7	891 631.7493	199.83	4.82	
7 6 B1 8	7 5 B2 8	891 632.2472	199.83	5.66	
7 6 B2 8	7 5 B1 8	891 632.2473	199.83	5.66	
7 6 B1 6	7 5 B2 6	891 632.3190	199.83	4.29	
7 6 B2 6	7 5 B1 6	891 632.3191	199.83	4.29	
6 6 B1 6	6 5 B2 6	891 657.2500	184.94	2.97	
6 6 B2 6	6 5 B1 6	891 657.2500	184.94	2.97	
6 6 B1 7	6 5 B2 7	891 657.9096	184.94	3.49	
6 6 B2 7	6 5 B1 7	891 657.9096	184.94	3.49	
6 6 B1 5	6 5 B2 5	891 658.0209	184.94	2.53	
6 6 B2 5	6 5 B1 5	891 658.0209	184.94	2.53	

Notes. Quantum numbers are J K_a Γ F, following the notation of Motiyenko et al. (2014).

References. (1) Motiyenko et al. (2014)

Appendix D: Methanimine, methyl cyanide and formamide

In this appendix, the detections of CH_2NH, the ^{13}C- and ^{15}N-methyl cyanide isotopologues and NH_2CHO are discussed in detail. The detected lines and best-fit models are shown in Figs. D.1–D.3.

D.1 Methanimine CH_2NH

A single (hyperfine split) transition of CH_2NH is covered by the data. The CH_2NH transition, located at 302.565 GHz, and best-fit synthetic spectrum for each of the regions are included in Fig. D.3. Unfortunately, the CH_2NH feature is situated in the wing of a much stronger transition, located at approximately 302.562 GHz, identified as CH_3OCHO. It should be noted however, that the peak in the data at 302.562 GHz is only partly reproduced by the synthetic spectrum of CH_3OCHO and additional contributions to the peak from other species, which are not included in the JPL or CDMS molecular databases, can therefore not be excluded. Because of this blend, we report only upper limits on the column density of CH_2NH in each of the studied regions. The CH_2NH column densities are $\leq 5.2\times10^{16}$ cm^{-2} assuming $T_{ex} = 215$ K for MM1 II, $\leq 5.0\times10^{16}$ cm^{-2} assuming $T_{ex} = 165$ K for MM2 I and $\leq 10^{15}$ cm^{-2} assuming $T_{ex} = 120$ K for MM3 I.

D.2 Methyl cyanide CH_3CN

There are no transitions of the main CH_3CN isotopologue covered by the observations but six transitions belonging to the ^{13}C- and five transitions belonging to the ^{15}N-methyl cyanide isotopologues are within the data range. Based on these, the column density of the main CH_3CN isotopologue is derived assuming a $^{12}C/^{13}C$ value of 62 and a $^{14}N/^{15}N$ value of 422, both derived assuming d_{GC} = 7.02 kpc and the $^{12}C/^{13}C$ and $^{14}N/^{15}N$ relations presented by Milam et al. (2005) and Wilson (1999), respectively. The detected transitions of both $^{13}CH_3CN$ and $CH_3C^{15}N$ belong to the J = 17→16 series around 303.6 GHz and 303.2 GHz, respectively, and have upper state energies in the range 131 to 310 K. No transitions of the ^{13}C-methyl cyanide isomer $CH_3^{13}CN$ are covered by the data. Figures D.1 and D.2 show the detected methyl cyanide transitions and best-fit models.

MM1 II: In the case of MM1 II, the best-fit methyl cyanide column densities and excitation temperature are 3.4×10^{15} cm^{-2} and 70 K for $^{13}CH_3CN$, respectively, and 3.3×10^{14} cm^{-2} and 110 K for $CH_3C^{15}N$, respectively. For $^{13}CH_3CN$, the uncertainty on N_s and T_{ex} is approximately 30% and 15%, receptively, while for $CH_3C^{15}N$, the approximate uncertainty is 15% and 45%, respectively. The ratio of the column densities of $^{13}CH_3CN$ to $CH_3C^{15}N$ is a factor of 10, higher than the expected value of 6.8 based on the $^{12}C/^{13}C$ and $^{14}N/^{15}N$ relations. Of the six detected transitions belonging to $^{13}CH_3CN$, five are largely uncontaminated by emission from other species and can be assigned distinct peaks in the data. The final transition, located at 303.661 GHz, is blended with a transition of NH_2CHO (to be discussed in detail below). The sum of the best-fit spectra of $^{13}CH_3CN$ and NH_2CHO results in a model with a peak that is ∼45% more intense than the data at 303.661 GHz. Optimising the column density of the $^{13}CH_3CN$ model to fit the blended transition results in underestimated model peak intensities for the remaining $^{13}CH_3CN$ lines with respect to the data. The best-fit column density optimised to the blended line is a factor two lower than the best-fit column density when optimising to all $^{13}CH_3CN$ transitions. In contrast to $^{13}CH_3CN$, the transitions of $CH_3C^{15}N$ are mostly blended and only two of the five transitions, located at 303.228 GHz and 303.257 GHz, can be assigned distinct counterparts in the data. The remaining transitions are blended with transitions of CH_3SH located around 303.187 GHz and 303.276 GHz respectively. Excluding the contribution from CH_3SH to the model does not change the value of the best-fit column density of $CH_3C^{15}N$ but it should be noted that the summed best-fit spectra of $CH_3C^{15}N$ and CH_3SH overshoot the data feature located at 303.276 GHz with approximately 50%.

MM2 I: The best-fit excitation temperature and column density for $^{13}CH_3CN$ in the MM2 I region is 80 K and 1.4×10^{15} cm^{-2}, respectively. For $CH_3C^{15}N$, the excitation is not well contained and therefore the best-fit excitation temperature for $^{13}CH_3CN$ is adopted. For this temperature, the best-fit column density is 1.8×10^{14} cm^{-2}. The uncertainty on N_s and T_{ex} is approximately 30% in the case of $^{13}CH_3CN$ and 20% in the case of $CH_3C^{15}N$. As is the case of MM1 II, a single $^{13}CH_3CN$ line and three $CH_3C^{15}N$ lines are contaminated by emission from NH_2CHO and CH_3SH respectively. However, while the best-fit $^{13}CH_3CN$ column density optimised purely based on the unblended transitions is higher by ∼20% with respect to the value derived when all transitions are included, the best-fit column density of $CH_3C^{15}N$ remains the same. The sum of spectra of $^{13}CH_3CN$ and NH_2CHO results in a model peak which is 15% brighter than the data at the location of the blended $^{13}CH_3CN$ line while including the contribution from CH_3SH to the model of $CH_3C^{15}N$ has only little effect on the summed spectra. The $^{13}CH_3CN$ to $CH_3C^{15}N$ ratio is lower than the ratio derived for MM1 II and has a value of 7.8.

MM3 I: The best-fit methyl cyanide column densities in region MM3 I are lower than for both MM1 II and MM2 I with values of 9×10^{13} cm^{-2} for $^{13}CH_3CN$ and 2.3×10^{13} cm^{-2} for $CH_3C^{15}N$, with excitation temperatures of 90 and 70 K, respectively. The uncertainty on N_s and T_{ex} is approximately 10% and 20%, respectively, for $^{13}CH_3CN$ and 30% and a factor of two, respectively, for $CH_3C^{15}N$. The ratio of the $^{13}CH_3CN$ to $CH_3C^{15}N$ column density is a factor of 3.9, lower than the expected value. For $^{13}CH_3CN$ as well as for $CH_3C^{15}N$, the best-fit column density remains unchanged when contributions from blending species are included.

D.3 Formamide NH_2CHO

While a total of 18 NH_2CHO transitions are covered by the data, only two are bright enough to be detected towards the NGC 6334I region. As discussed above, one of these lines, located at 303.661 GHz, is blended with a transition of $^{13}CH_3CN$. The second transition, located at 303.450 GHz, is also blended but with emission from CH_3SH. Figure D.3 shows the transitions and the best-fit model for each of the regions. In addition to the main NH_2CHO isotopologue, two transitions of $NH_2^{13}CHO$ are within the data range. Transitions belonging to the ^{15}N- and deuterated formamide isotopologues are too weak to be detected.

MM1 II: The synthetic spectrum that best reproduces the NH_2CHO lines detected towards the MM1 II region has a column density of 7.0×10^{15} cm^{-2}, assuming an excitation temperature of 215 K. The uncertainty on N_s is approximately 25%. In Sect. D.2 the NH_2CHO line blended with $^{13}CH_3CN$ was discussed and it was concluded that the sum of the optimised $^{13}CH_3CN$ and NH_2CHO spectra results in a modelled spectrum which overshoots the data by approximately 45%. The second detected NH_2CHO transition is blended with CH_3SH. However, the contribution from this species to the data feature at the location of the NH_2CHO transition is small. Excluding the contribution from CH_3SH to the full spectrum, results in a best-fit NH_2CHO column density which is less than a factor of two higher than the best-fit value which includes the blending species. For $NH_2^{13}CHO$ the best-fit column density is $\leq2.0\times10^{15}$ cm^{-2} assuming an excitation temperature of 215 K. Both the detected transitions of $NH_2^{13}CHO$ are located in the wing of brighter emission lines and therefore, as in the case of CH_2NH, the best-fit model parameters are listed as upper limits only. Neither of the features blended with the $NH_2^{13}CHO$ transitions are reproduced by the modelled spectra of the potential blending species listed in Table E.1.

MM2 I: For region MM2 I the best-fit column densities are 7.6×10^{15} cm^{-2} and $\leq5.0\times10^{14}$ cm^{-2} for NH_2CHO and $NH_2^{13}CHO$ respectively, both assuming an excitation temperature of 165 K. The uncertainty on the column density of NH_2CHO is $\sim$10%. As in the case of MM1 II, both the blended NH_2CHO transitions are slightly overproduced with respect to the data when the modelled spectra of $^{13}CH_3CN$ and other blending species are included in the fit. Excluding these blending species however, only increases the best-fit NH_2CHO column density by 10%. As in the case of MM1 II, the $NH_2^{13}CHO$ column density is listed as an upper limit.

MM3 I: In region MM3 I only the transitions of the main NH_2CHO isotopologue are detected. However, since the data features at the locations of the NH_2CHO transitions can also be reproduced by the respective blending species $^{13}CH_3CN$ and CH_3SH, the detection of NH_2CHO in this region is tentative and its column density reported as an upper limit. The best-fit modelled spectrum of NH_2CHO has a column density of $\leq5.0\times10^{13}$ cm^{-2} assumes an excitation temperature of 120 K.

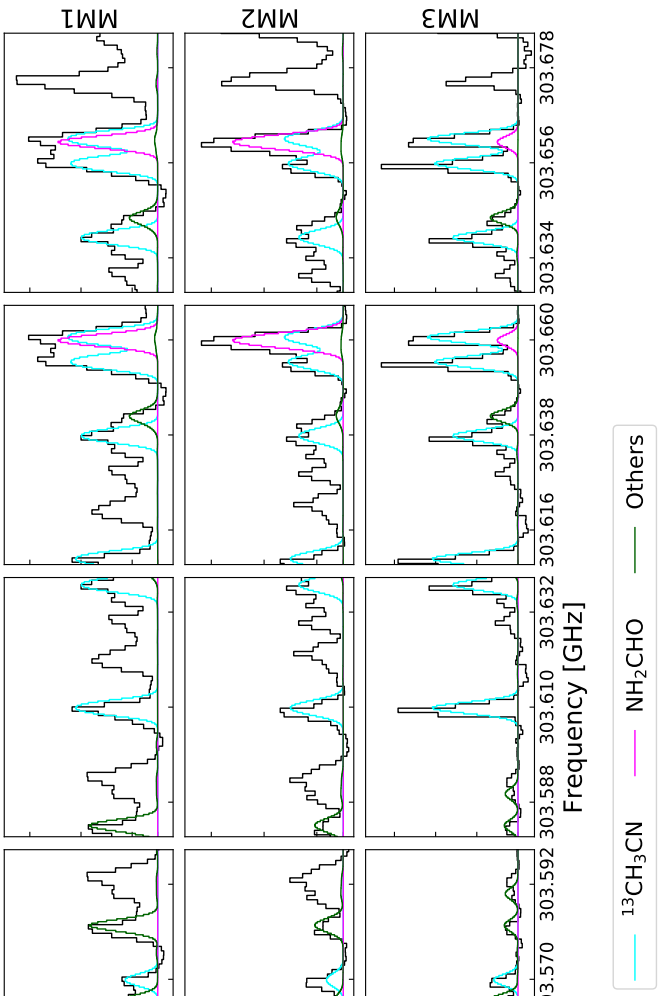

Figure D.1: $^{13}CH_3CN$ transitions detected towards NGC6334I. Turquoise, magenta and green lines represent the synthetic spectrum of $^{13}CH_3CN$ and NH_2CHO and the sum of spectra of other contributing species respectively. The abscissa is the rest frequency with respect to the radial velocity towards each of the hot cores (listed in Table 3.2). The data are shown in black. *Top panels*: MM1 II. *Middle panels*: MM2 I. *Bottom panels*: MM3 I.

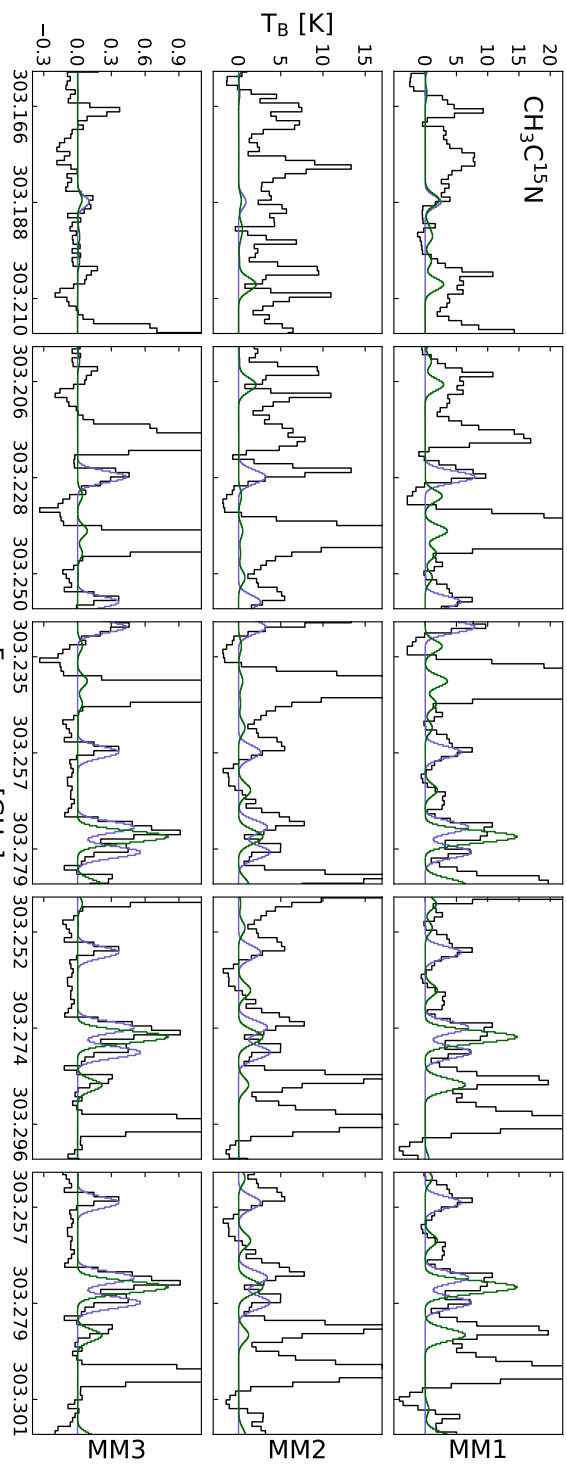

Figure D.2: $CH_3C^{15}N$ transitions detected towards NGC6334I. Blue and green lines represent the synthetic spectrum of $CH_3C^{15}N$ and the sum of spectra of other contributing species respectively. The abscissa is the rest frequency with respect to the radial velocity towards each of the hot cores (listed in Table 3.2). The data are shown in black. *Top panels*: MM1 II. *Middle panels*: MM2 I. *Bottom panels*: MM3 I.

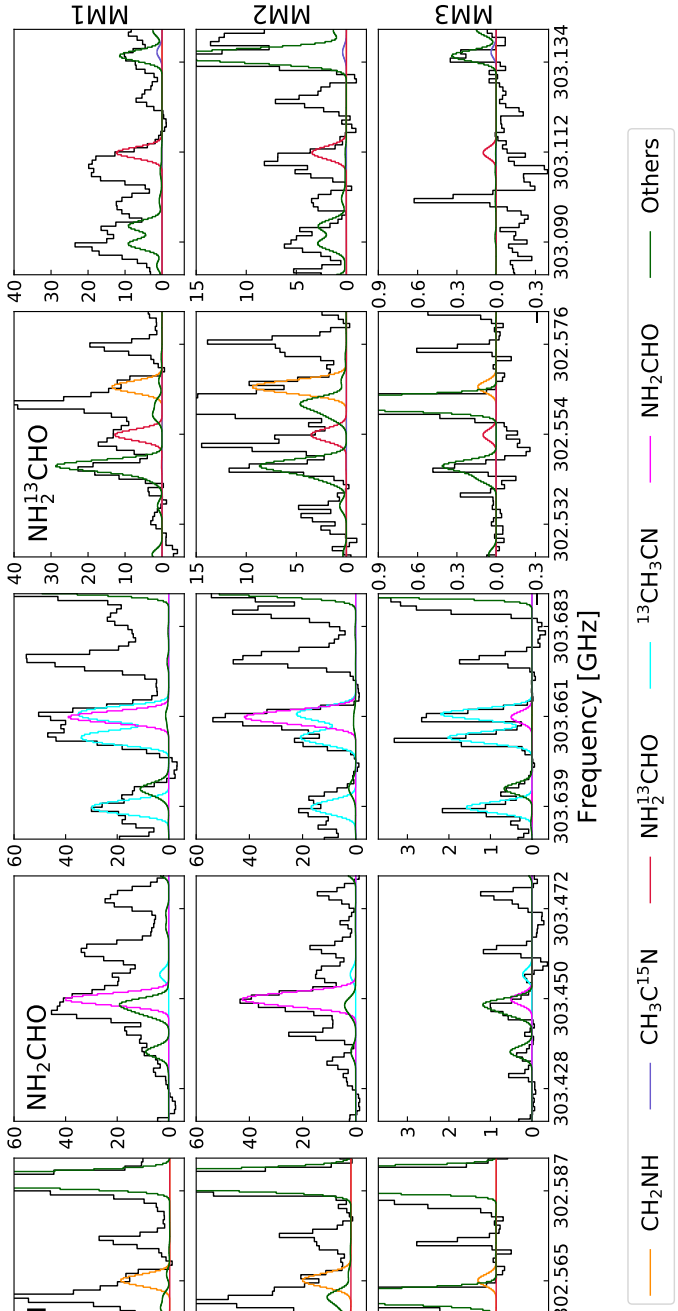

Figure D.3: CH_2NH, NH_2CHO and $NH_2^{13}CHO$ transitions detected towards NGC6334I. Orange, magenta, red and green lines represent the synthetic spectrum of CH_2NH, NH_2CHO and $NH_2^{13}CHO$ and the sum of spectra of other contributing species respectively. The abscissa is the rest frequency with respect to the radial velocity towards each of the hot cores (listed in Table 3.2). The data are shown in black. *Top panels:* MM1 II. *Middle panels:* MM2 I. *Bottom panels:* MM3 I.

Appendix E: Potential blending species

In this appendix, a list of the potential blending species and the column densities and excitation temperatures used to fit them, is present. The species have transitions which overlap in frequency with transitions of CH_3NH_2, CH_2NH, NH_2CHO or the CH_3CN isotopologues and may therefore be contributing to the observed spectrum extracted from each of the studied regions.

Table E.1: Model parameters of potential blending species

Species	Catalogue	MM1 II		MM2 I		MM3 I	
		N_s [cm^{-2}]	T_{ex} [K]	N_s [cm^{-2}]	T_{ex} [K]	N_s [cm^{-2}]	T_{ex} [K]
$^{13}CH_3OH^a$	CDMS	7.4×10^{17}	[215]	6.6×10^{17}	[165]	9.0×10^{16}	[120]
$CH_3^{18}OH^a$	CDMS	2.0×10^{17}	[215]	8.0×10^{16}	[165]	1.4×10^{16}	[120]
C_2H_5OH	JPL	5.0×10^{17}	[215]	2.0×10^{17}	[300]	6.0×10^{15}	[200]
CH_3CH_2OD	CDMS	5.0×10^{15}	[215]	6.0×10^{15}	[165]	6.0×10^{14}	[50]
CH_2DCH_2OH	CDMS	5.0×10^{15}	[215]	3.0×10^{15}	[165]	2.0×10^{14}	[50]
CH_3SH	CDMS	3.0×10^{16}	[215]	$<1.0\times10^{16}$	[165]	1.0×10^{15}	[120]
C_2H_3CN	CDMS	1.0×10^{15}	[215]	$<1.0\times10^{15}$	[165]	–	–
$^{13}CH_2CHCN$	CDMS	8.0×10^{14}	[215]	2.0×10^{14}	[165]	–	–
CH_3COCH_3	JPL	1.5×10^{17}	[215]	2.0×10^{17}	[165]	2.0×10^{15}	[120]
CH_3OCHO	JPL	1.2×10^{17}	[215]	2.5×10^{17}	[165]	9.0×10^{16}	[120]
$HCOCH_2OH$	JPL	3.5×10^{16}	[215]	8.0×10^{15}	[165]	–	–
C_2H_5SH	CDMS	3.0×10^{16}	[215]	4.0×10^{16}	[165]	7.0×10^{14}	[120]
CH_3C_3N	CDMS	1.0×10^{15}	[215]	5.0×10^{14}	[165]	5.0×10^{13}	[120]
C_3H_7CN	CDMS	5.0×10^{15}	[215]	5.0×10^{15}	[165]	–	–

Notes. All models assume θ_s = 1.″0, v_{LSR} = -6.7 km s^{-1} for MM1 II and v_{LSR} = -9.0 km s^{-1} for MM2 I and MM3 I, and FWHM = 3.5 km s^{-1} for MM2 I and FWHM = 3.0 km s^{-1} for MM1 II and MM3 I. N_s is the highest value consistent with the data. $^{(a)}$ Values from Bøgelund et al. (2018)

4

Molecular complexity on disk-scales uncovered by ALMA: The chemical composition of the high-mass protostar AFGL 4176

E. G. Bøgelund, A. G. Barr, V. Taquet,
N. F. W. Ligterink, M. V. Persson,
M. R. Hogerheijde and E. F. van Dishoeck

Submitted to Astronomy & Astrophysics

Abstract

Context. The chemical composition of high-mass protostars reflects the physical evolution associated with different stages of star formation. In addition, the spatial distribution and velocity structure of different molecular species provide valuable information of the physical structure of these embedded objects. However, so far most studies of these sources have been carried out using single-dish telescopes whose limited spatial resolution probe mainly the large-scale structure of the objects.
Aim. The molecular inventory of the forming high-mass star AFGL 4176, located at a distance of ∼3.7 kpc, is studied in detail at high angular resolution of ∼0.35″, equivalent to ∼1285 au at the distance of AFGL 4176. This high resolution makes it possible to separate the emission associated with the inner hot envelope and disk around the forming star from that of its cool outer envelope. The composition of AFGL 4176 is compared with other, both high- and low-mass sources, and placed in the broader context of star-formation.
Methods. Using the Atacama Large Millimeter/submillimeter Array (ALMA) the chemical inventory of AFGL 4176 is characterised. The high sensitivity of ALMA makes it possible to identify weak and optically thin lines and allows for many isotopologues to be detected, providing a more complete and accurate inventory of the source. For the detected species, excitation temperatures in the range 120–320 K are determined and column densities are derived assuming LTE and using optically thin lines. The spatial distribution of a number of species is studied.
Results. A total of 354 lines is identified towards AFGL 4176 with a signal-to-noise ratio of three or higher. Of these lines, 324 can be assigned to 23 different molecular species and their isotopologues. The most abundant species is methanol (CH_3OH) with a column density of 5.5×10^{18} cm^{-2} in a beam of ∼0.3″, derived from its ^{13}C-isotopologue. The remaining species are present at levels between 0.003 % and 15 % with respect to methanol. Hints that N-bearing species peak slightly closer to the location of the peak continuum emission than the O-bearing species are seen. A single species, propyne (CH_3C_2H), displays a double-peaked distribution.
Conclusions. AFGL 4176 comprises a rich chemical inventory including many complex species present on disk-scales. On average, the derived column density ratios with respect to methanol of O-bearing species are higher than those derived for N-bearing species by a factor of three. This may indicate that AFGL 4176 is a relatively young source since nitrogen chemistry generally takes longer to evolve in the gas-phase. Taking methanol as a reference, the composition of AFGL 4176 more closely resembles that of the low-mass protostar IRAS 16293–2422B than that of high-mass star-forming regions located near the Galactic centre. This similarity indicates that the production of complex species does not depend strongly on the luminosity of sources, but may be universal despite differences in physical conditions, or that the composition of species is set already in the ice during the cold cloud stage.

4.1 Introduction

The molecular composition of a star-forming region can be used to probe the physical conditions of its environment, define its evolutionary stage, identify chemical processes and in addition, sets the stage and starting conditions for chemistry in disks and eventually planetary systems. A large number of molecular species, ranging from simple to complex, that is molecules consisting of six or more atoms, have been identified in various interstellar environments, from giant molecular clouds to dense cores, protostars and protoplanetary disks (see reviews by Herbst & van Dishoeck, 2009; Caselli & Ceccarelli, 2012; Tielens, 2013; Sakai & Yamamoto, 2013). In context to the formation of high- and low-mass stars, the hot core or hot corino stage displays a particular rich chemistry. At this stage, the young protostar heats its surroundings and creates a bubble of warm ($\sim$200 K) gas, enriched in complex molecules. This complexity is a result of chemistry in the warm gas combined with thermal desorption of the icy mantles of dust grains (e.g. Charnley et al., 1992).

Over the last decades, many surveys, mostly using single-dish telescopes, have been undertaken to investigate the chemical complexity of high-mass hot cores (e.g. Blake et al., 1987; Hatchell et al., 1998; van der Tak et al., 2000; Ikeda et al., 2001; Bisschop et al., 2007; Isokoski et al., 2013; Suzuki et al., 2018). Much focus has been on the hot cores associated with Orion and Sagittarius B2 (hereafter Sgr B2), famous for their high abundances of complex molecules (see e.g. Neill et al., 2014; Crockett et al., 2014, and references therein), although recently, the low-mass counterparts of these sources have also been under investigations (e.g. Schöier et al., 2002; Cazaux et al., 2003; Bottinelli et al., 2004). A wealth of information on the chemistry associated with hot cores has been provided by these observations, although most are limited by the, in general, large beam sizes of single-dish telescopes. The consequence hereof is that observations do not only sample the hot core, but also the surrounding environments associated with the protostar, such as the large-scale envelope or outflows (e.g. Fayolle et al., 2015). Generally, this results in multi-component molecular emission, where each component may be characterised by a different line width, velocity, excitation temperature and column density. Furthermore, beam dilution effects may result in large uncertainties on derived molecular column densities if not accounted for correctly.

The emergence of interferometers such as the Submillimeter Array (SMA), the NOrthern Extended Millimeter Array (NOEMA) and, in particular, the Atacama Large Millimeter/submillimeter Array (ALMA), which provide much higher spatial resolutions than single-dish telescopes, has made it possible to study the molecular emission associated with hot cores on much smaller scales than were previously accessible. This means, that for the first time, an opportunity to "look into" the hot cores themselves is provided whereby the challenges of many single-dish studies can be overcome. In addition, the unprecedented sensitivity of ALMA has made possible the detection of a wealth of weak lines ensuring a more accurate characterization of the chemistry associated with the cores.

To date, the chemical inventory of only a handful of sources has been extensively studied with interferometers. These include the low-mass protobinary system IRAS 16293–2422 (hereafter IRAS 16293, Jørgensen et al., 2016) and the high-mass star-forming regions associated with Sgr B2(N) (Belloche et al., 2016) and Orion KL (Pagani et al., 2017). Therefore, there is a substantial need for the continued investigation of additional hot cores in order to build up a database of the molecular inventories and temperatures characterising these sources. Such a database will provide the statistics needed for new insights into the physical and chemical processes at play during the formation of hot cores

and will help the classification of sources according to evolutionary stage.

To this end, the high-mass hot core of AFGL 4176 has been investigated with ALMA and for the first time, a comprehensive study of the chemical inventory of the source is presented. The results of this work are compared with other high- and low-mass sources, in addition to the predictions of hot core chemical models.

4.1.1 AFGL 4176

AFGL 4176, located in the southern hemisphere at $13^{h}43^{m}01.704^{s}$, $-62°08'51''.23$ (ICRS J2000), was first identified by Henning et al. (1984) through its bright infrared spectrum as a young and massive star embedded in a thick dusty envelope. The source has been further characterised by Beltrán et al. (2006), who used large-scale millimetre continuum observations carried out with the Swedish-ESO Submillimetre Telescope (SEST), to identify a compact core of approximately 1120 $M_{\odot}$ with a diameter of 1 pc and luminosity of $2{\times}10^{5}$ $L_{\odot}$ (assuming a distance of 5.3 kpc). It should be noted however, that the distance to AFGL 4176 is not well-constrained and cited values range from 3.5 to 5.3 kpc (see, Boley et al., 2012, and references therein), with the most frequently cited distance being 4.2 kpc, based on observations of CH_3OH masers (Green & McClure-Griffiths, 2011). However, in this work we will assume a distance of 3.7 kpc, based on the recent second release of *Gaia* data, which places the source at a distance of $3.7^{+2.6}_{-1.6}$ kpc (Bailer-Jones et al., 2018).

In addition to the large-scale envelope, strong evidence that the system contains a Keplerian-like disk is presented by Johnston et al. (2015) who use observations of CH_3CN obtained with ALMA to trace the disk kinematics on scales of ∼1200 au. A disk-like structure is consistent with the models reported by Boley et al. (2012) who combine interferometric and photometric observations of AFGL 4176 and use radiative transfer and geometric models to characterise the source. Although the observations are generally well described by one-dimensional models, Boley et al. (2012) find substantial deviations from spherical symmetry at scales of tens to hundreds of astronomical units. On these scales, the observations are better described by a multi-component model consisting of a Gaussian halo and an inclined circumstellar disk. Knots of shocked H_2 emission have also been identified around AFGL 4176, potentially indicating an outflow, though no preferred spatial direction was revealed (De Buizer, 2003).

A limited number of detections of molecular species have been reported towards AFGL 4176. CO_2 and H_2O have been identified in observations carried out with the *Infrared Space Observatory* (van Dishoeck et al., 1996; van Dishoeck & Helmich, 1996; Boonman et al., 2003) and detections of CO, NH_3 and CH_3CN by the Atacama Pathfinder Experiment (APEX) and ALMA have been reported by Johnston et al. (2014, 2015). In addition, a number of CH_3OH masers are reported in the vicinity of the source (Phillips et al., 1998; Green & McClure-Griffiths, 2011). However, so far no reports of a more comprehensive chemical inventory of the source exist.

This paper presents an extensive study of the molecular species detected towards AFGL 4176, in addition to those previously reported. The work is based on the same set of high sensitivity, high resolution ALMA observations as analysed by Johnston et al. (2015), but focuses on identifying and characterising all molecular species with transitions in the observed frequency range associated with the source, rather than the disk kinematics. The high sensitivity of ALMA makes it possible to identify weak and optically thin lines while the unique spatial resolving power ensures that the analysed emission stems from the disk around the central forming star rather than the large-scale surrounding envelope.

The structure of the paper is as follows: Sect. 4.2 introduces the observations, calibration process and methods used for identifying molecular species. Section 4.3 lists all detected species, our derived molecular column densities and excitation temperatures and discusses the spatial distribution of selected molecules. Section 4.4 compares the results for AFGL 4176 with observations of other objects and with model predictions. Finally, Sect. 4.5 summaries the results and conclusions.

4.2 Observations and methods

4.2.1 Observations

Observations of AFGL 4176 were carried out with ALMA during Cycle 1 (program 2012.1.00469.S, see Johnston et al., 2015, for first results) with 39 antennas in the array, between August 16, 2014 and August 17, 2014 using the Band 6 receivers, covering the frequency range of 211 – 275 GHz. Four spectral windows were obtained covering a total bandwidth of ∼4.7 GHz. These consist of two wide windows, of 1875 MHz, centred at 240.5 and 254.0 GHz and two narrow windows, of 468.75 MHz, centred at 239.0 and 256.3 GHz. The spectral resolution of the observations is 976.6 kHz (∼1.2 km s^{-1}) and 244 kHz (∼0.3 km s^{-1}) for the wide and narrow windows, respectively. The angular resolution is ∼0.35″, equivalent to ∼1285 au at the distance of AFGL 4176.

The data were downloaded from the ALMA archive and reduced via the delivered pipeline script using the Common Astronomy Software Applications (CASA) version 4.2.1. Bandpass and absolute flux calibration was carried out, respectively, using J1617-5848 and Titan, on August 16 and J1427-4206 and Ceres on August 17. The phase and gain calibration was carried out, respectively, using J1308-6707 and J1329-5608 on both days. The uncertainty on the flux calibration is estimated to be ≤20%. The data were continuum subtracted using the most line-free channels and corrected for primary beam attenuation.

The continuum and line data were imaged separately in CASA version 5.1.1-5 using a pixel size of 0.04″, a velocity resolution for the spectral cubes of 1.2 km s^{-1} and Briggs weighting with a robust parameter of 1.5. The peak continuum emission is 29 mJy beam^{-1} (5.7 K at 247 GHz) with an rms noise of approximately 0.5 mJy beam^{-1} (0.1 K at 247 GHz) in a beam of 0.″33×0.″31. The coordinates of the continuum peak were determined by 2D Gaussian fitting in the image plane to be $13^{h}43^{m}01.699^{s}$, $-62°08'51.''249$ (IRCS J2000). Table 4.1 lists the frequencies covered and the rms noise per 1.2 km s^{-1} channel derived for each of the spectral windows.

For each of the imaged cubes, a spectrum is extracted at the location of the peak continuum emission. Each spectrum represents the average over an area equivalent to the size of the synthesised beam (∼0.″3). Figure 4.1 shows the continuum and the location at which the spectra were extracted. In addition to the main continuum peak, labelled mm1 by Johnston et al. (2015), a secondary peak is observed ∼1″ north-west of the primary peak; this peak is labelled mm2. A counterpart to this secondary peak is observed to the south-east of mm1 (outside the plotted region). These two peaks are located perpendicular to the major axis of mm1 and may indicate a large-scale outflow, consistent with the CO observations presented by Johnston et al. (2015). For this work however, the focus is on the main continuum peak and all subsequent discussion refers to this source only.

Table 4.1: Overview of spectral cubes

Frequency	Beam	rms noise	
[GHz]	[″ × ″ (P.A.°)]	[mJy beam^{-1}]	[K]
238.838 – 239.306	0.″35×0.″29 (-31.6)	1.9	0.40
239.604 – 241.478	0.″34×0.″30 (-31.2)	1.5	0.31
253.107 – 254.980	0.″33×0.″28 (-30.8)	1.7	0.35
256.115 – 256.583	0.″32×0.″28 (-32.3)	2.2	0.46

Notes. The listed rms noise is determined over the line-free channels. The channel width is 1.2 km s^{-1}.

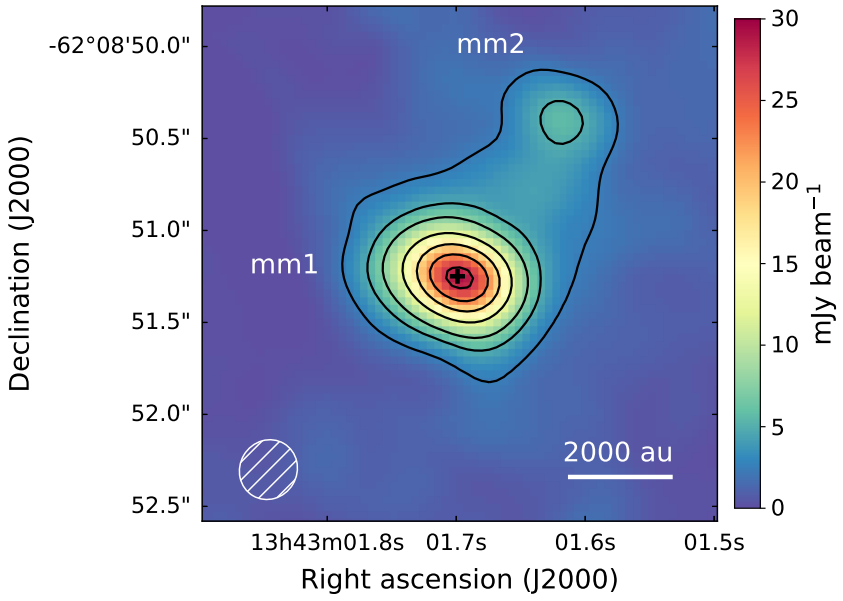

Figure 4.1: Continuum image of AFGL 4176 at 1.2 mm. Contours are [5, 10, 15, 25, 35, 45, 55]σ, with σ = 0.5 mJy beam^{-1}. The peak continuum location at which the spectra have been extracted is marked by the black cross. The synthesised beam (0.″33×0.″31 ∼1210×1140 au) is shown in the bottom left corner.

4.2.2 Methods for line identification and modelling

For the identification of spectral lines, catalogued transition frequencies from the JPL (Jet Propulsion Laboratory[1], Pickett et al., 1998) and CDMS (Cologne Database for Molecular Spectroscopy[2], Müller et al., 2001, 2005) molecular databases are compared with the extracted spectra. Observed lines are considered detected if the peak signal-to-noise ratio is three or higher. Species with fewer than five detected lines are considered tentative detections. Using the CASSIS[3] line analysis software and assuming local thermodynamic equilibrium (LTE) and optically thin lines, a synthetic spectrum is produced for each identified species. This is done by providing CASSIS with the following parameters: excitation temperature, $T_{\rm ex}$ [K], column density of the species, $N_{\rm s}$ [cm^{-2}], source velocity, $v_{\rm LSR}$ [km s^{-1}], line width at half maximum [km s^{-1}], and angular size of the emitting region (assumed to be equal to the area of the synthesised beam), $\theta_{\rm s}$ [$''$].

For two species, CH_3CN and HC_3N, vibrationally excited transitions are detected (see Sect. 4.3). For vibrationally excited CH_3CN the JPL database is used. This entry utilises a partition function in which vibrational contributions are taken into account. In contrast, the CDMS entries for vibrationally excited HC_3N, and isotopologues hereof, do not include vibrational contributions but list these separately. Therefore, vibrational correction factors of 1.17 and 1.48 for the main and ^{13}C-isotopologues of HC_3N, respectively, have been applied to all listed values.

Excitation temperatures and column densities are determined for species which have three or more unblended lines detected, that is lines with a signal-to-noise ratio of three or higher, whose emission can mainly be attributed to one molecule, and these span upper state energies of at least 100 K. This is done by creating grids of models varying $T_{\rm ex}$ and $N_{\rm s}$ and identifying the model with the minimal χ^2 as the best fit. The models are optimised to fit all unblended lines detected for each species. Table A.1 lists the model grids for each of the fitted species. The uncertainty on $T_{\rm ex}$ and $N_{\rm s}$ is listed as the standard deviation of models within the 95% confidence level. For most species these are about 20%, though for CH_3CHO and $(CH_2OH)_2$ the uncertainty on $T_{\rm ex}$ is up to 85%. The uncertainty on column density ratios with respect to methanol is calculated through the propagation of errors. For species where less than three unblended lines are detected, or species where upper state energies of the detected lines do not span more than 100 K, the column density is derived assuming a fixed excitation temperature. In the case of CH_3OH and the isotopologues of SO_2, the excitation temperature is assumed to be 120 K and 150 K, based on the ^{13}C-methanol isotopologue and main isotopologue of SO_2, respectively. For all other species, the excitation temperature is assumed to be 200 K. This value is the average of the best-fit excitation temperatures derived for the 12 species listed at the top of Table 4.2. However, since the spread in best-fit excitation temperatures in fairly large, standard deviation of $\sim$70 K, column densities are also derived assuming excitation temperatures of 130 K and 270 K. For all species but CH_3COCH_3, the column densities derived at these temperatures are within 50% of the value derived assuming $T_{\rm ex}$ = 200 K. For CH_3COCH_3, column densities at 130 K and 270 K are within a factor of three of the value derived assuming $T_{\rm ex}$ = 200 K.

To ensure that no lines are incorrectly assigned, three checks are conducted. First, that the best-fit model for each species does not predict lines at frequencies, covered by the observations, where no emission is detected. Second, that no other species, for which

[1] http://spec.jpl.nasa.gov

[2] http://www.ph1.uni-koeln.de/cdms/

[3] Centre d'Analyse Scientifique de Spectres Instrumentaux et Synthétiques; http://cassis.irap.omp.eu

the spectroscopy is known and listed in either of the databases mentioned above, can reproduce the line without predicting lines at frequencies where no emission is detected. Finally, that isotopically rare species do not predict lines of the main isotopologue where no emission is detected.

The excitation temperatures and column densities for $^{13}CH_3OH$ and CH_3CN are derived first because their lines are very numerous, bright and span a large range of upper state energies. Based on fits to these species, a source velocity of -53.5 km s^{-1} and FWHM line widths of 6 km s^{-1} are found. These values are kept fixed for the subsequent fitting of other species.

Finally, in order to compare the derived molecular column densities across different objects, CH_3OH is used as a reference. Methanol is used as a reference because it is usually one of the most abundant species in hot cores and is thought to be the parent molecule for most complex organics. However, because this species is very abundant, many of its lines are optically thick and therefore its column density cannot be derived directly. The column density of CH_3OH is instead estimated based on the best-fit value for its ^{13}C-isotopologue, adopting a $^{12}C/^{13}C$ values of 60, derived assuming a galactocentric distance (d_{GC}) of 6.64 kpc and the relation for $^{12}C/^{13}C$ reported by Milam et al. (2005).

4.3 Results

A total of 354 lines are identified towards AFGL 4176 with a signal-to-noise ratio of three or above. Of these, 324 lines can be assigned to a total of 23 different molecular species or their isotopologues. Fifteen species have five or more detected transitions while eight species have fewer than five detected transitions and are therefore considered tentative detections. For the remaining 30 lines no match to known transitions was found. A list of frequencies and peak intensities for these unidentified lines is given in Appendix B. With a total covered bandwidth of $\sim$4.7 GHz, the line density is roughly 75 lines per GHz or one line per 13.3 MHz (ALMA Band 6). For comparison, the ALMA-PILS survey towards the low-mass protobinary system IRAS 16293 found one line per 3.4 MHz (ALMA Band 7, Jørgensen et al., 2016).This high density means that detected lines are often blended with emission from other species. Therefore, as noted above, great caution is exercised when lines are assigned to species.

Table 4.2 list all identified species, isotopologues and isomers. The Table also summarises the number of identified lines, both unblended and blended, the range of upper state energies and Einstein A coefficients covered by these lines as well as the derived excitation temperature and column density for each species. It should be noted that hyperfine transitions with the same catalogued frequency are counted as a single line since these are indistinguishable in the data. After the identification and modelling of individual species the synthetic spectra are summed to obtain a full model for AFGL 4176. Figure 4.2 shows the full model for the spectral window centred at 239.1 GHz (see Appendix C for full model of other spectral windows).

The derived excitation temperatures range between 120 and 320 K with an average of 200 K, consistent with the range of temperatures derived for CH_3CN by Johnston et al. (2015). The highest column density is 5.5×10^{18} cm^{-2}, derived for CH_3OH (based on $^{13}CH_3OH$ and corrected with the $^{12}C/^{13}C$ ratio), while the lowest values is 1.8×10^{14} cm^{-2}, derived for $HC_3^{15}N$. While these column densities span more than four orders of magnitude, the majority of species have column densities between 10^{16} and 10^{17} cm^{-2}. The species with the highest number of detected lines, 41 in total, is CH_3OH.

Table 4.2: Summary of detected lines and derived values of N_s and T_{ex}

Species	Name	N_{lines}			E_{up}	A_{ij}	Catalogue	N_s	T_{ex}	X/CH_3OH
		Unblended	Blended	Total	[K]	$\times10^{-5}$ [s^{-1}]		[cm^{-2}]	[K]	[%]
$^{13}CH_3OH$	Methanol	7	5	12	60 – 644	2.31 – 8.81	CDMS	$(9.2 \pm 0.6)\times10^{16}$	120 ± 15	1.67 ± 0.16
CH_3C_2H	Propyne	9	1	10	86 – 346	3.85 – 5.83	CDMS	$(3.8 \pm 0.7)\times10^{16}$	320 ± 90	0.69 ± 0.14
CH_3CN	Methyl cyanide (Acetonitrile)	9	0	9	80 – 537	73 – 118	JPL	$(3.4 \pm 0.3)\times10^{16}$	270 ± 40	0.62 ± 0.07
CH_3CN, v_8=1		14	2	16	600 – 955	94 – 111	JPL	$(4.3 \pm 0.6)\times10^{16}$	220 ± 40	0.78 ± 0.12
CH_3CHO	Acetaldehyde	4	4	8	93 – 490	3.85 – 56.3	JPL	$(1.5 \pm 0.8)\times10^{16}$	160 ± 125	0.27 ± 0.15
NH_2CHO	Formamide	10	3	13	68 – 439	2.48 – 115	CDMS	$(1.0 \pm 0.09)\times10^{16}$	190 ± 35	0.18 ± 0.02
H_2CS		7	1	8	46 – 519	5.43 – 20.5	CDMS	$(4.3 \pm 0.2)\times10^{16}$	160 ± 10	0.78 ± 0.07
CH_3OCH_3	Methyl ether	17	5	22	26 – 502	2.40 – 8.72	CDMS	$(1.3 \pm 0.1)\times10^{17}$	160 ± 15	2.36 ± 0.25
C_2H_5OH	Ethanol	7	4	11	35 – 450	1.93 – 41	JPL	$(8.7 \pm 1.2)\times10^{16}$	120 ± 25	1.58 ± 0.25
C_2H_3CN	Vinylcyanide	8	4	12	153 – 388	114 – 136	CDMS	$(6.2 \pm 1.1)\times10^{15}$	240 ± 105	0.11 ± 0.02
CH_3OCHO	Methyl formate	14	5	19	101 – 473	0.66 – 24.8	JPL	$(1.7 \pm 0.3)\times10^{17}$	310 ± 75	3.09 ± 0.59
aGg'$(CH_2OH)_2$	Ethylene glycol	14	16	30	144 – 327	3.76 – 40.9	CDMS	$(3.0 \pm 0.5)\times10^{16}$	160 ± 130	0.55 ± 0.10
gGg'$(CH_2OH)_2$		12	8	20	62 – 229	2.93 – 14.3	CDMS	$(2.6 \pm 0.6)\times10^{16}$	140 ± 120	0.47 ± 0.11
SO_2	Sulphur dioxide	6	0	6	36 – 333	2.67 – 13.3	JPL	$(8.1 \pm 1.9)\times10^{17}$	150 ± 30	14.7 ± 3.6
CH_3OH		31	10	41	20 – 950	1.56 – 8.80	JPL	$[(5.5 \pm 0.4)\times10^{18}]^a$	[120]	≡100
H_2CCO	Ketene	1	0	1	88	15.5	CDMS	$(9.2 \pm 1.5)\times10^{15}$	[200]	0.17 ± 0.03
HNCO	Isocyanic acid	1	0	1	113	19.0	CDMS	$(6.2 \pm 1.3)\times10^{16}$	[200]	1.13 ± 0.25
NS	Nitrogen sulphide	4	2	6	39	0.93 – 28.4	JPL	$(1.2 \pm 0.1)\times10^{16}$	[200]	0.22 ± 0.02
$C^{34}S$	Carbon sulphide	1	0	1	35	28.6	JPL	$(8.1 \pm 1.6)\times10^{15}$	[200]	0.15 ± 0.03
t-HCOOH	Formic acid	1	1	2	70	15.7	CDMS	$(4.3 \pm 0.6)\times10^{16}$	[200]	0.78 ± 0.12
SO	Sulphur monoxide	1	0	1	100	0.43	JPL	$(7.0 \pm 1.5)\times10^{17}$	[200]	12.7 ± 2.9
^{34}SO		1	0	1	56	20.4	JPL	$(1.8 \pm 0.5)\times10^{16}$	[200]	0.33 ± 0.1
HC_3N, v=0	Cyanoacetylene	1	0	1	177	132	CDMS	$(6.2 \pm 2.2)\times10^{15}$	[200]	0.11 ± 0.04
HC_3N, v_7=2		1	2	3	820 – 823	132 – 133	CDMS	$(2.5 \pm 0.6)\times10^{16}{}^b$	[200]	0.45 ± 0.11
$HCC^{13}CN$		1	0	1	177	130	CDMS	$(3.8 \pm 0.8)\times10^{14}$	[200]	0.007 ± 0.002
$HCCC^{15}N$		1	0	1	184	134	CDMS	$(1.8 \pm 0.4)\times10^{14}$	[200]	0.003 ± 0.001
$HCC^{13}CN$, v_7=1		2	0	2	495 – 496	130 – 131	CDMS	$(8.1 \pm 1.2)\times10^{14}{}^c$	[200]	0.01 ± 0.002
C_2H_5CN	Ethyl cyanide (Propionitrile)	9	4	13	79 – 189	6.22 – 142	CDMS	$(6.4 \pm 0.8)\times10^{15}{}^d$	[200]	0.12 ± 0.02
CH_3COCH_3	Acetone	13	2	15	74 – 235	2.43 – 659	JPL	$(5.3 \pm 0.5)\times10^{16}{}^d$	[200]	0.96 ± 0.11
$CH_2(OH)CHO$	Glycolaldehyde	2	1	3	111 – 143	12.0 – 27.9	CDMS	$\leq1.1\times10^{16}{}^e$	[200]	≤0.2
$O^{13}CS$	Carbonyl sulphide	1	0	1	134	4.80	CDMS	$(5.5 \pm 0.7)\times10^{15}$	[200]	0.10 ± 0.01
$^{33}SO_2$		10	8	18	72 – 471	0.13 – 19.6	JPL	$(1.3 \pm 0.8)\times10^{16}{}^d$	[150]	0.24 ± 0.15
$^{34}SO_2$		1	1	2	82 – 182	2.66 – 12.8	JPL	$(8.1 \pm 1.8)\times10^{16}$	[150]	1.47 ± 0.34
$SO^{18}O$		1	2	3	69 – 89	0.11 – 18.3	JPL	$(7.6 \pm 1.0)\times10^{15}$	[150]	0.14 ± 0.02

Notes. Values in square brackets are fixed. $^{(a)}$ Based on $^{13}CH_3OH$, assuming a $^{12}C/^{13}C$ ratio of 60. $^{(b)}$ Includes the vibrational correction factor of 1.17. $^{(c)}$ Includes the vibrational correction factor of 1.48. $^{(d)}$ Column density derived assuming fixed T_{ex} due to insufficient range of E_{up} of unblended lines. $^{(e)}$ Upper limit due to low signal-to-noise.

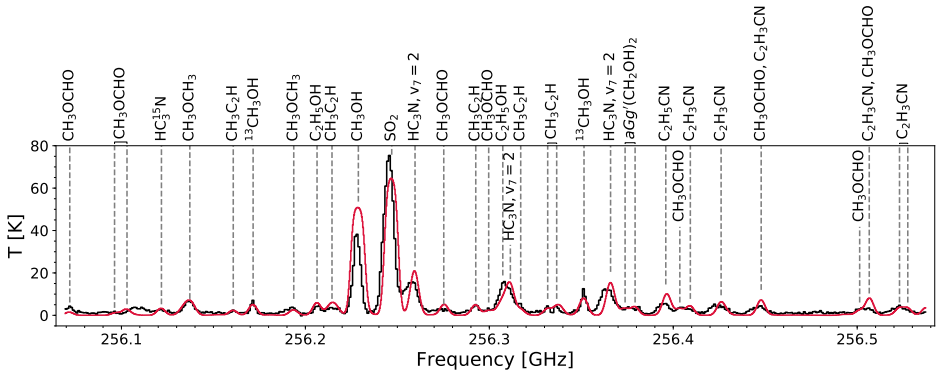

Figure 4.2: Full model (red), i.e., the sum of synthetic spectra, for all species detected towards AFGL 4176 in the spectral window centred at 256.3 GHz. Frequencies are shifted to the rest velocity of the region. The data are shown in black.

These lines also span the largest range of upper state energies ranging from 20 to 950 K. Similarly, the range of upper state energies of the ^{13}C-isotopologue of methanol span 60 to 640 K, though only twelve lines associated with this isotopologue are detected. For the remaining species, the number of detected lines range from a single line up to 30 lines in the case of *aGg'*$(CH_2OH)_2$, though it should be noted that more than half of these are blended with emission from other species. On average the upper state energies of species span a range of 300 K.

By far the highest column density ratios with respect to methanol are derived for SO_2 and SO with values of 14.7% and 12.7%, respectively. The remaining species have column density ratios with respect to methanol ranging between 0.003% and 3%, with most species showing ratios of the order of 0.1%. On average, the column density ratios derived for O-bearing species are a factor of three higher than those derived for N-bearing species. This trend will be further discussed in sect. 4.4.

Vibrationally excited transitions are detected for two species, CH_3CN and HC_3N. In both cases, the column density ratio derived from the vibrationally excited transitions are higher than those derived for the ground-state vibrational transitions; 0.78% vs 0.62% for CH_3CN/CH_3OH and 0.45% vs 0.11% for HC_3N/CH_3OH. Note that for the latter species only one and three lines are detected for the ground and vibrationally excited states respectively. That the column densities derived based on the vibrationally excited states are higher than those derived from the ground-state vibrational transitions is most likely not representative of the actual distribution of molecules but rather due to the fact that the vibrationally excited transitions are excited via shocks or infrared pumping and therefore not in LTE. The column densities derived from these transitions can therefore not be trusted.

4.3.1 Upper limit on the column density of glycolaldehyde

A number of transitions of glycolaldehyde are covered by the data although only three of these lines, one of which is blended, are considered detected. These lines have signal-to-noise ratios of approximately four. The remaining lines identified as likely to be due to

Table 4.3: Summary of isotopologues with only blended lines

Species	N_{lines}			E_{up}	A_{ij}	Catalogue	N_s	T_{ex}
	Unblended	Blended	Total	[K]	$\times10^{-5}$ [s^{-1}]		[cm^{-2}]	[K]
$CH_3^{13}CN$	0	6	6	80 – 259	100 – 118	JPL	[5.7×10^{14}]^a	[270]
$HC^{13}CCN$	0	1	1	177	130	CDMS	[3.8×10^{14}]	[200]
$H^{13}CCCN$, v_7=1	0	2	2	479 – 503	108 – 133	CDMS	[8.1×10^{14}]	[200]
$HC^{13}CCN$, v_7=1	0	2	2	493	130 – 131	CDMS	[8.1×10^{14}]	[200]

Notes. Values in square brackets are fixed. $^{(a)}$ Based on CH_3CN, assuming a $^{12}C/^{13}C$ ratio of 60.

glycolaldehyde, five in total, are detected with signal-to-noise ratios of between two and three and are therefore not included in the line list in Table 2.2. Due to the generally low signal-to-noise of the glycolaldehyde lines, we report an upper limit column density for this species. The upper limit is derived based on the two unblended lines and assumes an excitation temperature of 200 K. The column density upper limit is $\leq1.1\times10^{16}$ cm^{-2}, equivalent to $\leq$0.2% with respect to methanol.

The formation pathway of glycolaldehyde has recently been investigated in the laboratory by Chuang et al. (2017). They find that the relative abundance of this and other complex species, can be used as a diagnostic tool to derive the processing history of the ice in which the species formed. In particular, the ratio of glycolaldehyde to ethylene glycol provides a good handle on distinguishing ices processed purely by atom-addition (hydrogenation), ices processed purely by UV irradiation or ice processed by both. In the case of AFGL 4176, the ratio of glycolaldehyde to ethylene glycol is $\leq$0.4. This ratio is consistent with relative abundances of the species formed in experiments where ice analogues are exposed to both UV irradiation and hydrogenation.

4.3.2 Isotopologues with only blended lines

Three isotopologues of HC_3N and one of CH_3CN are detected towards AFGL 4176, although only through blended lines. For completeness, these isotopologues are included in the full model. Since no column density and excitation temperature can be derived from the blended lines these are adopted from the isotopologues for which unblended lines are detected. That is, for $HC^{13}CCN$ the column density derived for $HCC^{13}CN$ is adopted, while for vibrationally excited $H^{13}CCCN$ and $HC^{13}CCN$ the column density derived for vibrationally excited $HCC^{13}CN$ is adopted. In the case of $CH_3^{13}CN$, the column density derived for the main isotopologue has been corrected by the $^{12}C/^{13}C$ ratio of 60. The isotopologues and the adopted column densities and excitation temperatures are listed in Table 4.3. It should be noted that no lines of either $H^{13}CCCN$, $^{13}CH_3CN$ or $CH_3C^{15}N$, were covered by the data. A couple of transitions of vibrationally excited $CH_3^{13}CN$ are within the data range but since these are all weak and highly blended they could not be modelled.

4.3.3 Spatial distribution of selected species

Two line maps are produced for each of the species for which five or more unblended lines are detected. The imaged lines are chosen so that both high and low upper state energy transitions are represented, in order to investigate whether these occupy different

spatial regions. Also, only lines which are relatively isolated, that is to say whose peak frequency is separated by at least 3 km s^{-1} from neighbouring peaks, are imaged. This is done in order to minimise line confusion. After suitable lines have been identified for each species, the zero- and first-moment maps, that is the velocity integrated intensity map and intensity-weighted velocity map, respectively, are produced. The spatial extent of each species is determined by fitting a 2D Gaussian to the zero-moment maps. As a representative sample of these maps, the lines of CH_3OH, NH_2CHO and CH_3C_2H are shown in Fig. 4.3; maps for the remaining species are presented in Appendix D.

There are no large differences between the spatial distribution of O- and N-bearing species. Except for CH_3C_2H, all species have emission peaks near the position of the continuum peak. The N-bearing species (CH_3CN, C_2H_3CN and C_2H_5CN) peak very close to the continuum peak, while some O-bearing species (CH_3OH and CH_3OCH_3 e.g.) peak up to 0$''$.2 away from the continuum peak. Although this scale is of the same order as the size of the synthesised beam, the signal-to-noise of these maps (30 – 90) is large enough to make these spatial differences significant.

Noticeable differences in spatial distributions exist between transitions of the same species with low and high upper state energies. For SO_2, H_2CS, CH_3CN, C_2H_5OH and CH_3OCHO low E_{up} transitions are more extended (∼0$''$.7) than high E_{up} transitions (∼0$''$.55). The larger spatial extent of low E_{up} transitions indicates that these species are present in colder gas. This is consistent with the relatively low excitation temperatures derived for SO_2, H_2CS and C_2H_5OH, 150 K, 160 K and 120 K, respectively, but contradicts the high excitation temperatures derived for CH_3CN and CH_3OCHO, 270 K and 310 K, respectively. For C_2H_3CN and C_2H_5CN this trend is reversed, with the spatial extent of low E_{up} transitions smaller (∼0$''$.4) than that of high E_{up} transitions (∼0$''$.55). For the remaining species (CH_3OH, NH_2CHO, CH_3OCH_3 and CH_3COCH_3) the extent of low and high E_{up} transitions are similar.

Finally, as noted above, CH_3C_2H is the only species whose emission is not concentrated at the location of the continuum peak emission. Instead this species shows two peaks, of approximately similar intensity, with one roughly coinciding with that of the continuum and a second at the location of the secondary continuum peak, mm2. The spatially more diffuse emission of this species is consistent with trends observed towards other hot cores (see e.g. Fayolle et al., 2015).

For a number of species a velocity gradient is detected across the source. The gradient is most pronounced in the case of NH_2CHO but also visible in the high upper state energy lines of CH_3CN, CH_3OCHO, C_2H_3CN and C_2H_5CN. The presence of a velocity gradient across the sources is consistent with the result of Johnston et al. (2015) who model the emission of CH_3CN and find this to be consistent with a Keplerian-like disk.

4.4 Discussion

Table 4.4 presents an overview of all detected O-, N- and S-bearing species (isotopologues not included) towards AFGL 4176. These detected species are common in regions of star-formation (see review by Herbst & van Dishoeck, 2009, and references therein), although a few rarer iosotopologues such as $C^{34}S$ and ^{18}O-, ^{34}S- and ^{33}S-sulphur dioxide are also detected.

On average, the column density ratios with respect to methanol derived for the O-bearing species are a factor of three higher than the ratios derived for the N-bearing species. Also, the excitation temperatures derived for the O-bearing species are generally low, 120 – 160 K, while the excitation temperatures derived for the N-bearing species are

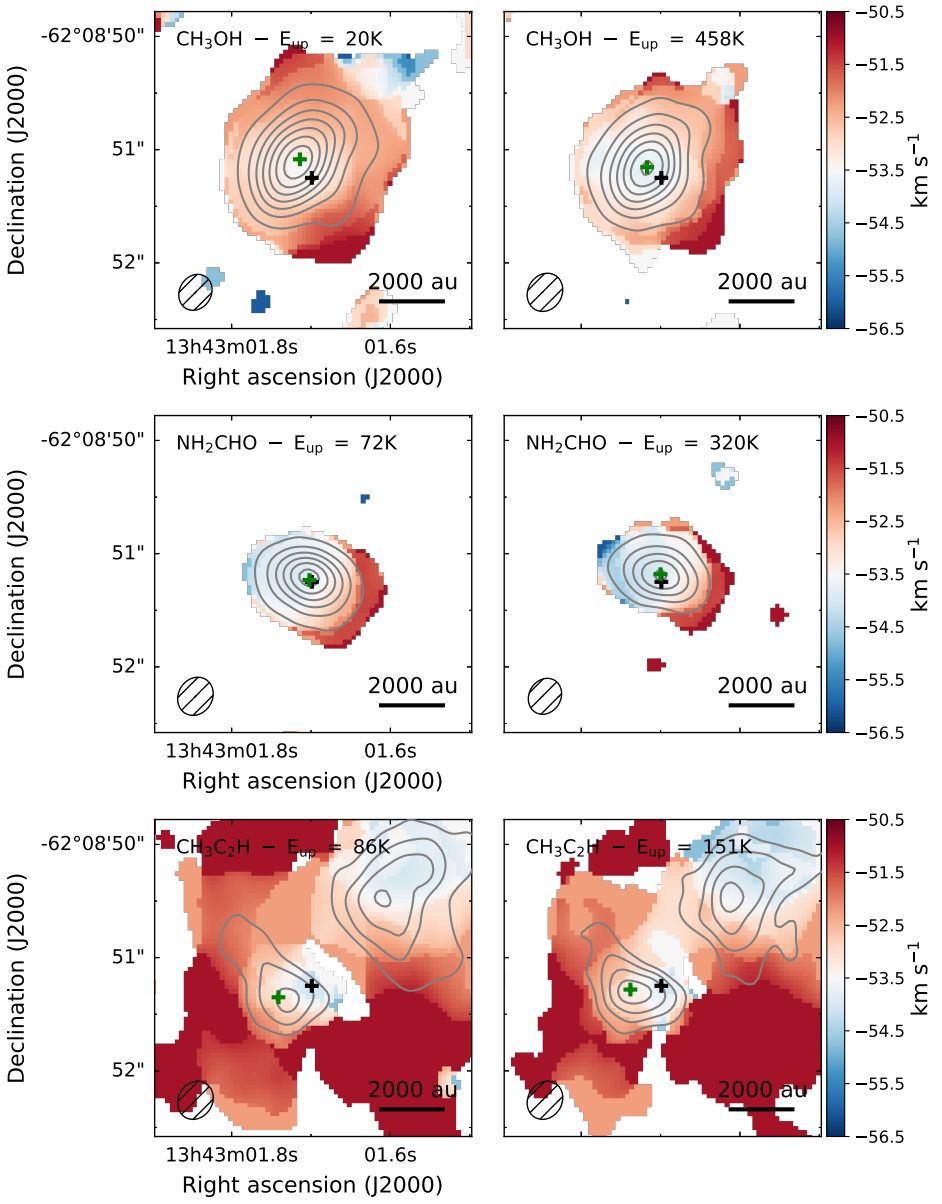

Figure 4.3: *Top panels:* First-moment (intensity-weighted velocity) map of CH_3OH lines at 254.0153 GHz (left) and 241.2679 GHz (right). Pixels with signal-to-noise ratios of less than three are masked out. The zero-moment (integrated intensity) map for each line is overlaid in grey contours. Contours start at 9σ and are in steps of 12σ, with $\sigma = 1.34\times10^{-2}$ and 7.16×10^{-3} Jy beam^{-1} km s^{-1}, for the left and right panel, respectively. The black and green crosses mark the locations of the peak continuum emission and peak integrated line intensity, respectively. *Middle panels:* Same as top panels but for NH_2CHO lines at 239.952 GHz (left) and 254.727 GHz (right). Contours start at 9σ and are in steps of 12σ, with $\sigma = 6.17\times10^{-3}$ and 6.25×10^{-3} Jy beam^{-1} km s^{-1}, for the left and right panel, respectively. *Bottom panels:* Same as top panels but for CH_3C_2H lines at 239.2523 GHz (left) and 239.2112 GHz (right). Contours start at 6σ and are in steps of 3σ, with $\sigma = 7.29\times10^{-3}$ and 6.35×10^{-3} Jy beam^{-1} km s^{-1}, for the left and right panel, respectively.

Table 4.4: Overview of oxygen-, nitrogen and sulphur-bearing species detected towards AFGL 4176

O-bearing	**N-bearing**	**S-bearing**
CH_3OH	CH_3CN	H_2CS
CH_3CHO	C_2H_3CN	**O, N-bearing**
C_2H_5OH	C_2H_5CN	NH_2CHO
CH_3OCH_3	HC_3N	HNCO
CH_3COCH_3	**Hydrocarbons**	**O, S-bearing**
CH_3OCHO	CH_3C_2H	SO_2
$(CH_2OH)_2$		SO
H_2CCO		**N, S-bearing**
t-HCOOH		NS
$CH_2(OH)CHO$		

Notes. Not including isotopologues. Species in red have fewer than five detected transitions and are considered tentative.

generally high, 190 – 240 K. This differentiation of species with excitation temperature is similar to trends observed in the Orion molecular cloud (Blake et al., 1987; Crockett et al., 2015) and in the high-mass star-forming complex G19.62-0.23 (Qin et al., 2010). Similar trends are also reported by Suzuki et al. (2018) who carry out a survey of N- and O-bearing species towards eight high-mass star forming regions, including Orion KL and G19.62-0.23, using the 45m radio telescope at the Nobeyama Radio Observatory. When comparing these observations with chemical models, Suzuki et al. (2018) conclude that the correlations between fractional abundances of different groups of species can be explained by a combination of different temperature structures inside the cores and different evolutionary phases of the studied regions. As examples of a younger, less evolved source and an older, more evolved source, Suzuki et al. (2018) discuss NGC 6334F (also known as NGC 6334I) and G10.47+0.03, respectively. While G10.47+0.03 displays a relatively high fractional abundance of N-bearing species, $\sim$2 – 10% with respect to methanol, the fractional abundances of the same species detected towards NGC 6334F are only $\sim$0.1%. By assuming a more dominant high-temperature region ($\sim$200 K) and later evolutionary stage for G10.47+0.03 with respect to NGC 6334F, Suzuki et al. (2018) reproduce the observed trends. The trend of younger regions being characterised by lower abundances of N-bearing species with respect to O-bearing species may be a consequence of gas-phase nitrogen chemistry taking longer to initiate compared with the chemistry of O-bearing species (Charnley et al., 1992).

The studies discussed above are primarily based on single-dish observations and therefore, mostly, spatially unresolved. This can be problematic when studying sites of star-formation, especially at large distances, since the emission associated with the inner hot envelope around the centrally forming star may not be distinguished from the emission of its cooler envelope. Also, since single-dish telescopes are generally less sensitive when compared with interferometric observations and especially ALMA, it may not be possible to identify enough optically thin lines from which excitation conditions can be derived. The generally larger beam sizes of single-dish telescopes may also result in underesti-

mated column densities of molecular species if effects of beam dilution are not accounted for correctly.

In the following, we compare our ALMA results for AFGL 4176 with a selection of ALMA studies, that suffer less from sensitivity and resolution limitations. These studies focus on the Galactic centre, Orion KL and the low-mass protostellar binary IRAS 16293. We conclude the section with a comparison to chemical models. Table 4.5 and Fig. 4.4 summarises the comparisons.

4.4.1 Comparison with the high-mass star-forming regions in Sgr B2(N) and Orion KL

Sgr B2(N): Located in the Galactic central region, the Sgr B2 molecular cloud hosts some of the most active sites of high-mass star-formation in the galaxy. One of these sites, Sgr B2 (N), is the subject of the ALMA line survey EMoCA (Exploring Molecular Complexity with ALMA, Belloche et al., 2016) aimed at characterising the molecular content of the region. Due to the high spatial resolution of the observations, $\sim$1.6″, probing scales down to 0.06 pc ($\sim$13300 au assuming a distance of 8.34 kpc), Bonfand et al. (2017) were able to identify three new hot cores towards Sgr B2, labelled N3, N4 and N5, in addition to the previously identified cores N1 and N2. Bonfand et al. (2017) find that the chemical composition of these new cores are very similar to each other and very different from that of the N2 core, suggesting that the N2 core is chemically less evolved than the three new cores.

For the hot cores in Sgr B2, the column density ratio with respect to methanol of N-bearing species (CH_3CN, NH_2CHO, C_2H_3CN and C_2H_5CN) are higher than those derived towards AFGL 4176 by up to two orders of magnitude. For the O-bearing species (C_2H_5OH and CH_3OCHO), the variations are smaller, though still up to an order of magnitude higher in Sgr B2 compared with AFGL 4176.

In addition to the main isotopologues, a number of ^{13}C- and ^{15}N-isotopologues, as well as deuterated and vibrationally excited species, have been detected towards Sgr B2(N2) (Belloche et al., 2016). While no deuterated species are detected towards AFGL 4176, a number of lines of ^{13}C-cyanoacetylene are detected in addition to $^{13}CH_3OH$ and some blended lines of $CH_3^{13}CN$. ^{13}C doubly substituted cyanoacetylene isotopologues are also detected towards Sgr B2(N2). Towards AFGL 4176, two transitions of ^{13}C doubly substituted cyanoacetylene are covered but both are weak and highly blended. The tentative detection of $HC_3^{15}N$ towards Sgr B2(N2) results in a ratio with respect to methanol identical to the value derived for AFGL 4176. It should be noted however, that only a very limited number of lines of these isotopologues are detected and therefore their detection is considered tentative and their ratios should be seen as indicative of trends rather than definite values.

Orion KL: Due to its proximity, $\sim$388 pc from the Sun, the high-mass star-forming regions associated with the Orion molecular clouds are some of the most studied. Using ALMA observations, the morphology and molecular composition of the region was recently studied by Pagani et al. (2017) who, thanks to the high angular resolution of their data of 1.7″, probing scales of $\sim$660 au, were able to separate the region into a number of components and report a complex velocity structure. However, due to the lack of zero-spacing data to recover the extended emission of many species, Pagani et al. (2017) do not derive column densities or excitation temperatures for the detected species and limit their analysis to line identification and determination of line velocity and line widths. Orion KL may therefore be qualitatively compared with AFGL 4176 though no quantitative comparison is possible.

Table 4.5: Summary of column density ratios with respect to methanol predicted by models and derived towards AFGL 4176, Sgr B2(N) and IRAS 16293B

		X/CH_3OH [%]						
		Sgr B2		AFGL 4176	IRAS 16293B[a]	Model		
		(N2)	(N3-5)			Fast	Medium	Slow
Hydrocarbons	CH_3C_2H	–	–	0.69 ± 0.14	–	–	–	–
O-bearing	CH_3CHO	–	–	0.27 ± 0.15	1.20	0.03	0.10	0.37
	C_2H_5OH	5.0	7.6 – 10.4	1.58 ± 0.25	2.3	0.54	0.64	1.29
	CH_3OCH_3	–	–	2.36 ± 0.25	2.4	0.44	0.69	0.74
	CH_3COCH_3	–	–	0.96 ± 0.11	0.17	0.01	0.11	0.05
	CH_3OCHO	3.0	18.9 – 32.0	3.09 ± 0.59	2.6	0.84	0.41	0.08
	$(CH_2OH)_2$	–	–	(0.47 – 0.55) ± 0.1	0.5 – 0.55[b]	0.03	0.01	10^{-4}
N-bearing	CH_3CN	5.78	10.6 – 13.4	0.62 ± 0.07	0.4	0.04	0.02	0.03
	NH_2CHO	8.75	0.83 – 1.16[c]	0.18 ± 0.02	0.1	3.55	1.65	0.08
	C_2H_3CN	1.05	0.6 – 1.25	0.11 ± 0.02	0.007	0.1	0.06	0.15
	C_2H_5CN	17.25	4.8 – 8.11	0.12 ± 0.02	0.04	0.05	0.85	0.79
S-bearing	NS	–	–	0.22 ± 0.02	–	–	–	–
	H_2CS	–	–	0.78 ± 0.07	0.02	–	–	–
	SO_2	–	–	14.7 ± 3.6	0.02	0.67	0.84	2.05
Reference		1, 2		this work	3, 4, 5, 6, 7, 8	9		

Notes. [(a)] Listed values are derived at 0.5″ (one beam) offset from IRAS 16293B. [(b)] Derived at 0.25″ (half beam) offset from IRAS 16293B. [(c)] Excluding the upper limit of ≤0.56% derived for N4.

References. (1) Belloche et al. (2016); (2) Bonfand et al. (2017); (3) Coutens et al. (2016); (4) Jørgensen et al. (2016); (5) Lykke et al. (2017); (6) Calcutt et al. (2018); (7) Drozdovskaya et al. (2018); (8) Jørgensen et al. (2018); (9) Garrod (2013)

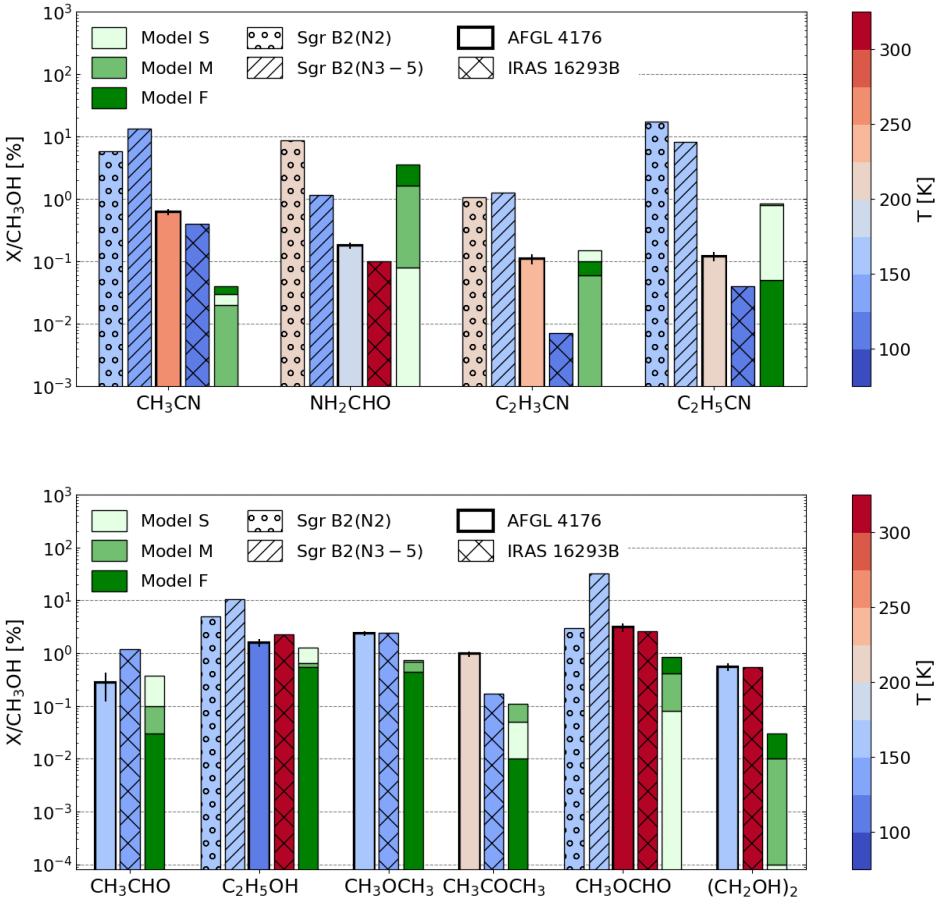

Figure 4.4: *Top panel:* Relative abundances of N-bearing species predicted by models and detected towards AFGL 4176, Sgr B2(N) and IRAS 16293B. For AFGL 4176, Sgr B2(N) and IRAS 16293B the colours of bars indicate the excitation temperature derived for each species. *Bottom panel:* Same as top panel but for O-bearing species.

With the exception of CH_3C_2H and NS, all species detected towards AFGL 4176 are also detected towards Orion KL by Pagani et al. (2017), including vibrationally excited HC_3N and its ^{13}C singly substituted isotopologues. The highest energy vibrationally excited state is the $v_6 = v_7 = 1$ state, detected towards the Orion KL hot core region. In contrast, only the first two vibration states (HC_3N, v_7=2 and $H^{13}CCCN$, v_7=1, $HC^{13}CCN$, v_7=1 and $HCC^{13}CN$, v_7=1) were tentatively detected towards AFGL 4176.

As for AFGL 4176, both conformers of ethylene glycol are detected towards Orion KL (Favre et al., 2017). This is interesting since previously only the more stable of the two, *aGg'*$(CH_2OH)_2$, was detected towards high-mass star-forming regions (see e.g. Lykke et al., 2015; Brouillet et al., 2015, and references therein), while the *gGg'*$(CH_2OH)_2$ conformer was only detected towards the low-mass system IRAS 16293 (Jørgensen et al., 2016). The ratio between the *aGg'* and *gGg'* ethylene glycol conformers is 1.2 in AFGL 4176, within the errors of the value of 1.1 derived for IRAS 16293, and half the values of 2.3 and 2.5 derived for the 5 and 8 km s^{-1} components of Orion KL respectively (Favre et al., 2017).

4.4.2 Comparison with the low-mass protobinary IRAS 16293–2422

The low-mass protobinary system IRAS 16293, located at a distance of 120 pc, was observed in the ALMA Protostellar Interferometric Line Survey (PILS, see Jørgensen et al., 2016, for overview and first results). The survey covers a total of 33.7 GHz between 329 and 363 GHz with spectral and angular resolutions of 0.2 km s^{-1} and 0.″5 ($\sim$ 60 au) respectively. The IRAS 16293 system is composed of two main components, IRAS 16293A and IRAS 16293B, with the narrow lines associated with the B source, $\sim$1 km s^{-1}, making it ideal for line identification.

Of the species for which five or more lines are detected towards AFGL 4176, all have also been identified towards IRAS 16293, although CH_3C_2H and NS are not reported in the PILS survey (van Dishoeck et al., 1995; Caux et al., 2011; Coutens et al., 2016; Jørgensen et al., 2016; Lykke et al., 2017; Calcutt et al., 2018; Drozdovskaya et al., 2018; Jørgensen et al., 2018). In addition, eight species with fewer than five transitions detected towards AFGL 4176 (CS and OCS only via their isotopologues) are also common between the sources. Figure 4.5 presents an overview of the relative abundances of all species detected towards AFGL 4176 and IRAS 16293B.

Overall, the composition of AFGL 4176 is more similar to that of IRAS 16293B than to the high-mass star-forming regions in the Galactic centre. Specifically, the relative column densities derived for the O-bearing species C_2H_5OH, CH_3OCH_3, CH_3OCHO and $(CH_2OH)_2$ towards IRAS 16293B are within a factor of two of the values derived for AFGL 4176. The remaining species show slightly larger variations with the ratio of CH_3CHO to CH_3OH being a factor of four higher in IRAS 16293B compared with AFGL 4176, and the ratio of CH_3COCH_3 to CH_3OH a factor of six lower. For N-bearing species, similar abundances are derived for CH_3CN and NH_2CHO, with variations within a factor of two between the sources. In contrast, lower ratios of both C_2H_3CN and C_2H_5CN, are reported towards IRAS 16293B compared to AFGL 4176, by factors of 16 and three, respectively. By far the largest variations between the sources are seen in the ratios of the S-bearing species with SO_2 being close to three orders of magnitude higher in AFGL 4176 compared to IRAS 16293B, and H_2CS higher by a factor 39. However, Drozdovskaya et al. (2018) note that the SO_2 emission detected towards IRAS 16293 is likely not homogeneously distributed within the 0.″5 PILS beam, which also misses a large extended component, and therefore the large difference between the sources could in part be explained by local variations in the distribution of the species towards IRAS 16293.

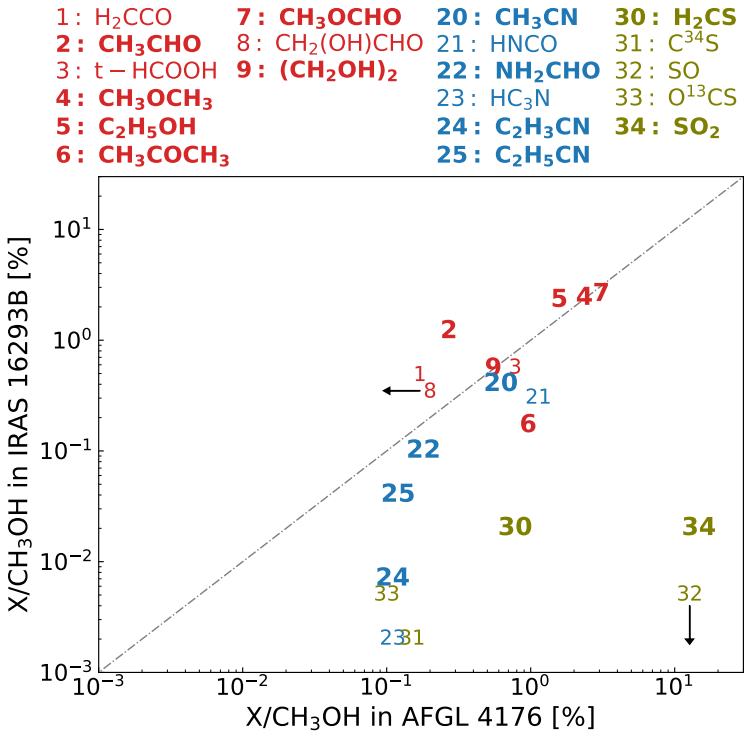

Figure 4.5: Relative abundances of species detected towards AFGL 4176 and IRAS 16293. Labels in bold refer to species with five or more detected transitions towards AFGL 4176. Oxygen-bearing species are labelled by numbers 1 through 9 in red, N-bearing species are labelled by numbers 20 through 25 in blue and S-bearing species are labelled by numbers 30 through 34 in yellow. Black arrows indicate upper limits on the relative abundance of $CH_2(OH)CHO$ in AFGL 4176 and of SO in IRAS 16293B. The dashed grey line indicates the 1:1 ratio of relative abundances in AFGL 4176 and IRAS 16293B.

4.4.3 Comparison with chemical models

The chemistry of hot cores is commonly divided into three main phases: 1) a cold collapse phase dominated by reactions on grain surfaces involving the diffusion of light species (i.e. H); 2) a warm-up phase where relatively complex species can be formed in the ice and subsequently released into the gas phase; 3) a hot core phase dominated by gas-phase reactions triggered by the evaporation of the icy content. The models presented by Garrod (2013) couple all of these phases to trace the gas-phase, grain-surface and bulk ice chemistry throughout the evolution of the core. The physical model adopted by Garrod (2013) consists of a collapse phase followed by a gradual warm-up of the gas and dust. Three warm-up timescales are adopted: a 'fast' scale with warm-up to 200 K in 5×10^4 yr, a 'medium' scale reaching 200 K in 2×10^5 yr and a 'slow' scale taking 1×10^6 yr to reach 200 K. Listed in Table 4.5 are the predicted peak gas-phase abundance ratios for each of these models.

In the models presented by Garrod (2013), the formation of the complex O-bearing species detected in this study (i.e. CH_3CHO, C_2H_5OH, CH_3OCH_3, CH_3COCH_3, CH_3OCHO and $(CH_2OH)_2$) is closely related to CH_3OH. Within the framework of the models, O-bearing species are formed primarily in warm (i.e. 30 K $<$ T $<$ 80 K) ices from the recombination of radicals formed through the UV-photodissociation of CH_3OH along with other simple solid species such as H_2CO and H_2O (see also Garrod et al., 2006, 2008). While the models match the abundances of CH_3CHO, C_2H_5OH and CH_3OCH_3 in AFGL 4176 within a factor of three, the abundances of CH_3COCH_3 and $(CH_2OH)_2$ are underpredicted by at least an order of magnitude. For CH_3OCHO, the most abundant O-bearing species after CH_3OH, with abundances of ∼2–3% in both AFGL 4176 and IRAS 16293B, the models predict values which are lower than the observed ones by a factor of four in the case of the fast model and a factor of 39 in the case of the slow model. A possible explanation for the mismatch between models and derived abundances of this species is poorly understood ice chemistry as well as missing gas-phase routes or included gas-phase routes which are more efficient than presumed. Indeed, a number of studies suggest that gas-phase chemistry could provide an important contribution to the formation of the molecule, either through ion-neutral or neutral-neutral reactions, following the sublimation of precursors from the ice (see e.g. Neill et al., 2011; Cole et al., 2012; Vasyunin & Herbst, 2013; Balucani et al., 2015; Taquet et al., 2016). A significant contribution from gas-phase reactions to the formation of CH_3COCH_3, as suggested by Charnley (2001), is also possible.

The abundances of complex N-bearing species detected in this study (i.e. CH_3CN, NH_2CHO, C_2H_3CN and C_2H_5CN) are likely the result of a combination of grain-surface and gas-phase reactions. For instance, CH_3CN can be formed on ices from the radical recombination of CH_3 and CN but also in the gas-phase via ion reactions between HCN and CH_3^+, followed by recombination with an electron or a proton transfer reaction. In the models of Garrod (2013), CH_3CN is formed primarily in ices via $CH_3 + CN \rightarrow CH_3CN$, though a formation channel via hydrogenation of C_2N on grains at early times is also included. C_2H_3CN and C_2H_5CN are formed mainly during the warm-up stage as a result of a series of both gas-phase and grain-surface reactions including the formation, recombination and hydrogenation of the CN radical as well as C_2H_2, C_2H_4 and HC_3N (Garrod et al., 2017). The formation of NH_2CHO is likely ice-dominated and proceeds via radical recombination reactions between NH_2 and HCO (e.g. Jones et al., 2011; Fedoseev et al., 2016). Alternatively, hydrogenation of HNCO may also lead to NH_2CHO. This idea is based on the strong correlation between the abundances of HNCO and NH_2CHO reported by Bisschop et al. (2007) and López-Sepulcre et al. (2015) for samples of pre-stellar and protostellar objects, indicating a connection between these species. However, such a connection contradicts the results of experimental works which show that solid-state HNCO hydrogenation does not produce NH_2CHO (Noble et al., 2015). A similar conclusion is reached by Ligterink et al. (2018b) who find that HNCO is likely not at the basis of the formation of NH_2CHO but rather formed simultaneously. Finally, a gas-phase formation route for NH_2CHO via reactions between NH_2 and H_2CO, has also been proposed (Barone et al., 2015; Codella et al., 2017).

For the detected N-bearing species, only the abundance ratio of C_2H_3CN is well-matched by the models. In contrast, the abundance ratios predicted by the models for CH_3CN, NH_2CHO and C_2H_5CN are all about an order of magnitude off with respect to the values derived for AFGL 4176. The abundances in AFGL 4176 do not favour either of the fast, medium or slow models over the other.

In summary, the presence of most of the detected complex molecules could be explained by warm ice chemistry triggered by UV photons. However, for some species, O- as well as N-bearing, formation routes via gas-phase reactions cannot be neglected. The chemical similarity between IRAS 16293B and AFGL 4176 suggests that the chemical composition of complex species may be set already in the cold cloud stage or that the production rates of complex species does not strongly vary with the source luminosity and might be universal in spite of the different physical conditions.

4.5 Summary

This paper presents a comprehensive study of the chemical inventory of the high-mass protostar AFGL 4176. Due to the exceptional resolving power offered by ALMA, the source is analysed on disk scales, making it possible to probe only the emission coming from the inner hot core region around the forming star while avoiding that of its large-scale cooler envelope. The source displays a rich chemistry consisting of 23 different molecular species, of which more than half, fourteen in total, are defined as complex, that is, consisting of six or more atoms. Of the detected species, the majority are oxygen-bearing while fewer contain nitrogen, sulphur or a combination thereof.

Assuming LTE, the column density is derived for all species detected towards AFGL 4176. With respect to methanol, the O-bearing species are approximately a factor of three more abundant than N-bearing species. This may indicate that AFGL 4176 is a relatively young source since nitrogen chemistry generally takes longer to evolve in the gas-phase compared with the chemistry of O-bearing species. Alternatively, if the composition of complex species is already set in the cold cloud stage, this gives an indication that formation of O-bearing species is favoured over that of N-bearing molecules. This may be due to inefficient reactions pathways (i.e. high diffusion energies and reactions barriers) for formation of N-bearing species, or due to a dominant nitrogen loss channel, for example into N2.

With the exception of CH_3C_2H, which shows two emission peaks, the spatial distribution of N- and O-bearing species is roughly similar. Generally, all species show emission peaks near the position of the continuum peak though some O-bearing species peak up to $0\farcs2$ away. Differences in the spatial extent of transitions of the same species with low and high $E_{\rm up}$ are seen for the majority of species. For a number of species a velocity gradient is detected across the source consistent with the Keplerian-like disk reported by Johnston et al. (2015).

Overall, the chemical composition of AFGL 4176 is more similar to that of the low-mass protostar IRAS 16293B than to that of the high-mass star-forming region Sgr B2(N). Taking methanol as a reference, the abundances of C_2H_5OH, CH_3OCH_3, CH_3OCHO and $(CH_2OH)_2$ in IRAS 16293B are within a factor of two of the abundances in AFGL 4176. In contrast, the C_2H_5OH/CH_3OH and CH_3OCHO/CH_3OH values derived for Sgr B2(N) are higher than those in AFGL 4176 by up to an order of magnitude. For the N-bearing species, the abundances of CH_3CN, C_2H_5CN and NH_2CHO are similar between AFGL4176 and IRAS 16293B while C_2H_3CN/CH_3OH is lower by a factor of 16 in IRAS 16293B. For Sgr B2(N) the abundances of all N-bearing species are significantly higher than in AFGL 4176. The similarity between abundances in AFGL 4176 and IRAS 16293B indicates that the production of complex species does not depend strongly on the luminosity of sources, but may be universal despite differences in physical conditions or that the composition of species is set already in the ice during the cold cloud stage.

Acknowledgements. This paper makes use of the following ALMA data: ADS/JAO.ALMA #2012.1.00469.S. ALMA is a partnership of ESO (representing its member states), NSF (USA) and NINS (Japan), together with NRC (Canada) and NSC and ASIAA (Taiwan) and KASI (Republic of Korea), in cooperation with the Republic of Chile. The Joint ALMA Observatory is operated by ESO, AUI/NRAO and NAOJ. This work is based on analysis carried out with the CASSIS software and JPL: http://spec.jpl.nasa.gov/ and CDMS: http://www.ph1.uni-koeln.de/cdms/ spectroscopic databases. CASSIS has been developed by IRAP-UPS/CNRS (http://cassis.irap.omp.eu).

Appendix A: Model grids

Table A.1: Overview of model grids

N_s range [cm^{-2}]	Species
10^{15} – 10^{16}	C_2H_3CN
5×10^{15} – 5×10^{16}	CH_3CHO NH_2CHO
10^{16} – 10^{17}	CH_3C_2H CH_3CN CH_3CN, v_8=1 H_2CS $(CH_2OH)_2$
5×10^{16} – 5×10^{17}	$^{13}CH_3OH$ CH_3OCH_3 CH_3OCHO
10^{16} – 5×10^{17}	C_2H_5OH
5×10^{17} – 5×10^{18}	SO_2

Notes. All grids have T_{ex} spanning 50 – 500 K in steps of 10 K and N_s sampled by 20 logarithmically spaced steps, apart from the grid for C_2H_5OH which has 30 logarithmically spaced steps.

Appendix B: Unidentified lines

Table B.1: List of unidentified lines

Rest frequency[a] [GHz]	Peak intensity [K]
238.806	1.9
239.078	4.2
239.082	3.6
239.651	1.9
239.655	2.7
239.926	1.9
240.129	2.0

Continued on next page

Continued from previous page

Rest frequency[a] [GHz]	Peak intensity [K]
240.132	2.0
240.155	2.1
240.517	2.5
240.562	2.0
240.565	2.2
240.574	1.9
240.579	2.2
240.702	2.1
240.718	2.0
240.753	2.0
241.102	1.4
241.127	1.5
254.192	2.9
254.340	2.0
254.346	2.6
254.581	3.9
254.669	3.0
254.686	7.0
254.713	5.7
254.716	5.2
254.858	4.6
256.107	3.8
256.111	3.8

Notes. [(a)] Assuming $v_{\rm LSR}$ = -53.5 km s^{-1} for AFGL 4176.

Appendix C: Full model

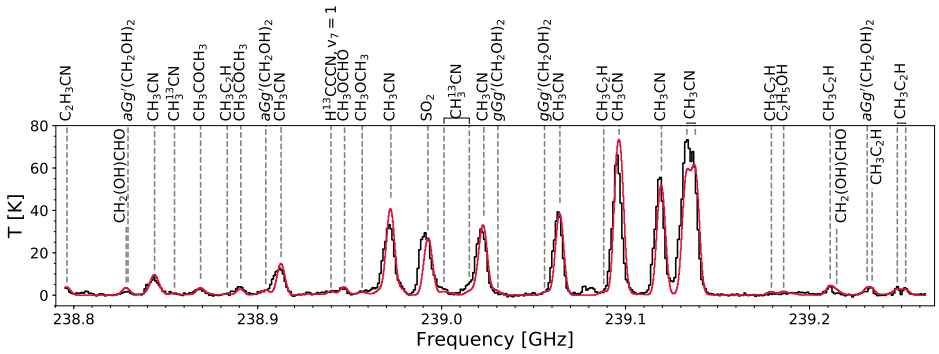

Figure C.1: Same as Fig. 4.2 for species detected towards AFGL 4176 in the spectral window centred at 239.0 GHz.

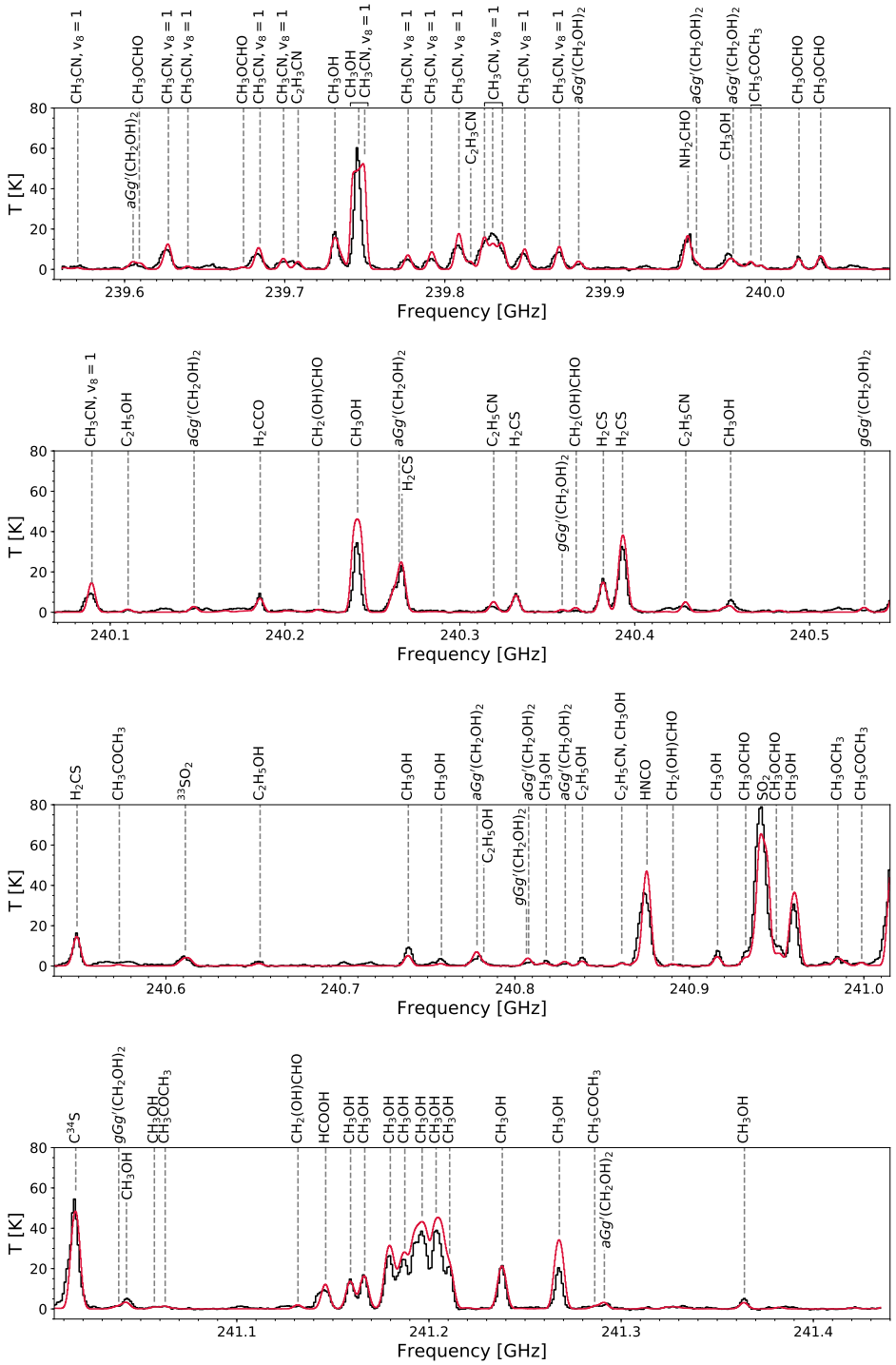

Figure C.2: Same as Fig. 4.2 for species detected towards AFGL 4176 in the spectral window centred at 240.5 GHz.

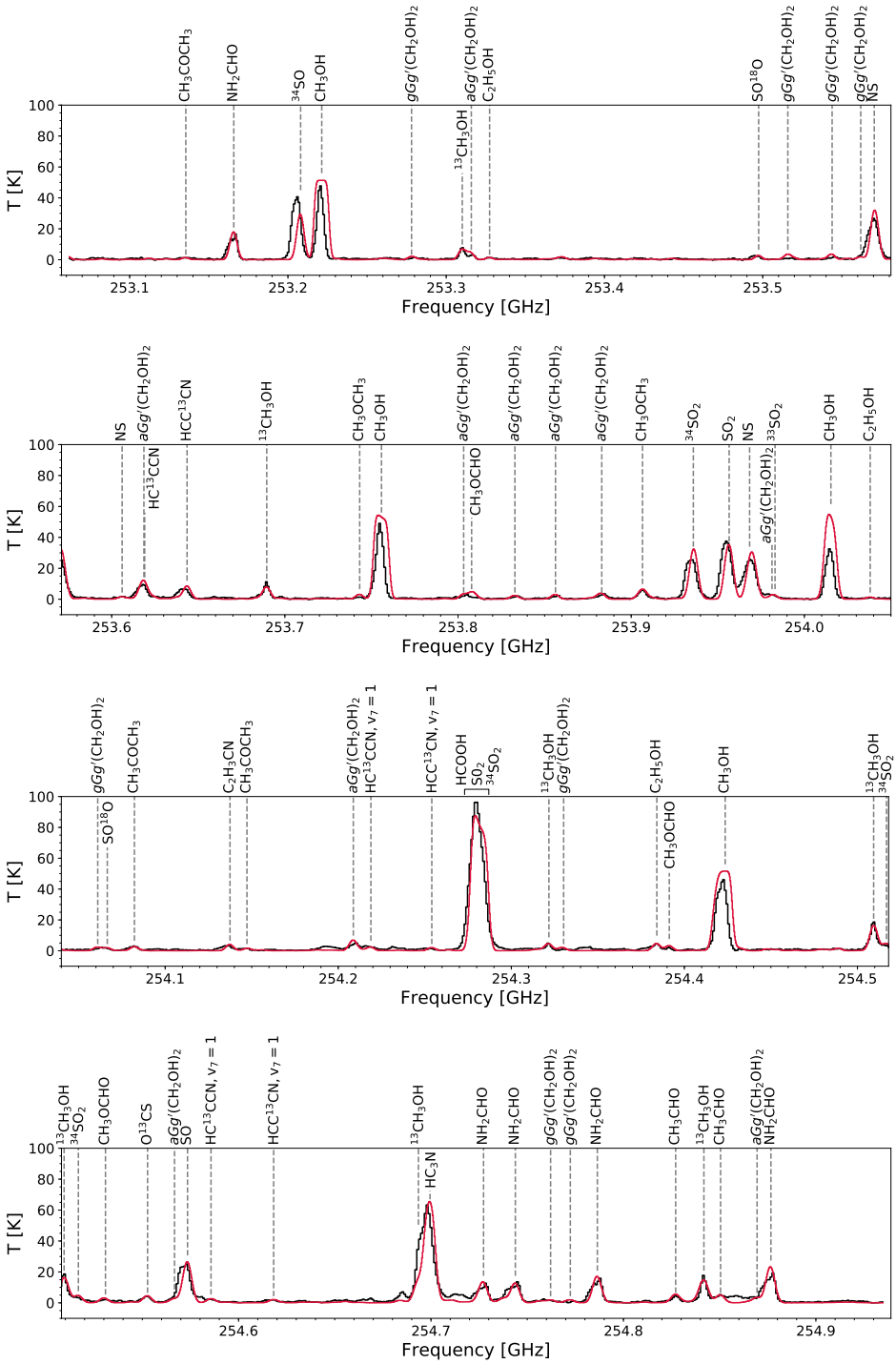

Figure C.3: Same as Fig. 4.2 for species detected towards AFGL 4176 in the spectral window centred at 254.0 GHz.

Appendix D: Line maps

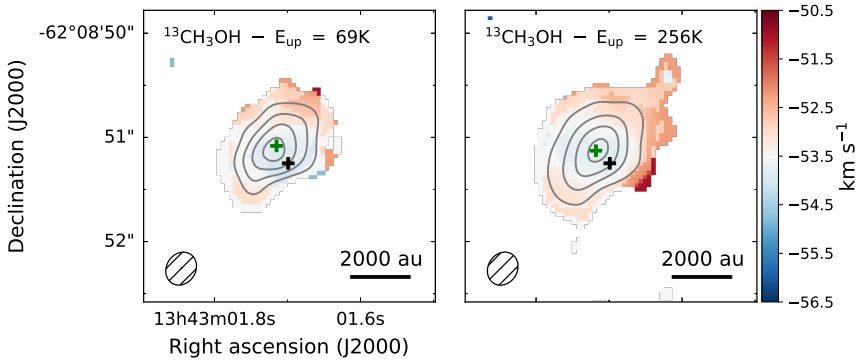

Figure D.1: Same as Fig. 4.3 for $^{13}CH_3OH$ lines at 256.1716 GHz (left) and 253.6895 GHz (right). Contours start at 9σ and are in steps of 6σ and 12σ, with $\sigma = 6.27\times10^{-3}$ and 6.87×10^{-3} Jy beam^{-1} km s^{-1}, for the left and right panel, respectively.

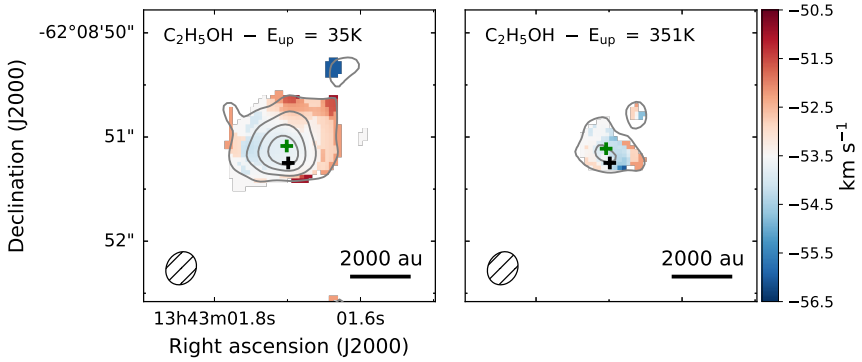

Figure D.2: Same as Fig. 4.3 for C_2H_5OH lines at 254.3841 GHz (left) and 253.3274 GHz (right). Contours start at 3σ and are in steps of 6σ, with $\sigma = 5.58\times10^{-3}$ and 5.39×10^{-3} Jy beam^{-1} km s^{-1}, for the left and right panel, respectively.

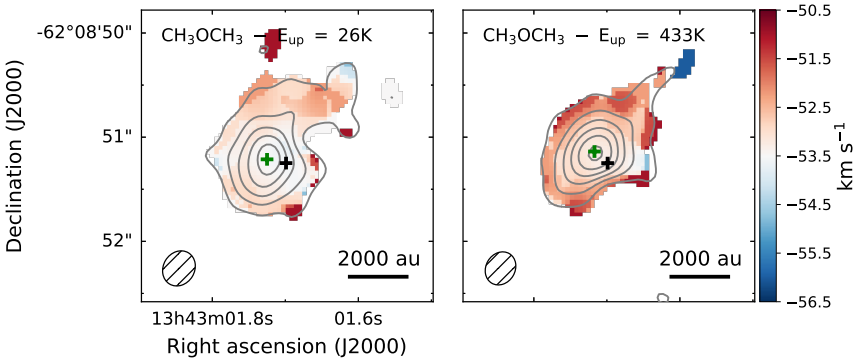

Figure D.3: Same as Fig. 4.3 for CH_3OCH_3 lines at 240.9851 GHz (left) and 253.9075 GHz (right). Contours start at 3σ and are in steps of 6σ, with $\sigma = 4.95\times10^{-3}$ and 6.08×10^{-3} Jy beam^{-1} km s^{-1}, for the left and right panel, respectively.

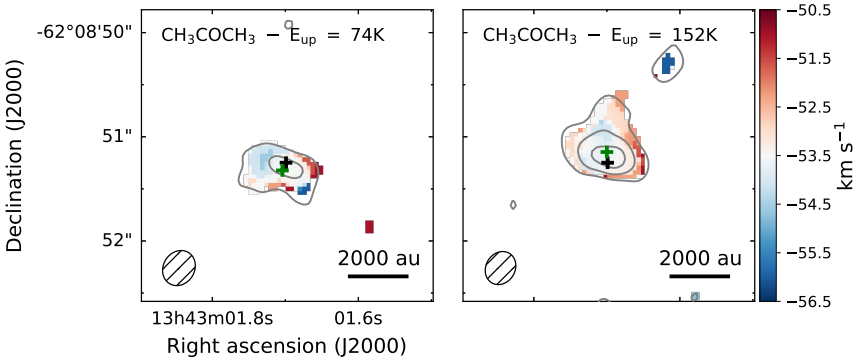

Figure D.4: Same as Fig. 4.3 for CH_3COCH_3 lines at 240.9988 GHz (left) and 254.0822 GHz (right). Contours start at 3σ and are in steps of 6σ, with $\sigma = 4.96\times10^{-3}$ and 5.32×10^{-3} Jy beam^{-1} km s^{-1}, for the left and right panel, respectively.

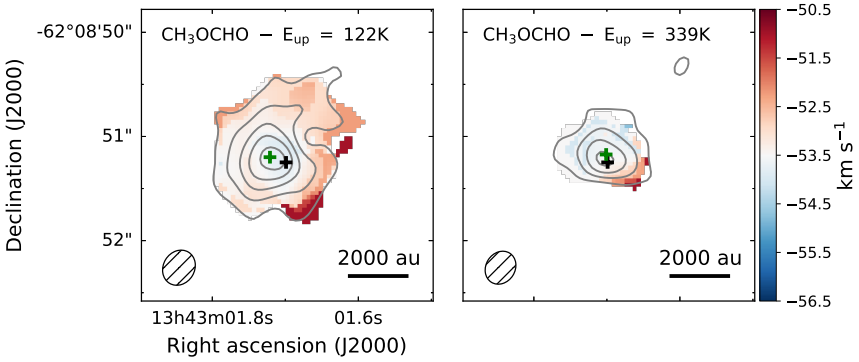

Figure D.5: Same as Fig. 4.3 for CH_3OCHO lines at 240.0211 GHz (left) and 256.4478 GHz (right). Contours start at 3σ and are in steps of 6σ, with $\sigma = 5.36\times10^{-3}$ and 5.96×10^{-3} Jy beam^{-1} km s^{-1}, for the left and right panel, respectively.

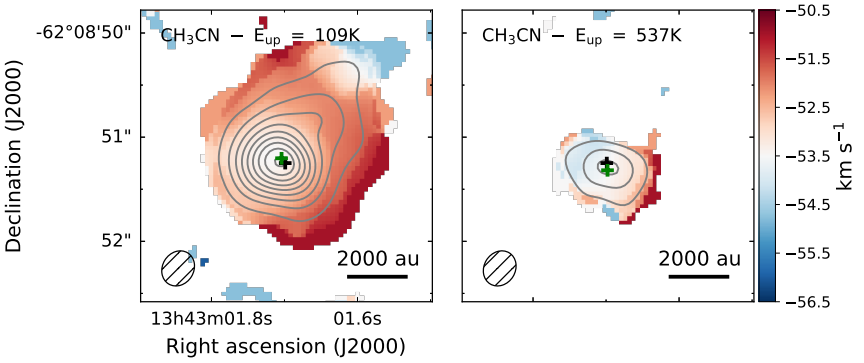

Figure D.6: Same as Fig. 4.3 for CH_3CN lines at 239.0965 GHz (left) and 238.8439 GHz (right). Contours start at 9σ and are in steps of 12σ, with $\sigma = 1.26\times10^{-2}$ and 5.78×10^{-3} Jy beam^{-1} km s^{-1}, for the left and right panel, respectively.

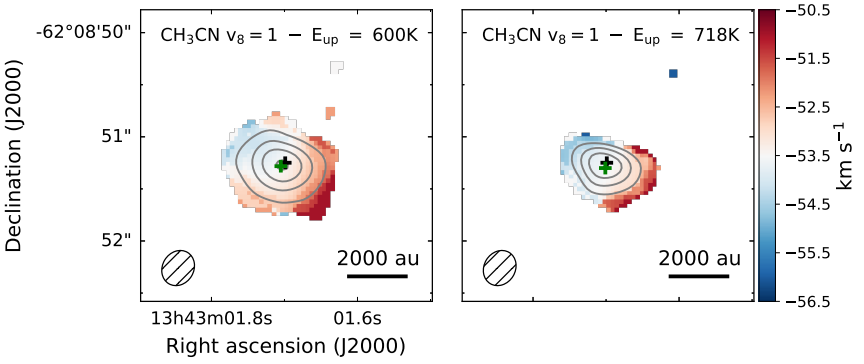

Figure D.7: Same as Fig. 4.3 for vibrationally excited CH_3CN lines at 240.0895 GHz (left) and 239.7917 GHz (right). Contours start at 9σ and are in steps of 12σ and 6σ for the left and right panel, respectively, with $\sigma = 5.41\times10^{-3}$ Jy beam^{-1} km s^{-1}.

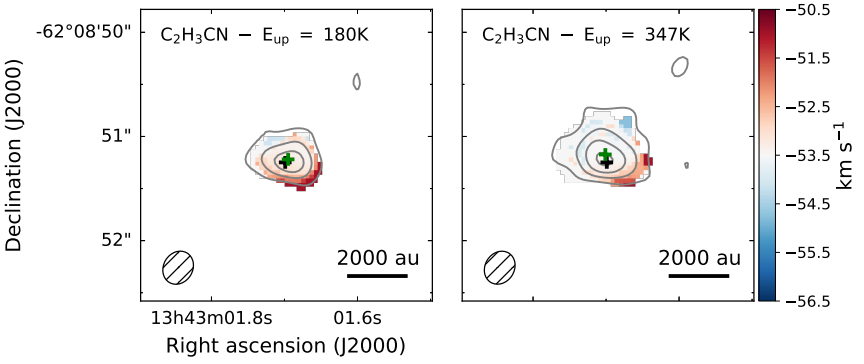

Figure D.8: Same as Fig. 4.3 for C_2H_3CN lines at 254.1375 GHz (left) and 256.4480 GHz (right). Contours start at 3σ and are in steps of 6σ, with $\sigma = 5.29\times10^{-3}$ and 6.0×10^{-3} Jy beam^{-1} km s^{-1}, for the left and right panel, respectively.

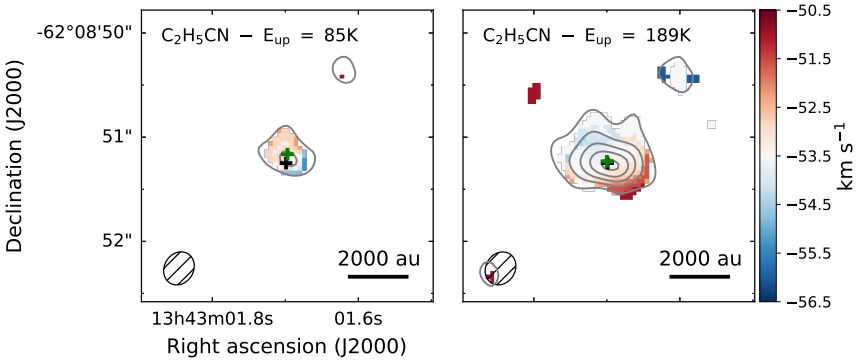

Figure D.9: Same as Fig. 4.3 for C_2H_5CN lines at 254.6336 GHz (left) and 256.3959 GHz (right). Contours start at 3σ and are in steps of 6σ, with $\sigma = 5.18\times10^{-3}$ and 5.7×10^{-3} Jy beam^{-1} km s^{-1}, for the left and right panel, respectively.

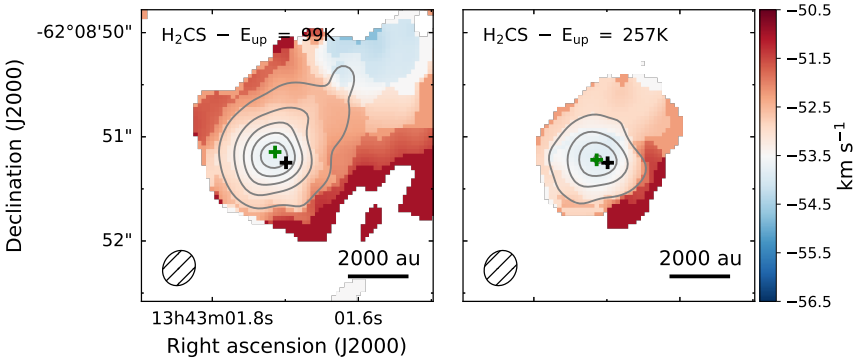

Figure D.10: Same as Fig. 4.3 for H_2CS lines at 240.5491 GHz (left) and 240.3322 GHz (right). Contours start at 9σ and are in steps of 12σ, with $\sigma = 6.81\times10^{-3}$ and 5.27×10^{-3} Jy beam^{-1} km s^{-1}, for the left and right panel, respectively.

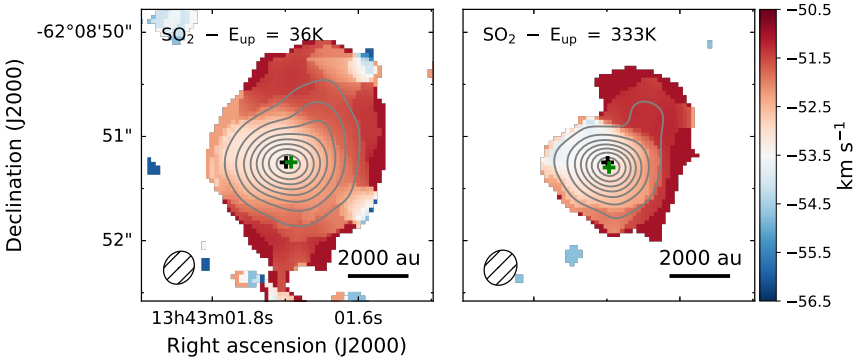

Figure D.11: Same as Fig. 4.3 for SO_2 lines at 256.2469 GHz (left) and 238.9925 GHz (right). Contours start at 9σ and are in steps of 12σ, with $\sigma = 1.96\times10^{-2}$ and 8.63×10^{-3} Jy beam^{-1} km s^{-1}, for the left and right panel, respectively.

5

Exploring the volatile composition of comets C/2012 F6 (Lemmon) and C/2012 S1 (ISON) with ALMA

E. G. Bøgelund and M. R. Hogerheijde

Astronomy & Astrophysics
Volume 604, Article A131 (2017)

Abstract

Context. Comets formed in the outer and cold parts of the disk which eventually evolved into our Solar System. Assuming that the comets have undergone no major processing, studying their composition provides insight in the pristine composition of the Solar Nebula.
Aim. We derive production rates for a number of volatile coma species and explore how molecular line ratios can help constrain the uncertainties of these rates.
Methods. We analyse observations obtained with the Atacama Large Millimeter/Submillimetre Array of the volatile composition of the comae of comets C/2012 F6 (Lemmon) and C/2012 S1 (ISON) at heliocentric distances of ∼1.45 au and ∼0.56 au, respectively. Assuming a Haser profile with constant outflow velocity, we model the line intensity of each transition using a 3D radiative transfer code and derive molecular production rates and parent scale lengths.
Results. We report the first detection of CS in comet ISON obtained with the ALMA array and derive a parent scale length for CS of ∼200 km. Due to the high spatial resolution of ALMA, resulting in a synthesised beam with a size slightly smaller than the derived parent scale length (0.″59×0.″39 corresponding to ∼(375×250) km at the distance of the comet at the time of observations), we are able to tentatively identify CS as a daughter species, i.e., a species produced in the coma and/or sublimated from icy grains, rather than a parent species. In addition we report the detection of several CH_3OH transitions and confirm the previously reported detections of HCN, HNC and H_2CO as well as dust in the coma of each comet, and report 3σ upper limits for HCO^+.
Conclusions. We derive molecular production rates relative to water of 0.2% for CS, 0.06 – 0.1% for HCN, 0.003 – 0.05% for HNC, 0.1 – 0.2% for H_2CO and 0.5 – 1.0% for CH_3OH, and show that the modelling uncertainties due to unknown collision rates and kinematic temperatures are modest and can be mitigated by available observations of different transitions of HCN.

5.1 Introduction

Comets are generally believed to be leftover fragments of the protoplanetary disk that formed our solar system. Stored in the outer parts of the disk, these icy fragments are kept well away from the heat of the newborn Sun. While some comets may have been subject to subsequent processing through thermal heating and exposure to radiation when visiting the inner regions of the Solar System, others remain pristine. Therefore, the characterisation of cometary ices provides a unique opportunity to study the initial composition of the Solar Nebula.

In the classical picture comets are divided in two groups. The first group is comprised of the Jupiter-family comets. These were formed in the Kuiper Belt but now also populate the scattered disk. The second group is comprised of the long-period comets. These were formed in the region of the giant planets but now reside in the Oort Cloud (see review by Rickman, 2010). Recent studies, though still debated, do not find this sharp division between groups of comets but suggest instead a much more extensive and continuous formation region around the CO and CO_2 snow lines (A'Hearn et al., 2012). In addition, the heterogeneity of the abundance of volatile species in comets indicates that a stationary formation scenario, where radial mixing is not accounted for, is unlikely (Bockelée-Morvan et al., 2004). On the other hand, a scenario in which comets are formed in a radially dynamic region of the disk fits well with the Grand Tack model (Walsh et al., 2011). In this model, inward and outward migrations of Jupiter and Saturn, during the first 100,000 years after the formation of the Sun, drove massive mixing in the disk.

In order to constrain the cometary formation sites further, it is essential to assess the composition of as many different comets as possible. To date, only a dozen comets have been studied in detail and only a handful of these in situ (see, e.g, A'Hearn, 2011, for an overview). The majority of studies show a vast compositional diversity amongst objects, demonstrating the need for more comprehensive statistical evaluations. Although in situ observations are undoubtedly the most precise and thorough way of quantifying cometary compositions, they are both expensive and rare. Therefore, we must rely largely on remote observations if we are to construct a statistically significant sample of objects, from which the emerging taxonomical database for comets can evolve (Mumma & Charnley, 2011).

In this paper we analyse archival observations obtained with the Atacama Large Millimeter/Submillimeter Array (ALMA) of two comets. Cordiner et al. (2014, 2017b) present an analysis of some of this data; here we present detections of additional species, add analysis of the Band 6 Science Verification data, and check the consistency of our new analysis by comparison to these papers. Assuming a Haser model with constant outflow velocity we derive molecular production rates and parent scale lengths for each of the detected species. In addition, we explore how line ratios can be used to mitigate the uncertainty on the derived production rates due to the unknown kinetic temperature of each comet and the unknown collisional rates of water molecules with respect to other simple molecular species.

The paper is structured in the following way: in Sect. 5.2 we summarise the observational setup, in Sect. 5.3 we present the observational results, in Sect. 5.4 we discuss our cometary model as well as the molecular production rates we derive and in Sect. 5.5 we summarise our findings.

5.2 Observations

C/2012 F6 (Lemmon) (hereafter referred to as Lemmon) is a long-period comet, with an orbital period ∼11,000 yr and semi-major axis ∼487 au, of high eccentricity, e=0.998, and orbital inclination, i=82.6°. The comet was discovered on 2012 March 23 and reached perihelion one year later on 2013 March 24 at a distance of 0.73 au[1].

C/2012 S1 (ISON) (hereafter referred to as ISON) was a dynamically new, sungrazing comet, discovered on 2012 September 21. The comet reached perihelion on 2013 November 28 at a distance of merely 0.013 au[2] (∼2.7 $R_\odot$), after which it disintegrated (Keane et al., 2016).

Observations of both comets were carried out with ALMA in Cycle 1 Early Science mode between 30 May and 2 June 2013 and 16 and 17 November 2013 for comets Lemmon and ISON respectively, using the ALMA Band 7 receivers (covering the frequency range 275 – 373 GHz).

Simultaneous observations of two sets of spectral lines (plus continuum) were made for each comet with the correlators configured to cover four frequency ranges in each set. Table 5.1 summarises these and general observation parameters (for clarity, spectral windows with no detections are not listed). All spectral windows have a total bandwidth of 937500 kHz with 3840 equally spaced channels providing a spectral resolution of 244 kHz corresponding to ∼0.20 km s^{-1} at 373 GHz. The cometary positions were traced using JPL Horizons ephemerides (JPL#78 for Lemmon and JPL#54 for ISON).

The quasars 3C279, J0006-0623, J2232+117 and J0029+3456 were used for phase and bandpass calibration while flux scale calibrations were done for Lemmon using Pallas and for ISON using Ceres and Titan. Weather conditions were good with low precipitable water vapour (PWV) at zenith between 0.44 – 0.83 mm and high atmospheric phase stability.

Additional observations of comet Lemon were made on 2013 May 11 as part of the Science Verification (SV) program to test the capability of the array to Doppler track ephemeris targets. These observations were carried out using the Band 6 receivers (covering the frequency range 211 – 275 GHz), targeting four spectral lines (see Table 5.1). The SV data bands have total widths of 234375 kHz with 3840 channels. The resolution is 61 kHz corresponding to 0.07 km s^{-1} at 275 GHz. Phase, bandpass and absolute flux scale calibrations are done using the quasars J2232+117, J0006-0623 and J0238+166.

We optimise the standard data delivery reduction scripts for each target and use these to flag and calibrate the data. Deconvolution is done in CASA 4.2.2 using the CLEAN algorithm with natural visibility weighting. The image pixel size was set to 0.″1×0.″1. This resolution element corresponds to (127×127) km and (64×64) km at the distances of Lemmon and ISON respectively, on the days of observations. The images were restored with a Gaussian beam between 0.″79×0.″50 and 0.″55×0.″37 (depending on the line frequency of the individual transitions) and the spectral coordinates were shifted to the rest-frequency of the targeted lines. As noted by Cordiner et al. (2014), no signal was detected on baselines longer than ∼500 m so we excluded these during imaging to avoid introducing unnecessary noise. This reduces the angular resolution of the data slightly but all species are still well-sampled.

For each set of observations we image both the continuum and individual line emission. We assume the cometary nucleus to be at the position of the continuum peak,

[1] http://ssd.jpl.nasa.gov/?horizons; 'JPL/HORIZONS 903922: COMET C/2012 F6 (LEMMON)'. JPL Solar System Dynamics.

[2] 'JPL/HORIZONS 903941: COMET C/2012 S1 (ISON)'. JPL Solar System Dynamics.

Table 5.1: Summary of Observations

Source	Setting	Species	Transition	Frequency (GHz)	Date	Int. Time[a] (min)	r_h[b] (au)	Δ[c] (au)	Ants.[d]	Baselines[e] (m)
C/2012 F6 (Lemmon)	I	HCN	4 – 3	354.50547	2013 May 31 – 2013 Jun 1	41.4	1.446	1.745	32	15 – 1284
		H_2CO	$5_{1,5} - 4_{1,4}$	351.76864						
		CH_3OH	$7_{2,5} - 6_{2,4}$	338.72169						
			$7_{1,6} - 6_{1,5}$	341.41564						
	II	HNC	4 – 3	362.63030	2013 May 30 – 2013 Jun 2	44.4	1.475	1.748	34	15 – 2733
		CH_3OH	$1_{1,1} - 0_{0,0}$	350.90507						
	SV	HCN	3 – 2	265.88640	2013 May 11	15.8	1.165	1.705	20	15 – 1175
		HCO^+	3 – 2	267.55753						
		CH_3OH	$5_{2,3} - 4_{1,3}$	266.83812						
C/2012 S1 (ISON)	I	CS	7 – 6	342.88286	2013 Nov 16 – 2013 Nov 17	68.5	0.589	0.887	29	17 – 1284
		HCN	4 – 3	354.50547						
		HCO^+	4 – 3	356.73424						
	II	HNC	4 – 3	362.63030	2013 Nov 16 – 2013 Nov 17	91.7	0.557	0.875	29	12 – 1284
		H_2CO	$5_{1,5} - 4_{1,4}$	351.76864						
		CH_3OH	$1_{1,1} - 0_{0,0}$	350.90507						

Notes. [(a)] Total time on source. [(b)] Heliocentric distance. [(c)] Geocentric distance. [(d)] Number of 12m antennas in array. [(e)] Deprojected antenna baseline range.

which can be clearly identified in all images. However, due to the nature of comets as non-gravitationally accelerating bodies, these are offset from the arrays pointing centre by ∼0.″9 in the case of Lemmon and ∼6.″5 in the case of ISON. To account for the offset of the pointing centre with respect to the position of the cometary nucleus, images were primary beam corrected. One execution block of observations of ISON was excluded completely due to incorrect tracking.

5.3 Spatial distribution of molecules

We present the first AMLA detections of carbon monosulfide, CS, in comet ISON, as well as several methanol, CH_3OH, transitions and the line rations of HCN(J=4–3)/(J=3–2) in comet Lemmon. For completeness, and in order to compare our method to that reported by Cordiner et al. (2014), we also present the detection of hydrogen cyanide, HCN, its metastable isomer hydrogen isocyanide, HNC, and formaldehyde, H_2CO. In contrast to Cordiner et al. (2017b), who discuss the time variability of the HNC, H_2CO and CH_3OH emission in comet ISON, our imaging is time averaged and our derived production rates are time and spherically averaged by assuming a spatially uniform production rate. Spectrally integrated flux maps of all species, as well as their model counterparts, to be discussed in Sect. 5.4, can be seen in Figs. 5.1 and 5.2, while spectrally integrated peak fluxes, spectrally and spatially integrated total fluxes and molecular production rates are listed in Table 5.2.

Toward each comet a transition of HCO^+ was targeted in the observations but not detected in either. For completeness we therefore report 3σ upper limits of 2.25×10^{-2} Jy beam^{-1} km s^{-1} for the velocity integrated peak intensity of HCO^+(J=3–2), observed towards comet Lemmon, and 3.06 $\times10^{-2}$ Jy beam^{-1} km s^{-1} for HCO^+(J=4–3), detected towards comet ISON. We do not model this emission because HCO^+ has an extended origin, probably a product of ion-neutral chemistry in the coma as seen in comets 67P/Churyumov-Gerasimenko (Fuselier et al., 2015) and Hale-Bopp (1995 O1) (Wright et al., 1998), and ALMA has limited sensitivity to such extended emission.

5.3.1 Comet Lemmon

Four species are detected towards comet Lemmon. HCN and CH_3OH show symmetric spatial distributions both of which peak at approximately the same location as the dust continuum, which we take as the location of the cometary nucleus, indicated by a cross in the figures. This is in agreement with HCN and CH_3OH being primary species, i.e., species released directly from the nucleus. While having the same general distribution, HCN and CH_3OH have very different velocity integrated line intensities, with that of HCN an order of magnitude higher than those of CH_3OH. In contrast to HCN and CH_3OH, HNC and H_2CO have much more distributed origins with similar integrated flux intensities, slightly below those of the CH_3OH transitions. The distributed origins indicate that HNC and H_2CO are either the result of gas-phase chemistry in the cometary coma, or that they are transported away from the nucleus by some refractory compound before being evaporated. In Sects. 5.4.1 and 5.4.2 we will discuss the parent scale lengths and production rates we derive for HNC, H_2CO and CH_3OH in detail and how these compare with the various formation routes discussed above.

5.3.2 Comet ISON

Towards comet ISON we detect five molecular species. As is the case for comet Lemmon, HCN and CH_3OH show centrally peaked distributions coinciding with the peak of the continuum. We see the same trend in integrated line flux in comet ISON as in comet Lemmon, with the HCN transition being brighter than that of CH_3OH by more than an order of magnitude. The spatial distributions of HNC and H_2CO are again more distributed compared to HCN and CH_3OH but to a lesser extent than in the case of comet Lemmon. This may be due to the generally higher activity, and consequently higher molecular production rates, of comet ISON compared to comet Lemmon. A higher production rate is consistent with the heliocentric distance of ISON being only one third of the heliocentric distance of comet Lemmon. A less extended spatial distribution would also imply that new molecules are released from the nucleus, or produced in the coma of comet ISON, faster than they are transported away. The integrated line intensities of HNC and H_2CO are lower than that of HCN but, in contrast to comet Lemmon, higher than for CH_3OH.

In addition to the species discussed above, we report the first detection of CS by ALMA in the coma of comet ISON. We find the integrated line flux of CS to be half that of HCN but greater than those of HNC, H_2CO and CH_3OH. CS was first detected in comet West (1975 VI) (Smith et al., 1980) through ultraviolet spectroscopy but has since been observed in a number of other objects, at a number of different wavelengths (see Mumma & Charnley, 2011, for a summay). In Sect. 5.4.1 we derive the production rate and parent length scale for CS and in Sect. 5.4.2 we will discuss the possible formation scenarios for this molecule.

5.4 Model

To calculate molecular production rates we model the emission of each of the detected species. This is done using LIME (Brinch & Hogerheijde, 2010), a code for non-LTE line excitation and radiative transfer. We assume a spherically symmetric model with constant outflow velocity (Haser, 1957; Combi et al., 2004) to describe the number density of molecules released from the cometary nucleus, i.e. parent molecules, (n_p), as a function of distance from the cometary nuclei (r)

$$n_\mathrm{p}(r) = \frac{Q}{4\pi v_\mathrm{exp} r^2} \exp\left(-\frac{r\beta}{v_\mathrm{exp}}\right), \tag{5.1}$$

with Q denoting the molecular production rate, v_exp the expansion velocity and β the molecular photodestruction rate.

Species produced by the destruction of parent molecules, referred to as daughter molecules, are described by

$$n_\mathrm{d}(r) = \frac{Q}{4\pi v_\mathrm{exp} r^2} \frac{\frac{v_\mathrm{exp}}{\beta_\mathrm{d}}}{\frac{v_\mathrm{exp}}{\beta_\mathrm{d}} - L_\mathrm{p}} \left[\exp\left(\frac{-r\beta_\mathrm{d}}{v_\mathrm{exp}}\right) - \exp\left(\frac{-r}{L_\mathrm{p}}\right)\right], \tag{5.2}$$

with L_p denoting the parent scale length, given by the ratio of the expansion velocity to the photodestruction rate of the parent species. For $L_\mathrm{p} = 0$, equation (5.2) reduces to equation (5.1).

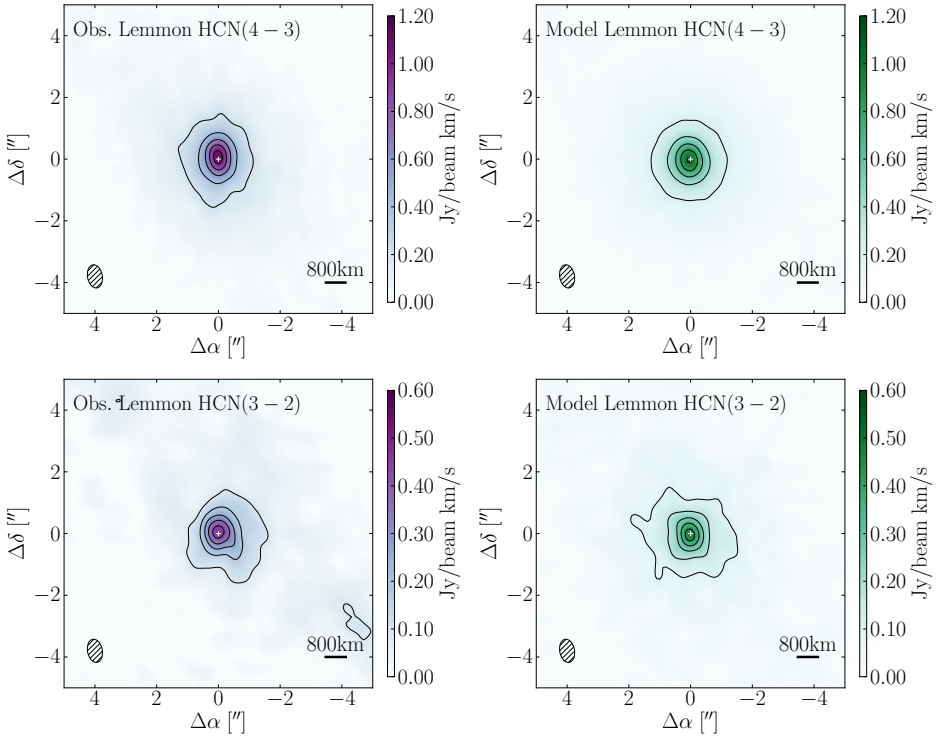

Figure 5.1: Velocity integrated intensity maps (contours and colour) of HCN(4–3), HCN(3–2), HNC(4–3), $H_2CO(5_{1,5}–4_{1,4})$, $CH_3OH(1_{1,1}–0_{0,0})$, $CH_3OH(5_{2,3}–4_{1,3})$, $CH_3OH(7_{1,6}–6_{1,5})$ and $CH_3OH(7_{2,6}–6_{2,4})$ detected in the coma of comet Lemmon in blue and model counterparts (Sect. 5.4) in green. Colours indicate intensity and contours are in steps of 30σ for HCN(4–3), 10σ for HCN(3–2), 3σ for $H_2CO(5_{1,5}–4_{1,4})$, $CH_3OH(1_{1,1}–0_{0,0})$, $CH_3OH(7_{1,6}–6_{1,5})$ and $CH_3OH(7_{2,6}–6_{2,4})$, starting at 6σ for $CH_3OH(1_{1,1}–0_{0,0})$, $CH_3OH(7_{1,6}–6_{1,5})$ and $CH_3OH(7_{2,6}–6_{2,4})$ and 1σ for HNC(4–3) and $CH_3OH(5_{2,3}–4_{1,3})$ starting at 3σ and 2σ respectively where σ is the RMS noise in each map. Crosses mark the peak continuum emission.

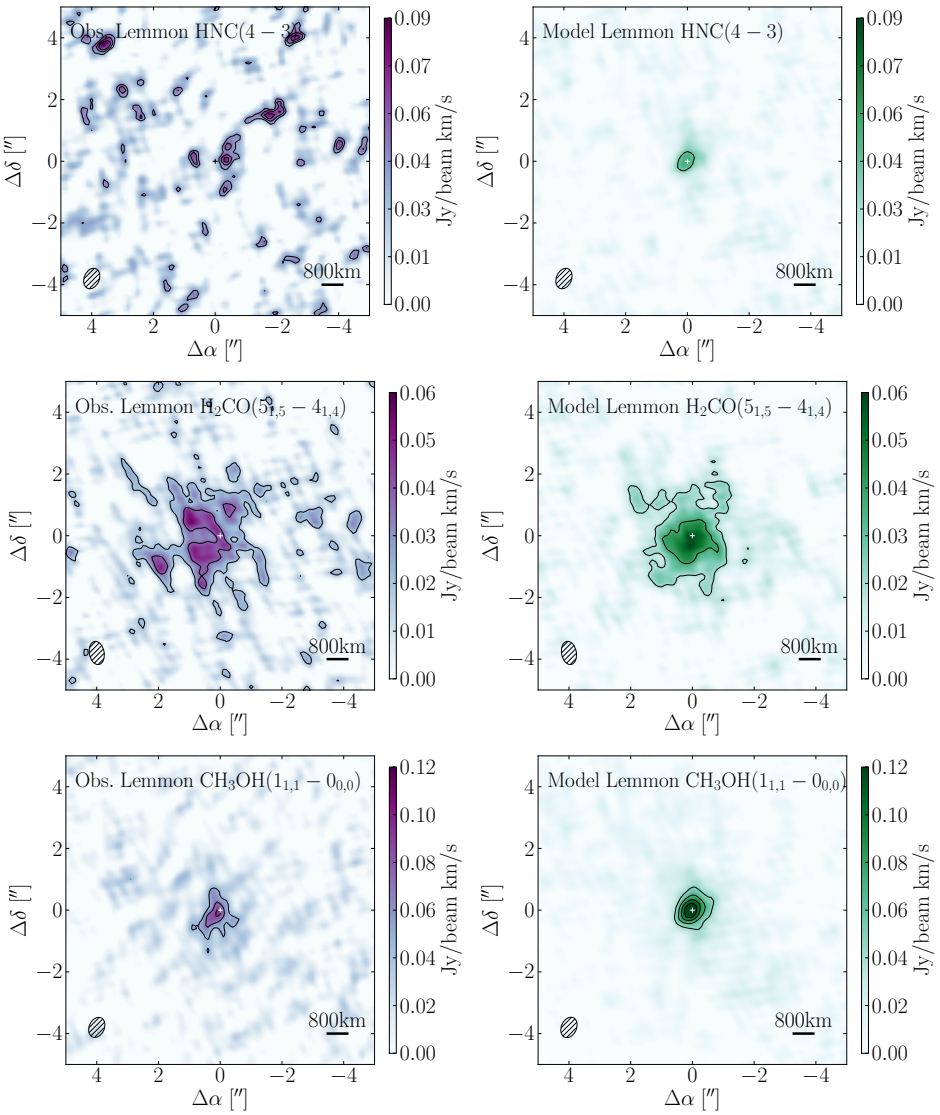

Figure 5.1: Continued

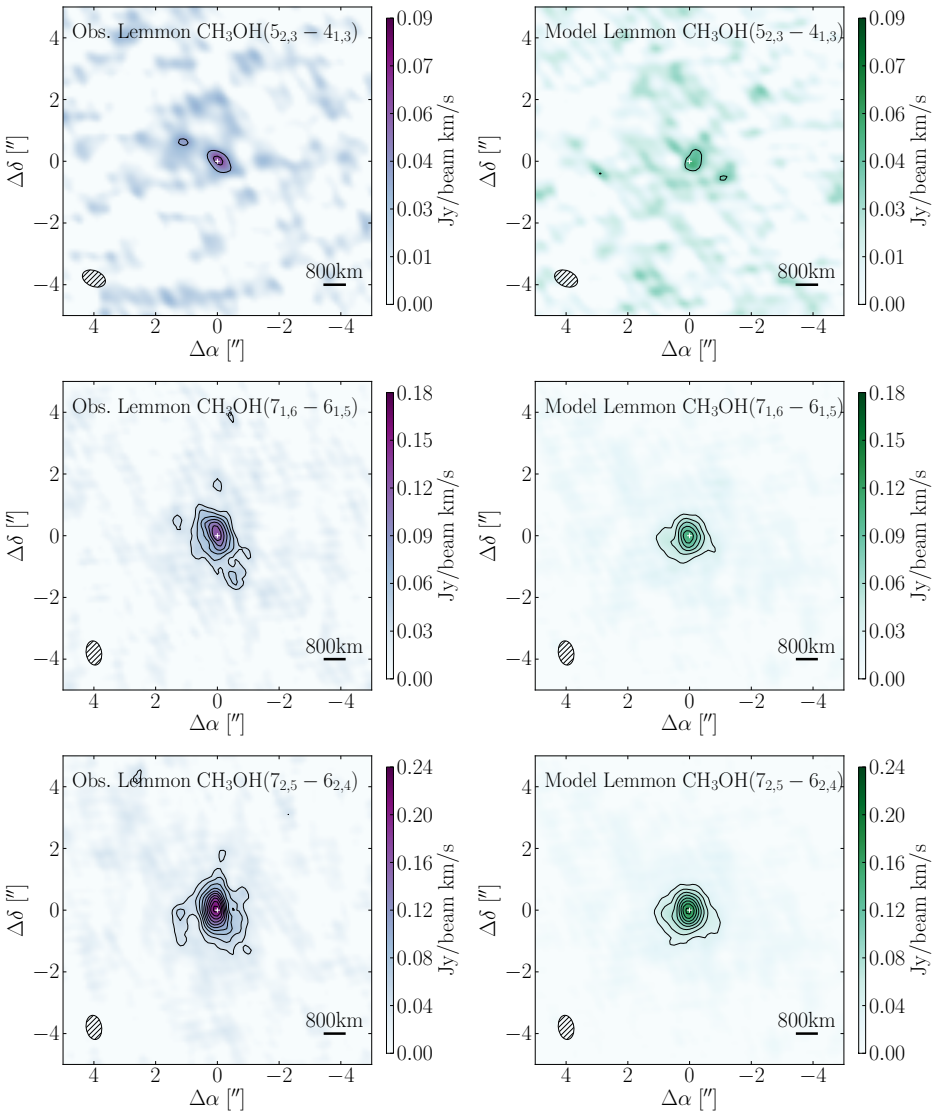

Figure 5.1: Continued

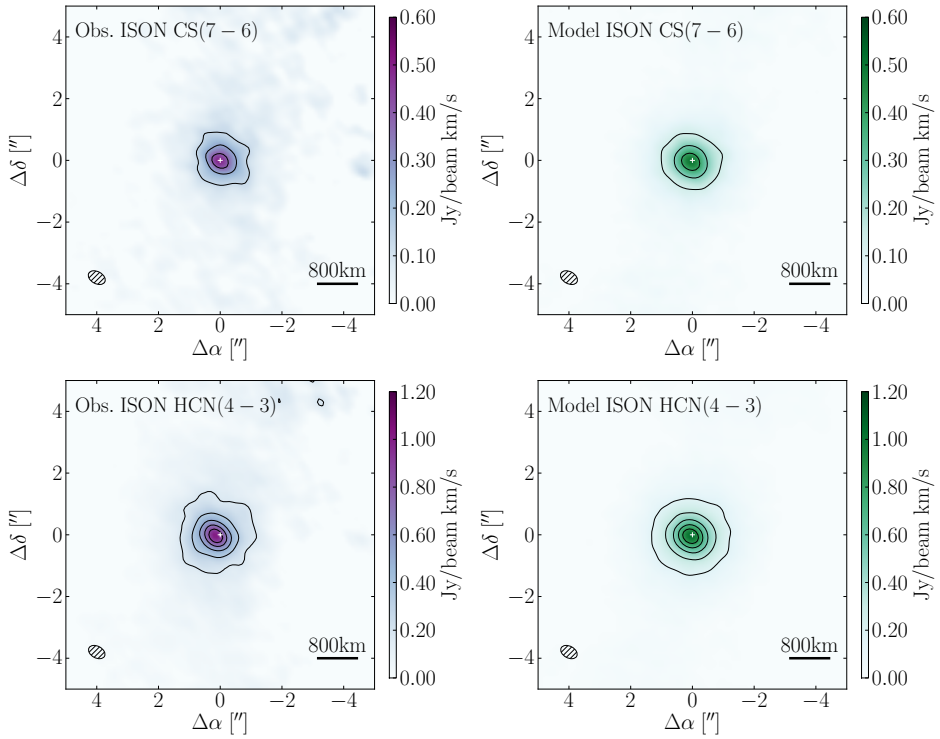

Figure 5.2: Velocity integrated intensity maps (contours and colour) of CS(7–6), HCN(4–3), HNC(4–3), $H_2CO(5_{1,5}–4_{1,4})$ and $CH_3OH(1_{1,1}–0_{0,0})$ detected in the coma of comet ISON in blue and model counterparts (Sect. 5.4) in green. Colours indicate intensity and contours are in steps of 10σ for CS(7–6) and HCN(4–3), 3σ for $H_2CO(5_{1,5}–4_{1,4})$ and 1σ for HNC(4–3) and $CH_3OH(1_{1,1}–0_{0,0})$ starting at 3σ and 2σ respectively where σ is the RMS noise in each map. Crosses mark the peak continuum emission.

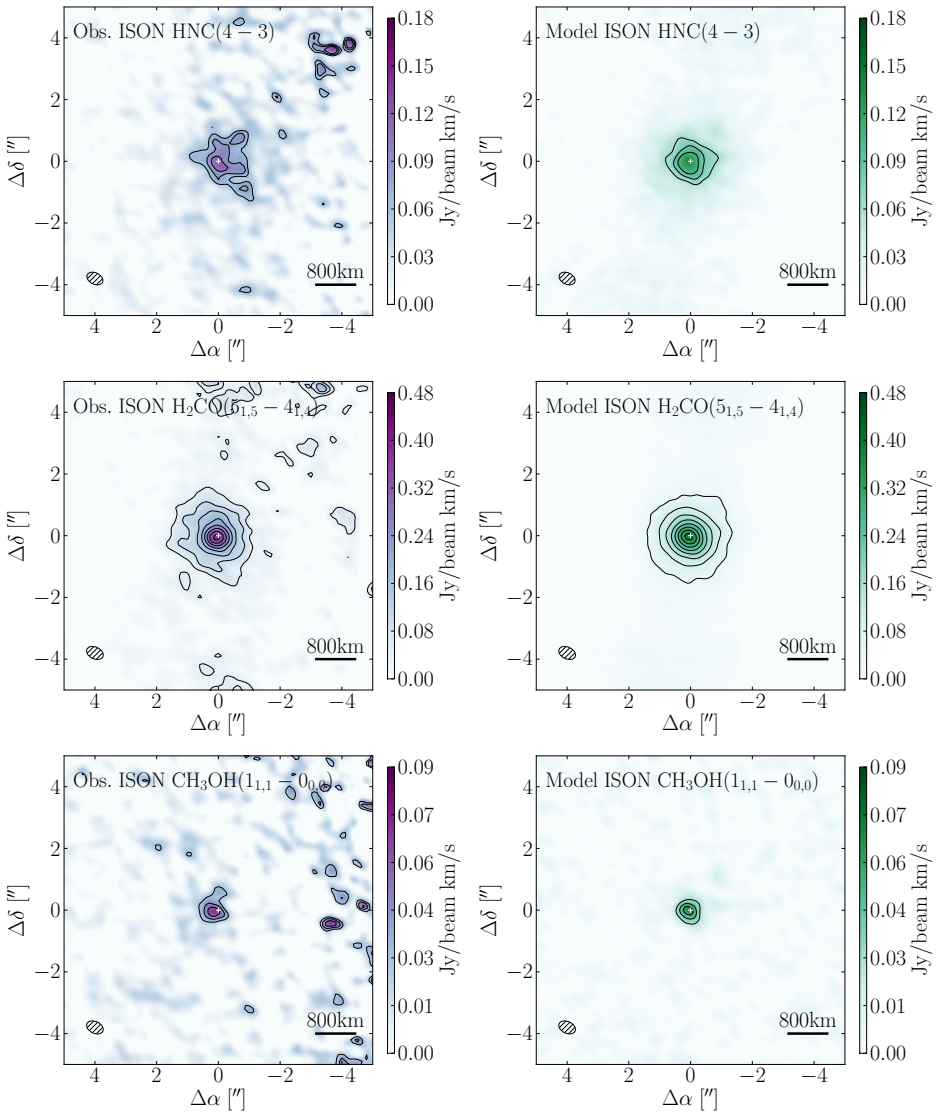

Figure 5.2: Continued

Table 5.2: Integrated Peak and Total Flux

Source	Species	Transition	E_{up} [K]	Q[a] [10^{26} s^{-1}]	Q_X/Q_{H_2O} [%]	L_p [km]	Peak Flux [Jy beam^{-1} km s^{-1}]		Total Flux[b] [Jy km s^{-1}]	
							Obs.[c]	Model	Obs.[c]	Model
C/2012 F6 (Lemmon)	HCN	3 – 2	25.52	$2.0\ ^{+0.4}_{-0.1}$	$0.064\ ^{+0.013}_{-0.003}$	10	0.47 ± 0.05	0.42	3.57 ± 0.08	4.24
		4 – 3	42.53	$2.3\ ^{+0.7}_{-0.1}$	$0.130\ ^{+0.040}_{-0.006}$	10	1.13 ± 0.11	1.03	8.63 ± 0.12	8.71
	HNC	4 – 3	43.51	$0.06\ ^{+0.04}_{-0.01}$	$0.003\ ^{+0.002}_{-0.001}$	10	0.07 ± 0.02	0.06	0.14 ± 0.06[d]	0.22[d]
	HCO^+	3 – 2	25.68	–	–	–	2.25×10^{-2} [e]	–	–	–
	H_2CO	$5_{1,5} - 4_{1,4}$	62.45	1.8 ± 0.3	0.102 ± 0.017	1400 ± 300	0.06 ± 0.01	0.06	0.79 ± 0.04	0.78
	CH_3OH	$1_{1,1} - 0_{0,0}$	16.84	17.1 ± 0.9[f]	0.967 ± 0.053	10	0.10 ± 0.01	0.14	0.80 ± 0.06	0.88
		$5_{2,3} - 4_{1,3}$	57.07	$12.0\ ^{+11.0}_{-2.0}$	$0.384\ ^{+0.352}_{-0.064}$	10	0.07 ± 0.02	0.06	0.42 ± 0.13	0.55
		$7_{1,6} - 6_{1,5}$	80.09	17.1 ± 0.9[f]	0.967 ± 0.053	10	0.13 ± 0.01	0.11	0.88 ± 0.04	0.76
		$7_{2,5} - 6_{2,4}$	87.26	17.1 ± 0.9[f]	0.967 ± 0.053	10	0.21 ± 0.02	0.18	1.28 ± 0.05	1.07
C/2012 S1 (ISON)	CS	7 – 6	65.83	$6.7\ ^{+0.8}_{-0.7}$	$0.191\ ^{+0.023}_{-0.020}$	200 ± 50	0.50 ± 0.05	0.50	5.21 ± 0.12	5.22
	HCN	4 – 3	42.53	4.0 ± 0.5	0.114 ± 0.014	150 ± 50	1.01 ± 0.10	1.02	11.78 ± 0.18	11.79
	HNC	4 – 3	43.51	$1.8\ ^{+0.1}_{-0.5}$	$0.051\ ^{+0.003}_{-0.014}$	$1200\ ^{+500}_{-100}$	0.12 ± 0.02	0.14	2.33 ± 0.19	2.22
	HCO^+	4 – 3	42.86	–	–	–	3.06×10^{-2} [e]	–	–	–
	H_2CO	$5_{1,5} - 4_{1,4}$	62.45	8.0 ± 1.0	0.229 ± 0.029	250 ± 50	0.38 ± 0.04	0.39	3.70 ± 0.14	3.72
	CH_3OH	$1_{1,1} - 0_{0,0}$	16.84	17.0 ± 5.0	0.486 ± 0.143	10	0.07 ± 0.02	0.07	0.25 ± 0.13	0.24

Notes. [a] Production rate including 1σ error. [b] Spectrally integrated line flux in circular aperture of 5 arcsec diameter centered on comet. [c] Errors assume a 10% absolute flux calibration error. [d] Spectrally integrated line flux in circular aperture of 3 arcsec diameter centered on comet. [e] 3σ upper limit. [f] Weighted average.

We adopt expansion velocities of 0.7 km s^{-1} for comet Lemmon and 1.0 km s^{-1} for comet ISON, derived from the half-width at half maximum (HWHM) of the HCN lines, and kinetic gas temperatures of 55 K for comet Lemmon and 90 K for comet ISON (Cordiner et al., 2014). In Sect. 5.4.4 we show how the line ratio of the HCN(4–3) and HCN(3–2) transitions constrain the kinetic temperature range to (20 – 110) K, and discuss how varying the kinetic temperature influences the molecular production rates we derive for each of the comets. We find that varying the temperature does not change the derived abundances significantly and therefore the temperatures of 55 K for Lemmon and 90 K for ISON are not critical parameters.

Photodestruction rates for HCN, CH_3OH and H_2CO are adopted from Crovisier (1994) (we assume that HNC has a similar photodestruction rate as HCN), H_2O from Budzien et al. (1994) and CS from Boissier et al. (2007). Water production rates of $(31.225 \pm 0.15)\times10^{28}$ s^{-1} on 2013 May 11 and $(17.68 \pm 0.26)\times10^{28}$ s^{-1} on 2013 May 30 for Lemmon and $(35.00 \pm 0.05)\times10^{28}$ s^{-1} for ISON are deduced by Combi et al. (2014a,b) using the SOHO satellite.

As input, the LIME code takes molecular collision rates which we adopt from the Leiden Atomic and Molecular Database (LAMDA; Schöier et al., 2005). The database holds collisional rates between H_2 and a number of the most abundant astronomical species. Since H_2O and not H_2 is the most important collisional partner in the inner part of cometary comae, we scale the LAMDA collision rates up with the hydrogen-to-water mass ratio of 9.0. To verify that this scaling does not bias our models, we vary the collisional scaling factor to investigate the effect. We find that for a collisional rate scaling factor higher than ∼5 our model outcome vary by only a few percent and that high scaling rate models converge to the outcome of a LTE model. The collisional rate scaling factor will be discussed further in Sect. 5.4.4.

In the inner part of cometary comae the excitation of molecules is dominated by collisions. As the distance from the nucleus increases, densities drop and radiative processes, e.g., fluorescence through solar pumping, or collisions with electrons, become important. Here we focus only on the inner $\sim3\times10^3$ km of the coma. In this range the local density ratio of H_2O to electrons is very large and radiative processes negligible (see Bockelée-Morvan et al., 2004, and references therein); therefore we only consider collisions with H_2O in our model. To make our models computationally efficient we assume an outer cut-off of 5×10^3 km.

To mimic the effect of the ALMA array, we run our model outputs through the tool "Simobserve" (part of the CASA package). By providing Simobserve with an antenna configuration file we sample our modelled sky brightness distribution with the same sampling function as that of the observations. We also simulate system noise and atmospheric effects in order to obtain a model as realistic and in accordance with observational effects as possible. After running Simobserve on all model outputs these are cleaned and imaged using the same parameters and routines as the observations.

5.4.1 Molecular production rates and parent scale lengths

We derive molecular production rates for all detected species. To do this, we create a grid of models spanning a large range of molecular production rates and parent scale lengths. We then select the model that best reproduces the velocity integrated peak intensity and the specially integrated line flux in an aperture centred on each of the comets by minimising the χ^2 values defined as the square of the difference between the observed and model flux divided by the square of the observational uncertainty. Our production rates are listed in Table 5.2.

We derive production rates of 6.7×10^{26} s^{-1} for CS in comet ISON and (12.0 – 17.1)$\times10^{26}$ s^{-1} and 17.0×10^{26} s^{-1} for CH_3OH in comets Lemmon and ISON respectively. The CH_3OH production rates derived for comet Lemmon are based on four transitions. For the transitions $CH_3OH(1_{1,1}–0_{0,0})$, $CH_3OH(7_{1,6}–6_{1,5})$ and $CH_3OH(7_{2,6}–6_{2,4})$, which are observed on the same date, we report the weighted average of the production rate of the best-fit model of the individual transitions. The derived production rates have a standard deviation of 5.3×10^{26} s^{-1}.

Using high-resolution spectroscopy DiSanti et al. (2016) derive production rates on ten pre-perihelion dates, including the dates of the observations presented here, of water and a number of trace molecules in ISON. They observe CH_3OH on 17 November and find a production rate of $(16.0 \pm 3.0)\times10^{26}$ s^{-1} consistent with our value of $(17.0 \pm 5.0)\times10^{26}$ s^{-1}. On 19 November DiSanti et al. (2016) find that the production rate of CH_3OH has increased by a factor ∼2.5 to $(39.0 \pm 3.8)\times10^{26}$ s^{-1}. On similar dates (13 – 16 November), Agúndez et al. (2014) derive a CH_3OH production rate of 43×10^{26} s^{-1} from observations carried out with the IRAM 30 m telescope. This range of CH_3OH production rate values clearly demonstrates the high variability of comets at decreasing heliocentric distances.

As mentioned in Sect. 5.3.2, we detect CS in the coma of comet ISON and derive a Q_{CS}/Q_{H_2O} production rate ratio of 0.19%. CS is not included in either of the studies by DiSanti et al. (2016) nor Agúndez et al. (2014) but compared to the sample of four objects for which CS has been observed (see Table 4 of Mumma & Charnley, 2011), the CS-to-water production rate ratio we derive here is a little high, by ∼40%, but consistent with CS being a product of CS_2 which is generally present in comets at a level of ∼(0.04 – 0.3) percent relative to water (Cochran et al., 2015).

Within errors, we derive production rates in agreement with those presented by Cordiner et al. (2014) for HCN and HNC in both comets. We derive a parent length scale of 1200 km for HNC in comet ISON, corresponding to a photodissociation rate of 8.3×10^{-4}s^{-1}. Due to the low signal-to-noise of the HNC observation in comet Lemmon we are unable to distinguish between parent and daughter models, which both fit the data. Compared to the list of molecular production rates relative to water summarised by Bockelée-Morvan et al. (2004), the rates we derive for HCN in each of the comets are consistent while our Q_{HNC}/Q_{H_2O} values are lower by ∼40% and higher by ∼25% for comets Lemmon and ISON respectively. It should be noted that including the uncertainty in L_p for HNC in comet ISON results in a production rate range of $(1.2 – 2.6)\times10^{26}$ s^{-1}, within the errors of what is listed by Bockelee-Morvan et al. (1994). The best-fit model for HCN in comet ISON has a non-zero parent scale length which is unexpected. Because of the size of the synthesised beam, structures in the coma of comet ISON which are smaller than ∼370 km will not be resolved. For L_p=10 km, we derive a production rate of HCN in ISON of 3.7×10^{26} s^{-1}.

For H_2CO we derive production rates of 1.8×10^{26} s^{-1} and 8.0×10^{26} s^{-1} for Lemmon and ISON respectively. These values are both lower than what has been reported by Cordiner et al. (2014). When modelling H_2CO, we only take into account ortho-H_2CO. Adopting an ortho-to-para ratio of 1 this implies that the production rates derived here only account for 50% of the H_2CO present in the comae of each of the comets and therefore the rates we report are lower limits. Taking the L_p uncertainties into account the range of production rates we derive for H_2CO are $(1.3 – 2.4)\times10^{26}$ s^{-1} for Lemmon and $(6.0 – 10.0)\times10^{26}$ s^{-1} for ISON. The parent scale lengths we derive for H_2CO are (1400 ± 300) km for Lemmon and (250 ± 50) km for ISON. These lengths correspond to photodissociation rates of 5×10^{-4} s^{-1} and 4×10^{-3} s^{-1} respectively, an order of magnitude higher that the photodissociation rate of CH_3OH (Crovisier, 1994). This mismatch

between parent scale length and dissociation rate, combined with the methanol-to-water rate ratio of ∼1% for Lemmon and only ∼0.5% for ISON, makes CH_3OH an unlikely predecessor of H_2CO.

While the derived Q_{HCN}/Q_{H_2O} ratios are fairly similar for comets Lemmon and ISON, other rate ratios vary. For instance, the Q_{CH_3OH}/Q_{H_2O} rate ratio we derive for comet Lemmon is higher by about a factor two compared to that derived for comet ISON. This difference may however be due to the fact that we derive the production rate of CH_3OH in comet ISON based solely on the $CH_3OH(1_{1,1}–0_{0,0})$ transition whereas the rate derived for comet Lemmon uses multiple transitions. If we derive the production rate of CH_3OH in comet Lemmon only taking into account the $CH_3OH(7_{1,6}–6_{1,5})$ and $CH_3OH(7_{2,6}–6_{2,4})$ transitions, we derive a value which is 20% higher than the value we derive when we also include the $CH_3OH(1_{1,1}–0_{0,0})$ transition. On the other hand, the Q_{HNC}/Q_{H_2O} and Q_{H_2CO}/Q_{H_2O} rates are both higher in comet ISON compared to comet Lemmon. In particular, the Q_{HNC}/Q_{H_2O} rate shows a difference of more than an order of magnitude between the two comets. As noted above, the uncertainty in the determination of the production rate of HNC in comet ISON, due to the uncertainty in L_p, is not negligible. However, this uncertainty is insufficient to account for the large variation between the comets and thus underlines the importance of, and need for, comprehensive cometary studies to sample as many different bodies as possible in order to reveal the full range of cometary compositions. In their study Cordiner et al. (2017b) suggest that the observations of comet ISON may have coincided with the release of a clump of material rich in HNC (-precursor) molecules. Such an event may provide an explanation for the large Q_{HNC}/Q_{H_2O} ration seen in comet ISON. It is also interesting to note that the production rate of H_2CO in comet ISON is high compared to the other detected species. This high rate may likewise be caused by an increase in the release of H_2CO-rich material, as the comet reaches perihelion shortly after the time of observation. In order to investigate similar events in the future, follow-up observations are essential.

5.4.2 Formation scenarios for detected molecules

As discussed above, we identify HNC as a dughter species, formed in the expanding coma material. A gas-phase formation route of HNC is in agreement with the findings of Irvine et al. (1998) who determined the HNC/HCN ratio in the bright comet Hale-Bopp. They show that the HNC/HCN ratio varies with heliocentric distance in a way that is consistent with models of gas-phase chemical production of HNC but which cannot be explained if the HNC molecules are released directly from the cometary nucleus. Another possible formation route for HNC is via isomerisation of HCN through proton transfer reactions (Rodgers & Charnley, 1998). However, in order for the HCN-HNC conversion to be efficient, hydrogen atoms in the cometary coma need to be suprathermal and the process is therefore insufficient to explain the HNC/HCN ratios observed in comets less active than Hale-Bopp. For these objects, the HNC/HCN ratio cannot be explained by neither ion-neutral coma chemistry nor isomerisation reactions (Rodgers & Charnley, 2001) and Rodgers et al. (2003) instead suggest that HNC is formed from degradation of some complex organic component, e.g., some variant of polymerized HCN, as also suggested by Cordiner et al. (2017b).

From a sample of 14 moderately active comets at heliocentric distances spanning 0.1 – 1.5 au, Lis et al. (2008) derive HNC/HCN ratios ranging from ∼0.03 to 0.3. They note that the HNC/HCN ratio is independent of the water production rate but dependent strongly on the heliocentric distance, with the largest ratios observed in objects with $r_h < 0.8$ au. Here we derive a HNC/HCN ratio of ∼0.03 for comet Lemmon. This value

is in the range of what is reported by Lis et al. (2008) and illustrates well the strong dependence of the HNC/HCN ratio on heliocentric distance (the heliocentric distance of comet Lemmon at the time of observations is ∼1.5 au). For comet ISON, we derive a HNC/HCN ratio of 0.45, consistent with ISONs small heliocentric distance and high HNC activity.

Observations of H_2CO in a number of cometary comae, both in-situ and from the ground, have likewise established that the radial profile of H_2CO cannot be explained by sublimation from the nucleus alone (see Cottin & Fray, 2008, for an overview). To account for the extended distribution of H_2CO a number of scenarios have been put forward. One possible formation route of H_2CO is through photodissociation of CH_3OH. This route is investigated by Cottin et al. (2004) who calculate the amount of CH_3OH required to account for the detected H_2CO in observations of comet 1P/Halley. Assuming H_2CO to be the main photoproduct of CH_3OH they find that CH_3OH would have to constitute 16% relative to water of the nucleus. Generally, CH_3OH is only found at levels up to ∼6.5% relative to water (Cochran et al., 2015), and we find ratios of ∼1% and ∼0.5% for Lemmon and ISON respectively. Moreover, they note that H_2CO is not the main dissociation product of CH_3OH but rather the CH_3O radial and therefore an abundance of CH_3OH of 16% is a lower limit. Cottin et al. (2004) therefore conclude that the extended source of H_2CO in comet Halley is inconsistent with a CH_3OH parent. As an alternative, Cottin et al. (2004) show that the distributed origin of H_2CO can be explained by photo- and/or thermal-degradation of refractory organic material in grains ejected from the cometary nucleus, with a simple addition-polymer of H_2CO as a likely candidate for the parent species. Cottin et al. (2004) are able to reproduce the observed distribution of H_2CO in comet Halley if the H_2CO-polymer is present in the grains at a mass fraction of a few percent. A similar explanation is given by Milam et al. (2006) who study the distribution of H_2CO in comets Hale-Bopp, Q4/NEAT and T7/LINEAR and likewise conclude that H_2CO must be coming from a source other than the nucleus. In contrast to Cottin et al. (2004) however, Milam et al. (2006) exclude a H_2CO-polymer as the most likely source for H_2CO, arguing that the required levels of such a polymer to efficiently account for the observed H_2CO are too high and that the possibility of forming such quantities of the polymers in interstellar space and the early solar system is low. Instead they propose that H_2CO is simply embedded in volatile grain matrices, entrained by solar radiation and released directly into the coma upon vaporization.

CS is thought to be a daughter species formed through photolysis of a parent molecule, such as CS_2, with a very short photodissociation lifetime of $(10^2 - 10^3)$ s at 1 au (see Feldman et al., 2004, and references therein). This short lifetime of the parent species indicates that CS is formed in the innermost part of the coma which is consistent with the observation of comet ISON were we find a spatial distribution of CS which is centrally peaked and coincide with the peak of the continuum emission. Due to the short lifetime of the CS parent molecule, high spatial resolution observations are needed to distinguish between parent and daughter formation scenarios. This is clearly illustrated when comparing the results presented here with those of previous studies, e.g., Snyder et al. (2001), who use the BIMA array to characterise CS in comet Hale-Bopp, have identified CS as a parent species. In contrast, we derive a parent scale length of (200 ± 50) km for the production of CS corresponding to a lifetime of the parent species of $(1.5 - 2.5) \times 10^2$ s (assuming an outflow velocity of 1.0 km s^{-1}), consistent with the predictions of Feldman et al. (2004) and supporting a coma formation route for CS. The apparent discrepancy between the results can however be explained by the large difference in spatial resolution (the smallest BIMA beam diameter is more than twenty times that of the synthesised ALMA beam). The new results therefore clearly demonstrate the superior resolving

power of ALMA compared to previous interferometric arrays. However, it should be noted that with a synthesised beam of $0\farcs59 \times 0\farcs39$ for the CS observations, corresponding to $\sim (375 \times 250)$ km at the distance of comet ISON, a parent scale length of 200 km is on the limit of what can be resolved. To unambiguously determine the origin of CS, higher spatial resolution observations are therefore essential.

5.4.3 Integrated intensity maps

In the case of comet Lemmon our models reproduce total integrated fluxes within ∼20% for HCN and ∼60% for HNC. For CH_3OH the total integrated flux of the $CH_3OH(1_{1,1}–0_{0,0})$ and $CH_3OH(5_{2,3}–4_{1,3})$ transition are overestimated by ∼10% and ∼30% respectively whereas the modelled $CH_3OH(7_{1,6}–6_{1,5})$ and $CH_3OH(7_{2,6}–6_{2,4})$ transitions are under-predicted with about 15% with respect to the observed values. The fact that our model under-predicts the total intensity suggests that we are not treating extended emission in a correct way. This is not surprising since we use a single parameter to express the outflow velocity of molecules. Such a single-parameter approach may very well be too much of a simplification, as indicated in the study of comet 17P/Holmes by Qi et al. (2015), where two distinct components in the molecular emission are identified. Adopting a lower outflow velocity will result in a higher abundance of material in the outer coma relative to a high outflow-velocity scenario and may provide a better fit to the data. However, introducing a variable temperature and velocity model, such as the one presented by Friedel et al. (2005), is beyond the scope of this paper. In addition, as shown by Cordiner et al. (2017b) for comet ISON, temporal variations on time scales < 20 min affect the production of the cometary species. This means that our peak intensity and integrated intensity sample different time averages which cannot necessarily be matched by a single time averaged production rate. In the case of comet ISON total integrated fluxes are reproduced within ∼5% of all observations.

5.4.4 HCN(4–3)/(3–2) line ratio

The uncertainty in the production rates we derive arise from uncertainties in excitation caused by the unknown hydrogen-to-water collisional rate scaling and coma temperature. As a means to constrain these uncertainties the ratio between lines can be of help. In the data presented here multiple HCN transitions are observed, albeit not on the same date. With the combination of observations in Band 6 and 7 of comet Lemmon we can study the line ration of HCN(4–3) to HCN(3–2). Using the velocity integrated peak intensity of each of the transitions we derive a line ratio for HCN(4–3)/(3–2) of 2.40 ± 0.34.

Ideally we want to observe multiple transitions of a single molecule (almost) simultaneously ensuring that transitions are observed under similar physical conditions. Unfortunately this is not the case for our observations where the HCN(4–3) and HCN(3–2) transitions are observed three weeks apart. Because of this, excitation conditions are not directly comparable i.e. water production rates vary by a factor ∼2 (Combi et al., 2014a).

As a workaround, we scale the HCN production rate of one set of observations to the other under the following assumptions; firstly, that the coma temperature and collision rate scaling are the same on both dates; secondly, that the water production rates on the individual dates are known, and thirdly, that the HCN/H_2O ratio is constant and does not change over time. Since HCN-variations are small between objects (see, e.g., Bockelée-Morvan et al., 2004; Mumma & Charnley, 2011; Cochran et al., 2015), it is reasonable to assume that HCN is constant within a single source. These assumptions allow us

to calculate the HCN(4–3) and HCN(3–2) lines for their respective dates (assuming the same, but unknown, HCN/H_2O ratio), and explore the effects of the adopted kinetic temperature and collisional rate scaling on the inferred Q_{HCN}/Q_{H_2O} ratio.

To investigate the extent to which the detection of a set of molecular transitions, and the ratio between them, can constrain the molecular production rate and kinetic temperature of a comet better than an individual transition, we construct a grid of models and calculate the HCN(4–3)/(3–2) line ratio for each grid cell varying the HCN production rate and kinetic temperature. We vary the temperature between 5 and 150 K and the Q_{HCN}/Q_{H_2O} ratio between 10^{-4} and 1.

Figure 5.3 shows the model grid with the HCN(4–3)/(3–2) line ration in green and the HCN(4–3) velocity integrated peak intensity in purple. The green and purple colour gradients indicate the 1, 2 and 3 σ ranges. We adopt a conservative 10% error on the absolute flux calibration which we add to the RMS noise in quadrature. In the same plot, the solid black lines show the reduced χ^2 contours equal to 1 and 3.

Our models show that the Q_{HCN}/Q_{H_2O} ratio is very well constrained to (0.5 – 3.0)$\times 10^{-3}$ for kinetic temperatures above 40 K. The HCN(4–3)/(3–2) line ratio excludes temperatures above 110 K at 1σ; higher temperatures are allowed at lower significance.

If the temperature drops below 30 K the Q_{HCN}/Q_{H_2O} rate increases rapidly. This means that very cold regions (<30 K) are not likely to contribute to the observed emission, as they would require Q_{HCN}/Q_{H_2O} ratios much larger than commonly found in comets. It also shows that the observations are not very sensitive to such cold material in the coma. Temperatures below 20 K can be ruled out entirely for the HCN line emitting vapor. Together, this shows that the adopted temperature of 55 K is not a critical parameter in determining Q_{HCN}/Q_{H_2O} except if we consider very cold regions in the coma.

To investigate the effect of the collisional rate scaling on Q_{HCN}/Q_{H_2O}, we construct a model grid varying the collisional rate scaling factor between 1 and 20. Figure 5.4 shows the model gird. Colours and lines are the same as in Fig. 5.3. It is clear that the Q_{HCN}/Q_{H_2O} ratio is not sensitive to the collisional rate scaling for scaling factors higher than ∼5. This shows that our adopted collisional rate scaling factor of 9.0 does not play a vital role when determining Q_{HCN}/Q_{H_2O}.

From Figs. 5.3 and 5.4 it is evident that the Q_{HCN}/Q_{H_2O} ratio is well constrained as long as temperatures below 30 K can be excluded and the collisional rate scaling factor is kept above 5.

Because we do not have multiple transitions of other species, we use the constraints on kinetic temperature and collisional rate scaling factor derived from the HCN(4–3)/HCN(3–2) line ratio to investigate how the derived molecular production rates of other species are effected. To do this, we run a set of four models representing each of the extreme cases; high temperature (T = 110 K (Lemmon) and T = 180 K (ISON)) and high collisional rate scaling (scaling rate factor = 20), high temperature and low collision rate scaling (scaling rate factor = 1), low temperature (T = 20 K) and high collisional rate scaling and low temperature and low collisional rate scaling. We run models for CS, HCN and CH_3OH in comet ISON and CH_3OH in comet Lemmon. We do not run models for the distributed sources, HNC and H_2CO, because the uncertainty on the production rates derived here is dominated by uncertainties in L_p.

For collisional scaling rates less than 5, the molecular production rate vary within 3% for CS, 9% for HCN and 26% for CH_3OH. For collisional scaling rates higher than 5 the molecular production rate become independent of collisional rate scaling. This is reassuring for the robustness of our model but also illustrates that even if the molecular production rate of a specific species can be very well constrained, no constraint can be set on the collisional cross section of water with respect to this species. Thus the precise

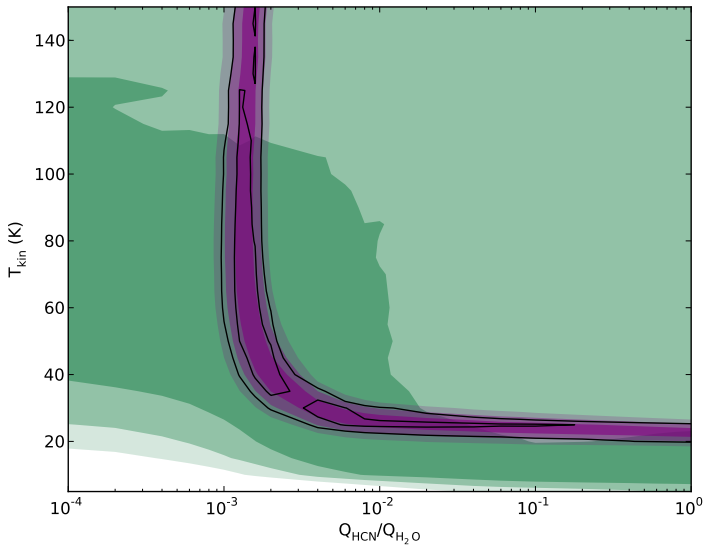

Figure 5.3: Model grid of HCN(4–3)/(3–2) line ratio as function of production rate and kinetic temperature. Green and purple colour scales represent the 1, 2 and 3 σ ranges of the HCN(4–3)/(3–2) line ratio and HCN(4–3) velocity integrated peak intensity respectively. The black solid lines indicate the reduced χ^2 contours equal to 1 and 3.

determination of collisional cross sections of water with respect to other species presents a challenge for future laboratory works. Until such collisional cross section are available, ALMA provides a particularly beneficial tool since its small beam allows us to probe only the innermost part of the cometary coma where molecular densities are high enough to ensure that excitations are close to LTE, i.e., the exact values of the collisional rates are no longer significant.

In contrast to the case of the collisional rate scaling factor, we do see a dependence of the derived production rate on kinetic temperature. In the case of CS and HCN, the high temperature case returns production rates within ∼40% and ∼50% of those derived using the temperatures of 55 K and 90 K for comets Lemmon and ISON respectively (with the derived molecular production rates ranging $(1.7 - 3.0)\times10^{26}$ s^{-1} for HCN in comet Lemmon and $(6.0 - 9.5)\times10^{26}$ s^{-1} for CS, and $(3.5 - 5.9)\times10^{26}$ s^{-1} for HCN in comet ISON). In the low temperature cases, production rates need to be unreasonably high, i.e., orders of magnitude higher than what is commonly observed in comets, in order to reproduce the observations. It is important to note that if very low-temperature regions exist in the coma, e.g., as a result of adiabatic expansion, molecular line observations are essentially 'blind' to them. As shown by Cordiner et al. (2017a) for comet C/2012 K1 (PanSTARRS), such very cold regions may exist in the cometary coma and it is therefore important for future studies to characterize the coma temperature profile in order to derive reliable molecular production rates. In the case of CH_3OH, the high and low temperature models result in a range of derived production rates of $(4.1 - 36.3)\times10^{26}$ s^{-1} for comet Lemmon and $(2.4 - 45.0)\times10^{26}$ s^{-1} for comet ISON.

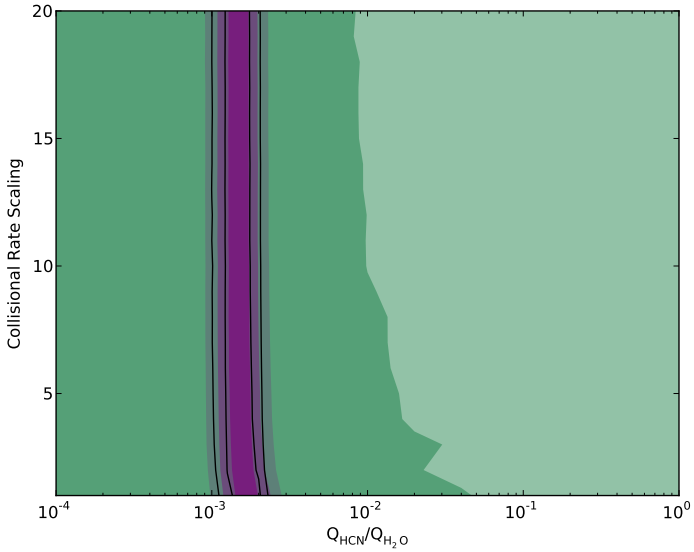

Figure 5.4: Model grid of HCN(4–3)/(3–2) line ratio as function of production rate and collisional rate scaling factor. Green and purple colour scales represent the 1,2 and 3 σ ranges of the HCN(4–3)/(3–2) line ratio and HCN(4–3) velocity integrated peak intensity respectively. The black solid lines indicate the reduced χ^2 contours equal to 1 and 3.

From our analysis, it is clear that while the collisional rate scaling factor only plays a minor role when determining molecular production rates, and has no effect on the model outcome when they are higher than 5, an accurate estimate of the kinetic gas temperature is important. It is also clear that multiple transitions, observed simultaneously, can help constrain molecular production rates considerably.

5.5 Conclusion

In this paper we analyse archival ALMA observations of volatile species in the comae of comets Lemmon and ISON. We report the first ALMA detection of CS in the coma of comet ISON as well as several CH_3OH transitions and the HCN(4–3)/HCN(3–2) line ratio in comet Lemmon. In addition we confirm the detection of HCN, HNC and H_2CO in each comet, as reported by Cordiner et al. (2014).

We derive a parent scale length of (200 $\pm$ 50) km for CS. A structure of this size is similar to that of the ALMA synthesised beam and therefore supports the theory of CS being a daughter rather than parent species.

We have mapped the spatial distribution of each molecule and find centrally peaked, symmetric distributions for HCN and CH_3OH, indicative of parent species, i.e., species sublimated directly from the cometary nucleus. In contrast we see distributed origins for HNC and H_2CO in both comets consistent with these species being either the result of gas-phase chemistry in the coma or transported away from the nucleus by some refractory compound before being evaporated.

To model the individual line transition intensities we use the 3D radiative transfer code LIME, assuming a Haser profile with constant outflow velocity to represent the density of molecules in the comae. Based on these models we derive molecular production rates for each of the detected species. Assuming a kinetic gas temperature of 55 K for comet Lemmon and 90 K for comet ISON we derive production rates of 6.7×10^{26} s^{-1} for CS, $(2.0-4.0)\times10^{26}$ s^{-1} for HCN, $(0.06-1.8)\times10^{26}$ s^{-1} for HNC, $(1.8-8.0)\times10^{26}$ s^{-1} for H_2CO and $(12.0-17.1)\times10^{26}$ s^{-1} for CH_3OH. Our derived production rates are consistent with production rates relative to water in the literature (e.g. Mumma & Charnley, 2011; Bockelée-Morvan et al., 2004).

Because collisional cross sections of water with respect to the species detected here are unknown, we scale the H_2 collisional rates up with the hydrogen-to-water mass ratio of 9.0. We investigate the effect of this scaling on the derived production rates and conclude that the scaling factor is not a critical parameter in our model. The independence of the derived production rate with respect to the collisional rate scaling is a consequence of the small ALMA beam which allows us to only sample the inner and high density region of the coma where excitations are close to LTE and the exact value of the water collisional cross sections therefore become less important.

Under the assumption of a constant temperature and Q_{HCN}/Q_{H_2O} ratio, simultaneous modelling of the HCN(3–2) line of 2013 May 11 and the HCN(4–3) line of 2013 June 1, shows that the line ratio of HCN(4–3)/HCN(3–2) provides good constraints on the kinetic gas temperature and molecular production rate. The HCN(4–3)/HCN(3–2) line ratio excludes temperatures above 110 K at 1σ, while temperatures below 30 K would require unusually large Q_{HCN}/Q_{H_2O} ratios in order to reproduce the observations. Observations are not sensitive to material below 20 K. With the constraints on temperature derived from the HCN(4–3)/HCN(3–2) line ratio, we investigate the effect of this range on the derived production rate of other species. In both comets Lemmon and ISON the production rate of HCN is reproduced within 50% in the high-temperature scenario, while the low-temperature scenario can be excluded completely. For CS this number is 40%. In the case of CH_3OH, we find a variation in the derived production rate from the low to high temperature case corresponding to an order of magnitude. This illustrates how the constraints on temperature derived from multi-transition observations of cometary volatiles can improve the accuracy of inferred production rates.

Acknowledgements. The authors would like to thank Dr. Martin Cordiner for valuable discussions and the anonymous referee for constructive comments that significantly improved our manuscript. We acknowledge data reduction support from Allegro, the European ALMA Regional Center node in the Netherlands, and Markus Schmalzl in particular for expert advice. This paper makes use of the following ALMA data: ADS/JAO.ALMA#2012.A.00020.S, #2012.A.00033.S and #2011.0.00012.SV. ALMA is a partnership of ESO (representing its member states), NSF (USA) and NINS (Japan), together with NRC (Canada) and NSC and ASIAA (Taiwan) and KASI (Republic of Korea), in cooperation with the Republic of Chile. The Joint ALMA Observatory is operated by ESO, AUI/NRAO and NAOJ

Bibliography

Agúndez, M., Biver, N., Santos-Sanz, P., Bockelée-Morvan, D., & Moreno, R. 2014, A&A, 564, L2

A'Hearn, M. F. 2011, ARA&A, 49, 281

A'Hearn, M. F., Feaga, L. M., Keller, H. U., et al. 2012, ApJ, 758, 29

Aikawa, Y., Wakelam, V., Hersant, F., Garrod, R. T., & Herbst, E. 2012, ApJ, 760, 40

Altwegg, K., Balsiger, H., Berthelier, J. J., et al. 2017, MNRAS, 469, S130

Anderson, T., Crownover, R. L., Herbst, E., & De Lucia, F. C. 1988, ApJS, 67, 135

Anderson, T., Herbst, E., & Delucia, F. 1993, Journal of Molecular Spectroscopy, 159, 410

André, P., Di Francesco, J., Ward-Thompson, D., et al. 2014, Protostars and Planets VI, 27

Andrews, S. M., Wilner, D. J., Zhu, Z., et al. 2016, ApJ, 820, L40

Aponte, J. C., Elsila, J. E., Glavin, D. P., et al. 2017, ACS Earth and Space Chemistry, vol. 1, issue 1, pp. 3-13, 1, 3

Bacmann, A., Taquet, V., Faure, A., Kahane, C., & Ceccarelli, C. 2012, A&A, 541, L12

Bailer-Jones, C. A. L., Rybizki, J., Fouesneau, M., Mantelet, G., & Andrae, R. 2018, AJ, 156, 58

Balucani, N., Ceccarelli, C., & Taquet, V. 2015, MNRAS, 449, L16

Barone, V., Latouche, C., Skouteris, D., et al. 2015, MNRAS, 453, L31

Belloche, A., Müller, H. S. P., Garrod, R. T., & Menten, K. M. 2016, A&A, 587, A91

Belloche, A., Müller, H. S. P., Menten, K. M., Schilke, P., & Comito, C. 2013, A&A, 559, A47

Beltrán, M. T., Brand, J., Cesaroni, R., et al. 2006, A&A, 447, 221

Bergin, E. A., Aikawa, Y., Blake, G. A., & van Dishoeck, E. F. 2007, Protostars and Planets V, 751

Bianchi, E., Codella, C., Ceccarelli, C., et al. 2017, A&A, 606, L7

Bisschop, S. E., Jørgensen, J. K., van Dishoeck, E. F., & de Wachter, E. B. M. 2007, A&A, 465, 913

Bizzocchi, L., Caselli, P., Spezzano, S., & Leonardo, E. 2014, A&A, 569, A27

Blake, G. A., Sutton, E. C., Masson, C. R., & Phillips, T. G. 1987, ApJ, 315, 621

Bockelee-Morvan, D., Crovisier, J., Colom, P., & Despois, D. 1994, A&A, 287, 647

Bockelée-Morvan, D., Crovisier, J., Mumma, M. J., & Weaver, H. A. 2004, The composition of cometary volatiles, ed. M. C. Festou, H. U. Keller, & H. A. Weaver (University of Arizona Press), 391–423

Bockelée-Morvan, D., Wink, J., Despois, D., et al. 1997, Earth Moon and Planets, 78, 67

Bøgelund, E. G., McGuire, B. A., Ligterink, N. F. W., et al. 2018, A&A

Boissier, J., Bockelée-Morvan, D., Biver, N., et al. 2007, A&A, 475, 1131

Boley, P. A., Linz, H., van Boekel, R., et al. 2012, A&A, 547, A88

Bonfand, M., Belloche, A., Menten, K. M., Garrod, R. T., & Müller, H. S. P. 2017, A&A, 604, A60

Boogert, A. C. A., Gerakines, P. A., & Whittet, D. C. B. 2015, ARA&A, 53, 541

Boonman, A. M. S., van Dishoeck, E. F., Lahuis, F., & Doty, S. D. 2003, A&A, 399, 1063

Bossa, J.-B., Duvernay, F., Theulé, P., et al. 2009, A&A, 506, 601

Bottinelli, S., Ceccarelli, C., Lefloch, B., et al. 2004, ApJ, 615, 354

Brinch, C. & Hogerheijde, M. R. 2010, A&A, 523, A25

Brogan, C. L., Hunter, T. R., Cyganowski, C. J., et al. 2016, ApJ, 832, 187

Brouillet, N., Despois, D., Lu, X.-H., et al. 2015, A&A, 576, A129

Budzien, S. A., Festou, M. C., & Feldman, P. D. 1994, Icarus, 107, 164

Calcutt, H., Jørgensen, J. K., Müller, H. S. P., et al. 2018, A&A, 616, A90

Carney, M. T., Fedele, D., Hogerheijde, M. R., et al. 2018, A&A, 614, A106

Carral, P., Kurtz, S. E., Rodríguez, L. F., et al. 2002, AJ, 123, 2574

Caselli, P. & Ceccarelli, C. 2012, A&A Rev., 20, 56

Caux, E., Kahane, C., Castets, A., et al. 2011, A&A, 532, A23

Cazaux, S., Tielens, A. G. G. M., Ceccarelli, C., et al. 2003, ApJ, 593, L51

Ceccarelli, C., Castets, A., Loinard, L., Caux, E., & Tielens, A. G. G. M. 1998, A&A, 338, L43

Cernicharo, J., Marcelino, N., Roueff, E., et al. 2012, ApJ, 759, L43

Charnley, S. 2001, in The Bridge Between the Big Bang and Biology: Stars, Planetary Systems, Atmospheres, Volcanoes: Their Link to Life, ed. F. Giovannelli, 139

Charnley, S. B., Tielens, A. G. G. M., & Millar, T. J. 1992, ApJ, 399, L71

Charnley, S. B., Tielens, A. G. G. M., & Rodgers, S. D. 1997, ApJ, 482, L203

Chibueze, J. O., Omodaka, T., Handa, T., et al. 2014, ApJ, 784, 114

Chuang, K.-J., Fedoseev, G., Qasim, D., et al. 2017, MNRAS, 467, 2552

Chuang, K.-J., Fedoseev, G., Qasim, D., et al. 2018, ApJ, 853, 102

Cieza, L. A., Casassus, S., Tobin, J., et al. 2016, Nature, 535, 258

Cochran, A. L., Levasseur-Regourd, A.-C., Cordiner, M., et al. 2015, Space Sci. Rev., 197, 9

Codella, C., Ceccarelli, C., Caselli, P., et al. 2017, A&A, 605, L3

Cole, C. A., Wehres, N., Yang, Z., et al. 2012, ApJ, 754, L5

Combi, M. R., Bertaux, J.-L., Quémerais, E., et al. 2014a, AJ, 147, 126

Combi, M. R., Fougere, N., Mäkinen, J. T. T., et al. 2014b, ApJ, 788, L7

Combi, M. R., Harris, W. M., & Smyth, W. H. 2004, Gas dynamics and kinetics in the cometary coma: theory and observations, ed. M. C. Festou, H. U. Keller, & H. A. Weaver (University of Arizona Press), 523–552

Cordiner, M. A., Biver, N., Crovisier, J., et al. 2017a, ApJ, 837, 177

Cordiner, M. A., Boissier, J., Charnley, S. B., et al. 2017b, ApJ, 838, 147

Cordiner, M. A., Remijan, A. J., Boissier, J., et al. 2014, ApJ, 792, L2

Cottin, H., Bénilan, Y., Gazeau, M.-C., & Raulin, F. 2004, Icarus, 167, 397

Cottin, H. & Fray, N. 2008, Space Sci. Rev., 138, 179

Coutens, A., Jørgensen, J. K., van der Wiel, M. H. D., et al. 2016, A&A, 590, L6

Crockett, N. R., Bergin, E. A., Neill, J. L., et al. 2015, ApJ, 806, 239

Crockett, N. R., Bergin, E. A., Neill, J. L., et al. 2014, ApJ, 787, 112

Crovisier, J. 1994, J. Geophys. Res., 99, 3777

Crovisier, J., Bockelée-Morvan, D., Colom, P., et al. 2004, A&A, 418, 1141

Danger, G., Borget, F., Chomat, M., et al. 2011, A&A, 535, A47

De Buizer, J. M. 2003, MNRAS, 341, 277

Dickens, J. E., Irvine, W. M., DeVries, C. H., & Ohishi, M. 1997, ApJ, 479, 307

DiSanti, M. A., Bonev, B. P., Gibb, E. L., et al. 2016, ApJ, 820, 34

Dobbs, C. L., Krumholz, M. R., Ballesteros-Paredes, J., et al. 2014, Protostars and Planets VI, 3

Drozdovskaya, M. N., van Dishoeck, E. F., Jørgensen, J. K., et al. 2018, MNRAS, 476, 4949

Drozdovskaya, M. N., Walsh, C., van Dishoeck, E. F., et al. 2016, MNRAS, 462, 977

Dunham, M. M., Stutz, A. M., Allen, L. E., et al. 2014, Protostars and Planets VI, 195

Faure, A., Faure, M., Theulé, P., Quirico, E., & Schmitt, B. 2015, A&A, 584, A98

Favre, C., Pagani, L., Goldsmith, P. F., et al. 2017, A&A, 604, L2

Fayolle, E. C., Öberg, K. I., Garrod, R. T., van Dishoeck, E. F., & Bisschop, S. E. 2015, A&A, 576, A45

Fedoseev, G., Chuang, K.-J., van Dishoeck, E. F., Ioppolo, S., & Linnartz, H. 2016, MNRAS, 460, 4297

Fedoseev, G., Cuppen, H. M., Ioppolo, S., Lamberts, T., & Linnartz, H. 2015, MNRAS, 448, 1288

Feldman, P. D., Cochran, A. L., & Combi, M. R. 2004, Spectroscopic investigations of fragment species in the coma, ed. G. W. Kronk (University of Arizona Press), 425–447

Ferrière, K. M. 2001, Reviews of Modern Physics, 73, 1031

Förstel, M., Bergantini, A., Maksyutenko, P., Góbi, S., & Kaiser, R. I. 2017, ApJ, 845, 83

Friedel, D. N., Remijan, A. J., Snyder, L. E., et al. 2005, ApJ, 630, 623

Fuchs, G. W., Cuppen, H. M., Ioppolo, S., et al. 2009, A&A, 505, 629

Fuselier, S. A., Altwegg, K., Balsiger, H., et al. 2015, A&A, 583, A2

Garrod, R., Park, I. H., Caselli, P., & Herbst, E. 2006, Faraday Discussions, 133, 51

Garrod, R. T. 2013, ApJ, 765, 60

Garrod, R. T., Belloche, A., Müller, H. S. P., & Menten, K. M. 2017, A&A, 601, A48

Garrod, R. T., Widicus Weaver, S. L., & Herbst, E. 2008, ApJ, 682, 283

Geppert, W. D., Hellberg, F., Österdahl, F., et al. 2005, in IAU Symposium, Vol. 231, Astrochemistry: Recent Successes and Current Challenges, ed. D. C. Lis, G. A. Blake, & E. Herbst, 117–124

Gezari, D. Y. 1982, ApJ, 259, L29

Goesmann, F., Rosenbauer, H., Bredehöft, J. H., et al. 2015, Science, 349

Goldman, N., Reed, E. J., Fried, L. E., William Kuo, I.-F., & Maiti, A. 2010, Nature Chemistry, 2, 949

Green, J. A. & McClure-Griffiths, N. M. 2011, MNRAS, 417, 2500

Halfen, D. T., Ilyushin, V. V., & Ziurys, L. M. 2013, ApJ, 767, 66

Hasegawa, T. I. & Herbst, E. 1993, MNRAS, 263, 589

Haser, L. 1957, Bulletin de la Societe Royale des Sciences de Liege, 43, 740

Hatchell, J., Thompson, M. A., Millar, T. J., & MacDonald, G. H. 1998, A&AS, 133, 29

Henning, T., Friedemann, C., Guertler, J., & Dorschner, J. 1984, Astronomische Nachrichten, 305, 67

Herbst, E. & van Dishoeck, E. F. 2009, ARA&A, 47, 427

Heyer, M. & Dame, T. M. 2015, ARA&A, 53, 583

Hidaka, H., Watanabe, M., Kouchi, A., & Watanabe, N. 2009, ApJ, 702, 291

Holtom, P. D., Bennett, C. J., Osamura, Y., Mason, N. J., & Kaiser, R. I. 2005, ApJ, 626, 940

Hunter, T. R., Brogan, C. L., MacLeod, G., et al. 2017, ApJ, 837, L29

Hunter, T. R., Brogan, C. L., Megeath, S. T., et al. 2006, ApJ, 649, 888

Ikeda, M., Ohishi, M., Nummelin, A., et al. 2001, ApJ, 560, 792

Irvine, W. M., Bergin, E. A., Dickens, J. E., et al. 1998, Nature, 393, 547

Isokoski, K., Bottinelli, S., & van Dishoeck, E. F. 2013, A&A, 554, A100

Jeans, J. H. 1902, Royal Society of London Philosophical Transactions Series A, 199, 1

Johnston, K. G., Beuther, H., Linz, H., et al. 2014, in Astrophysics and Space Science Proceedings, Vol. 36, The Labyrinth of Star Formation, ed. D. Stamatellos, S. Goodwin, & D. Ward-Thompson, 413

Johnston, K. G., Robitaille, T. P., Beuther, H., et al. 2015, ApJ, 813, L19

Jones, B. M., Bennett, C. J., & Kaiser, R. I. 2011, ApJ, 734, 78

Jørgensen, J. K., Müller, H. S. P., Calcutt, H., et al. 2018, A&A, 620, A170

Jørgensen, J. K., van der Wiel, M. H. D., Coutens, A., et al. 2016, A&A, 595, A117

Kahane, C., Ceccarelli, C., Faure, A., & Caux, E. 2013, ApJ, 763, L38

Kaifu, N., Morimoto, M., Nagane, K., et al. 1974, ApJ, 191, L135

Keane, J. V., Milam, S. N., Coulson, I. M., et al. 2016, ApJ, 831, 207

Kim, Y. S. & Kaiser, R. I. 2011, ApJ, 729, 68

Kumar, A., Sharma, R., & Kamaluddin. 2014, Astrobiology, 14, 769

Le Roy, L., Altwegg, K., Balsiger, H., et al. 2015, A&A, 583, A1

Lee, C.-W., Kim, J.-K., Moon, E.-S., Minh, Y. C., & Kang, H. 2009, ApJ, 697, 428

Leurini, S., Schilke, P., Parise, B., et al. 2006, A&A, 454, L83

Ligterink, N. F. W., Calcutt, H., Coutens, A., et al. 2018a, A&A, 619, A28

Ligterink, N. F. W., Tenenbaum, E. D., & van Dishoeck, E. F. 2015, A&A, 576, A35

Ligterink, N. F. W., Terwisscha van Scheltinga, J., Taquet, V., et al. 2018b, MNRAS, 480, 3628

Linnartz, H., Ioppolo, S., & Fedoseev, G. 2015, International Reviews in Physical Chemistry, 2015, Volume 34, Issue 2, pages 205-237

Linsky, J. L. 2003, Space Sci. Rev., 106, 49

Lis, D. C., Bockelée-Morvan, D., Boissier, J., et al. 2008, ApJ, 675, 931

López-Sepulcre, A., Jaber, A. A., Mendoza, E., et al. 2015, MNRAS, 449, 2438

Lykke, J. M., Coutens, A., Jørgensen, J. K., et al. 2017, A&A, 597, A53

Lykke, J. M., Favre, C., Bergin, E. A., & Jørgensen, J. K. 2015, A&A, 582, A64

Martin, R. G. & Livio, M. 2015, ApJ, 810, 105

Mathis, J. S., Mezger, P. G., & Panagia, N. 1983, A&A, 128, 212

Matthews, C. N. & Minard, R. D. 2006, Faraday Discussions, 133, 393

McBreen, B., Fazio, G. G., Stier, M., & Wright, E. L. 1979, ApJ, 232, L183

McCutcheon, W. H., Sandell, G., Matthews, H. E., et al. 2000, MNRAS, 316, 152

McGuire, B. A., Brogan, C. L., Hunter, T. R., et al. 2018, ApJ, 863, L35

McGuire, B. A., Shingledecker, C. N., Willis, E. R., et al. 2017, ApJ, 851, L46

Milam, S. N., Remijan, A. J., Womack, M., et al. 2006, ApJ, 649, 1169

Milam, S. N., Savage, C., Brewster, M. A., Ziurys, L. M., & Wyckoff, S. 2005, ApJ, 634, 1126

Minissale, M., Moudens, A., Baouche, S., Chaabouni, H., & Dulieu, F. 2016, MNRAS, 458, 2953

Motiyenko, R. A., Ilyushin, V. V., Drouin, B. J., Yu, S., & Margulès, L. 2014, A&A, 563, A137

Motte, F., Bontemps, S., & Louvet, F. 2018, ARA&A, 56, 41

Müller, H. S. P., Schlöder, F., Stutzki, J., & Winnewisser, G. 2005, Journal of Molecular Structure, 742, 215

Müller, H. S. P., Thorwirth, S., Roth, D. A., & Winnewisser, G. 2001, A&A, 370, L49

Mumma, M. J. & Charnley, S. B. 2011, ARA&A, 49, 471

Murray, N. 2011, ApJ, 729, 133

Nagaoka, A., Watanabe, N., & Kouchi, A. 2005, ApJ, 624, L29

Neill, J. L., Bergin, E. A., Lis, D. C., et al. 2014, ApJ, 789, 8

Neill, J. L., Crockett, N. R., Bergin, E. A., Pearson, J. C., & Xu, L.-H. 2013, ApJ, 777, 85

Neill, J. L., Steber, A. L., Muckle, M. T., et al. 2011, Journal of Physical Chemistry A, 115, 6472

Noble, J. A., Theule, P., Congiu, E., et al. 2015, A&A, 576, A91

Oba, Y., Tomaru, T., Lamberts, T., Kouchi, A., & Watanabe, N. 2018, Nature Astronomy, 2, 228

Öberg, K. I., Fuchs, G. W., Awad, Z., et al. 2007, ApJ, 662, L23

Öberg, K. I., Guzmán, V. V., Furuya, K., et al. 2015, Nature, 520, 198

Ohishi, M., Suzuki, T., Hirota, T., Saito, M., & Kaifu, N. 2017 [e-prints[arXiv]1708.06871]

Pagani, L., Favre, C., Goldsmith, P. F., et al. 2017, A&A, 604, A32

Parise, B., Castets, A., Herbst, E., et al. 2004, A&A, 416, 159

Parise, B., Ceccarelli, C., Tielens, A. G. G. M., et al. 2006, A&A, 453, 949

Parise, B., Ceccarelli, C., Tielens, A. G. G. M., et al. 2002, A&A, 393, L49

Patel, B. H., Percivalle, C., Ritson, D. J., Duffy, C. D., & Sutherland, J. D. 2015, Nature Chemistry, 7, 301

Pearson, J. C., Yu, S., & Drouin, B. J. 2012, Journal of Molecular Spectroscopy, 280, 119

Peng, T.-C., Despois, D., Brouillet, N., Parise, B., & Baudry, A. 2012, A&A, 543, A152

Pérez, L. M., Carpenter, J. M., Andrews, S. M., et al. 2016, Science, 353, 1519

Persi, P., Roth, M., Tapia, M., et al. 1996, A&A, 307, 591

Persi, P. & Tapia, M. 2008, Star Formation in NGC 6334, ed. B. Reipurth, 456

Phillips, C. J., Norris, R. P., Ellingsen, S. P., & McCulloch, P. M. 1998, MNRAS, 300, 1131

Pickett, H. M., Poynter, R. L., Cohen, E. A., et al. 1998, J. Quant. Spec. Radiat. Transf., 60, 883

Plunkett, A. L., Arce, H. G., Mardones, D., et al. 2015, Nature, 527, 70

Prodanović, T., Steigman, G., & Fields, B. D. 2010, MNRAS, 406, 1108

Qi, C., Hogerheijde, M. R., Jewitt, D., Gurwell, M. A., & Wilner, D. J. 2015, ApJ, 799, 110

Qin, S.-L., Wu, Y., Huang, M., et al. 2010, ApJ, 711, 399

Qiu, K., Wyrowski, F., Menten, K. M., et al. 2011, ApJ, 743, L25

Ratajczak, A., Quirico, E., Faure, A., Schmitt, B., & Ceccarelli, C. 2009, A&A, 496, L21

Ratajczak, A., Taquet, V., Kahane, C., et al. 2011, A&A, 528, L13

Reid, M. J., Menten, K. M., Brunthaler, A., et al. 2014, ApJ, 783, 130

Remijan, A. J., Milam, S. N., Womack, M., et al. 2008, ApJ, 689, 613

Rickman, H. 2010, in Lecture Notes in Physics, Berlin Springer Verlag, Vol. 790, Lecture Notes in Physics, Berlin Springer Verlag, ed. J. Souchay & R. Dvorak, 341–399

Roberts, H., Herbst, E., & Millar, T. J. 2003, ApJ, 591, L41

Rodgers, S. D., Butner, H. M., Charnley, S. B., & Ehrenfreund, P. 2003, Advances in Space Research, 31, 2577

Rodgers, S. D. & Charnley, S. B. 1998, ApJ, 501, L227

Rodgers, S. D. & Charnley, S. B. 2001, MNRAS, 323, 84

Russeil, D., Schneider, N., Anderson, L. D., et al. 2013, A&A, 554, A42

Russeil, D., Zavagno, A., Adami, C., et al. 2012, A&A, 538, A142

Sakai, N. & Yamamoto, S. 2013, Chemical Reviews, 113, 8981

Saladino, R., Carota, E., Botta, G., et al. 2016, Origins of Life and Evolution of the Biosphere, 46, 515

Saladino, R., Crestini, C., Ciciriello, F., Costanzo, G., & di Mauro, E. 2006, Origins of Life and Evolution of the Biosphere, 36, 523

Salinas, V. N., Hogerheijde, M. R., Mathews, G. S., et al. 2017, A&A, 606, A125

Schöier, F. L., Jørgensen, J. K., van Dishoeck, E. F., & Blake, G. A. 2002, A&A, 390, 1001

Schöier, F. L., van der Tak, F. F. S., van Dishoeck, E. F., & Black, J. H. 2005, A&A, 432, 369

Smith, A. M., Stecher, T. P., & Casswell, L. 1980, ApJ, 242, 402

Snyder, L. E., Veal, J. M., Woodney, L. M., et al. 2001, AJ, 121, 1147

Stahler, S. W. & Palla, F. 2005, The Formation of Stars, 865

Suzuki, T., Ohishi, M., Hirota, T., et al. 2016, ApJ, 825, 79

Suzuki, T., Ohishi, M., Saito, M., et al. 2018, ApJS, 237, 3

Tan, J. C., Beltrán, M. T., Caselli, P., et al. 2014, Protostars and Planets VI, 149

Taquet, V., Ceccarelli, C., & Kahane, C. 2012, ApJ, 748, L3

Taquet, V., Charnley, S. B., & Sipilä, O. 2014, ApJ, 791, 1

Taquet, V., Peters, P. S., Kahane, C., et al. 2013, A&A, 550, A127

Taquet, V., Wirström, E. S., & Charnley, S. B. 2016, ApJ, 821, 46

Testi, L., Birnstiel, T., Ricci, L., et al. 2014, Protostars and Planets VI, 339

Theule, P., Borget, F., Mispelaer, F., et al. 2011, A&A, 534, A64

Tielens, A. G. G. M. 1983, A&A, 119, 177

Tielens, A. G. G. M. 2013, Reviews of Modern Physics, 85, 1021

Tielens, A. G. G. M. & Charnley, S. B. 1997, Origins of Life and Evolution of the Biosphere, 27, 23

Tielens, A. G. G. M. & Hagen, W. 1982, A&A, 114, 245

Tobin, J. J., Kratter, K. M., Persson, M. V., et al. 2016, Nature, 538, 483

Tuomi, M., Jones, H. R. A., Barnes, J. R., Anglada-Escudé, G., & Jenkins, J. S. 2014, MNRAS, 441, 1545

van der Marel, N., van Dishoeck, E. F., Bruderer, S., et al. 2013, Science, 340, 1199

van der Tak, F. F. S., van Dishoeck, E. F., & Caselli, P. 2000, A&A, 361, 327

van Dishoeck, E. F. 2014, Faraday Discuss., 168, 9

van Dishoeck, E. F. & Black, J. H. 1988, ApJ, 334, 771

van Dishoeck, E. F., Blake, G. A., Jansen, D. J., & Groesbeck, T. D. 1995, ApJ, 447, 760

van Dishoeck, E. F. & Helmich, F. P. 1996, A&A, 315, L177

van Dishoeck, E. F., Helmich, F. P., de Graauw, T., et al. 1996, A&A, 315, L349

van Dishoeck, E. F., Herbst, E., & Neufeld, D. A. 2013, Chemical Reviews, 113, 9043

Vasyunin, A. I. & Herbst, E. 2013, ApJ, 769, 34

Walsh, C., Loomis, R. A., Öberg, K. I., et al. 2016, ApJ, 823, L10

Walsh, K. J., Morbidelli, A., Raymond, S. N., O'Brien, D. P., & Mandell, A. M. 2011, Nature, 475, 206

Walsh, M., Xu, L.-H., Lees, R., et al. 2000, Journal of Molecular Spectroscopy, 204, 60

Watanabe, N. & Kouchi, A. 2002, ApJ, 571, L173

Watson, W. D. 1976, Reviews of Modern Physics, 48, 513

Williams, J. P. & Cieza, L. A. 2011, ARA&A, 49, 67

Wilson, T. L. 1999, Reports on Progress in Physics, 62, 143

Winn, J. N. & Fabrycky, D. C. 2015, ARA&A, 53, 409

Woon, D. E. 2002, ApJ, 571, L177

Wright, M. C. H., de Pater, I., Forster, J. R., et al. 1998, AJ, 116, 3018

Zernickel, A., Schilke, P., Schmiedeke, A., et al. 2012, A&A, 546, A87

Nederlandse Samenvatting

Ons sterrenstelsel, de Melkweg, bevat ongeveer 400 miljard sterren. Een van deze sterren is onze zon. Rond de zon draaien acht planeten. Vier hiervan zijn zogenaamde rotsplaneten, wat betekent dat ze een hard oppervlak hebben. Tussen deze rotsplaneten bevindt zich onze thuisplaneet: aarde. De andere vier planeten zijn zogenaamde gasreuzen. Deze planeten zijn veel groter en zwaarder dan de rotsplaneten en bestaan voornamelijk uit gas zonder hard oppervlak. Behalve planeten draaien kleinere rotsen, die asteroïden genoemd worden, en ijs- en rotsformaties genaamd kometen om de zon. Samen vormen de zon, planeten, asteroïden en kometen het zonnestelsel.

In astronomische termen is de zon een niet zo bijzondere ster. Sterker nog, de meeste sterren in de Melkweg lijken veel op onze zon; ze hebben ongeveer dezelfde massa, ze bestaan uit hetzelfde materiaal en ze zijn van vergelijkbare grootte. Ons planetenstelsel is ook niet ongewoon: in de Melkweg hebben het merendeel van de sterren, die vergelijkbaar zijn met onze zon, tenminste één planeet. Hierbij moet vermeld worden dat de combinatie van planeten in ons zonnestelsel wel redelijk uniek lijkt te zijn. Wat het zonnestelsel special maakt, is dat het de enige plek in het heelal is waarvan we zeker weten dat er leven bestaat. Maar, hoe heeft leven hier tot stand kunnen komen? En, misschien wel een spannendere vraag, wat is de kans dat leven bestaat of zal ontstaan op andere plekken in het heelal? Om deze vragen te beantwoorden, moeten we eerste begrijpen hoe zowel het zonnestelsel als leven op aarde zijn ontstaan. We moeten ontrafelen hoe sterren en planeten vormen, maar ook de vorming van moleculen (structuren van atomen die bij elkaar gehouden worden door chemische bindingen) die de bouwstenen vormen voor leven zoals wij het kennen.

De vorming van sterren en planetenstelsels

De plekken waar sterren geboren worden, worden stervormingsgebieden genoemd. Deze gebieden bestaan uit wolken van gas en stof. De meest voorkomende gassen zijn waterstof en helium, maar kleine hoeveelheden zuurstof, koolstof en stikstof zijn ook aanwezig. Deze atomen zijn interessant voor de vorming van leven, aangezien zuurstof, koolstof, waterstof en stikstof de vier meest voorkomende elementen zijn in het menselijk lichaam. Een voorbeeld van een stervormingsgebied is te zien in Figuur 1. Deze spectaculaire afbeelding toont hoe een groot aantal sterren gevormd wordt in de gas en stof structuren van deze regio.

Zodra een stervormingsgebied genoeg in massa is toegenomen wordt deze onstabiel en stort deze in elkaar. Deze ineenstorting wordt veroorzaakt door zwaartekracht die werkt op alle atomen in het gas en stof en deze naar elkaar toe trekt. Na de ineenstorting wordt een jonge ster, een zogenaamde protoster, gevormd in de kern van de stervormingswolk. Rondom de protoster ontstaat een schijf van gas en stof, die materiaal van de stervormingswolk voedt aan de jonge ster. Gedurende dit proces zal een gedeelte van

Figuur 1: De 'Mystieke Berg' in de Carina Nevel gefotografeerd door de *Hubble* Space Telescope. Dit stervormingsgebied staat 7500 lichtjaar van ons af in het zuidelijke sterrenbeeld Carina. De afbeelding toont bergen en pilaren van stof en gas waarin de kraamkamers voor nieuwe sterren verborgen zijn. De pilaren worden gevormd en samengedrukt door de sterke straling van pasgeboren sterren, wat op die manier zorgt voor de vorming van meer nieuwe sterren. Op de toppen van de bergen zijn sterren te zien die omgeven worden door gasstromen. Langs de randen van de wolk zijn stromen geïoniseerd gas te zien, gecombineerd met normaal gas en stof dat verlicht wordt door sterren. De hoge concentratie gas en stof in de binnenste gedeeltes van de bergen en pilaren voorkomt dat sterrenlicht deze gedeeltes van de wolk eroderen. Afbeelding van: NASA, ESA, M. Livio en het Hubble 20th Anniversary Team (STScI).

het materiaal in deze schijf samenklonteren en over tijd zullen deze klonten meer materiaal uit de schijf opvegen en een planeetachtig object vormen. Sommige planeetachtige objecten zullen verder groeien tot planeten, terwijl andere klein blijven. Deze kleinere objecten worden asteroïden genoemd als ze voornamelijk uit rotsachtig materiaal bestaand en kometen als ze voornamelijk uit ijs bestaan. Het gas in de stervormingswolk warmt op doordat energie uit zwaartekracht omgezet wordt naar warmte. Nadat de protoster is gevormd en in zijn kern een temperatuur van ongeveer 1 miljoen graden Celsius bereikt, zal kernfusie beginnen. In eerste instantie fuseren deuterium atomen naar heliumatomen, totdat de temperatuur verder is toegenomen en hoog genoeg is om waterstofatomen te laten fuseren. Dit gebeurt wanneer de temperatuur van de kern ongeveer 10 miljoen graden Celsius is. De hoeveelheid energie die vrijkomt bij kernfusie is gigantisch. Zodra de ster waterstof begint te verbranden, is de straling die de ster uitzendt sterk genoeg om het overgebleven materiaal van de planeetvormende schijf weg te blazen. Op dit punt zijn de ster en het planetenstelsel volledig gevormd. Afhankelijk van de massa van de nieuwe ster wordt het een hoge-massa ster of een lage-massa ster genoemd. In het algemeen hebben lage-massa sterren een massa kleiner of gelijk aan dat van de zon. Hoge-massa sterren kunnen echter meer dan honderd keer zo zwaar zijn als de zon. Afhankelijk van de massa van de ster zullen verschillende elementen gevormd worden in het kernfusieproces. Uiteindelijk, wanneer de ster sterft, worden deze elementen verstrooid door de ruimte en gerecycled in nieuwe sterren en planeten. Een overzicht van het stervormingsproces wordt gegeven in Figuur 2.

De vorming van een ster en planetenstelsel is slechts de eerste stap op weg naar een leefbare planeet zoals aarde. In het geval van het zonnestelsel is 4,6 miljard jaar gepasseerd tussen haar ontstaan en hoe de aarde in haar huidige vorm is. Gedurende deze tijd heeft het stelsel een aantal radicale veranderingen ondergaan. De meest dramatische hiervan zijn een verschuiving van de positie van gasreuzen die zich waarschijnlijk heeft voorgedaan en de botsingen tussen verschillende objecten, die tot op de dag van vandaag voortduren. Voor aarde zijn de meest belangrijke veranderingen de vorming van een atmosfeer en de komst van water aan haar oppervlakte geweest. De aanwezigheid van water op de jonge aarde was waarschijnlijk van groot belang voor het ontstaan van de eerste levensvormen. Mogelijk zijn de moleculen waaruit deze eerste levensvormen zijn ontstaan op aarde gebracht door asteroïden en kometen.

Aangezien we niet direct kunnen onderzoeken hoe de jonge zon en aarde er uitzagen, kijken we naar andere stelsels die op dit moment gevormd worden. Door deze stelsels te observeren en de moleculen die zich daar bevinden te bestuderen krijgen wij een beter idee wat er gebeurde gedurende de vorming van ons eigen zonnestelsel. Om deze stelsels te bestuderen zijn geavanceerde telescopen nodig. Deze telescopen kunnen inzoomen op de gebieden waar nieuwe sterren geboren worden en hebben de gevoeligheid om de vele atomen en moleculen die daar aanwezig zijn te detecteren.

De studie van atomen en moleculen in de ruimte

Het meest krachtige instrument om atomen en moleculen in de ruimte te bestuderen zijn hun spectroscopische vingerafdrukken. Net zoals vingerafdrukken van mensen hebben atomen en moleculen hun eigen unieke vingerafdrukken waarmee ze geïdentificeerd kunnen worden. Deze vingerafdrukken bestaan uit duidelijke patronen van lijnen die gemeten kunnen worden in laboratoriumexperimenten en het spectrum van een atoom of molecuul genoemd worden. Als meerdere atomen en moleculen aanwezig zijn in een bepaald stervormingsgebied, kunnen meerdere spectroscopische vingerafdrukken tegelijk geobserveerd worden. Figuur 3 is een voorbeeld van zo'n spectrum waarin meerdere vingerafdrukken

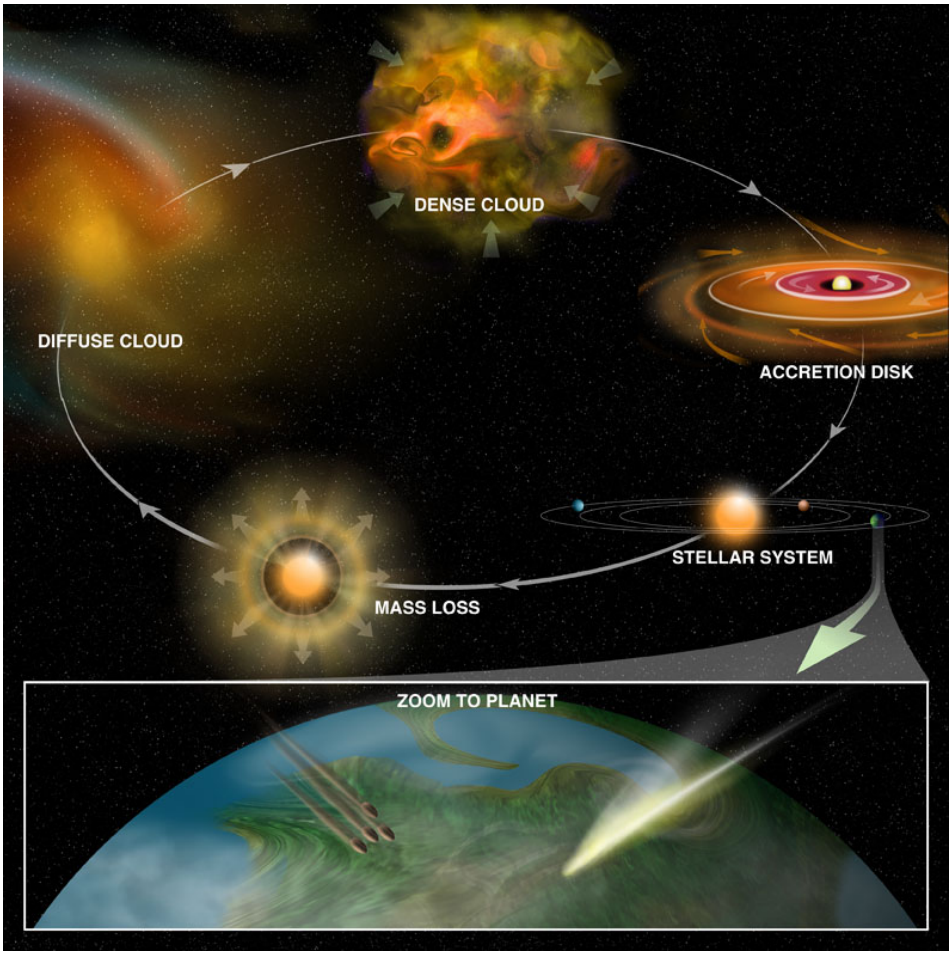

Figuur 2: Schematisch overzicht van ster en planeet vorming in de cyclus van interstellair materiaal. Uit de compacte stervormingswolk (Dense Cloud) die bestaat uit gas en stof, wordt een zogenaamd protostellair object gevormd. Dit stelsel bestaat uit een protoster in het midden omgeven door een roterende schijf van gas en stof (Accretion Disk) die materiaal vanuit de stervormingswolk naar de protoster brengt. Gedurende de evolutie van het stelsel zullen de temperatuur en dichtheid toenemen wat leidt tot de start van kernfusie. In dit proces worden lichte elementen omgevormd tot zwaardere elementen in de binnenste regionen van de ster. Straling van de nieuwgevormde ster verwijdert gas en stof uit de schijf, waarna alleen planeten, kometen en asteroïden overblijven (Stellar System). Een uitvergroting van één van de planeten in dit stelsel laat zien hoe organisch materiaal mogelijk op het oppervlakte van de planeet terecht is gekomen door kometen en asteroïden. Gedurende de evolutie van de ster worden nieuwe geproduceerde elementen de ruimte in gebracht en gerecycled (Mass Loss). Dit kan bijvoorbeeld door zonnewinden die materiaal de ruimte in slingeren of door een supernova wanneer de ster sterft. Het vrijgekomen materiaal wordt uiteindelijk gerecycled in nieuwe stervormingswolken (Diffuse Cloud), waar nieuwe sterren en planeten vormen. Afbeelding van: B. Saxton, NRAO/AUI/NSF.

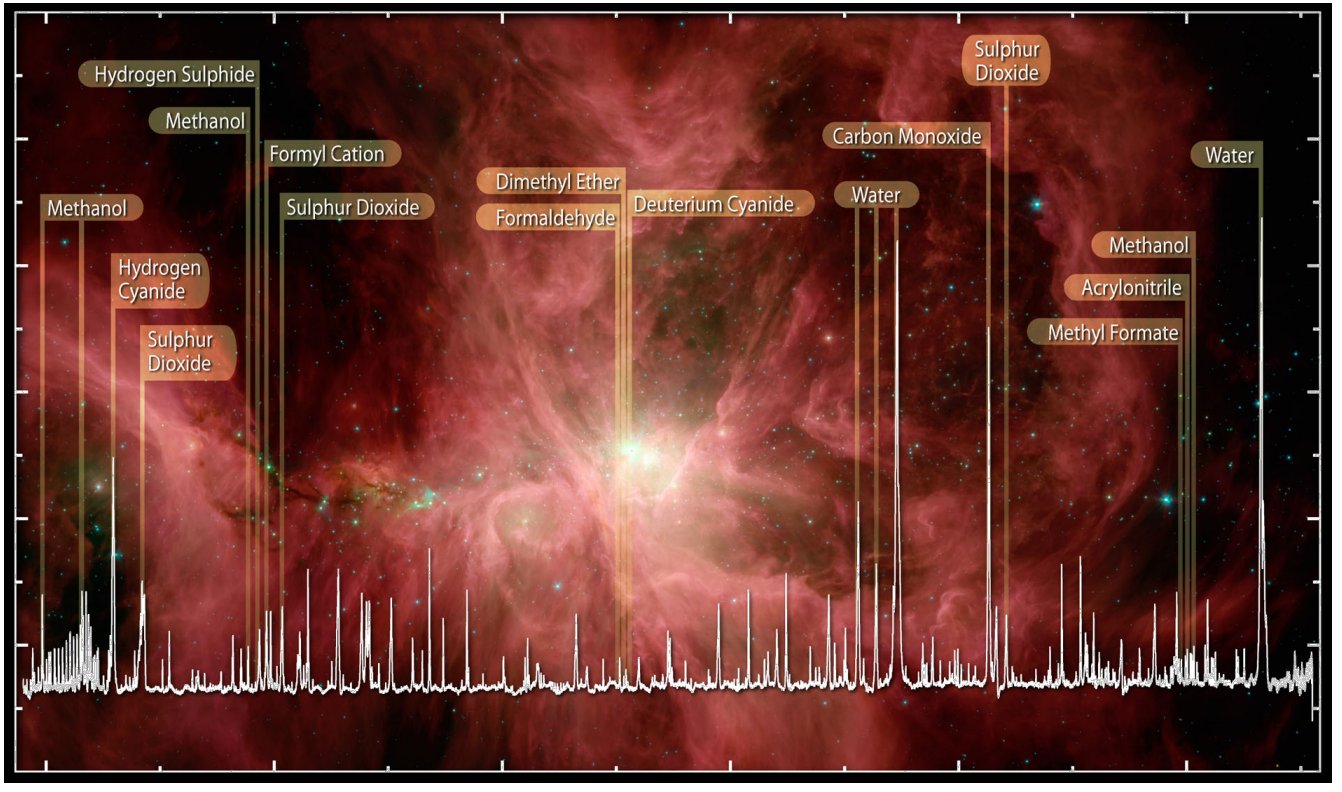

Figuur 3: Een gedetailleerd spectrum (weergegeven in wit) van de Orion Nevel (achtergrond afbeelding). De Orion Nevel staat ongeveer 1300 lichtjaar van ons vandaan, waarmee het één van de meest dichtbijstaande kraamkamers voor nieuwe sterren in de Melkweg is. Dit spectrum is genomen met het HIFI instrument op het *Herschel* Space Observatory. Het patroon aan 'pieken' in het spectrum, emissielijnen genaamd, laat de straling op specifieke golflengtes door specifieke elementen of moleculen zien. Enkele van de meest prominente pieken zijn gelabeld. De gedetecteerde moleculen zijn onder andere: water (H_2O), koolstofmonoxide (carbon monoxide, CO), formaldehyde (H_2CO), methanol (CH_3OH), dimethylether (CH_3OCH_3), waterstofcyanide (hydrogen cyanide, HCN), zwavelmonoxide (sulphur oxide, SO) en zwaveldioxide (sulphur dioxide, SO_2). Afbeelding van: ESA/HIFI/HEXOS; NASA/Spitzer (achtergrond afbeelding).

van verschillende moleculen gedetecteerd zijn in de richting van een stervormingsgebied in het sterrenbeeld Orion. Door de waarnemingen van dit gebied te vergelijken met spectra die in het laboratorium gemeten zijn kan bepaald worden welke moleculen aanwezig zijn in Orion. Veel gedetecteerde moleculen zijn 'organische' moleculen, wat niet betekent dat er leven is, maar dat deze moleculen bepaalde koolstof en waterstofverbindingen hebben. Dit soort moleculen waren waarschijnlijk aanwezig op en rond de jonge aarde. De organische moleculen zijn interessant omdat ze aan de basis staan van de vorming van leven. De identificatie van deze zogenaamde prebiotische moleculen in een stervormingsgebied zoals Orion geeft informatie over hoe deze moleculen gevormd worden.

Dit proefschrift

In mijn proefschrift heb ik de moleculen die aanwezig zijn in verschillende stervormingsgebieden onderzocht. Ik heb de moleculaire inboedel van de verschillende gebieden vergeleken om te bepalen of sommige moleculen specifiek zijn voor een gebied. Op deze manier probeer ik te begrijpen welke condities nodig zijn om bepaalde moleculen te vormen. Tevens heb ik de moleculen bestudeerd die aanwezig zijn in twee kometen in ons zonnestelsel. Door de samenstelling van stervormingsgebieden te vergelijken met deze kometen kan er een link worden gemaakt tussen stervormingsgebieden en ons zonnestelsel. Dit kan omdat kometen materiaal bevatten uit de vroegste tijden toen het zonnestelsel gevormd werd.

Dit proefschrift is verdeeld in vijf hoofdstukken. Het eerste hoofdstuk bevat een introductie van het stervormingsproces en de gerelateerde chemische processen. De volgende hoofdstukken presenteren de resultaten van de analyse van verschillende stervormingsgebieden. De belangrijkste resultaten en conclusie van ieder hoofdstuk zijn als volgt:

Hoofdstuk 2: In dit hoofdstuk heb ik onderzocht in welke hoeveelheden het molecuul methanol (CH_3OH) aanwezig is in het stervormingsgebied NGC 6334I. Dit is een actief hoge-massa stervormingsgebied, waar nieuwe sterren die veel zwaarder zijn dan de zon gevormd worden. We zijn in methanol geïnteresseerd, omdat het één van de meest voorkomende organische moleculen in stervormingsgebieden is en daarom vaak een referentie om te bepalen of de moleculaire samenstelling vergelijkbaar is in verschillende gebieden. Een nauwkeurige bepaling van de hoeveelheid methanol is hiervoor noodzakelijk. De analyse die uitgevoerd wordt in dit hoofdstuk laat zien dat de samenstelling van methanol in NGC 6334I vergelijkbaar is met andere gebieden waar veel hoge-massa sterren gevormd worden, maar anders dan gebieden waar sterren met een massa gelijk aan de zon worden gevormd. Met computermodellen kunnen we bepalen dat dit verschil in de methanol samenstelling veroorzaakt kan worden door verschillen in de temperatuur van het stof dat aanwezig is in stervormingsgebieden. In dat geval is de temperatuur van het stof dat aanwezig is in NGC 6334I waarschijnlijk iets hoger dan het stof in gebieden waar sterren met een massa kleiner of gelijk aan de zon vormen.

Hoofdstuk 3: Dit hoofdstuk vervolgt de karakterisering van de moleculen in NGC 6334I, waarbij nu de focus ligt op simpele moleculen die stikstof atomen bevatten. Ik heb de moleculen methanimine (CH_2NH), methylamine (CH_3NH_2), formamide (NH_2CHO) en methylcyanide (CH_3CN) bestudeerd. Deze moleculen zijn van belang voor de bouwstenen van het leven, aangezien verscheidene stikstofverbindingen essentieel zijn voor de vorming van biologische structuren, zoals nucleobasen, de basis voor DNA. Vooral van het molecuul CH_3NH_2 wordt gedacht dat het van groot belang is. Echter, CH_3NH_2 is slechts in één stervormingsgebied met zekerheid gedetecteerd, namelijk een hoge-massa

stervormingsgebied in het centrum van de Melkweg. Als CH_3NH_2 inderdaad een belangrijke bouwsteen voor biologische moleculen is, dan verwachten we dat het aanwezig is in meerdere stervormingsgebieden. Om te bepalen hoe CH_3NH_2 gevormd wordt en hoe belangrijk het is voor de vorming van complexere moleculen, is het noodzakelijk om dit molecuul in andere stervormingsgebieden naast het centrum van het Melkweg te detecteren. Dit hoofdstuk presenteert de eerste detectie van CH_3NH_2 in NGC 6334I. Dit resultaat geeft aan dat CH_3NH_2 niet een zeldzaam molecuul is. De reden dat het niet eerder gedetecteerd wordt ligt aan de zwakke spectroscopische vingerafdruk van dit molecuul en het is nu pas dat we telescopen hebben die gevoelig genoeg zijn om het signaal te detecteren.

Hoofdstuk 4: In dit hoofdstuk wordt een uitgebreide analyse van de moleculaire samenstelling van de hoge-massa protoster AFGL 4176 gepresenteerd. Het AFGL 4176 systeem is interessant aangezien het één van de weinige hoge-massa protosterren is waar een schijf omheen draait. In vergelijking met lage-massa sterren waar deze schijven vrijwel altijd gezien worden, gebeurt dit zelden voor hoge-massa sterren. In het spectrum van AFGL 4176 werden 23 verschillende moleculen gevonden. De meerderheid van deze moleculen bevat een zuurstofatoom. Een kleinere hoeveelheid moleculen bevat een stikstof of zwavel atoom. Ik heb de moleculaire samenstelling van AFGL 4176 vergeleken met die van andere stervormingsgebieden. Hieruit wordt duidelijk dat AFGL 4176 een grotere overeenkomst vertoont met de lage-massa protoster IRAS 16293-2422B dan met het hoge-massa stervormingsgebied Sagittarius B2(N). De vergelijkbare samenstelling van AFGL 4176 en IRAS 16293-2422B geeft aan dat de productie van moleculen niet veel afhangt van het type object. Aan de andere kant geeft het aan dat de moleculen die gedetecteerd zijn in de twee objecten al gevormd zijn in de stervormingswolk voordat er een protoster is.

Hoofdstuk 5: In dit hoofdstuk bestudeer ik twee kometen, genaamd C/2012 F6 (Lemmon) en C/2012 (ISON). Kometen bestaan uit ijs en stof die hun oorsprong hebben in de vroegste momenten dat het zonnestelsel gevormd werd. In tegenstelling tot planeten, is er weinig gebeurd met het materiaal op kometen sinds deze gevormd zijn. Daarom kunnen kometen gezien worden als fossielen van de schijf waaruit het zonnestelsel gevormd is. Door kometen te bestuderen kan een link worden gemaakt tussen de samenstelling van de stervormingswolk waaruit de zon is ontstaan en het planetenstelsel wat tegenwoordig rond de zon draait. Het grootste gedeelte van hun leven zijn kometen ver weg van de zon en bevroren. Echter, wanneer een komeet dicht bij de zon komt zal het ijs gaan verdampen. In dit hoofdstuk worden waarnemingen van een aantal moleculen getoond die van de komeet afkomen als deze verwarmd wordt door de zon. Ik heb de waarnemingen gemodelleerd om te bepalen welke gedetecteerde moleculen direct van het oppervlakte van de komeet komen, en welke gevormd worden door chemische reacties in het gas. Hierdoor hebben we een beter idee welke moleculen aanwezig waren in de schijf rond de proto-zon.

Gebaseerd op de resultaten van ieder hoofdstuk, is de conclusie van dit proefschrift dat de meeste moleculen die aanwezig zijn in hoge- en lage-massa stervormingsgebieden ook aanwezig zijn in kometen in het zonnestelsel. Dit geeft aan dat moleculen die aanwezig waren toen het zonnestelsel vormde, en waar uiteindelijk leven ontstaan is, ook aanwezig zijn in andere stervormingsgebieden. Dus ook al is er nog geen leven gevonden buiten dat op aarde, de moleculaire bouwstenen voor leven zijn zeker aanwezig in andere stervormingsgebieden. Verdere studies van deze objecten zullen belangrijke informatie opleveren om de vraag te beantwoorden hoe het leven in het zonnestelsel is ontstaan.

Dansk resumé

Vores galakse, Mælkevejen, er hjemsted for omkring 400 milliarder stjerner. Én af disse stjerner er Solen. Omkring Solen kredser otte planeter. Fire af disse planeter er såkaldte klippeplaneter, det vil sige at de hovedsageligt består af klipper og sten og at de har faste overflader. Blandt klippeplaneterne er vores hjem: Jorden. De resterende fire planeter er såkaldte gaskæmper. Disse planeter er langt større og tungere end klippeplaneterne og består hovedsageligt af gas. Udover planeterne kredser mindre klippestykker, kaldet asteroider, samt mindre klumper af is og støv, kaldet kometer, også omkring Solen. Tilsammen udgør Solen, planeterne, asteroiderne og kometerne vores solsystemet.

Set med astronomiske briller er Solen ikke nogen særlig speciel stjerne. Faktisk er de flest af Mælkevejens stjerner meget lig Solen: De har nogenlunde samme masse, de består af det samme slags materiale og de har mere eller mindre samme størelse. Planeter i kredsløb omkring stjerner er heller ikke ualmindelige og det ser ud til at de fleste af Mælkevejens sollignende stjerner omkredses af mindst én planet. Det der virkelig gør solsystemet til noget specielt er kombinationen, og den indbyrdes konfiguration af planeter, samt det faktum, at det er det eneste sted i hele universet, hvor vi er sikre på at der er liv. Med hvad er det, der har gjort det muligt for liv at udvikle sig i solsystemet? Og måske endnu mere spændende, hvad er chancen for at liv har, eller vil, udvikle sig et andet sted i universet? For at besvarer disse spørgsmål er det nødvendigt først at forstå hvordan solsystemet og livet på Jorden blev til. Dette indbefatter at forstå hvordan stjerner og planetsystemer bliver til, men også hvordan de molekyler (strukturer af atomer bundet sammen af kemiske forbindelser) der udgør de basle byggesten for liv, er blevet dannet.

Dannelsen af stjerner og planetsystemer

Områder hvor nye stjerner bliver født kaldes stjernedannelsesområder. Disse områder består af skyer af gas og små støvpartikler. De mest almindelige typer af gas i stjernedannelsesområderne er brint og helium, mens ilt, kulstof og kvælstof kan findes i mindre mængder. Disse grundstoffer er af særlig interesse for liv fordi ilt, kulstof, brint og kvælstof tilsammen udgør de fire mest almindelige grundstoffer i den menneskelige krop. Figur 1 viser et billed af et af Mælkevejens stjernedannelsesområder. På det spetakulære billed ses et utal af nye stjerner, der er i færd med at blive dannet af støvet og gassen i den stjernedannende sky.

Når en stjernedannende sky har opnået en tilstrækkelig masse, bliver den ustabil og begynder at kollapse. Dette kollaps sker som konsekvens af tyngdekraften, der trækker alle skyens atomer og støvpartikler mod hinanden. Efter at skyen er kollapset, dannes en nyfødt stjernes i dens centrum. Denne nyfødte stjerne kaldes for en protostjerne. Omkring protostjernen dannes en skive af materiale, som fodre den nye stjerne med støv og gas fra den stjernedannende sky, og derved hjælper protostjernen med at vokse. Med tiden

Figur 1: Det 'Mystiske Bjerg' i stjernetågen Carina fotograferet af *Hubble*-rumteleskopet. Dette stjernedannelsesområde befinder sig cirka 7500 lysår fra os i stjernebillede Kølen (Carina) på den sydlige himmelkugle. Billedet her viser bjerge og søjler af støv og gas hvori stjernefødselsstuer er gemt. Gassen og støvet i søjlerne bliver trykket sammen og formet på grund af den stærke stråling der udsendes af de nyfødte stjerner. Denne sammenpresning resulterer i endnu flere nydannede stjerner. Ved toppen af søjlerne ses nyfødte stjerne der er skjult i strømme af gas. Langs kanterne af strukturen ses strømme af varm, ioniseret gas. Rundt omkring ses slør af støv og gas der bliver oplyst af lyset fra omkringliggende stjerner. Den høje koncentration af støv og gas i de indre dele af søjlerne forhindre at disse bliver eroderet af strålingen. Foto: NASA, ESA, M. Livio and the Hubble 20th Anniversary Team (STScI).

begynder materialet i skiven at klumpe sammen. I takt med at protostjernen og dens skive udvikler sig, begynder de større materialeklumper i skiven at opsamle de mindre klumper, og vokser på den måde til såkaldte planetesimaler. Nogle af disse planetesimaler vokser sig til planeter mens andre forbliver små. Disse mindre klumper kaldes for asteroider hvis de hovedsageligt består af klippestykker og for kometer hvis de hovedsageligt består af is. Gassen i skyen som protostjernen dannes af bliver opvarmet på grund af tyngdekraften der fortsat trækker skyen sammen og derved omdanner gravitationsenergi til varme. Når protostjernens temperatur når cirka 1 million grader, antændes de første fusionsreaktioner mellem atomkernerne i protostjernens centrum. Disse reaktioner omdanner deuterium til helium indtil temperaturen i den nydannede stjernes centrum når cirka 10 million grader hvorefter også brintfusion antændes. Energien der frigives ved disse reaktioner er enorm og efter at brintfusionsreaktionerne er sat i gang, er strålingen fra den nydannede stjerne så stærk, at resten af materialet i den omkringliggende skrive blæses væk. På dette tidspunkt er den nye stjerne og dens planetsystem færdigdannet. Afhængigt af den nyformede stjernes masse vil den blive kategorisetet som enten en stjerne med høj masse eller en stjerne med lav masse. Som tommelfingerregel har stjerner med lav masse (lavmassestjerner) en masse der er mindre eller sammenlignelig med Solens masse mens stjerner med høj masse (højmassestjerner) kan være mere end 100 gange tungere. Afhængigt af dens masse, vil forskellige grundstoffer blive dannet i stjernen i løbet af dens liv. Når stjernen dør vil disse grundstoffer blive kastet tilbage ud i rummet hvor de bliver inkorporeret i nye stjernedannelsesområder. Figur 2 viser en skematisk oversigt over de forskellige stadier af stjernedannelsesprocessen.

Dannelsen af en stjerne og et planetsystem er kun første skridt på vejen mod en beboelig planet. I solsystemets tilfælde gik der yderligere cirka 4,6 milliarder år fra Solen og planeterne blev dannet til Jorden så ud som vi kender den i dag. I løbet af denne periode gennemgik solsystemet betydelige forandringer. De mest dramatiske af disse forandringer er en formodet ændring af gaskæmpernes baner samt de konstante kollisioner mellem større og mindre objekter som også finder sted i solsystemet i dag. For Jorden omfatter de mest betydningsfulde forandringer bl.a. dannelsen af en atmosfære samt tilstedeværelsen af vand på planetens overflade. Specielt vandet spiller en betydningsfuld rolle fordi det antages, at tilstedeværelsen af vand på den unge Jord var nøglen til fremkomsten af de første livsformer. Potentielt kan molekylerne, der udviklede sig til disse tidligste livsformer, være blevet leveret til Jorden af nedstyrtende kometer eller asteroider.

Fordi vi ikke direkte kan undersøge hvordan solsystemet så ud lige efter det blev til, vender vi i stedet vores opmærksomhed mod lignede systemer, der i øjeblikket er ved at blive dannet. Ved at observere disse systemer og studerer molekylerne der er til stede der, kan vi få en ide om hvad der skete da vores eget solsystem blev dannet. Brugen af avancerede teleskoper, der i stand til at zoome ind på de stjernedannende områder og som kan detektere de mange atomer og molekyler der er til stede der, er nødvendig for at kunne studerer disse systemer.

Hvordan studeres atomer og molekyler i rummet?

Det mest effektive værktøj, når man studerer atomer og molekyler i rummet, er brugen af spektroskopiske fingeraftryk. På samme måde som menneskelige fingeraftryk, har atomer og molekyler deres egne og unikke fingeraftryk, hvormed de kan identificeres. Disse fingeraftryk består af et veldefineret mønster af linjer, der opstår når atomet eller molekylet udsender stråling. Mønstret af linjer kan måles i laboratorieforsøg og kaldes for atomets eller molekylets spektrum. Hvis flere atomer eller molekyler er til stede i et område og

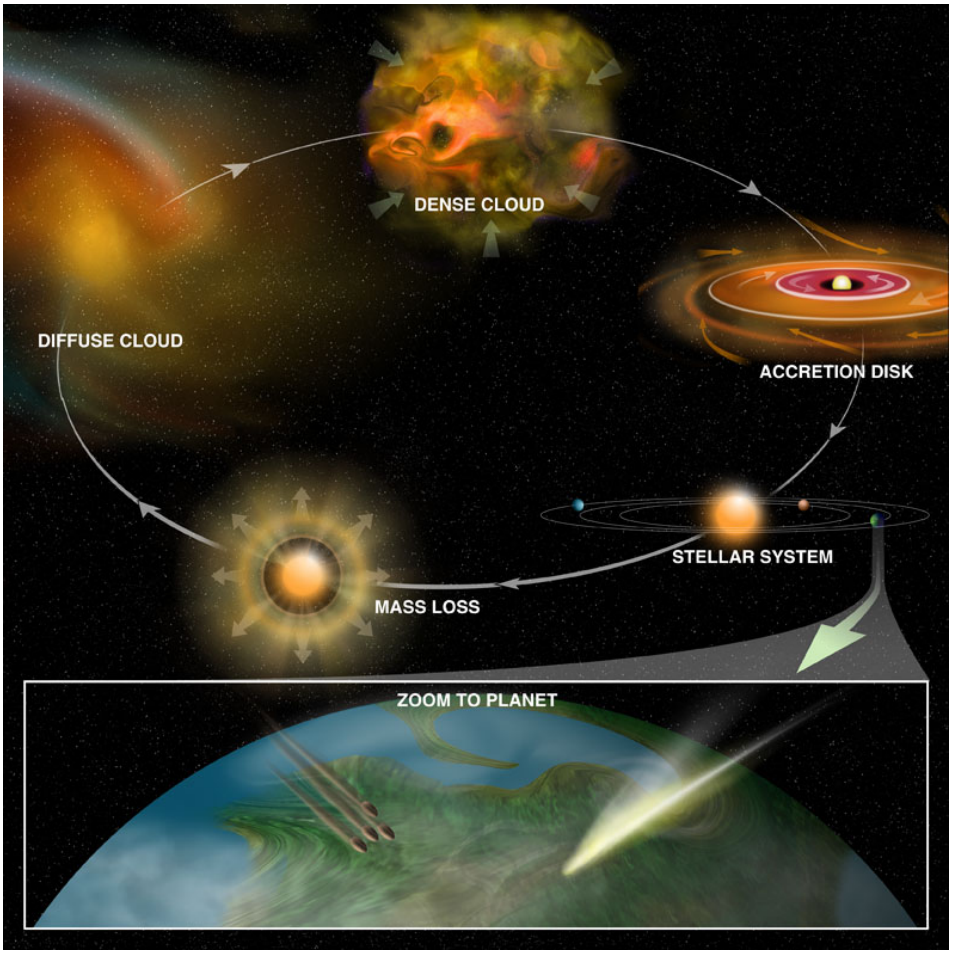

Figur 2: Skematisk oversigt over dannelsesprocessen af en stjerne med tilhørende planetsystem som del af cyklusen af interstellart materiale. Et såkaldt protostjernesystem bliver dannet af en tæt sky af støv og gas (Dense Cloud). Dette system består af en protostjerne der er placeret i midten af en roterende skive af støv og gas (Accretion Disk). Den roterende skive transporterer materiale fra skyen til det nydannede system, og det er af stoffet i skiven, at planet og komet senere i processen vil blive dannet. I takt med, at systemet udvikler sig, stiger tætheden (densiteten) og temperaturen i centrum af protostjernen indtil fusionsreaktioner (kernereaktioner) antændes. I disse reaktioner bliver lette atomkerner omdannet til tungere atomkerner under frigørelsen af enorme mængder af energi. Strålingen fra den nydannede stjerne fjerner gas og støv fra skiven således at kun planeter, kometer og små støvpartikler er tilbage i kredsløb om stjernen (stellar system). Et zoom til en af systemets planeter viser hvordan organisk materiale kan være blevet leveret til planetens overflade via passerende kometer og asteroider. I løbet af stjernens udvikling bliver det materiale der er dannet i dens midte via fusionsreaktioner kastet tilbage ud i det interstellare rum. Processerne der deriver denne udkastning af materiale omfatter vinde fra stjernes overflade men også supernovaeksplosioner når stjerner dør (Mass Loss). Med tiden vil det materiale der er blevet dannet i stjernerne og kastet tilbage ud i rummet, begynde at trække sig sammen igen og danne nye skyer hvorfra nye stjerner kan dannes (Diffuse Cloud). Figur: B. Saxton, NRAO/AUI/NSF.

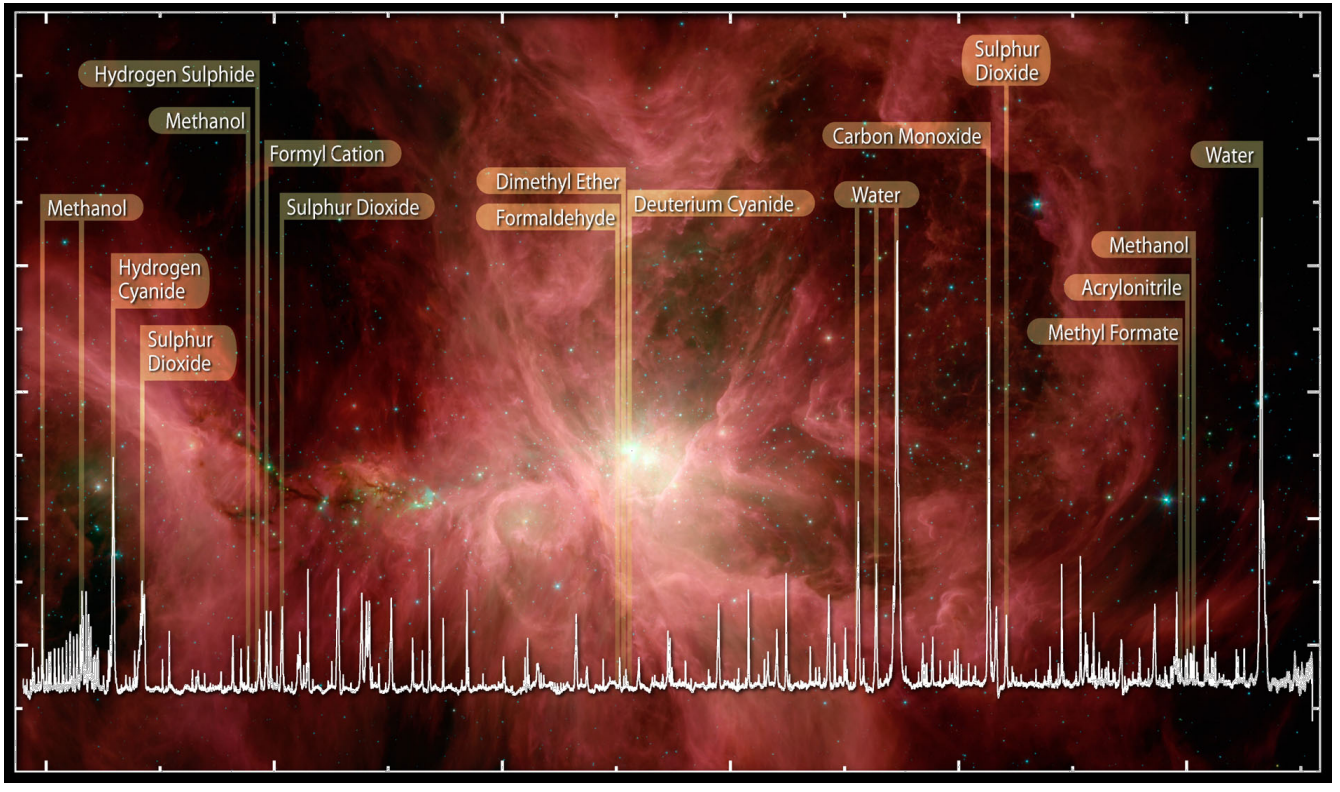

Figur 3: Detaljeret spektrum (vist i hvidt) af Orion stjernetågen (baggrundsbilled). Orion stjernetågen befinder sig cirka 1300 lysår fra os, hvilket gør den til en af de allernærmeste stjernedannende områder i Mælkevejen. Dette spektrum er målt med HIFI-instrumentet ombord på *Herschel*-rumobservatoriet. Mønsteret af linjer der ses i spektrumet opstår fordi atomerne og molekylerne, der er til stede i Orion stjernetågen, udsender lys ved bestemte bølgelængder, der svarer til atomare overgange fra et højere til et lavere energiniveau. Et spektrum som dette kaldes derfor også for et linjespektrum. Nogle af de mest prominente linjer er markerede. Disse indbefatter bl.a. vand (water, H_2O), kulilte (carbon monoxide, CO), formaldehyd (formaldehyde, H_2CO), metanol (methanol, CH_3OH), dimetylæter (dimethyl ether, CH_3OCH_3), blåsyre (hydrogen cyanide, HCN), svovloxid (sulphur oxide, SO) og svovldioxid (sulphur dioxide, SO_2). Figur: ESA/HIFI/HEXOS; NASA/Spitzer (baggrundsbilled).

udsender stråling samtidigt, vil mange spektroskopiske fingeraftryk blive observeret på samme tid. Figur 3 viser et spektrum der indeholder fingeraftrykkene fra mange forskellige molekyler detekteret i retning mod et stjernedannende område der befinder sig i stjernebillede Orion. Ved at sammenligne observationerne af dette område med de spektre der måles i laboratoriet, kan molekylerne, som er til stede i stjernedannelsesområdet, identificeres. Mange af de identificerede molekyler er såkaldte organiske molekyler. Dette navn refererer dog ikke til noget levende, men blot det faktum at molekylerne indeholder konstellationer af brint- og kulstofatomer. Molekyler som disse må også have været tilsted på den unge Jord. De organiske molekyler er af særlig interesse, fordi de er forstadier for vigtige biologiske molekyler. Dannelsen af disse molekyler kan derfor betragtes som det første skridt på vejen mod udviklingen af liv. At observerer disse såkaldte præbiotiske molekyler i et stjernedannelsesområde som Orion kan give vigtig information om, hvordan sådanne molekyler bliver til i stjernedannende miljøer.

Denne afhandling

I min afhandling har jeg undersøgt hvilke molekyler, der er til stede i en række forskellige stjernedannelsesområder. Jeg har sammenlignet de forskellige områders tilstedeværende molekyler for at finde ud af, om nogle molekyler er unikke for bestemte typer af miljøer. Herved forsøger jeg at forstå hvilke betingelser der skal være til stede i et stjernedannende område for at forskellige typer af molekyler kan dannes der. Jeg har også undersøgt den molekylære sammensætning af to af solsystemmets kometer. Ved at sammenligne sammensætningen af molekyler i henholdsvis de stjernedannende områder og kometerne, kan der drages en parallel mellem disse områder og vores solsystem. Dette er muligt, fordi kometerne indeholder materiale fra den sky som solsystemet blev dannet af.

Afhandlingen er opdelt i fem kapitler. I det første kapitel introduceres teorien for stjerne- og planetdannelse samt de kemiske processer der er forbundet hermed. De efterfølgende kapitler præsenterer resultaterne af den dybtgående analyse af hvert af de undersøgte områder. De overordnede resultater samt konklusioner der er draget på baggrund af disse analyser opsummeres som følger:

Kapitel 2: I dette kapitel har jeg undersøgt indholdet af metanol (CH_3OH) i det stjernedannende område NGC 6334I. I dette område dannes nye højmassestjerner, det vil sige stjerner der er mange gange tungere end Solen. Metanol er af særlig interesse fordi det er et af de mest almindelige organiske stoffer der findes i stjernefdannelsesområder. Metanol bruges derfor ofte som reference når den molekylære sammensætning af forskellige områder sammenlignes med hinanden. Det er derfor vigtig at indholdet af metanol i et stjernedannende område er bestemt så præcist som muligt. Analysen som er udført i dette kapitel afslørede, at indholdet af metanol i området NGC 6334I er meget lig indholdet af metanol i områder der ligeledes danner højmassestjerner. Desuden viste analysen at indholdet af metanol i NGC 6334I er forskelligt fra indholdet af stoffet i områder hvor der dannes lavmassestjerner, det vil sige stjerner med masser svarende til Solens. Med udgangspunkt i teoretiske modeller konkluderer kapitelet, at denne forskel i indholdet af metanol kan skyldes, at temperaturen af de støvkorn der er til stede i de forskellige områder, ikke er ens. Hvis det er tilfældet, var temperaturen af støvkornene i NGC 6334I sandsynligvis højere end temperaturen af støvkornene i de områder hvor der dannes lavmassestjerner.

Kapitel 3: Dette kapitel fortsætter undersøgelsen af området NGC 6334I, denne gang med fokus på simple kvælstofholdige molekyler. Specifikt har jeg undersøgt molekylerne metanimin (CH_2NH), metylamin (CH_3NH_2), formamin (NH_2CHO) og acetonitril (CH_3CN). Disse molekyler er interessante i forbindelse med søgen efter livets byggesten fordi kemiske forbindelser der indeholder kvælstof er afgørende for dannelsen af forskellige biologiske strukturer som for eksempel de grundlæggende bestanddele af DNA. I denne forbindelse antages især molekylet CH_3NH_2 for at have en nøglefunktion. Hidtil er CH_3NH_2 kun sikkert detekteret ét sted i rummet, nemlig i et område af højmassestjerner beliggende nær Mælkevejens centrum. Hvis det er korrekt at CH_3NH_2 udgør en vigtig byggesten for biologiske molekyler, er det forventeligt at molekylet er til stede i langt større udstrækning end i blot et enkelt stjernedannende område. For bedre at forstå hvordan CH_3NH_2 dannes, og hvor vigtigt det er for dannelsen af mere komplekse biologiske molekyler, er det vigtigt at forsøge at detekterer CH_3NH_2 i andre områder af Mælkevejen. Dette kapitel præsenterer den første detektion af CH_3NH_2 i området NGC 6334I. Resultaterne der præsenteres i kapitlet indikerer, at CH_3NH_2 sandsynligvis ikke er et sjældent molekyle men at årsagen til at det ikke er detekteret før er, at dets spektroskopiske fingeraftryk er meget svagt.

Kapitel 4: Dette kapitel præsenterer en dybdegående analyse af det molekylære indhold af protostjernen AFGL 4176. AFGL 4176-systemet er interessant fordi det er ét af kun en håndfuld kendte systemer bestående af en højmassestjerne med omkredsende materialeskive. I modsætning til lavmassestjerner, der næsten altid er omgivet af en materialeskive, ses materialeskiver omkring højmassestjerner kun sjældent. Spektrumet af AFGL 4176 afslører tilstedeværelsen af i alt 23 forskellige typer af molekyler. Størstedelen af de tilstedeværende molekyler er iltholdige, det vil sige, at de indeholder mindst et iltatom. Færre af molekylerne indeholder et atom af kvælstof eller svovl. I dette kapitel sammenligner jeg de forskellige molekyler, der er detekteret i henholdsvis AFGL 4176-systemet og i andre stjernedannelsesområder. Herved står det klart, at AFGL 4176 har mere til fælles med lavmasseprotostjernen IRAS 16293–2422B end med det stjernedannende område kaldet Sagittarius B2(N), der danner højmassestjerner. Lighederne mellem de molekylære indhold af højmassesystemet AFG 4176 og lavmassesystemet IRAS 16293–2422B indikerer, at dannelsen af de detekterede molekyler ikke afhænger kritisk af typen af objekt (højmasse- versus lavmassestjerne). En alternativ forklaring på det lignende indhold af molekyler i AFGL 4176 og IRAS 16293–2422B er, at molekylerne er dannet allerede i den stjernedannende sky og derfor til stede i systemet endnu før protostjernen dannes.

Kapitel 5: I dette kapitel har jeg undersøgt de to kometer C/2012 F6 (Lemmon) og C/2012 (ISON). Kometer er klumper af støv og is, dannet omkring det samme tidspunkt og af det samme materiale som solsystemets planeter. I modsætning til planeterne er materialet i kometerne forblevet forholdsvis uforandret siden de blev dannet. Derfor kan kometerne opfattes som en slags fossiler, der indeholder dybfrosne prøver af det materiale som fandtes i den skive af støv og gas som kredsede omkring den nyfødte Sol, og som sidenhen udviklede sig til solsystemet. Studier af kometernes materiale kan derfor give et billede af sammensætningen af de molekyler der var til stede i den stjernedannende sky hvorfra Solen blev født, og det planetsystem der omkredser Solen idag. Det meste af deres liv befinder kometerne sig langt væk fra Solen og deres materiale forbliver derfor dybfrossent. Hvis en komet derimod kommer tæt på Solen, vil dens is begynde at fordampe. I dette kapitel analyserer jeg observationer af en række forskellige molekyler, der frigives fra de to kometer, i takt med at disse opvarmes af Solen. Jeg modellerer observationerne

for at finde ud af hvilke af de detekterede molekyler der frigives direkte fra kometerne, såkaldte forældremolekyler, og hvilke der dannes som følge af reaktioner mellem forældremolekyler, såkaldte dattermolekyler. Herved får vi indsigt i hvilke molekyler der var til stede i materialeskiven der omgav den unge Sol.

På baggrund af de enkelte kapitlers resultater er afhandlings overordnede konklusion, at størstedelen af de molekyler, som er til stede i både høj- og lavmassestjernedannende områder, også er at finde i solsystemets kometer. Dette indikerer, at mange af de samme molekyler der var til stede da solsystemet blev dannet og som efterhånden udviklede sig til livet på Jorden, også er til stede i andre stjernedannelsesområder. Det vil sige, at selvom der endnu ikke er påvist liv noget andet sted i universet end på Jorden, er de grundlæggende byggesten for livets molekyler i høj grad at finde i stjerne- og planetdannende systemer. Ved fortsat at undersøge disse systemer kommer vi tættere på at finde de stykker af information, der stadig mangler, for at spørgsmålet om hvordan og hvorfor livet har kunnet udvikle sig i solsystemet, endelig kan besvares.

English Summary

Our galaxy, the Milky Way, is home to approximately 400 billion stars. One of these stars is the Sun. Orbiting the Sun are eight planets. Four of these are so-called rocky planets, that is, they have solid surfaces. Among the rocky planets is our home: Earth. The remaining four planets are so-called gas giants. These planets are much larger and more massive than the rocky planets and are predominately composted of gas, with no solid surface. In addition to the planets, smaller rocky bodies known as asteroids, and icy bodies known as comets also orbit the Sun. Together, the Sun, the planets, the asteroids and the comets are refereed to as the Solar System.

Astronomically speaking, the Sun is not a very special stars, in fact, the majority of stars in the Milky Way are very similar to the Sun; they have approximately the same mass, they consist of the same material and are of similar size. Orbiting planets are also not uncommon. Actually, the majority of Sun-like stars in the Milky Way seem to host at least one planet, although the combination of planets seen in the Solar System is fairly unique. What truly sets the Solar System apart is the fact that it is the only place, in the entire Universe, where we are sure that there is life. But what enabled life to evolve here? And, maybe even more exciting, what are the chances that life has evolved, or will evolve, somewhere else in the Universe? To address these questions, we first have to understand how the Solar System and life on Earth came to be. This includes understanding how stars and planets are formed, but also understanding the formation of the molecules (structures of atoms bound together by chemical bonds) which provided the basic building blocks of life as we know it.

The formation of stars and planetary systems

The areas were stars are born are known as star-forming regions. These regions consist of clouds of small dust particles and gas. The most common types of gas in the star-forming regions are hydrogen and helium but small amounts of oxygen, carbon and nitrogen are also present. These atoms are of particular interest to life since oxygen, carbon, hydrogen and nitrogen are the four most abundant elements in the human body. An example of a star-forming region is shown in Figure 1. In this spectacular image, a myriad of new stars are being formed within the dusty and gaseous structures of the region.

Once a star-forming cloud is sufficiently massive, it becomes unstable and starts to collapse. This collapse is due to the force of gravity which acts on all the atoms in the gas and dust, pulling them together. After the collapse, an infant star, a so-called protstar, is formed at the centre of the cloud. Surrounding the protostar is a disk of material, which feeds the young star with gas and dust from the parent cloud. Over time, some of the material in the disk starts to clump together. As the star-disk system evolves, the bigger disk-clumps start sweeping up smaller clumps and in this way grow to so-

Figure 1: The 'Mystic Mountain' of the Carina Nebula captured by the *Hubble* Space Telescope. This star-forming region is located 7500 light-years away in the southern constellation of Carina. The image shows mountains and pillars of dust and gas within which stellar nurseries are hidden. Due to the strong radiation coming from the newborn stars the pillars are shaped and compressed, triggering the formation of even more new stars. Streaming from the top of the towering peaks, infant stars buried inside jets of gas can be seen. Along the ridges of the structure, streamers of hot ionised gas can be seen while wispy veils of gas and dust, illuminated by starlight, float around it. The high densities in the inner parts of the pillars protect them from being eroded by radiation. Image credit: NASA, ESA, M. Livio and the Hubble 20th Anniversary Team (STScI).

called planetesimals. Some of the planetesimal continue to grow and eventually become planets while other remain small. These smaller clumps are refereed to as asteroids if they are mostly rocky and comets if they are mostly icy. The gas in the cloud which forms the protostar is heated due to the accretion of material onto the forming star. In this process gravitational energy is converted to heat. Once the protostar is formed and the temperature at its centre exceeds approximately 1 million degrees Celsius, nuclear fusion reactions begin to take place. In these reactions, deuterium is fused into helium until the temperature becomes high enough to also ignite hydrogen fusion. This happens when the temperature at the center of the star reaches approximately 10 million degrees Celsius. The energy released from the nuclear fusion processes is enormous and after the hydrogen fusion has kicked in, the radiation coming from the newborn star is so strong that the remaining material in the disk is cleared out. At this point, the star and planetary system is fully formed. Depending on the mass accumulated by the newly formed star, it will be referred to as either a high-mass star or a low-mass star. Generally speaking, low-mass stars have masses which are lower or similar to the Sun. High-mass stars on the other hand, may be more than 100 times heavier than the Sun. Depending on the mass of the star, different elements will be formed in its centre. Eventually, when the star dies, these elements will be recycled back into space where they will be incorporated into new stars and planets. An overview of the star formation process is presented in Figure 2.

The formation of a star and planetary system is only the first step on the road to forming a habitable planet like Earth. In the case of the Solar System, 4.6 billion years has passed from the Sun and planets were formed to the Earth we inhabit today. During this time, the system has undergone considerable changes. The most dramatic of these include a proposed shift in the position of the giant gas planets and the continues collisions between bodies which still occur in the Solar System today. For the Earth, the dominant changes include the formation of an atmosphere and the presence of water on the surface of the planet. It is thought that the presence of water on the young Earth was key for the emergence of the first forms of life. Potentially, the molecules which evolved into these earliest forms of life may have been delivered to Earth by impacting comets or asteroids.

Because we cannot directly investigate what the newly formed Sun and Earth looked like, we turn our attention towards other systems which are currently being formed. By observing these systems and studying the molecules which are present there, we get a better idea of what may have happened during the formation of our own Solar System. In order to study these systems, advanced telescopes are needed. These telescopes are able to zoom in on the regions where the new stars are being formed and have the sensitivity to detect the multitude of atoms and molecules which are present there.

Studying atoms and molecules in space

The most powerful tool when studying atoms and molecules in space is the use of spectroscopic fingerprints. Just like human fingerprints, atoms and molecules have their own and unique fingerprints by which they can be identified. These fingerprints consist of a well-defined pattern of lines that arise when the atom or molecule emits radiation. The patterns of lines can be measured in laboratory experiments and are referred to as the spectrum of the atom or molecule. If multiple atoms or molecules are emitting radiation in the same region, many spectroscopic fingerprints will be observed at the same time. Figure 3 is an example of a spectrum containing the fingerprints of many different molecules detected towards a star-forming region located in the constellation Orion. By comparing the observations of this region with the spectra that are measured in the laboratory, the molecules which are present in Orion can be identified. Many of the

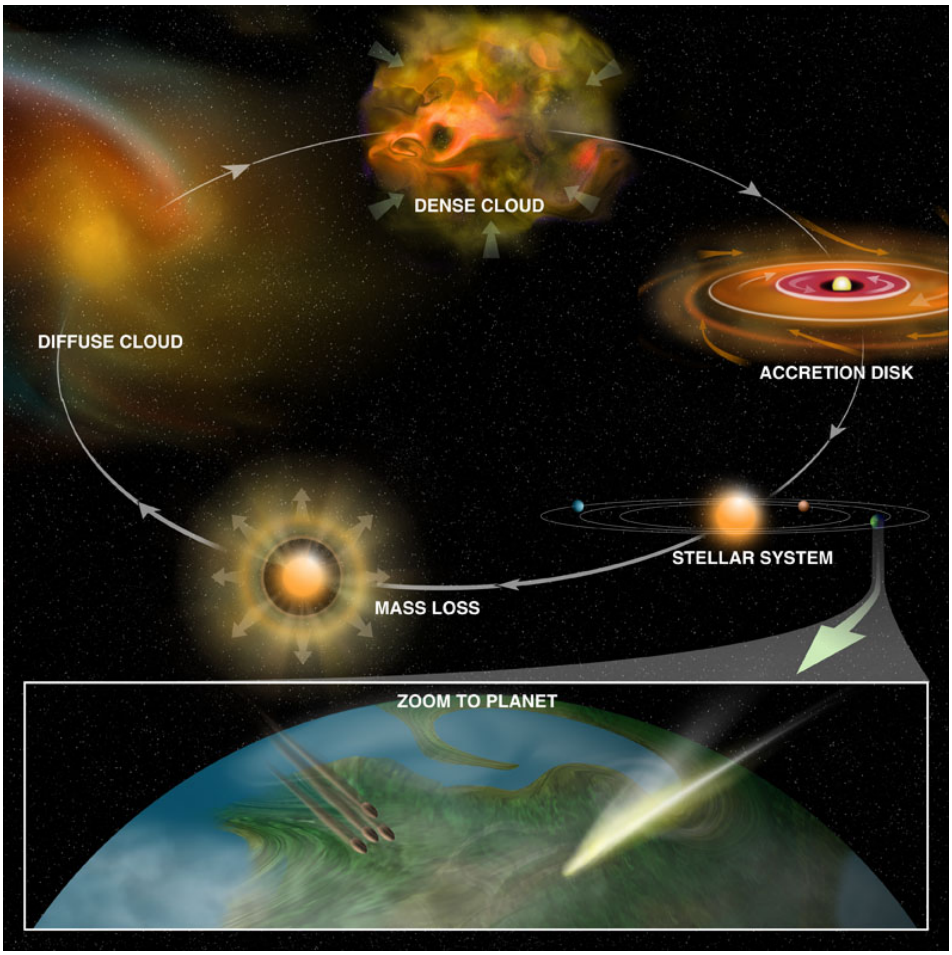

Figure 2: Schematic view of the formation of a star and planetary system in the life cycle of interstellar material. From a dense cloud of dust and gas, a so-called protostellar system is formed. This system consists of a central protostar and a rotating disk of dust and gas that accretes material from the parent cloud. Planets and comets will eventually form from the material in the accretion disk. As the system evolves, the temperature and density of the forming star increase, igniting thermonuclear reactions. In this process, light elements are processed into heavier ones in the stars interior. Radiation from the newly formed star removes gas and dust from the disk leaving only planets, comets and small interplanetary dust particle in orbit around the star. A zoom to one of the planets in the system shows how organic material may have been delivered to the planetary surface by passing comets and asteroids. As the star evolves, the enriched materials which are formed in its centre are recycled back into interstellar space in processes known as mass loss. These include the continuous removal of material from the stellar surface via stellar winds but also supernova explosions as the stars die. Finally, the material which has been recycled in the stars and blown back into interstellar space, accumulates into new clouds from which new stars can form. Image credit: B. Saxton, NRAO/AUI/NSF.

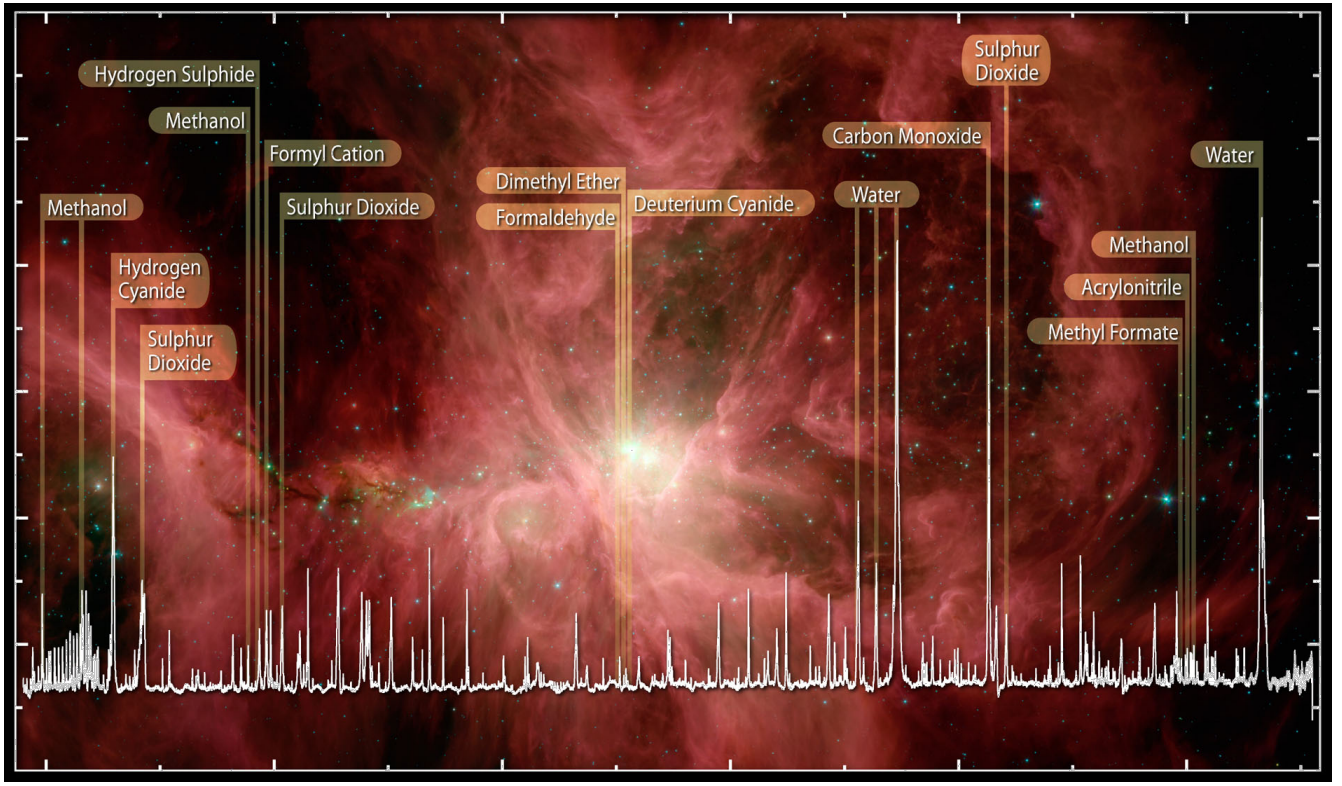

Figure 3: Detailed spectrum (shown in white) of the Orion Nebula (background image). The Orion Nebular is located approximately 1300 light years away, making it one of the nearest stellar nursery in our Milky Way galaxy. This spectrum is recorded by the *Herschel* Space Observatory using the HIFI instrument. The dense pattern of 'spikes', known as emission lines, seen in the spectrum, represents the emission of light at particular wavelengths by particular atoms and molecules in the Orion Nebula. Some of the most prominent lines are labelled. The detected species included: water (H_2O), carbon monoxide (CO), formaldehyde (H_2CO), methanol (CH_3OH), dimethyl ether (CH_3OCH_3), hydrogen cyanide (HCN), sulphur oxide (SO) and sulphur dioxide (SO_2). Image credit: ESA/HIFI/HEXOS; NASA/Spitzer (background image).

detected molecules are 'organic' molecules, which does not mean that anything is alive, but simply that they contain particular arrangements of carbon and hydrogen atoms. Similar molecules must have been present on the early Earth. The organic molecules are of particular interest because they are precursors of important biological molecules and therefore can be considered the first step on the way to forming life. Seeing these so-called prebiotic molecules in a star-forming region such as Orion can provide key information as to how they are formed in star-forming environments.

Thesis overview

In my thesis I have investigated the molecules which are present in a number of different star-forming regions. I have compared these molecular inventories to each other in order to find out if different molecules are specific to particular regions. By doing so, I try to understand what conditions are needed for the different molecular species the be formed. I have also investigated the molecular composition of two Solar System comets. By comparing the composition of the star-forming regions with that of the comets, a direct link between the star-forming regions and the Solar System can be made. This is possible because the comets contain remnants of the material from which the Solar System formed.

The thesis is divided into five chapters. The first chapter presents an introduction to star formation and the chemical processes related thereto. The subsequent chapters present the results of the in-depth analysis of each of the studies regions. The main results and conclusions of these chapters are summaries as follows:

Chapter 2: In this chapter, I have investigated how much of the molecule methanol (CH_3OH) is present in the region NGC 6334I. This region is a high-mass star-forming region, actively forming new, massive stars, much heavier than the Sun. Methanol is of particular interest because it is one of the most abundant organic species in star-forming regions and therefore is often used as a reference when comparing the molecular composition of different sources to each other. An accurate characterisation of methanol is therefore essential. The analysis in this chapter revealed that the methanol composition of NGC 6334I is similar to the composition of other regions which are forming massive stars but different from systems forming stars with masses similar to the Sun. Based on models, we conclude that this difference in methanol content may be due to a difference in the temperature of the dust grains in the different regions. If that is the case, the temperature of the dust grains in NGC 6334I was likely higher than the temperature of the dust grains in the regions which form stars similar to the Sun.

Chapter 3: This chapter continues the exploration of the molecular composition of NGC 6334I, this time focusing on simple molecules which contain nitrogen atoms. Specifically, I have studied the molecules methanimine (CH_2NH), methylamine (CH_3NH_2), formamide (NH_2CHO) and methyl cyanide (CH_3CN). These molecules are of particular interest when searching for the building blocks of life because nitrogen-containing bonds are essential for the formation of different biological structures, for example, nucleobases which are the basic components of DNA. In particular, the molecule CH_3NH_2 is thought to be a key molecule. However, so far CH_3NH_2 has only been securely detected at one location, namely in a region forming high-mass starts located near the Galactic Center. If it is true that CH_3NH_2 is an important building block for biological molecules, we expect it to be present in many more star-forming regions. To better understand how CH_3NH_2 is formed and how significant it is for the formation of more complex species,

it is important to detect CH_3NH_2 in other regions of the Galaxy. This chapter reports the first detection of CH_3NH_2 towards NGC 6334I. These results indicate that CH_3NH_2 is not a very rare molecule and that the reason why we have not detected it before is because its spectroscopic fingerprint is weak and only now do we have telescopes sensitive enough to detect it.

Chapter 4: This chapter presents an extensive analysis of the molecular inventory of the high-mass protostar AFGL 4176. The AFGL 4176 system is interesting because it is one of the few known examples of a high-mass protostar which has a disk surrounding it. In contrast to low-mass stars which are almost always surrounded by a disk, disks around high-mass stars are rarely observed. Studying the spectrum of AFGL 4176, revealed the presence of 23 different molecular species. The majority of the detected molecules are oxygen-bearing, that is to say, they contain at least one oxygen atom. Fewer of the detected molecules contain an atom of nitrogen or sulphur. I compare the molecules detected in AFGL 4176 with the molecules detected in other star-forming regions. When doing so, it becomes clear that AFGL 4176 has more in common with the low-mass protostar IRAS 16293–2422B than with the high-mass star-forming region called Sagittarius B2(N). The similar molecular composition of AFGL 4176, which is a high-mass protostar, and IRAS 16293–2422B, which is a low-mass protostar, indicates that the production of molecules does not depend at lot on the type of sources. Alternatively, the molecules observed towards AFGL 4176 and IRAS 16293–2422B may have been formed already in the cloud before the protostars appear.

Chapter 5: In this chapter, I have investigated two comets, called C/2012 F6 (Lemmon) and C/2012 (ISON). Comets are bodies of dust and ice that were leftover from the time when the planets of the Solar System were formed. In contrast to the planets, the material in the comets has remained fairly unprocessed since they were formed. Therefore, the comets can be seen as a sort of fossils, each containing a frozen sample of the material in the disk which eventually evolved into the Solar System. Studying the material in the comets can therefore provide a link between the composition of the cloud of dust and gas from which the Sun formed and the planetary system which orbits the Sun today. For most of their life, the comets are far away from the Sun and remain deeply frozen. However, if a comet gets close to the Sun, its ice will start to evaporate. In this chapter, observations of a number of different molecules which are released from the comets as they are heated by the Sun are presented. I model the observations in order to figure out which of the detected molecules are released from the comets directly, so-called parent molecules, and which are formed from reactions between parent molecules, so-called daughter molecules. By doing so, we get a better understanding of the molecules which were present in the disk surround the proto-Sun.

Based on the results of the individual chapters, the overarching conclusion of the thesis is that the majority of the molecules which are present in both high- and low-mass star-forming regions, are also present in the Solar System comets. This indicates that many of the same molecules which were present when the Solar System formed, and which eventually evolved into life on Earth, are also present in other star-forming regions. So even though life has still not been detected in any other place than on Earth, the basic building blocks for the molecules of life are definitely present in other forming systems. Continued studies of these systems may provide the key pieces of information need to answer the question of how and why life was able to evolved in the Solar System.

List of Publications

Refereed publications

Low levels of methanol deuteration in the high-mass star-forming region NGC 6334I
E. G. Bøgelund, B. A. McGuire, N. F. W. Ligterink, V. Taquet, C. L. Brogan, T. R. Hunter, J. C. Pearson, M. R. Hogerheijde, E. F. van Dishoeck, 2018, Astronomy & Astrophysics, 615, 88

Exploring the volatile composition of comets C/2012 F6 (Lemmon) and C/2012 S1 (ISON) with ALMA
E. G. Bøgelund & M. R. Hogerheijde, 2017, Astronomy & Astrophysics, 604, 131

Submitted publications

*Methylamine and other simple N-bearing species in the hot cores NGC 6334*I *MM1 – 3*
E. G. Bøgelund, B. A. McGuire, M. R. Hogerheijde, E. F. van Dishoeck, N. F. W. Ligterink, Astronomy & Astrophysics, under review

Molecular complexity on disk-scales uncovered by ALMA: The composition of the high-mass protostar AFGL 4176
E. G. Bøgelund, A. G. Barr, V. Taquet, N. F. W. Ligterink, M. V. Persson, M. R. Hogerheijde, E. F. van Dishoeck, submitted to Astronomy & Astrophysics

Curriculum Vitae

I was born at Hvidovre Hospital, Denmark, on the 12th of November 1987 and grew up in Valby, a suburbial area located in the south-western corner of the Copenhagen Municipality. As most kids, I went through a number of careers I wanted to pursue when I grew up, including becoming an actress, a hairdresser and a veterinarian, whereas scientist or astronomer never made the list. This gradually changed as I worked my way through primary and secondary school and discovered that I had a talent for the natural sciences. In addition, visits to Experimentarium (an interactive science museum in Copenhagen), in particular accompanied by my granddad, who worked as a physics teacher and was excellent at explaining everything from the colours on the surface of soap bubbles to why it doesn't hurt to lie on a bed of pointed nails (if you do it right!), taught me the playful nature of these sciences.

From 2004 to 2007 I attended Vestre Borgerdyd Gymnasium where I followed the exact science track. Although both biology and chemistry had my fancy during my high school years, I liked geography the best and especially the field of meteorology fascinated me. After learning that meteorology is categorised as a subfield of geophysics, my path seemed set and I enrolled in the physics program at the University of Copenhagen. However, my ambition of studying geophysics did not last long into the first year of the bachelor program where many other fields of physics, including astronomy and biophysics, caught my attention. Finally, I decided on particle physics and in the summer of 2010, I graduated from the bachelor program with a project on the interactions of gauge bosons under the supervision of Dr. Jørgen Beck Hansen.

It was not until halfway through my master studies that astronomy again caught my attention. This was at the time where I had to pick a topic for my master project. After meeting with Dr. Jes Jørgensen at the Center for Star and Planet Formation, I was quickly convinced that I wanted to do a project with him. We decided on a project which focused on identifying and classifying young stellar objects using data from the Spitzer Space Telescope. As I had only limited experience with astronomy, having followed only introductory courses during my bachelor, I spent the second half of my master catching up on relevant astrophysical courses.

Towards the end of my master studies, an invitation to apply for the first edition of the Leiden/ESA Astrophysics Program for Summer Students (LEAPS) landed in my mailbox. The summer school was to take place in the summer of 2013, which clashed horribly with the submission deadline for my master thesis. Nonetheless, Jes convinced me that I should apply for the program and I am very happy he did! I was accepted into the program and enjoyed three exciting months in Leiden where I worked with Dr. Lynn Carlson on a project aimed at characterising star-forming regions in the Small Magellanic Cloud.

The time I spent at Leiden Observatory during the LEAPS summer school, opened my eyes to the possibility of pursuing a PhD at the institute and in the winter of 2013

I applied to the graduate program at Leiden University. After a second visit, in the beginning of 2014, I was convinced that Leiden was the place for me and I was very happy to accept the offer of a PhD position with Prof. dr. Michiel Hogerheijde, starting in June 2014. During my PhD I have attended schools in the Netherlands, Germany, Switzerland, France and Belgium and presented my work at conferences in Berlin, London and Indian Wells, California, with support from the Leids Kerkhoven Bosscha Fonds.

After obtaining my PhD, I will be seeking challenges outside of the world of classic academia and I am very excited at the prospect of applying and further developing the skills I have acquired during my PhD in a broader societal context.

Acknowledgements

The PhD experience has presented me with some of the biggest challenges of my life and there are so many wonderful people I need to thank for their help and support during this time, as I am certain I would not be where I am today if it was not for them.

First of all, I want to thank my supervisors Michiel and Ewine for giving me time and allowing me to grow with the PhD, both professionally and personally. Without your patience, guidance and understanding, completing this thesis would have been an impossible task. To my fellow PhD's with Michiel: Nico, Mason, Leon and Jeroen, you guys are the best colleagues and friends one can wish for and I am so grateful to have met you. Thank you for sharing meetings, offices, summer schools, winter schools and conferences. The four of you can brighten up even the rainiest of Monday mornings and have made the many hours spent in the office both pleasant and fun. To Leon and Jeroen, I wish you both the best of luck with finishing your dissertation. To Jeroen, thank you also for proofreading my samenvatting and for providing bunny care when needed. Mason, we embarked on the PhD journey together and it has been a true pleasure sharing this experience with you. Nico, you have become one of my closest friends and your support has meant the world to me. No matter where our paths take us in the future, I am sure I can always count on you. I would also like to thank the Allegro team for always having time to answer questions related to ALMA and the processing of interferometric data, in particular, Markus Schmalzl and Luke Maud for expert advice on data calibration. Also, a special thanks to Brett McGuire, Vianney Taquet and Andrew Barr for their collaboration on various projects.

A big thank you to the people who keep the institute running smoothly. In particular the secretariat staff for their support on a variety of day-to-day activities and Erik Deul and the computer systems support group for quickly resolving any technical problem I have faced over the past years. Also, I would like to thank the members of the borrel and social committees for arranging Friday borrels, Christmas lunches, Sinterklaas events and summer barbecues. Your hard work made social time at the Observatory a lot of fun. Finally, I would like to thank Xander Tielens and the PBC for support and encouragement, especially during the times when the completion of my thesis seemed very far off.

To the current and past PhDs and postdocs of the Sterrewacht: Vincent, Claudia, Aayush, Mieke, Arthur, Merel, Sierk, Lukasz, Eleonora, Valeriya, Gabi, Jorryt, Ko-Ju, Kirsten, Danna, Michal, Nadia, Anna-Lea, Heather, Nienke, Ricardo, David, Cam, Emanuelle, Pablo, Margot, Magnus, Mihkel, Maria, Anna, Andreas and many, many others, thank you for the many scientific and friendly discussions over coffee or in the corridors and for making the Observatory an amazing place to work. A special thank you to Allison for lending an understanding ear at the time when completing my PhD seemed an endless uphill climb and for introducing me to the concept of emergency wine. To Jeroen for sharing your love of beer and for putting up with my feeble and mispronounced attempts at Dutch during 'Dutch lunch'. And to Niels for your help and moral

support during the ups and downs I have encountered over the past years.

To Mike, Charlotte, Chris, Zoë, Geert Jan and Andrew: Thank you for your friendship, for the talks, the lunches, coffee breaks and borrels, for the nights with movies (although some of you have truly horrible tastes!) and boardgames, for dinners, delicious cakes, proper English breakfast and servings of tea, for carrying a countless number of boxes when moving needed to be done and for letting me cuddle your cats. Leiden is not the same without you.

Til mine med-eksildanskere i Leiden: Chris, Eistrup og Henriette. Jeres tilstedeværelse bragte Leiden lidt tættere på det kendte derhjemme. En helt særlig tak til Ann-Sofie for altid at have tid til at lytte, for din støtte, for at gide at stå op søndag morgen og tage i sportscenteret med mig, for altid at sende postkort når du er ude og for gavmildt at dele ud af dine hækle-færdigheder.

Also outside of the Observatory there are people who have filled my life in Leiden with joy. When I first moved to the city I was fortunate enough to find a house with the best house mates one can dream of: Eva and Ilo. I will forever be grateful to you for taking a chance with a non-dutch house mate and inviting me to live with you. You made my arrival in Leiden easy and comfortable and provided a home, complete with hamster. I'm so happy to have met you and look forward to sharing many more dinners, parties and FouLaNi dates with you in the future. A very big thank you also to Wijnand for helping me with the design of my thesis cover, but even more so for your kindness, warm heart and cheerfulness. To my team mates at Volleybal Club Oegstgeest: Thank you for making me feel welcome from the very first day, for the teamavonds and high teas and for the many trips around Zuid-Holland for Friday night matches. Playing volleyball with you is the best stress-cure imaginable.

Moving to Leiden was both exciting and scary and it was not without a heavy heart that I left Copenhagen and my friends. Til alle mine smukke, kloge og helt igennem vidunderlige veninder: I er mit sikkerhedsnet, I lytter, støtter og trøster, I er med mig lige meget hvor min vej fører mig hen. Jeres venskab betyder alt. Til mine efterskolepiger: Anja, Marlene, Julie, Mia og Mette, selvom der nogle gange går alt for lang tid imellem at vi ses, kan jeg altid stole på at I er der. Til pigerne fra VB: Louise, Laura, Mobi og Anja, tak for altid at stille op når jeg kommer forbi København og at tage jer tid til at komme og besøge mig i Leiden. Til fysikpigerne: Bitten, Mette, Simone, AK, Turi, Pernille, Maria og Mathilde, jeg er ubeskriveligt glad for at I alle valgte fysikstudiet netop dét år og jeg ved, at selvom vi blev spredt for all vinde efter vores tid i København, er I aldrig længere væk end en skypebesked eller snapchat. At følge med i jeres dagligdag og at vide at I altid står klar med virtuelle kram giver mig en ubeskrivelig tryghed.

Til min familie: Jeres støtte og opbakning har bragt mig hertil, og jeg er jer evigt taknemmelig.